# Ultrafast electron dynamics and the role of screening

Im Fachbereich Physik
der Freien Universität Berlin
eingereichte Dissertation

**Daniel Wegkamp**

November 2014

This work was performed between October 2009 and November 2014 in the Department of Physical Chemistry (Professor Martin Wolf) at the Fritz Haber Institute of the Max Planck Society.

Berlin, November 2014

Erstgutachter:    Prof. Dr. Martin Wolf

Zweitgutachter: Prof. Dr. Martin Weinelt

# Abstract

This thesis focuses on the *ultrafast dynamics of electronic excitations* in solids and how they are influenced by the *screening of the Coulomb interaction* between charged particles. The impact of screening on electron dynamics is manifold, ranging from modifications of electron-electron scattering rates over trapping of excess charges to massive renormalisation of electronic band structures. The timescales of these dynamical processes are directly accessible by femtosecond time-resolved photoemission and optical spectroscopy. Three exemplary systems are investigated to shed light onto these fundamental processes:

Vanadiumdioxide undergoes a phase transition from a monoclinic insulator to a rutile metal. Apart from temperature, doping and other influences, the insulator-to-metal transition can also be driven by photoexcitation. This, in the past, gave rise to a controversy about the timescales of structural and electronic transition and raised the question which of them constitutes the driving mechanism. Using time-resolved photoelectron spectroscopy, it is shown that the electronic band gap of the insulator collapses instantaneously with photoexcitation and without any structural involvement. The reason is a change of screening due to the generation of photoholes. At the same time, the symmetry of the lattice potential changes, as seen by coherent phonon spectroscopy. This potential change is likely to initiate the structural phase transition from monoclinic to rutile structure. However, the initial non-equilibrium situation can be described by a metallic electronic structure with the atoms still in the monoclinic lattice positions.

The $SrTiO_3$/vacuum interface exhibits a two-dimensional electron gas (2DEG), which is delocalised within the surface plane, but localised perpendicular to it. The lower dimensionality changes the form of the screened Coulomb interaction and the phase space within the 2DEG, leading to modified hot carrier lifetimes. These are investigated by time-resolved photoemission spectroscopy: The predicted 2D behaviour is confirmed and two distinct final states within the unoccupied electronic band structure are discovered. Furthermore, the population of the 2DEG is transiently increased by photoexcitation from localised in-gap states into the 2DEG.

A different type of screening by dipole moments in amorphous ice layers, is exploited to stabilise and trap electrons within the polar medium in front of a metal surface. Thereby, the mean free path of low energy electrons in amorphous ice is estimated. Moreover, the trapped electrons are used to drive a chemical reaction: A persistent modification of the surface electronic structure of the ice layer is explained via the 'dielectron hydrogen evolution reaction'.

Understanding the role of screening in these systems allows to explain seemingly unrelated effects, like trapping of excess electrons in ice and the insulator-to-metal transition in $VO_2$, within the same concept.

# Kurzfassung

Diese Arbeit beschäftigt sich mit *ultraschneller Dynamik elektronischer Anregungen* in Festkörpern und dem Einfluss der *Abschirmung der Coulomb-Wechselwirkung* zwischen geladenen Teilchen. Die Auswirkungen dieser Abschirmung sind vielfältig und reichen von der Modifizierung von Elektron-Elektron-Streuraten über das Einfangen von Überschussladungen bis hin zur vollständigen Renormierung der elektronischen Bandstruktur. Zeitaufgelöste optische und Photoelektronenspektroskopie kann die Femtosekunden Zeitskala dieser dynamischen Prozesse direkt erfassen. Drei Beispielsysteme werden untersucht, um solche grundlegenden Prozesse zu beleuchten:

Vanadiumdioxid weist einen Phasenübergang von monoklinem Isolator zu rutilem Metall auf. Neben Temperatur, Dotierung und weiteren Einflüssen kann man den Phasenübergang auch durch Anregung mit Licht induzieren. Dies führte zu einer kontroversen Diskussion über die Zeitskalen des strukturellen und elektronischen Phasenübergangs und warf die Frage auf, welcher der beiden die treibende Kraft darstellt. Durch zeitaufgelöste Photoelektronenspektroskopie wird gezeigt, dass sich die Bandlücke des Isolators sofort mit der Photoanregung schließt, ohne dass die Gitterstruktur beteiligt ist. Der Grund ist eine Änderung der Abschirmung der Coulomb-Wechselwirkung durch photoinduzierte Löcher. Die Spektroskopie von kohärenten Phononen zeigt, dass sich gleichzeitig das Gitterpotential ändert. Diese Potentialänderung initiiert vermutlich den Phasenübergang von monokliner zu rutiler Struktur. Die anfängliche Ungleichgewichtssituation kann dennoch durch eine metallische elektronische Struktur beschrieben werden, während die Atome sich an ihren monoklinen Gitterplätzen befinden.

An der $SrTiO_3$/Vakuum-Grenzfläche existiert ein zwei-dimensionales Elektronengas (2DEG), welches entlang der Oberfläche delokalisiert, senkrecht dazu jedoch lokalisiert ist. Die Form der abgeschirmten Coulomb-Wechselwirkung und der Phasenraum im 2DEG sind durch die niedrige Dimensionalität modifiziert, was zu veränderten Lebensdauern von heißen Ladungsträgern führt. Diese Lebensdauern werden mit zeitaufgelöster Photoelektronenspektroskopie untersucht: Das vorhergesagte 2D-Verhalten wird bestätigt und es werden zwei ausgeprägte Endzustände in der unbesetzten elektronischen Bandstruktur entdeckt. Weiterhin wird die Besetzung des 2DEG durch Photoanregung aus lokalisierten Defektzuständen in der Bandlücke vorübergehend erhöht.

Eine andere Art der Abschirmung mit Hilfe von Dipolmomenten in einer amorphen Eisschicht, wird ausgenutzt um Elektronen in einem polaren Medium vor einer Metalloberfläche zu stabilisieren und einzufangen. Hierbei wird die mittlere freie Weglänge von niederenergetischen Elektronen in amorphem Eis abgeschätzt. Weiterhin werden die eingefangenen Elektronen dazu benutzt eine chemische Reaktion anzutreiben: Eine langlebige Änderung der elektronischen Oberflächenstruktur der Eisschicht wird durch die sogenannte "dielectron hydrogen evolution reaction" erklärt.

Das Verständnis der Abschirmung der Coulomb-Wechselwirkung in diesen Systemen erlaubt es, scheinbar unverwandte Effekte, wie den Einfang von Überschusselektronen in Eis oder den Phasenübergang von Isolator zu Metall in $VO_2$, im Rahmen des gleichen Konzeptes zu erklären.

# Contents

# List of Figures

# List of Tables

# 1 Introduction

All matter consists of atoms, which are 'glued' together by the Coulomb interaction between the involved particles. In order to understand matter, it is thus important to understand the Coulomb interactions in the various situations encountered in different types of materials. The high density of atoms (and thus also valence electrons) in solids of approx. $10^{23}$ per cm$^3$ makes such an understanding challenging. Fortunately, the Coulomb interaction is modified in most solids: It is screened by the charges within the solid. Especially mobile carriers, but also bound ones and dipole moments of polar materials that surround a single charged particle, react to its presence by spatial redistribution. This leads to a reduction of the range and magnitude of the Coulomb interaction, making it act more locally. One can thus rephrase the initial statement: In order to understand matter it is important to understand the *screening* of the Coulomb interaction.

One example, where screening plays a crucial role, is the Mott-insulating behaviour of materials that due to their valency would be expected to be metallic (NiO, V$_2$O$_3$, etc.) [Mot49]: The Coulomb interaction in such a system is badly screened, therefore, the attractive Coulomb potential between lattice sites (ions) and valence electrons supports bound states and the valence electrons localise at these lattice sites: A 'Mott insulator' is formed. These bound states disappear, when screening is enhanced due to an increased density of free carriers, and the system becomes metallic. Such a Mott insulator-to-metal transition can, for example, be initiated by chemical doping or increasing the pressure.

Transforming the Coulomb interaction between many particles into a (changed) screened potential is also related to the concept of *quasiparticles*: A quasiparticle 'consists' of the bare particle and the (averaged) interaction with its environment. For example interacting electrons in an electron liquid are 'transformed' into non-interacting quasi-electrons. Here, the interaction is manifested in a finite quasi-particle lifetime and e.g. effective masses. Other quasiparticles, e.g. phonons or plasmons, result from the collective excitation of atomic lattice or electron density, respectively. Even when polar molecules reorient to screen an excess electron, a quasiparticle (solvated electron) is formed.

The degree of screening, being part of the interactions that form the quasi-electrons, therefore influences quasiparticle lifetimes in solids. As mentioned before, the lack of screening (i.e. the existence of 'correlation') between valence electrons can also substantially influence the band structure of solids, even turning a metal into an insulator.

The *timescales* of such processes are in the range of femtoseconds (fs) to picoseconds (ps). In order to monitor ultrafast dynamics in condensed matter, it is useful to apply a pump-probe scheme to spectroscopic measurements: Thereby, the investigated system is perturbed by a first fs (pump) pulse and its response during the return to the equilibrium is probed by a second (probe) pulse after a certain time delay. This time delay is adjustable with the precision of fs, and also the laser pulses are tens of fs short, giving access to dynamics on similar timescales. The measurement of the transient

properties by the second pulse can be achieved in various ways, for instance by optical and photoelectron spectroscopy.

In this thesis, I use time-resolved optical and photoelectron spectroscopy in order to investigate three different model systems with a focus on the electron dynamics and how they are influenced by the screening in the respective system. The thesis's title *Ultrafast electron dynamics and the role of screening* can be understood in two ways: ① How does Coulomb screening influence the quasiparticle dynamics and ②, how can the degree of screening be dynamically changed to modify material properties on ultrafast timescales? Both aspects are investigated in this thesis for three model systems, as outlined in the following:

**Instantaneous band gap collapse in $VO_2$: Photoinduced change of screening**
A seemingly concurrent electronic (insulator-metal) and crystallographic (monoclinic-rutile) phase transition in $VO_2$ was discovered more than 50 years ago. However, the driving mechanism, the underlying cause, and even the concurrency are still under debate [Goo71, Zyl75, Wen94, Bie05, Lav14, Mor14, Bud14]. As $VO_2$, from valency of V and O, should be metallic, the formation of an insulating ground state is often discussed in the context of *electronic correlation* versus *structural distortion*. In other words, the question was raised, whether the screening of the Coulomb interaction defines the electronic structure of $VO_2$ or if the distinct lattice structure is the reason for the insulating behaviour. And even more intriguing: How can this behaviour (e.g. the screening) be modified by an external stimulus? The latter question is motivated by the fact that the phase transition in $VO_2$ can be induced by various means, for example by ultrashort light pulses [Roa71, Cav04, Bau07, Had10, Pas11, Mor14].

A new interpretation was initiated, when Cavalleri et al. [Cav04] observed that, after photoexcitation, the optical response does not evolve arbitrarily fast and suggested that a structural bottleneck is involved, implying a structurally driven mechanism for the photoinduced phase transition. The idea was that distinct phonon modes map the monoclinic crystal structure of insulating $VO_2$ onto the rutile structure of metallic $VO_2$. Excitation of those phonons would then act as a driving force for the structural transformation and the electronic band structure would respond by becoming metallic.

In this thesis, the phase transition of $VO_2$, induced by ultrashort ($\sim$ 40 fs) laser pulses, is investigated by two complementary experimental techniques and theoretical investigations. The coherent lattice response is probed by broadband all-optical spectroscopy, where it is shown that the potential energy landscape for the ions changes arbitrarily fast at high excitation densities. A highly non-equilibrium, transient-phase with raised lattice symmetry is observed after photoexcitation. The electronic band structure is investigated directly by time-resolved photoemission spectroscopy. A quasi-instantaneous collapse of the band-gap in $VO_2$ is observed simultaneously with photoexcitation. Theoretical investigations[1] using many-body perturbation theory within a frozen (monoclinic) lattice confirm: Photoexcitation results in a collapse of the electronic band gap *within* the monoclinic lattice structure.

These results show that the a photoinduced change of screening leads to an instantaneous collapse of the band gap in $VO_2$, as a *direct* consequence of the photoexcitation.

---

[1]The calculations were initiated by the experimental results and performed in the group of Prof. Angel Rubio, San Sebastian.

No structural involvement is observed, nor needed to explain this effect. The lattice, of course, responds to this new potential energy landscape and electronic structure on various timescales [Bau07, Had10]. Relaxation of hot carriers, on timescales on the order of 100 fs, are observed directly in time resolved photoelectron spectroscopy and indirectly by optical pump probe experiments within the photo-excited transient phase.

This is a significant step forward towards the complete understanding of the photoinduced phase transition in $VO_2$ and emphasises the importance of screening: The photoinduced change of screening transforms insulating $VO_2$ into a metal.

## Screening and electron dynamics in two-dimensions: The $SrTiO_3$/vacuum interface

The $SrTiO_3$/vacuum interface exhibits a two-dimensional electron gas (2DEG) [SS11, Mee11]. Two dimensional systems are interesting because of their unique properties (e.g. quantisation) and technological relevance (e.g. found in semiconductor devices).

With the dimensionality of the system also the screened Coulomb interaction changes. This leads, in the framework of Fermi liquid theory (FLT), to a modification of the dependence of hot carrier lifetimes on excess energy $\xi$. The $1/\xi^2$-scaling of quasiparticle lifetimes in three dimensions is corrected by a logarithmic factor in 2D, due to the competition between decreased screening (higher scattering rates) and decreased phase space for scattering events (lower scattering rates) [Qia05].

In this thesis, time-resolved photoelectron spectroscopy is used to investigate the occupied and unoccupied electronic band structure of the STO(001)-surface and the ultrafast electron dynamics therein. Interestingly, the 2D-character of the electron-electron scattering rates is indeed observed at large excess energies, while a deviation in the low-energy region is found, due to an increased density-of-states there. Furthermore, two distinct final states that are delocalised within, but localised normal to the surface plane, are discovered. Moreover, it is shown that photoexcitation from occupied, localised surface states within the bulk band gap of the material into the 2DEG leads to a photoinduced transient filling of the 2DEG. This increased filling energetically relaxes on the order 100 ps, due to equilibration with the environment and recombination.

## Screened excess electrons in amorphous ice: transmission, trapping and reactivity

A more local aspect of screening of the Coulomb interaction comes into play when excess electrons are injected into a polar, dielectric environment, for example amorphous solid water (ASW, an amorphous phase of ice). In the liquid phase of a polar solvent, an excess charge is screened by a rearrangement of the dipoles, termed solvation. Dipole moments in a solid are not as easily rotated, but are still able to screen excess charges efficiently. This occurs, for instance, in thin ASW layers adsorbed on metal substrates. Here, excess electrons are excited from the metal, injected into the ASW and stabilise energetically by molecular reorganisation of their environment [Bov03, Stä07a].

In this thesis, such solvated electrons are used to estimate the mean free path of low energy electrons in ASW, an important quantity in radiation chemistry, where interaction cross sections of secondary electrons with water are important. It is furthermore shown that an increase of the adsorbate layer thickness decouples excess electrons trapped in surface defects of the ice layer to such an extent that their lifetimes increase

at least to tens of seconds (i.e. by 14 orders of magnitude). These trapped electrons are then used to drive an electron-induced chemical reaction, the *dielectron hydrogen evolution reaction*: Thereby, two water molecules are transformed into two hydroxide ions ($OD^-$) and a hydrogen molecule ($D_2$) is formed, with the help of two trapped electrons. The hydroxide ions change the work function of the system, which is directly observed in the photoemission experiment.

In summary, I investigated very different aspects of the influence of the *screening of the Coulomb interaction* on electron dynamics in three model systems. Thereby, I succeeded to answer the two questions, raised in the beginning: ① How does Coulomb screening influence the quasiparticle dynamics and ②, how can the degree of screening be dynamically changed to manipulate material properties on an ultrafast timescale? The second question is addressed first, by showing that the photoinduced change of screening transforms insulating $VO_2$ into a metal. The first question is answered by the remaining two systems: The two dimensional electron gas at the STO surface shows modified quasiparticle lifetimes due to the changed screening in two dimensions. In $D_2O$, excess electrons are screened to such an extent by the dipolar ice matrix that they reside in surface traps for tens of seconds and enhance chemical reactivity.

To get back to the initial statement that 'in order to understand matter it is important to understand the *screening* of the Coulomb interaction', one can conclude: By learning about the details of screening, a lot of knowledge has been gained about the investigated systems. The long-standing question of the driving mechanism of the photoinduced insulator-to-metal transition in $VO_2$ is finally answered. Electron induced chemical reactions in amorphous solid water, an abundant form of water in earth's atmosphere and interstellar space, have been observed and enhanced. Finally, it is possible to transiently enhance the charge carrier density of the highly relevant two-dimensional electron gas in STO by photoexcitation.s

# 2 Questions and Background

The Coulomb potential $\Phi(r) \propto q/r$ defines the interaction between charged particles (electrons and nuclei) on a fundamental level. Most of the macroscopic and microscopic properties of matter are in turn defined by these interactions. As soon as many carriers are involved, they react to an excess charge as schematically depicted in Figure 2.1. Electrons (red) move away from a positive excess charge (marked by the dashed circle) in a) and move closer to a positive excess charge (blue) in b). This process is called *screening* of the Coulomb interaction. The local environment reacts to the excess charge by reorganisation within a screening cloud of displaced carriers. Another example for screening is shown in c), where dipole moments (e.g. of polar molecules) reorient to screen the excess electron.

Screening of a point charge due to (quasi-)free electrons can be expressed by a modified *screened* Coulomb potential $\Phi(r)$ of the Yukawa form (see Appendix A)

$$\Phi(r) = \frac{q}{4\pi\epsilon_0 r} e^{-r/\lambda_\mathrm{D}}, \tag{2.1}$$

where $r$ is the distance to the charge $q$ and $\lambda_\mathrm{D}$ is the so called *Debye length* [Cha99], which is a measure of the size of the screening cloud. The difference to the unscreened case is visualised in Figure 2.1 d). The screened potential is not simply renormalised, but exhibits even qualitatively a different shape. Its spatial extension is smaller and the interaction range is thus decreased. When the screened potential is attractive (e.g. the Coulomb interaction of a positive ion is screened by surrounding mobile electrons) it exhibits a limited amount of bound states or even no bound states at all, depending on $\lambda_\mathrm{D}$ [Li06].
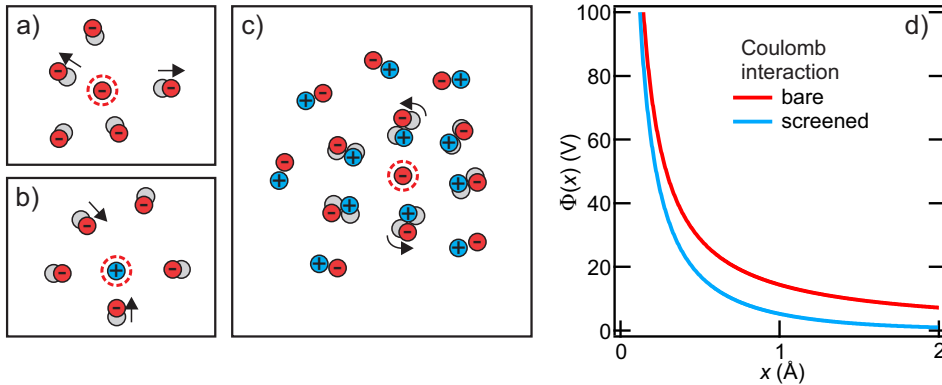


**Figure 2.1:** screening of a negative a) and positive b) excess charge (marked by the dashed circle) by other electrons (red). c) screening of a negative excess charge by reorientation of dipoles. The initial positions of the screening electrons is indicated by the grey circles. d) Comparison of unscreened (red) and screened (blue) repulsive Coulomb potential.

The amount of screening and its structure determines material properties in equilibrium and lead to interesting phenomena like phase transitions and solvation of excess charges. In addition, screening influences important dynamical properties (e.g. electrical conductivity) by modification of electron scattering rates. It is therefore vital to

understand the manifold aspects of screening to gain insight into macroscopic material properties and understand them on a fundamental level.

This chapter first presents concepts of solid state physics that are important for the understanding of the investigated systems. Those systems and their properties are subsequently introduced in the following sections.

## 2.1   Electron interactions and screening in the investigated systems

The chemical composition of the material alone does not necessarily explain its macroscopic properties. Drude- and Sommerfeld-model and later quantum mechanical band structure theory, to different levels of precision, provided the basis for understanding simple solid state systems and their electrical properties microscopically. A typical metal consists of around $1 \times 10^{23}$ atoms per cm$^3$ contributing the same amount of conduction electrons. Interesting phenomena like insulator-to-metal transitions can often only be explained by taking the screened Coulomb interaction between these particles into account.

But often it is not possible to handle such a many-body problem computationally without simplifications. The Born-Oppenheimer-Approximation (Adiabatic Approximation) is used to decouple the wave function of the systems' nuclei from its electronic one. This separation of electronic and lattice subsystems is used in conjunction with the concept of an electron gas or liquid. Thereby a single particle band structure (single-electron approximation) of electronic states in a solid is used to describe the many-body system. It is effectively reduced to that of a single particle, which interacts with more or less degrees of freedom of its environment via an interaction potential. The following degrees of simplification can be distinguished:

- **Free electron gas (Drude-Sommerfeld model)** Only the periodicity of the crystalline lattice of the solid is superimposed on the free electron dispersion leading to a folded band structure (Figure 2.2 a)). Fermi-Dirac statistics is used to find the occupation of the density of states.

- **Nearly free electron gas** A static, periodic and weak potential representing the screened ionic atoms is used to generate the band structure for a quasi-free conduction electron in a metal (Figure 2.2 b)), thus opening band gaps at the Brillouin zone boundaries $E_{\mathrm{gap}}$. Complete filling of the valence band yields an insulator, or if a small band overlap in k-space is maintained a semimetal (Figure 2.2 c) and d)).

- **Fermi-liquid** (proposed by Landau) The non-interacting Fermi-gas is transformed into an interacting Fermi-liquid of dressed quasiparticles with finite lifetimes, by switching on interactions in an adiabatic manner. The quasiparticles then behave again like non-interacting particles, while the interactions of the real particles are included in the complex self energy of the quasiparticle. This leads to a finite lifetime $\tau_{\mathrm{e\text{-}e}}$ of electrons with excess energy $\xi = E - E_{\mathrm{F}}$ (with respect
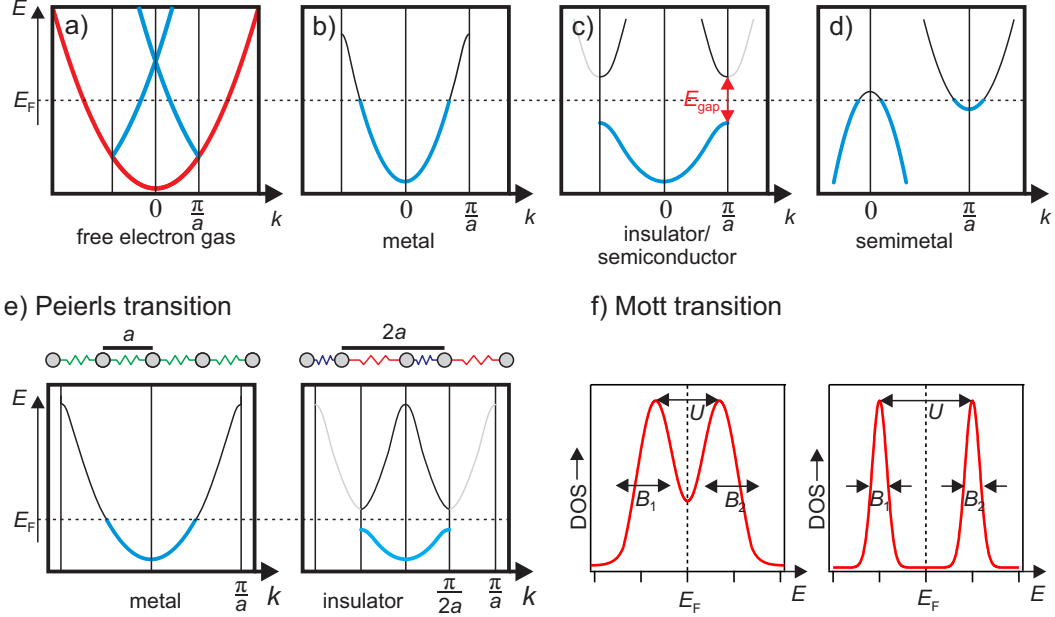
**Figure 2.2:** Energy bands for electrons in solids: a) free-electron dispersion (red) and back-folding due to lattice periodicity (blue) as a starting point for: b) half filled conduction band of a metal, c) filled valence- and empty conduction-band of insulator/semiconductor with band-gap $E_{\mathrm{gap}}$, d) semimetal. e) The Peierls-mechanism leads to insulating behaviour where simple band theory would predict a metal, when lattice distortion is allowed. f) Mott insulator: Coulomb interaction and screening define insulating versus metallic behaviour.

to the Fermi level $E_{\mathrm{F}}$) following [Kir09, Qia05].

$$\tau_{\text{e-e}} = \Gamma_{e-e}^{-1} = 176.481[\text{fs} \times \text{m}^{-2/5} \times \text{eV}^2] \times \frac{n^{5/6}}{\xi^2} \tag{2.2}$$

Additionally the DOS, i.e. the real band structure, can be considered, introducing corrections by modifying scattering phase space and importantly the screening of the Coulomb interaction itself.

- **Strongly correlated systems** exhibit interaction strengths, that do not allow the above approximation of non-interacting quasiparticles. E.g. interaction with the crystal lattice can result in a Peierls-Transition and one approach to take electronic correlations into account is to employ simplified model Hamiltonians (e.g. Mott-Hubbard) (Figure 2.2 e) and f)).

Modern solid state theory is able to qualitatively and, to a growing extent, quantitatively predict the band structure of many solids and distinguishes between metals, semiconductors and insulators as shown in Figure 2.2. The filling of the Bloch bands is simply determined by counting the electrons per unit cell. For a half-filled band, as displayed in b), a small energy is sufficient to move the occupation by a small amount in k-space corresponding to a non-zero net momentum of all conduction electrons (i.e. a current). The presence of a band gap, shown in c), prevents conductivity, as a much larger amount of energy is needed ($E_{\mathrm{gap}}$) to create a non-zero total momentum.

**Beyond single particles:** Figure 2.2 e) and f) show two of the most prominent simplifying models for collective effects and correlations beyond single-particle band-theory. Half filled bands are susceptible to a Peierls transition if the energy gain by opening a gap at half the original Brillouin zone (i.e. lowering occupied electronic states in energy at $\pi/2a$) is larger than the energy needed to modulate the lattice structure, such that the original unit cell size is doubled. For one dimensional chains (1D) the distorted, insulating structure is in fact the ground state of the system. [Grü94] Therefore, quasi-1D systems are susceptible to Peierls transitions along with the formation of charge-density-waves [Sch08, Ros11].

A Mott transition on the other hand, is based on the screened Coulomb interaction between electrons, also termed strong electronic correlation. In a metal with delocalised conduction electrons, the Coulomb interaction is well screened. In this case, the narrow attractive potential around the nuclei thus prohibits bound electronic states. When screening is reduced e.g. by reduction of the charge density (i.e. the effective Coulomb interaction increases), at some point the screened Coulomb potential gets wide enough to support bound states. These states localise electrons at the atomic sites and remove them from the delocalised conduction band. This results in a further reduction of the screening, stabilising the localised state, and leads to a metal-to-insulator transition [Mot49, Geb97]. Especially in transition metal compounds with rather localised $d$ valence orbitals, the Coulomb interaction is not well screened, which makes those systems susceptible to such a Mott metal-to-insulator transition. Mott first formulated an empirical expression for the band gap of size $E_{\mathrm{gap}}$

$$E_{\mathrm{gap}} = U - \frac{1}{2}(B_1 + B_2) \tag{2.3}$$

where $U$ is the Hubbard intra-atomic correlation energy (Coulomb repulsion) and $B_{1/2}$ the bandwidth of lower and upper Hubbard band (i.e. the degree of localisation). [Zyl75] In Figure 2.2 f) the resulting 'band structure' is sketched. Large screening leads to delocalised bands with large bandwidths $B_{1/2}$ and weak repulsion $U$ (left). A conducting, metallic material is formed. When screening is reduced (e.g. by lowering the charge density), the bandwidths get smaller and the interaction increases (right). This leads to the opening of a gap, characteristic for an insulating material.

Advancing this model into the framework of a proper quantum mechanical treatment in the second quantisation, the so called Mott-Hubbard Hamiltonian can be used to describe such systems [Geb97]. More advanced theoretical methods like hybrid DFT, including non-local interactions, and the GW approximation (W = screened Coulomb interaction, G = Greens function) are nowadays able to describe correlated systems without a the above model assumptions to an increasing extent, but at the expense of comparably high computational cost [Gat07b, Ior12].

**Effects of dimensionality:** So far mainly three-dimensional (3D) systems where discussed. Confining an electronic wave function in one direction, can demand the description in two dimension, e.g. as a two-dimensional electron gas (2DEG), leading to new phenomena. Fermi liquid theory then predicts both, a different scattering behaviour due to the decrease in phase space for electron scattering, and also a modification of the screened Coulomb interaction. These modifications lead to a logarithmic

correction of electron-electron scattering rate, which then becomes [Kir09, Qia05]

$$\tau_{\text{e-e}} = \Gamma_{\text{e-e}}^{-1} = 264[\text{m}^2 \times \text{eV}^2 \times \text{fs}] \times \frac{n_{\text{2D}}}{\xi^2 \ln(47.88\frac{n_{\text{2D}}}{\xi})} \tag{2.4}$$

With 2D-electron density $n_{\text{2D}}$ and excess energy (with respect to the Fermi energy) $\xi = D - E_{\text{F}}$. Of course the 2D system is never completely decoupled from its environment. The screening and phase space in the real system will most likely also depend on the electronic band structure of its surrounding.

**Dipolar screening:**   As shown already in Figure 2.1 c), not only electrons can screen the Coulomb interaction. Electric dipoles screen charges effectively by reorientation as well. This results in the well known phenomenon of solvation in polar solvents (The ions of NaCl are solvated in water). The dipole moments are carried by polar molecules like water or ammonia. Solvation therefore plays an important role in chemistry in the liquid phase. But also frozen solvents (like water clusters of interstellar or atmospheric ices) are able to solvate excess charges. These charges can even be effectively trapped in such polar environments, if the energetic stabilisation due to the screening and the decoupling from the environment are strong enough. Localised excess charges are a very reactive species and especially important in atmospheric physics and chemistry.

**Topics of this thesis:**   Al previously discussed aspects of screening - strong electronic correlation, effects of dimensionality and dipolar screening - are examined by investigating different model systems:

- VO$_2$ and its phase transitions are investigated to clarify how correlated this material really is and whether electronic correlations (Mott) or crystallographic structure (Peierls) generate the driving force for its photoinduced phase transition.

- The effect of low dimensionality and the surrounding environment on electronic screening is investigated by examining the electron dynamics in the 2D electron gas (2DEG) at the SrTiO$_3$/vacuum interface.

- Dipolar screening is exploited to trap excess electrons in amorphous ice layers adsorbed on a copper single crystal by tuning the coupling to the substrate and exploiting the stabilising properties of polar media.

From this diverse selection of systems it becomes clear that the screened Coulomb interaction is important in many fields and aspects and results in interesting phenomena, that would not be expected from such a simple thing as the Coulomb force. In the following a detailed overview over those systems is given.

## 2.2   Crystallographic and electronic phase transition in VO$_2$

VO$_2$, exhibits a thermally induced, first-order, reversible, phase transition in crystallographic [Wes61] and electronic [Mor59] structure from an insulating-monoclinic to
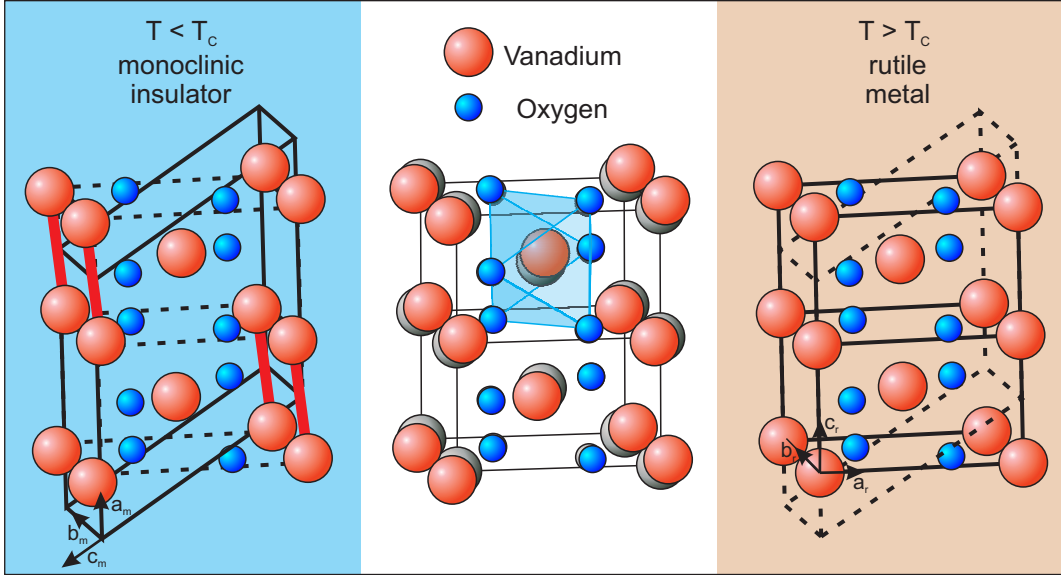
**Figure 2.3:** Comparison of crystallographic phases in $VO_2$: on the left the monoclinic unit cell is indicated by the solid lines. Vanadium atoms are represented by the red balls, oxygen atoms are in blue. For comparison two unit cells of the rutile phase corresponding to the monoclinic one are indicated by the dashed lines. On the right side the rutile, metallic, high temperature phase is depicted. Two rutile unit cells are indicated by the solid black lines, the dashed lines show the corresponding monoclinic unit cell. In the central panel both structural arrangements are superimposed (rutile phase in greyscale).

a metallic-rutile phase, both discovered nearly 60 years ago by Westman and Morin. The transition temperature $T_C \simeq 340$ K is easily accessible in experiments and very suitable for applications, as it lies slightly above room temperature. The corresponding

| structure | $a$ (Å) | $b$ (Å) | $c$ (Å) | $\alpha$ (°) | volume (Å$^3$) |
|---|---|---|---|---|---|
| monoclinic | 5.7517 | 4.5378 | 5.3825 | 122.646 | 118.2899 |
| rutile | 4.5546 | $= a$ | 2.8514 | - | 59.1505 |

**Table 2.1:** Lattice constants of monoclinic and rutile $VO_2$, determined by X-ray diffraction experiments. [Lon70, McW74]

lattice structures for temperatures below and above $T_C$ are displayed in Figure 2.3, based on structural data from X-ray diffraction experiments [Lon70, McW74]. The lattice parameters for the two phases are summarised in Table 2.1. Two unit cells (each containing 2 vanadium and 4 oxygen atoms) are shown in the right panel of the figure, corresponding to the high temperature, rutile phase. When lowering the temperature below $T_C$, the vanadium atoms dimerise and the dimers tilt away from the rutile $c_r$-axis. In the central panel both structures are superimposed to highlight the differences (rutile structure in grey): Oxygen octahedra (one is indicated by the blue shaded shape) are only slightly disturbed, while the vanadium atoms move by a larger amount. This structural change constitutes a lowering of symmetry and an effective

doubling of the unit cell (the monoclinic unit cell contains 4 vanadium and 8 oxygen atoms). The volume changes by approx. 0.045 % [Kuc79].

Besides direct observation of the lattice structure by diffraction techniques, both phases exhibit a distinct response in Raman spectroscopy: The insulating monoclinic phase (space group: $P2_1/c$, No. 14) [Eye02] has 18 Raman active phonon modes (at the $\Gamma$ point), as shown in [Sch02, Jon10]. In contrast the rutile phase (space group: $P4_2/mnm$, No. 136) exhibits only 4 Raman active modes, detected as very broad peaks by Raman spectroscopy [Sch02].

Remarkably, at about the same $T_C$, the conductivity of $VO_2$ changes by up to five orders of magnitude [Ber69], which constitutes a metal-to-insulator transition.[2] The phase transitions in $VO_2$ are of first order due to the existence of latent heat and a diverging heat capacity [Ber69]. Considering the atomic orbitals of $V^{4+}$ and $O^{2-}$ ions
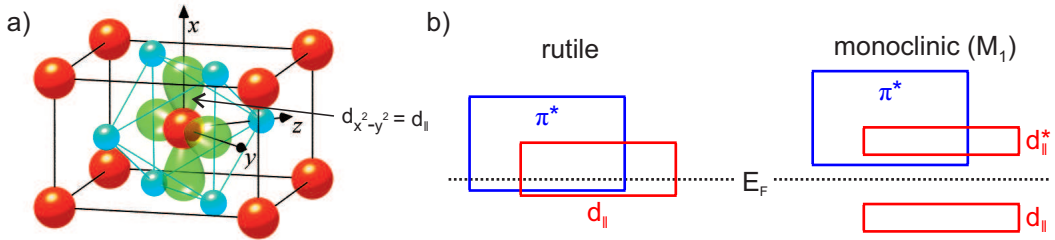


**Figure 2.4:** Rutile unit cell with $c_r$-axis along $x$ a) and schematic representation of the $VO_2$ electronic band structure in the vicinity of the Fermi level b). Adopted from [Eye02].

and the respective crystallographic structure, Goodenough gave a first description of the electronic structure in both phases, which is illustrated by Figure 2.4. [Goo71] In a), the rutile unit cell is shown. The central V atom (red) sits inside an O-octahedron (blue). Therefore the 5 V-$3d$ orbitals are split by the octahedral crystal field into the usual $e_g$ and $t_{2g}$ manifold. Degeneracy of the $t_{2g}$ manifold is lifted further and the $d_{x^2-y^2}$[3] (green translucent shape) orbital is split off at lower energies and named $d_\parallel$, while the remaining $t_{2g}$ orbitals are termed $\pi^*$. The resulting $d_\parallel$ and $\pi^*$ bands of the solid are illustrated in Figure 2.4 b). In the rutile phase both bands overlap with the Fermi energy.

When undergoing the phase transition, the displacement of the V-atoms and their pairing along the rutile $c_r$-axis leads to a splitting of the $d_\parallel$ band (which also points along the $c_r$-axis) and a shift of $\pi^*$ to higher energies, as displayed in b). Goodenough assumed that this splitting, which results from the structural distortion, i.e. the lattice structure only, is sufficient to open up a band gap.

Such a Peierls-insulator type of description was contradicted by Mott [Zyl75]. He

---

[2]The conductivity changes from approximately 0.1 to 1000 $\Omega^{-1}cm^{-1}$. A good conductor (e.g. copper) has a conductivity of $6 \times 10^5$ $\Omega^{-1}cm^{-1}$, while good insulators (e.g. fused silica) have conductivities on the order of $1 \times 10^{-20}$ $\Omega^{-1}cm^{-1}$. It would therefore be more accurate to speak of a semiconductor-to-bad-metal or non-metal-metal transition. For simplicity it is nevertheless called insulator-to-metal transition.

[3]The unusual choice of coordinates leads specific naming conventions. The $t_{2g}$ manifold consists of $d_{x^2-y^2}$, $d_{xz}$ and $d_{yz}$ orbitals, not the usual $d_{xy}$, $d_{xz}$ and $d_{yz}$.

argued that for a quantitatively correct description electronic correlations have to be considered. The underlying Mott-Hubbard insulator model predicts a band gap between lower (occupied) and upper (empty) Hubbard band of size $E_G$ (see Equation 2.3), which depends on the bandwidths $B_1$ and $B_2$ of the two Hubbard bands and the intra-atomic correlation energy $U$, due to electron-electron interaction [Mot74]. According to Mott, the displacement of the V-atoms in the monoclinic phase only decreases the bandwidth of the d-bands. This narrowing on the other hand makes the system susceptible to a discontinuous Mott transition. To clarify which of those two models, if any, yields an appropriate description of $VO_2$, a great deal of theoretical and experimental studies were performed.

For a long time a single theoretical framework was not able to explain both phases of $VO_2$ at the same time. *Ab initio* molecular dynamics (MD) simulation based on density functional theory (DFT) in the local-density approximation (LDA) does yield correct crystallographic structures, but in the monoclinic phase no electronic band-gap is observed, even though the electronic structure (band overlap) around the Fermi energy is significantly altered [Wen94]. The opposite failure, an insulating rutile and insulating monoclinic ground state was found when using DFT in the spin polarised local-density approximation (LSDA) [Kor02, Kor03]. Choosing the 'right' hybrid functional (Heyd, Scuseria and Ernzerhof (HSE), including electron-electron interaction exactly to some extent) results in correct insulating monoclinic and metallic rutile electronic structure [Eye11], but concerns have been raised that similar problems occur, when including spin polarisation [GC12, Yua12, Cou13]: The rutile ground state becomes insulating and the monoclinic one magnetic.

Fortunately theoretical methods and models have evolved, leading to more consistent results: Simplified model $GW$ calculations [4] yield the correct electronic structure for both crystallographic phases [Con99]. Also cluster dynamical mean field theory (DMFT) plus DFT+LDA including a parameter $U$ (constant for both phases) yields the right electronic structure in rutile and monoclinic phase. Last but no least DFT-LDA plus a self-consistent $GW$ correction on the COHSEX (Coulomb hole and statically screened exchange) level plus a one-step, perturbative $G_0W_0$[5] calculation also successfully describes both phases in $VO_2$. It seems that different theoretical approaches are able to describe the electronic properties of the monoclinic phase correctly when they a) use the monoclinic crystallographic structure and b) accommodate for non-local electron-electron interaction and screening, but still on a single quasiparticle band-structure level (moderate correlations). The simplified Peierls and Mott model pictures are not needed to explain the equilibrium properties of $VO_2$ in both its phases, but both structure and correlations play a role to some degree.

Static experimental methods, e.g. photoemission spectroscopy [Shi90, Koe06, Sae09, Sug09], Raman-spectroscopy [Sch02, Jon10] and diffraction techniques [Lon70, McW74] are able to identify the expected signatures of the two phases of $VO_2$, but lack the ability to consistently explain the underlying mechanism of the transition. Photoemission for instance probes the electronic structure, while diffraction and Raman-spectroscopy are

---

[4]In Hedin's $GW$ approximation [Hed65] the complex self energy $\Sigma$ of a quasiparticle is approximated by the product of the single particle Greens function $G$ and the screened Coulomb interaction $W$. In the model $GW$ the self energy only mimics this definition.

[5]Eigenvalues and orbitals are not calculated self consistently in this last step

sensitive to the crystallographic one. Neither of them can directly reveal the interconnection between electronic and lattice degrees of freedom. Also, the driving mechanism for any change is per definition dynamic and static snapshots will always have a hard time to unambiguously reveal its nature. In addition, the concurrency of crystallographic and electronic phase transition is questioned in general and the existence of a monoclinic metallic phase is observed [Arc07, Qaz07, Lav14].

A common approach to disentangle cause and effect is to perform time resolved out-of equilibrium studies. A system is perturbed by a momentary stimulus (often ultrashort laser pulses are employed to access the timescales of electron-electron scattering and nuclear motions) and its relaxation or transient change with time is monitored subsequently. The electronic and crystallographic phase transition in VO$_2$ can in fact be photoinduced, paving the way for such studies, as described in the following.

**Photoinduced phase transition**   Roach and Balberg [Roa71] first showed that the phase transition in VO$_2$ can be photoinduced by pulsed lasers in an ultrafast manner. Such a photoinduced phase transition (PIPT) is important for applications as it would allow e.g. ultrafast electro-optical switching. Driving the phase transition on a non-equilibrium pathway has also raised hopes for understanding the underlying physics in general: If electronic correlation is responsible for the insulating gap, photo-excitation could instantly remove it, while a in a lattice-mediated scenario, first the lattice structure would have to change, before the electronic gap could close.

Time-dependent studies of the PIPT have been conducted in the past, using various types of probes. The structural evolution has been probed by electron [Bau07] and X-ray diffraction [Cav01, Had10, Had11], showing that the evolution of the ionic positions happens on various timescales. Those timescales start at sub-ps but extend up to ns, due to different steps in atomic rearrangements until the atoms resemble the equilibrium high-temperature structure. Unfortunately, the initial ultrafast timescale (sub-100 fs), that would give possible insights into the driving mechanism, is not accessible due to the lack of time resolution. Also the ionic positions are probed, not the dynamical potential energy landscape, that defines the driving force of ionic motion.

Transient optical reflectivity and transmission with superior time resolution showed a threshold behaviour for the maximum speed in the optical response [Cav04]. There the phase 'transition time' was determined for various pump-pulse durations and no faster transition than 80 fs was observed, even with 15 fs pump pulses. This *structural bottleneck* suggested a lattice-mediated, Peierls-type mechanism. The idea was that the photo-excitation coherently excites a phonon that maps the monoclinic onto the rutile crystallographic structure[6], thereby driving the transition. However, optical techniques do not probe the electronic structure directly, but the dielectric function instead, including e.g. low-energy lattice excitations and thermal effects and lacking an absolute energy scale. This lack of an absolute energy scale does not allow to distinguish between free carriers within the conduction band (of the insulating band structure) due to photoexcitation and truly metallic response of a system due to a band gap collapse.

---

[6]The assumption that a 6 THz phonon mode maps monoclinic to rutile structure was refined in [Yua13]: The phonon mode *along* the V-dimers oscillates at 10 THz, tilting of the dimers happens at 6 THz

To partially circumvent this problem, broadband THz probing was employed [Küb07, Pas11] to disentangle lattice and electronic contributions via the probe photon energy. There, it is shown that only between $h\nu = 40$ and 80 meV, IR-active phonons are probed, and above 80 meV the THz conductivity shows no (vibrational) lattice contributions (but still no absolute energy for electronic transitions is possible to determine). A phase transition threshold on the other hand was extracted at the arbitrary pump-probe delay of 1 ps for the wavelength-integrated spectra. This assumes that the overall reflectivity change at 1 ps is directly connected to the electronic phase transition *only*. The authors observe a coherent wave packet motion in an excited, transient state and a ultrafast onset of a metallic response in the THz conductivity without evidence of a structural bottleneck.

Another approach to disentangle electronic and lattice response was performed by Siwick and co-workers [Mor14]. Ultrafast electron diffraction was used to probe lattice and valence orbital structure and simultaneously time resolved optical IR-spectroscopy was used to monitor the electronic response. A state with metal-like IR-reflectivity is reported with the monoclinic lattice structure intact, i.e. a *monoclinic Metal*.

A transient phase with monoclinic lattice structure exhibiting metallic signatures has also been reported in time-resolved studies by [Kim06, Coc12, Tao12, Yos14] and statically at high pressure (>10 GPa) by [Arc07]. The problem of all of the presented experiments is the lack of an absolute energy scale, when probing the dielectric function of a material optically. Highly excited matter can show a 'metallic signature' just because carriers are freed by the excitation and not because its electronic structure changed. In other words it is unclear from optical experiments whether the metallic response is generated due to low-energy transitions across the Fermi energy (i.e. due to a band gap collapse) or within the transiently populated conduction band (i.e. with the band gap intact).

A technique that provides a direct view into the electronic band structure, including absolute energies, is photoelectron spectroscopy. Time-resolved photoemission spectroscopy is very challenging on $VO_2$[7]. Unfortunately the few successful attempts [Dac11, Yos14] so far, do not possess the time resolution to identify a driving mechanism initially after photoexcitation.

**Open questions regarding $VO_2$:**   Despite countless investigations concerning $VO_2$, from which only a fraction was mentioned above, various open questions remain. The driving force of the photoinduced phase transition is still under debate: Is the detour via the lattice after photoexcitation (of electrons) really necessary to reach a metallic phase, i.e. does the 80 fs phonon bottleneck exist, and if not, how fast can one drive the transition ultimately? What is the nature of the photoexcited phase before all components of the system thermalise and is there a (transient) monoclinic metal?

To shed light onto these questions, in this work, a complementary approach of time-resolved broadband optical and photoemission experiments were used. The comprehensive set of performed experiments is illustrated by Figure 2.5: The equilibrium phases (M1 and R) of $VO_2$ are characterised statically and following weak perturbation (narrow

---

[7]Preparation of a stoichiometric $VO_2$ surface in UHV is non-trivial, due to oxygen loss upon heating, which affects surface sensitive techniques like PES strongly.
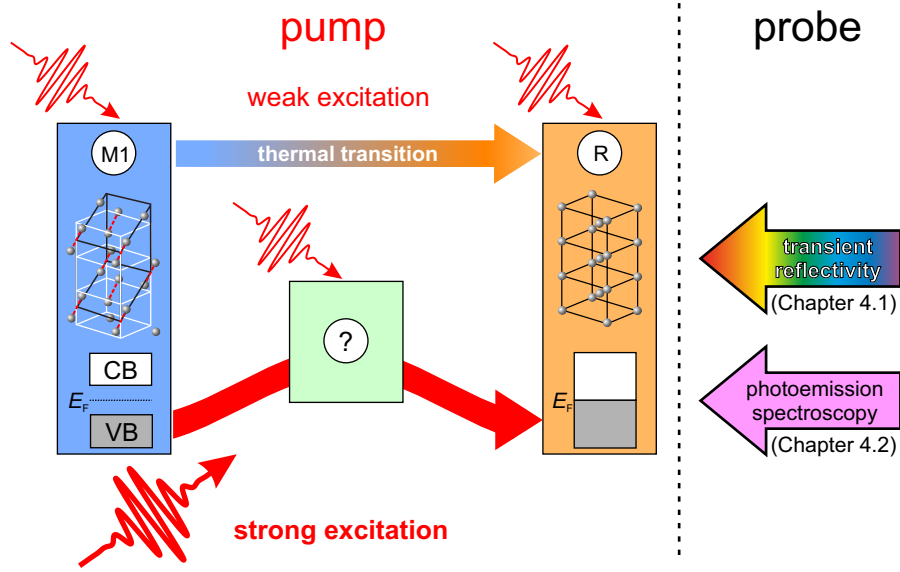
**Figure 2.5:** Experiments employed to shed light onto open questions regarding $VO_2$, as described in the main text (schematic overview). Weak excitation (narrow pulse) perturbs monoclinic (M1), transient (?) and metallic (R) phase. Strong excitation (bold pulse) drives the PIPT. The lattice potential symmetry is probed optically via coherent phonon response (Chapter 4.1) and the electronic structure is probed by photoelectron spectroscopy (Chapter 4.2).

pulses) in a time-resolved manner. Strong photoexcitation (bold pulse) is used to drive the PIPT via a transient non-equilibrium phase ⑦. Weak perturbation of the transient phase via three-pulse experiments permits its further characterisation. Their lattice potential energy landscape [Wal11, Wal13] is probed via coherent phonon response using optical broadband whitelight spectroscopy [Weg11] (Chapter 4.1). Time resolved photoemission spectroscopy reveals a quasi-instantaneous metallisation [Weg14] (Chapter 4.2). Theoretical calculations in the monoclinic lattice structure confirm that photoexcitation can instantaneously generate a monoclinic metallic phase due to a massive change in screening. A purely electronic effect is sufficient to generate this transient phase.

## 2.3 Surface 2D electron gas in insulating SrTiO₃

SrTiO₃ (STO) is the 'Silicon of the emerging field of oxide electronics' [SS11], as it is easy to fabricate (and therefore commonly used as a substrate), but also shows intriguing properties, as for example a high mobility two-dimensional electron gas (2DEG) at the $LaAlO_3/SrTiO_3$ interface [Oht04]. This 2DEG between two insulating solids can be controlled by field effects [Cen08], is superconducting at temperatures below 200 mK [Rey07] and conductivity can be modulated by electric fields in prototypical field effect transistors [Eer13].

The discovery of a 2DEG that is localised in the surface normal direction of the vacuum cleaved or annealed SrTiO₃/vacuum interface provides a comparable model

system with easy experimental access. As the 2DEG is situated at the vacuum interface, surface sensitive photoelectron spectroscopy can be used to shed light onto its quantised structure [SS11, Mee11].
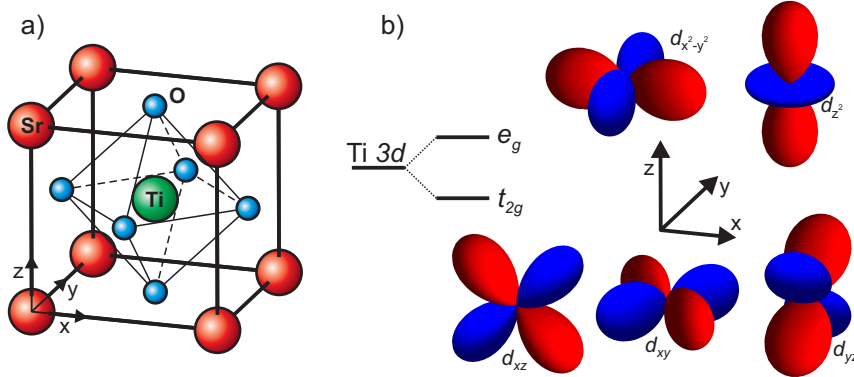


**Figure 2.6:** Bulk STO crystal and orbital structure: a) cubic unit cell of STO. b) Angular part of $3d$ atomic orbitals and crystal field splitting of $e_g$ (top: $d_{x^2-y^2}$ and $d_{z^2}$) and $t_{2g}$ (bottom: $d_{xz}$, $d_{xy}$ and $d_{yz}$) manifolds.

SrTiO$_3$ has a perovskite cubic lattice structure with a lattice constant of 3.9 Å, as shown in Figure 2.6 a), and is an insulator with an indirect band gap of 3.25 eV and a direct gap of 3.75 eV [vB01, Pis04]. Strontium atoms (red) are at the corners of the unit cell while the titanium atom (green) is in the centre, surrounded by 6 oxygen atoms (blue). The highest occupied states are derived mainly from oxygen $2p$ orbitals.

The empty conduction band originates from titanium $3d$ orbitals. Figure 2.6 b) shows this Ti $3d$ manifold, which is split by the octahedral crystal field of the oxygen octahedron. The orbital lobes of the $t_{2g}$ manifold (bottom) point in between the oxygen atoms and are therefore lowered in energy. As each of the $t_{2g}$ orbitals extend further in two directions, they form bands that are more localised (heavier) in one and more delocalised (lighter) in the other two directions. The orbitals of the $e_g$ manifold (top) point along the $x$, $y$ and $z$ axes directly towards oxygen atoms, hence their increased relative energetic position.

Figure 2.7 illustrates the electronic structure of STO further. Panel a) displays the cubic Brillouin zone of the simple cubic lattice structure. High symmetry points are indicated by the red circles and letters. For investigations of the STO(100) surface the $\Gamma$-$X$ direction is the most relevant. Angular resolved photoemission data, presented in Chapter 5, is recorded in the direction $k_x$, indicated by the dashed red line and therefore also named $k_p$ (parallel to the examined surface). Due to the cubic symmetry of bulk STO, this direction is equivalent to the momentum direction perpendicular to the surface ($k_z$).

Screened hybrid DFT calculations yield a quantitative picture [EM11] of the occupied and unoccupied electronic band structure of STO. The calculated bands in $\Gamma$-$X$ direction from Brillouin zone centre to one of the cubic face centres is shown in b). The calculations yield a direct band gap at the $\Gamma$ point between 3.59 and 3.87 eV and an indirect band gap (between $R$ and $\Gamma$, not shown) between 3.18 and 3.53 eV, depending
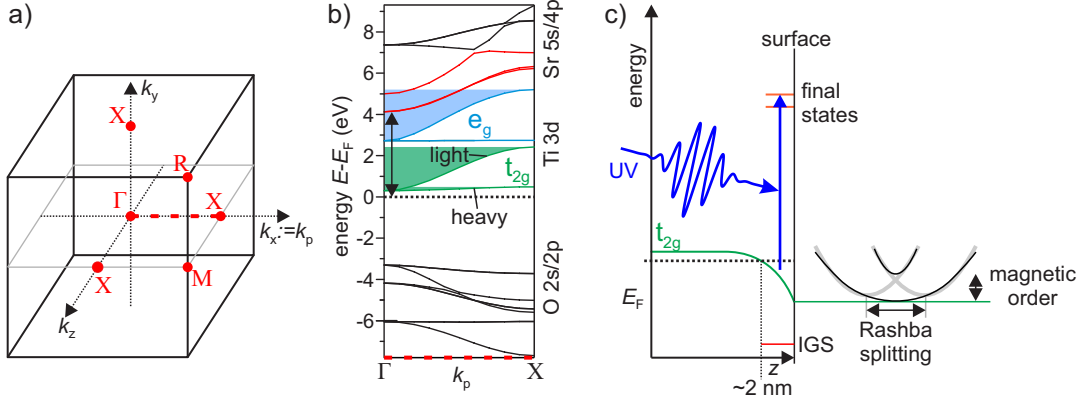
**Figure 2.7:** Electronic band structure of $SrTiO_3$: a) shows the Brillouin zone of a simple cubic lattice structure. High symmetry points are marked in red. The red dashed line ($\Gamma$-$X$) corresponds to the angular direction that is probed in angle-resolved measurements. The calculated band structure of bulk STO (adopted from [EM11]) is partially shown in b). c) Displays the spatial dependence of the electronic structure with downward bent conduction band (green) and Rashba-split sub-bands [SS14] around $\Gamma$ in the surface region. Excitation from initial to potential final states is indicated by the blue arrow.

on the used basis set. This is in good agreement with experimental values of 3.75 and 3.25 eV, respectively.

As mentioned before, two of the three $t_{2g}$ orbitals (green) have a good overlap in this direction (i.e. in each of the $\Gamma$-$X$ directions), yielding two degenerate[8] dispersive bands with more delocalised character. The other orbital with less overlap results in a single heavier, less dispersive band. Similar arguments hold for the energetically higher $e_g$ manifold (blue). The position of the Fermi level was shifted slightly below the conduction band to indicate the common n-doped character of the system [Fuj92, Cha10].

Many studies, predominantly photoelectron spectroscopy, have investigated the bulk and surface electronic structure of STO. Bulk crystals become metallic upon various types of electron doping. Nb- and La-doped STO samples show metallic states at the Fermi energy in photoemission studies [Tak09, Ish08, Aiu02, Fuj92]. Bulk oxygen deficiency after annealing undoped STO above $1000°$ C in ultrahigh vacuum [Cha10] has a similar effect and leads to conducting samples with a metallic Fermi surface. Often, broad in-gap states[9] (IGS) are observed at 1.3 to 1.5 eV binding energy in such doped metallic samples.

Metallic STO surfaces can be generated by adsorption of hydrogen [D'A12], elec-

---

[8]The phase transition from high temperature cubic to low temperature tetragonal structure at $T_C = 110$ K does neither change the crystallographic nor electronic structure by a significant amount. A slight tilting of the oxygen octahedra leads to a lifting of the degeneracy in the conduction band manifold by tens of meV [Mat72].

[9]The exact origin of the in-gap state is still not clear: It is observed in most experimental studies of electron doped STO [Tak13, Ahn03, Aiu02, Fuj92, Ish08, SS11, Mee11, Plu14], but interpretations range from incoherent satellites due to electron correlation [Fuj92, Ish08] to defect states in the band gap due to O-vacancy clustering [Sha98] or O-vacancy induced states located at the Ti ions [Ric03].

tron irradiation [Tak13] and UV irradiation [Plu14, Mee11] and are interestingly also observed on vacuum fractured surfaces [Hen78, SS11]. There, the broad IGS and the metallic state at the Fermi level both disappear upon dosage of $\sim 0.3$ L of oxygen[Hen78, Aiu02] and it is therefore concluded that the doping mechanism is connected to oxygen vacancies at the surface, generated by the fracturing.

Only recently such metallic states on the STO-vacuum interface have been identified as truly confined to the surface, i.e. as a 2D electron gas (2DEG), via photon energy dependent high resolution ARPES [SS11, Mee11] and scanning tunneling spectroscopy [DC12b] studies. These showed various quantised sub-bands, originating from STO's bulk Ti $3d$ $t_{2g}$ manifold. These bands are delocalised in the surface plane, but localised in surface normal direction, hence the term 2DEG. Figure 2.7 c) illustrates these findings: Oxygen vacancies generated by fracturing [SS11] or UV-illumination [Mee11] lead to a downward band bending of the bulk conduction band ($t_{2g}$ manifold in green) towards the sample surface ($z_0$). Because the band is bent below the Fermi level $E_{\mathrm{F}}$, the respective states become occupied and a high mobility 2DEG with possibly quantised sub-bands is formed.

Even more recent experiments revealed additional intriguing features of the 2DEG: In [SS14], using spin-resolved photoemission spectroscopy, the quantised sub-bands are reinterpreted as giant Rashba-split bands. This is illustrated in on the right side of panel c): Rashba splitting (indicated by the arrow) leads to two bands (grey) that appear as one band with strong and one with weak dispersion (black) due to a lifted degeneracy at $\Gamma$ due time-reversal symmetry breaking (i.e. magnetic order). In [Plu14] it is found that only the band derived from the $d_{xy}$ orbital is truly 2D (zero dispersion in $k_z$, i.e. surface normal, direction), while $d_{xz}$ and $d_{yz}$ exhibit large effective masses (weak dispersion), but still a 3D character. In the latter two studies, polished and etched samples were used and in [Plu14] different types of annealing treatments were compared, all resulting in the same, universal surface electronic structure, virtually independent of surface treatment and bulk doping.

**Open questions regarding SrTiO₃:**   There are a few open questions regarding this highly interesting surface electronic structure of STO: How does the different dimensionality of the electronic band structure modify the screening of the Coulomb interaction and thereby affect hot electron lifetimes in the system? How does the surface electronic structure couple to the bulk bands?

In fact the unoccupied electronic structure has so far been experimentally investigated only with low energy resolution by means of inverse photoemission spectroscopy (IPS) [Hig02, Bab03] and electron energy loss spectroscopy (EELS) [Gue95].

Therefore, in this work, unoccupied states and their dynamics are investigated by means of time resolved single- and two-photon-photoemission. In this way distinct final states are found 4.1 and 4.5 eV above the Fermi energy (Figure 2.7 c)), that are delocalised in the surface plane. Furthermore, hot electron lifetimes are investigated and compared to Fermi liquid theory. Deviations are explained by datails of the STO band structure. Furthermore, a transient filling of the 2DEG from in-gap states is observed that leads to a shift of the Fermi level to higher energies, which relaxes on timescales of ballistic electron transport.

# 2.4   Electron solvation and trapping in amorphous solid water

When excess charges are placed in a polar environment (e.g. water, ammonia, etc.) the free energy is minimised by reorientation of surrounding dipole moments, which thereby screen the Coulomb potential generated by the excess charge. This process is called solvation (or hydration, if the polar medium is water). Solvated electrons in liquids are known and investigated for a long time [Dav08], and according to Zhao et al. [Zha06] constitute a 'most fundamental chemical reagent'.
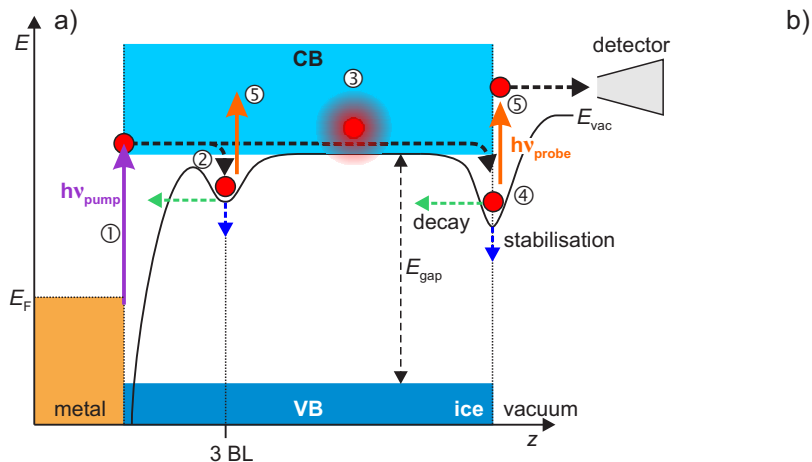


**Figure 2.8:** Illustration of transfer and stabilisation processes in ice: ① photoexcitation from metal substrate into ice conduction band (CB) via UV photons ($h\nu_{\mathrm{pump}}$). ② Localisation of excess charges in pre-existing traps, approx. 3 bilayers (BL) from the substrate. Relaxation e.g. back to the substrate and energetic stabilisation within the solvation site are indicated by the green and blue dashed arrows, respectively. Delocalised electrons (③) can also localise in surface traps (④). ⑤ probing excess electrons by photoemission with visible light ($h\nu_{\mathrm{probe}}$).

Solvation of excess charges occurs also in the condensed phase of polar solvents, e.g. water or ammonia ice. Ice layers adsorbed on a metallic single crystal at low temperatures and under UHV conditions constitute a very controlled environment to study various steps of excess electron transfer, stabilisation, localisation and trapping within the polar solvent. Figure 2.8 illustrates these processes: The metal substrate is indicated in orange on the left and the ice adsorbate, exhibiting a large band gap of $E_{\mathrm{gap}} \sim 8$ eV [Shi77], in blue on the right. Electrons are excited (①) exclusively from the substrate and partially into the ice conduction band (CB) by UV light ($h\nu_{\mathrm{pump}} < E_{\mathrm{gap}}$). From there, they can be trapped in pre-existing sites (②) close to the metal substrate [Bov09, Stä11, Stä14] in amorphous ice layers. In crystalline ice layers, they are trapped in surface defects instead (④) [Stä12], which they can reach due to their initially delocalised nature (③) within the CB [Gah02]. At each of those sites, energetic stabilisation (blue dashed arrows) is possible via a dynamical increase in screening due to dipolar rearrangement (i.e. solvation). At the same time the electron can decay (dashed green arrows) e.g. back to the metal substrate. The timescales of relaxation and stabilisation depend strongly on the substrate and the location of the trap relative

19
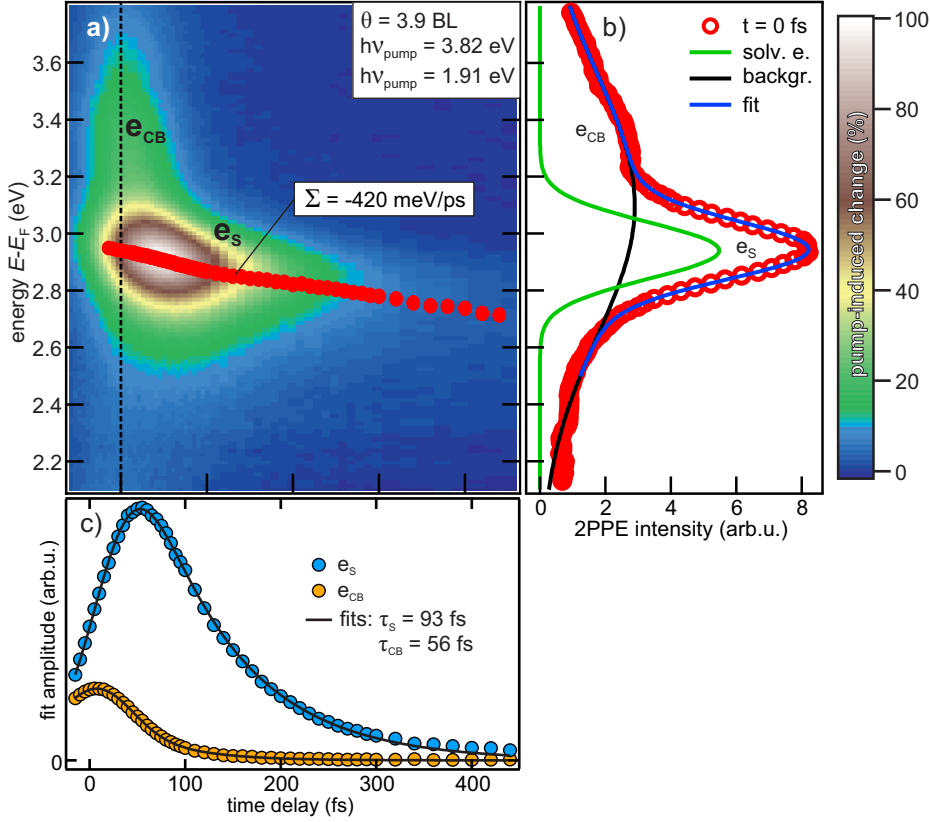
**Figure 2.9:** Time-resolved 2PPE spectra for amorphous $D_2O/Cu(111)$. a) 2PPE intensity on false colour scale with respect to intermediate state energy $E - E_F$ and pump-probe delay. Red circles indicate the peak position of $e_S$ (solvated electrons) that is extracted via the fit shown in b), together with a continuum-like feature $e_{CB}$ (conduction band). Panel b) shows a simplified fit of an exemplary spectrum at a delay $t = 0$ fs with two Gaussian peaks. c) Shows peak amplitudes from the fits in b) with respect to pump-probe delay. Their temporal evolution is quantified by a single exponential fit (characterised by the time constants $\tau_S$ and $\tau_{CB}$) towards positive delays, convolved with the laser pulse XC.

to it [Stä12]. These timescales can be directly probed by photoemission via a time delayed visible light pulse ($h\nu_{probe}$).

As a starting point for further investigations, measurements of solvation and relaxation dynamics in thin ($\sim 4$ BL) ASW[10] layers adsorbed on a Cu(111) single crystal are reproduced (e.g. from [Bov03]) in this thesis: Figure 2.9 a) shows time- and energy-resolved two-photon photoemission (2PPE) data. The change of photoemission signal upon photo-excitation by a pump pulse ($h\nu = 3.82$ eV) is shown in a false colour representation with respect to intermediate state energy (with respect to the Fermi energy of the metal substrate) and pump-probe delay. A short lived continuum ($e_{CB}$) is at-

---

[10]$D_2O$ is used in this work (instead of $H_2O$) for historical and practical reasons: It has been preferred in preceeding studies [Gah04, Stä07b], because $H_2O$ adsorbs in a more complex way on Ru(001) surfaces and does not show any significant isotope effect with respect to electron solvation [Gah04]. Also it can be distinguished from residual $H_2O$ in the vacuum system via its larger mass.

tributed to hot electrons in the ice conduction band that are injected by photoexcitation from the metal substrate (step ① in Figure 2.8). A longer-lived state ($e_S$) corresponds to electrons that are continuously solvated by the surrounding ice matrix (step ② in Figure 2.8) and therefore shift to higher binding energies (blue arrow in Figure 2.8). The intensity vanishes with time as the population relaxes back to the metal substrate (green arrow in Figure 2.8).

Figure 2.9 b) shows an exemplary lineout (red circles) at a single pump-probe delay, that was fitted by a simple model consisting of two Gaussian peaks (solid lines). The evolution of the peak amplitudes (i.e. the relaxation of the solvated electrons e.g. back to the substrate) from these fits with pump-probe delay is shown in c). The characteristic relaxation timescales are $\tau_S = 93$ fs and $\tau_{CB} = 56$ fs for the solvated electrons (blue) and hot electrons in the CB (orange), respectively[11].

In addition, it has been shown previously that these solvation sites are located at a fixed distance to the metal substrate [Mey08], when increasing the adsorbate layer thickness.

In contrast to these ultrafast solvation and relaxation dynamics of electrons *close* to the metal substrate on timescales on the order of 100 fs in ASW, excess electrons can be literally trapped at surface defects of crystalline water ice [Bov09, Stä12] (Figure 2.8 ④). In these defects, the electrons are observed from femtoseconds to minutes after injection, over an incredibly large timespan. These long residence times are a result of the nature of these traps: Figure 2.10 a) shows the calculated electron density (at 70 % of its maximum value) in front of a surface defect at the crystalline $D_2O$/vacuum interface from [Bov09]. Clearly the electron resides within the vacuum half-space. b) Shows the integrated in-plane density and the first two surface bilayers of $D_2O$. The electrons wave function shows negligible overlap with the ice layers, explaining the strong decoupling an long residence time. A complex reconstruction and subsequent conformational states stabilise these electron further energetically.

Interestingly, these trapped electrons in crystalline ice enhance chemical reactions, e.g. the dissociation of $CFCl_3$ via dissociative electron attachment [Ber09, Stä12], due to their extraordinary long residence time and their exposed location at the ice/vacuum interface.

**Open questions regarding excess electrons in ASW:** There are many aspects of excess electrons in ASW to be investigated: How do electrons interact (scatter) within the ice matrix, i.e. what is the mean free path of low energy excess electrons in ASW? Is it possible to trap electrons at the surface of amorphous ice, similar to trapping in crystalline ice and can these trapped electrons be used to enhance chemical reactions?

In this work, starting at thin ASW layers (Figure 2.9), the layer thickness is subsequently increased from 4 to 30 BL and several effects are observed: First, the photoemission signature from solvated electrons (Figure 2.9) reduces, as fewer and fewer electrons reach the vacuum interface from their location (2-3 BL from the substrate), due to their finite mean free path. Thereby, an upper limit of 10 Å for the mean free path of low energy electrons in ASW is determined. Secondly, a new state at the

---

[11]The values for $\tau_S$ and the energetic stabilisation rate $\Sigma = -420$ meV/ps deviate slightly from previously measured $\tau_S = 110$ fs [Gah02] and $\Sigma = -270$ meV/ps [Bov03]. The deviation is most likely due to the simplified data analysis and slight variation in $D_2O$ layer preparation/thickness.

**Figure 2.10:** Calculated trapped electron probability density at pre-existing surface defects of crystalline ice, adopted from [Bov03]: a) the electron density $|\Phi(r)|^2$ (at 70 % of its maximum value) in front of an exemplary $S_{AD}$ surface defect resides completely in the vacuum. b) The in surface-plane average of $|\Phi|^2$ shows negligible overlap with the $D_2O$ surface plane.
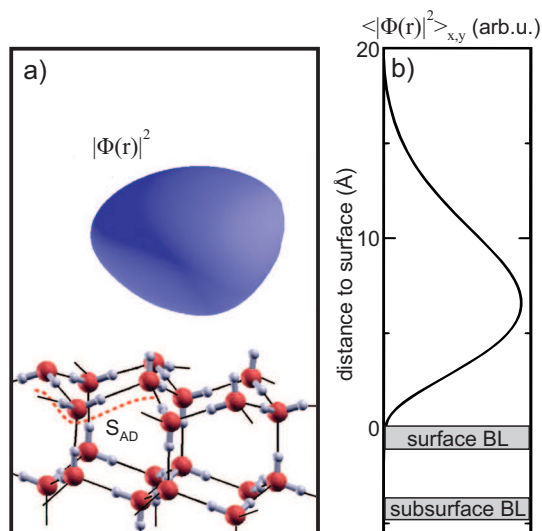
ice/vacuum interface appears that shows extremely long residence times of tens of seconds. Potential traps at the ASW/vacuum interface are effectively decoupled from the metal substrate, most likely similar to trapped electrons at the surface of ice crystallites. Finally, a massive work function change is observed (up to 1 eV) with ongoing excitation of surface trapped electrons, which is interpreted as a result of the *dielectron hydrogen evolution reaction*, confirming the high reactivity of this trapped electron species.

# 3 Experimental details and techniques

In this chapter an overview will be given over the experimental setup and techniques used in this work. For both time-resolved photoemission spectroscopy and time-resolved optical experiments a versatile and powerful laser system is used, as described in the first part. Fundamental knowledge about nonlinear optics is provided in C and good overviews over ultrashort laser pulses and nonlinear optics can for example be found in [Rul05] and [Boy08].

Time- and angle-resolved photoemission spectroscopy, including time-resolved two-photon photoemission, are introduced in the subsequent sections. Finally an introduction into time-resolved optical pump-probe spectroscopy is given, with a focus on optical coherent phonon generation. Details about sample preparation and characterisation is provided in the respective experimental chapters.

## 3.1 The femtosecond laser system

The investigation of a variety of different systems by means of time-resolved and static optical and photoemission spectroscopy experiments, requires a well defined light source with unique properties, such as wide tunability with respect to photon energy and pulsed operation for pump-probe measurements. A schematic overview over the employed laser system and subsequent nonlinear optical conversion stages is depicted in Figure 3.1. A commercial tunable femtosecond laser system, consisting of a femtosecond oscillator (Coherent *Micra*), a regenerative amplifier (Coherent *RegA*) and a broadband grating stretcher/compressor, provides amplified laser pulses of up to $\sim 6.7~\mu$J per pulse (at a repetition rate of 300 kHz, which is tunable down to 40 kHz) at a central wavelength of 800 nm (i.e. 1.55 eV photon energy) and a pulse duration of 40 fs. Oscillator and amplifier are both pumped by a continuous wave (CW) solid state laser (Coherent *Verdi*). For a focused beam (radius 100 $\mu$m) this yields immense field strengths on the order of 1 MW/cm$^2$, and is therefore an ideal starting point to drive different types of nonlinear optical processes, extending the range of photon energies from 1.55 up to 6.2 eV (indicated by the schematic spectrum shown on the bottom of the figure).

The laser system, used in the presented experiments, has been described in [Fog11] and [Dei11], and a detailed description of a very similar setup can be found for example in [Gah04]. The most important components, especially the newly developed parts in the context of this thesis, are described in this section.

### 3.1.1 Commercial oscillator and amplifier

The broadband femtosecond oscillator (Coherent *Micra*) uses a titanium-doped sapphire crystal (Ti:Sa), that is pumped by a 532 nm CW laser (Coherent *Verdi V-18*), as active medium to generate broadband lasing. Passive Kerr lens modelocking in connection with intra-cavity pulse compression (using a prism compressor), yields broadband femtosecond pulses at a repetition rate of 80 MHz (defined by the cavity length of the oscillator). To effectively drive nonlinear optical processes the pulse energy of the oscillator of 6.3 nJ is not sufficient. Before the pulses are amplified, they are stretched in time in the *stretcher* using a dispersive grating (working principle e.g. in [Tre69, Kan97])
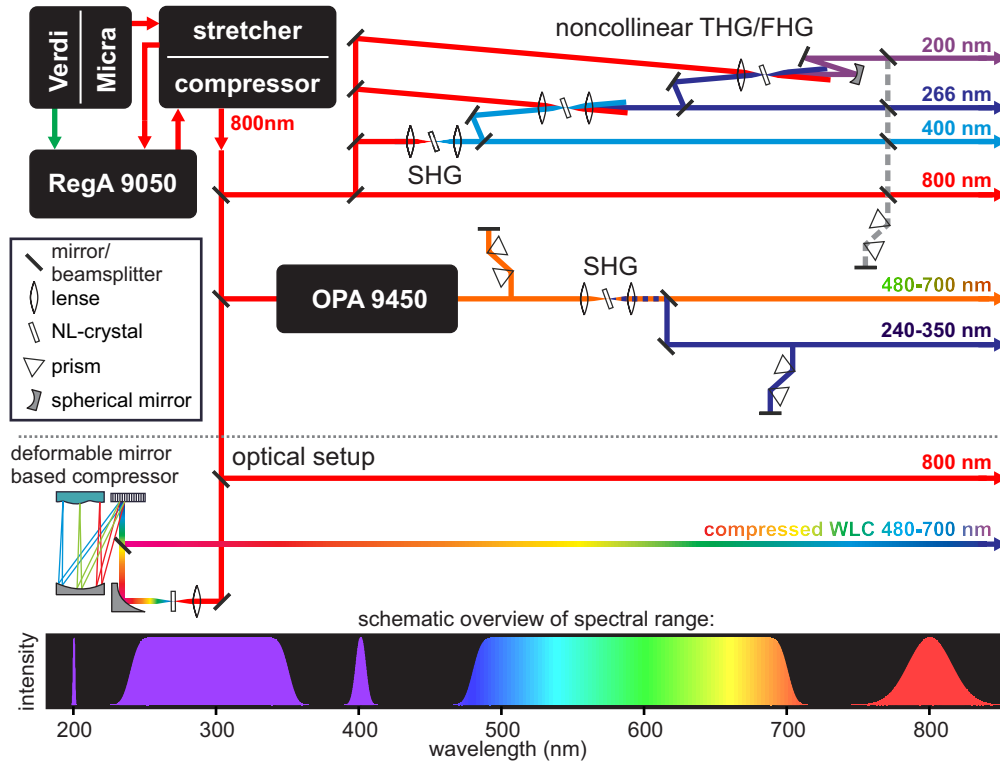
**Figure 3.1:** Schematic overview of the optical setup: The commercial Coherent laser system involving CW-pump-laser (*Verdi*), femtosecond oscillator (*Micra*), regenerative amplifier (*RegA 9050*) and collinear optical parametric amplifier (*OPA 9450*) generates ultrashort laser pulses tunable over the visible spectral range. This range is extended into the UV by exploiting nonlinear optical effects, yielding a widely tunable light source. Achievable photon energies are depicted schematically at the bottom of the figure. For the all-optical experiments the fundamental 800 nm pulses as well as adaptively compressed WLC pulses, spanning the whole visible wavelength range, are used.
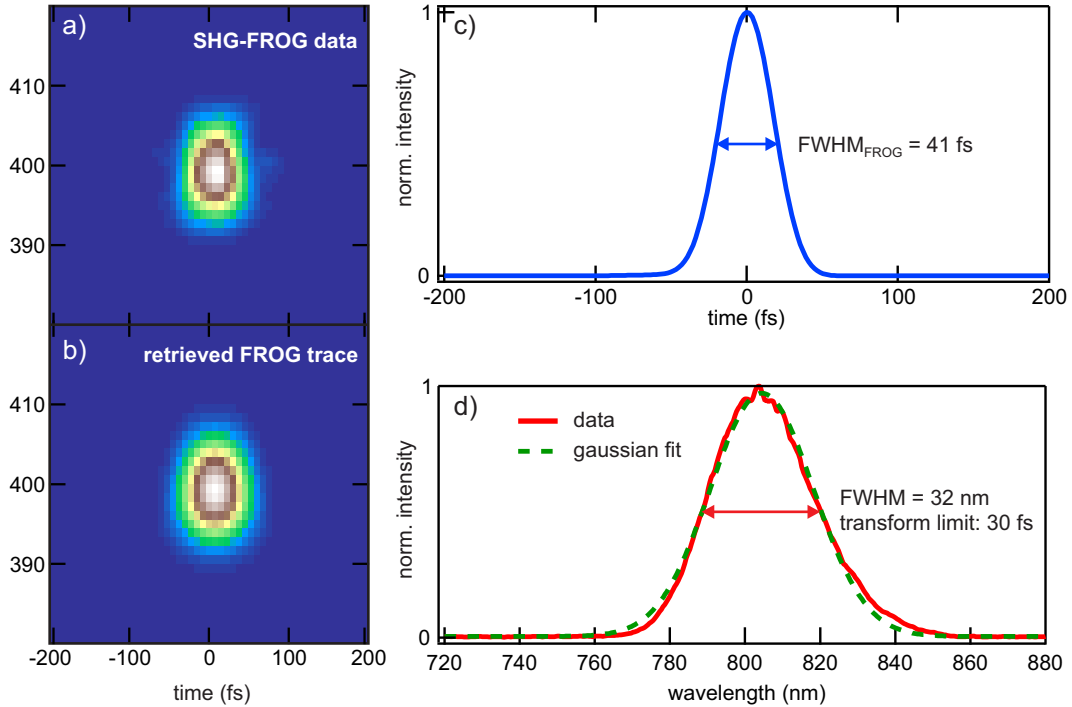
**Figure 3.2:** Pulse characterisation of amplifier output: a) shows a spectrogram measured with the commercial *Grenouille* device, described in the text. The retrieved FROG trace generated by a commercial software package (Femtosoft Technologies *QuickFrog*) is shown in b) and agrees very well with the measured trace. This allows for extraction of the temporal pulse shape depicted in c). The separately measured laser-spectrum is shown in d).

and introducing normal group velocity dispersion (GVD). As the stretching introduces a so called 'chirp'[12] in the laser pulse, this method is called 'chirped pulse amplification'(CPA). Such a scheme is necessary to reduce the peak intensity of the pulses below the damage threshold of the amplifier's active medium (Ti:Sa).

A single, stretched pulse is then coupled into the regenerative amplifier via an acousto-optical modulator (AOM, termed *cavity dumper*). There, it is amplified by traversing a laser cavity for an adjustable amount of round trips (usually around 20), before it is diffracted out, again by the cavity dumper. The switching rate of the cavity dumper defines the repetition rate of the amplified laser pulses and can easily be tuned between 40 and 300 kHz, depending on the needs of the experiments. In the 'dead' time, between one amplified pulse is coupled out and the next pulse from the oscillator is coupled in, the quality of the amplifier cavity is suppressed by a second AOM (termed Q-switch), to maximise population inversion when a pulse is in the cavity.

Finally the amplified laser pulses are compressed again in a grating compressor, that introduces a negative GVD and thereby compensates for the previous stretching [Squ98]. A pulse energy of up to 6.7 mJ after compression was achieved at 300 kHz. An exemplary characterisation, using a commercially available device (Swamp Optics

---

[12]The phase relation of the Fourier components of the laser pulse is modified such that the instantaneous frequency is time-dependent which sounds like a chirp if the waves were acoustic.

*Grenouille*), that uses the second-harmonic-generation (SHG) based frequency-resolved optical gating (FROG) technique [Tre00]. A clever arrangement of cylindrical lenses and a prism maps the frequency resolved second harmonic auto-correlation directly onto a camera, yielding the dataset shown in Figure 3.2 a). An algorithm (also described in [Tre00]) is used to simulate the detected intensity distribution, as depicted in b) from which the laser pulse duration can be extracted. The Gaussian laser pulse displayed in Figure 3.2 c), with a pulse duration (full-width at half-maximum, FWHM) of 41 fs has been extracted from this exemplary analysis. A separately measured intensity spectrum (using an OceanOptics *MAYA2000* optical grating spectrometer) and a Gaussian fit is shown in d). Using the well-known formula for the time-bandwidth product for transform-limited Gaussian pulses [Rul05],

$$\Delta\nu\Delta t = 0.441 \tag{3.5}$$

the extracted bandwidth of 32 nm would even support pulses down to 30 fs. Higher order chirp or limited conversion bandwidth of the *Grenouille* device can explain this discrepancy. For the different experiments presented in this work, the specific laser pulse durations (and therefore the individual experiment's time resolution) are often determined via in-situ cross- or autocorrelation measurements, rather than using separate devices for characterisation.

### 3.1.2   Noncollinear third and fourth harmonic generation

For single-photon photoemission experiments, the employed photon energy has to be larger than the work function $\Phi$ of the investigated sample surface. The fourth harmonic of the fundamental at 800 nm has a photon energy of 6.2 eV (200 nm) and fulfils this requirement, as typical work functions are on the order of 5 eV. The most direct approach would be to use 2 consecutive second-harmonic generation (SHG) stages to first generate 400 nm and in a second step 200 nm [Kor07]. As the phase matching condition for SHG (Appendix C) in the commonly used nonlinear crystal $\beta$-Barium borate (BBO) can only be fulfilled for fundamental energies up to $\sim 3.02$ eV, a different approach was used to generate as much photon energy as possible:

When adding photons of the fundamental via sum-frequency generation (SFG) in consecutive steps, phase matching can be achieved up to 6.7 eV (in a collinear geometry). This is already above the absorption threshold of BBO at 6.56 eV (189 nm [Müc88]), which then becomes the limiting factor for fourth harmonic generation. In [Fau12] such a scheme has been employed in a collinear fashion to generate the fourth harmonic centred at 6.28 eV.

To avoid the use of achromatic beamsplitters, a noncollinear setup was chosen, as displayed schematically in Figure 3.3 a). Approximately half of the amplifier output at 800 nm (i.e. $\sim 3$ $\mu$J/cm$^2$) is used to generate second, third and fourth harmonic: A fraction of this 800 nm-fundamental is split off by a beamsplitter (BS) and frequency doubled in C1. The second harmonic is then mixed with another fraction of the fundamental to generate the third harmonic in C2. The linear translation stage D1 is used to optimise the temporal overlap of the two pulses. In a last step the third harmonic is mixed with the fundamental in C3, to generate the fourth harmonic. Again a linear translation stage (D2) is used to optimise temporal overlap.
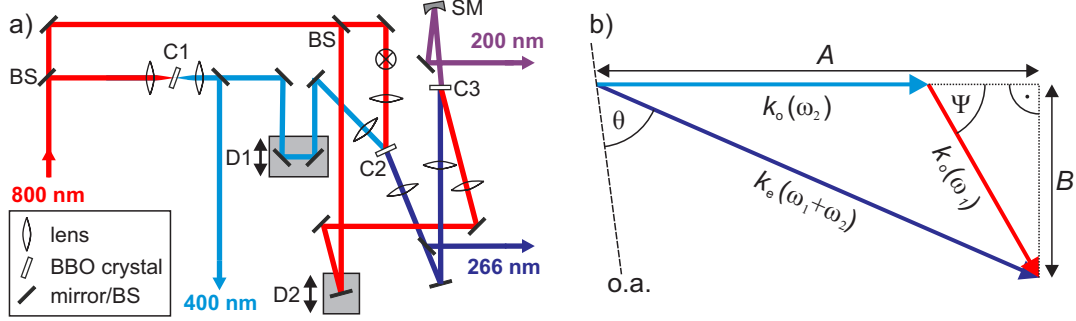
**Figure 3.3:** Noncollinear third and fourth harmonic setup and geometry: a) schematic representation of the beam paths, details are described in the text. b) type I phase matching geometry: the two fundamental beams are affected by the ordinary refractive index ($k_o(\omega)$), while the resulting sum frequency is affected by the effective extraordinary refractive index ($k_e(\theta, \omega)$) and therefore by the angle $\theta$, it encompasses with the optical axis (o.a.). The angle $\Psi$ is the angle of noncollinearity between the two fundamental beams.

To determine the angles of noncollinearity for the two mixing processes in C2 and C3, one has to consider the phase matching conditions (see Appendix C) and also spatial constraints of the setup (i.e. the possibility to spatially separate the beams, due to their noncollinearity).[13] From Figure 3.3 b) the equations for noncollinear phase matching can be determined:

$$A = k_o(\omega_2) - k_o(\omega_1)\cos\Psi \tag{3.6}$$

$$B = k_o(\omega_1)\sin\Psi \tag{3.7}$$

$$k_e(\theta, \omega_1 + \omega_2) = n_{\text{eff}}(\theta, \omega_1 + \omega_2)\frac{(\omega_1 + \omega_2)}{c} = \sqrt{A^2 + B^2} \tag{3.8}$$

$$= \sqrt{k_o^2(\omega_2) - 2k_o(\omega_2)k_o(\omega_1)\cos\Psi + k_o^2(\omega_1)} \tag{3.9}$$

Employing Equation C.98 and Sellmeier's equations for BBO from [Nik91], phase matching curves for third- and fourth-harmonic generation via SFG are calculated and shown in Figure 3.4. Angles between ordinary beams in the setup for third-harmonic (fourth-harmonic) generation (THG/FHG) are 32° (17°), from which internal angles of $\Psi = 19°$ ($\Psi = 10°$) are calculated, assuming a symmetric arrangement. In general the phase matching angle increases and the cut-off for phase-matching decreases when increasing the angle of noncollinearity $\Psi$. For an angle of $\Psi = 19°$ ($\Psi = 10°$) in a) for THG (in b) for FHG) and a fundamental photon energy of $h\nu = 1.55$ eV (800 nm) the curves are still far away from the cut-off angle (90°). Furthermore, at these angles, the slope of the phase-matching curve is similar to the collinear case ($\Psi = 0°$), which guarantees an equal phase-matching bandwidth.

---

[13]Group velocity mismatch (GVM) of the pulses was not considered. It has been shown in [Rad95], that an optimal noncollinear geometry substantially lowers GVM from 400 fs/mm (collinear) to 3 fs/mm, i.e. noncollinearity improves the situation.
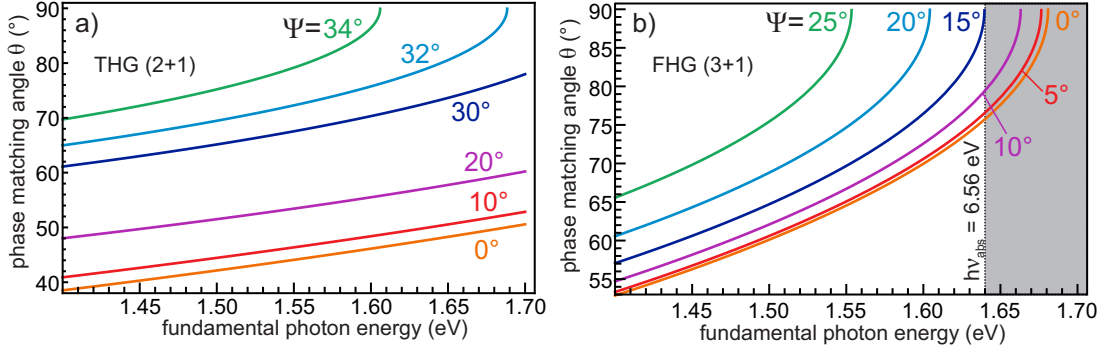
**Figure 3.4:** Phase matching angle for a) third and b) fourth harmonic generation via SFG with respect to fundamental photon energy for different angles of noncollinearity $\Psi$. In b) the absorption threshold for four times the fundamental photon energy is indicated by the grey region.

### 3.1.3 Adaptive white-light continuum compression for broadband optical probing

Time resolved optical experiments (measurements of transient or static reflectivity or transmittivity) give access to the temporal evolution of the electronic structure of the investigated system in a rather indirect way as compared to photoemission. The measurement has to be performed over a wide frequency range to properly calculate the dielectric function in a fixed geometry. Therefore measuring at various frequencies over the broadest possible range is essential if a reliable picture of the fundamental physics is to be extracted from the data. Wavelength-resolved broadband experiments, using white-light continuum (WLC) pulses in combination with an energy-dispersive detector, fulfil this condition and allow for such measurements in a single run.

For time-resolved measurements not only the spectral content, but also the relative phase of the spectral components (i.e. the temporal pulse shape) have to be known and controlled to achieve the best possible time resolution (i.e. transform limit) and avoid misinterpretation of the spectrally resolved response. In this work the setup of a broadband whitelight continuum (WLC) light source together with an adaptively controlled compressor for the whitelight pulses [Weg11] was realised, as depicted in Figure 3.5 a):

A part of the 800 nm fundamental beam is split off by a beamsplitter (BS), the rest is used as a pump pulse. A variable aperture (A) and a variable optical density attenuator (VA) are used to optimise the fundamental power and beam shape for WLC generation in a YAG crystal (YAG). The beam is recollimated by an off-axis parabolic mirror (OA) and enters the pulse compressor, consisting of a diffraction grating (G), a spherical mirror (SM) and a deformable mirror at the Fourier-plane of this 4-f-compressor setup. After compression, the WLC beam is directed and focused onto the sample (S) where it is used as a probe in a pump-probe scheme together with the 800 nm pump. A spectrometer (SP) is used to acquire the spectrally resolved WLC intensity, reflected from the sample, with respect to pump-probe delay $\Delta t$, which is adjusted by a linear translation stage (LTS) in the pump arm of the experiment.
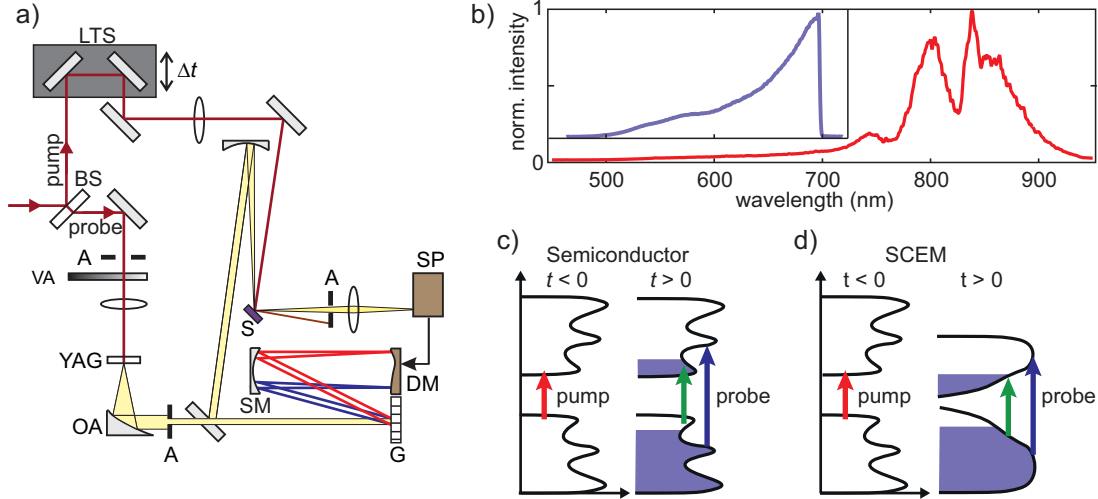
**Figure 3.5:** a) Schematic representation of the 800 nm-pump-WLC-probe setup including WLC-generation and compression by means of a deformable mirror compressor DM (see text for details). b) WLC spectrum spanning from visible to IR (red curve). Only the visible spectral content (blue curve) was used for compression. c) Schematic view of difference in optical response for regular semiconductor and strongly correlated system (SCEM). Figure is adapted from [Weg11].

**WLC generation & characterisation**   A simple and yet powerful method for generating broadband WLC pulses is by focusing ultrashort laser pulses into transparent solids [Alf70, Alf06]. Filamentation and spectral broadening occurs due to third-order nonlinear effects (Kerr-lens effect and self-phase-modulation), as described in Appendix C. A complex interplay between those and additional effects (e.g. plasma formation) [Gae00] leads to broadband white-light filaments with moderate power (i.e. pulse energy densities on the order of 10 pJ/nm [Bra09]), a perfect light source for probing the optical response of a system. The spectral content of such WLC pulses is shown in Figure 3.5 b) (red curve, the region around the fundamental at 800 nm is attenuated by a filter). In the context of this work, only the visible part (blue curve, inset) of the WLC continuum between 500 and 700 nm was used.

The mechanisms involved in WLC generation and the propagation of such broadband pulses through dispersive media (air, lenses, etc.) leads to significant chirp, i.e. a temporal stretching of the pulses with a time-dependent frequency. A spectrotemporal characterisation is therefore necessary before pulse compression is attempted. The comparably low power and broad bandwidth prohibit traditional pulse characterisation techniques like frequency-resolved-optical-gating [Kan93], nonlinear interferometry [Iac98] and modified versions of those [Wal09], as it is hard to achieve phase-matching in nonlinear techniques over the whole bandwidth (thin nonlinear crystals) and at the same time efficiently generate a signal using rather low peak powers. Instead, in-situ temporal characterisation is employed by measuring the spectrally resolved transient reflectivity [Cil10] of a $La_{0.5}Sr_{1.5}MnO_4$ (LSMO) after excitation with 40 fs, 800 nm pulses within the pump-probe setup displayed in Figure 3.5 a).
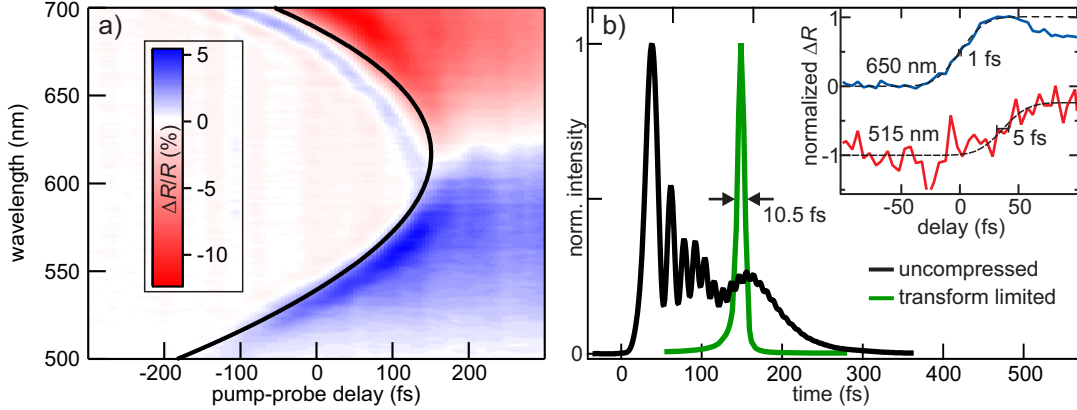
**Figure 3.6:** Pulse analysis via transient reflectivity changes: a) The transient change of reflectivity of LSMO upon excitation by a pump pulse of 40 fs duration, probed by uncompressed WLC pulses. b) Uncompressed pulse shape (black) in the time domain. For comparison the transform limited pulse is calculated (green). The inset illustrates the extraction method for the group delay $\tau_G(\omega)$ for two exemplary line-outs. Figure is adapted from [Weg11].

It has been shown that the broadband transient response of LSMO in the visible spectral range is not only sufficient in amplitude [Oga01, Tob08], but also simultaneous over the whole frequency range [Weg11] of the WLC pulse and can therefore be used as a substitute for nonlinear optical characterisation. The reason is sketched in Figure 3.5 c). When photo-exciting conventional semiconductors (at moderate fluence), as depicted on the left, electrons are excited across the band gap $(t > 0)$ and subsequently relax back to their ground state, while the band-structure stays constant and only occupations transiently change. Different probe wavelengths (as indicated by the green and blue arrows) are sensitive to different regions in the band structure, which in turn might exhibit different, even time-delayed responses (due to intrinsic relaxation mechanisms in the material). Strongly correlated electron materials (SCEMs) on the other hand show more drastic changes over the whole band-structure because of strong interactions (e.g. due to reduced screening) between the electrons. This is schematically illustrated on the right hand side of Figure 3.5 c), where the band structure changes significantly due to optical excitation. All probing wavelengths are affected by a pump pulse simultaneously on an ultrashort timescale.[14]

Figure 3.6 a) shows the transient reflectivity change $\Delta R(\lambda, t)/R(\lambda, t < 0)$ with respect to probe wavelength of LSMO, measured by the previously described optical pump-probe setup. The visible part of the WLC pulses $(500 - 700$ nm$)$ was transmitted through the switched-off 4-f compressor setup (described in detail further below) and used as a reflectivity probe. The time-zero response was extracted for each wavelength as depicted in the inset of b): Two exemplary normalised line-outs at 515 and 650 nm were analysed by a normalised error function fit $(I(t) = [\mathrm{erf}((t - \tau_G(\omega))/\tau_{\mathrm{rise}}) + 1]/2)$. The resulting half-rise points represent the frequency dependent group-delay $\tau_G(\omega)$ of the uncompressed WLC pulse. The rising edge is broadened by the finite pump-pulse

---

[14]In [Weg11] the initial response of LSMO was compared to the initial response of $VO_2$, which has been shown to be comparable to standard X-FROG type of measurements in [Cil10].

duration (approximately 40 fs), but the half-rise point can still be extracted with good accuracy. The estimated error (standard deviation $\sigma$) depends on the signal-to-noise ratio and is sufficiently low ($2\sigma \leq 5$ fs).[15]

The solid line in a) is a polynomial fit to the extracted frequency dependent group delay (GD) of the pulse. The spectral phase of the WLC continuum is then easily calculated from $\tau_{\mathrm{G}}(\omega)$ by integration:

$$\Phi(\omega) = \int_0^\omega \tau_{\mathrm{G}}(\omega')\mathrm{d}\omega'. \tag{3.10}$$

With the knowledge of spectral intensity $I(\omega)$ (from Figure 3.5 b)) and phase $\Phi(\omega)$, inverse Fourier transformation yields the WLC pulse shape (intensity) in the time domain:

$$I(t) \propto \left| \int_{-\infty}^{+\infty} \sqrt{I(\omega)} e^{i\Phi(\omega)} e^{-i\omega t} \mathrm{d}\omega \right|^2 \tag{3.11}$$

The resulting temporal pulse shape is displayed in Figure 3.5 b) (black curve). It is very asymmetric and spans hundreds of fs. The oscillating structure is due to third and higher order terms in the spectral phase. For comparison a transform limited (i.e. phase is constant or a linear function of $\omega$) pulse is calculated. While a slight asymmetry remains due to the spectral intensity distribution of the WLC, the pulse duration can easily be extracted, yielding a FWHM of 10.5 fs.

In the following it is shown, that the WLC pulse can be compressed by subtracting the appropriate spectral phase with a 4-f compressor-configuration including a deformable mirror.

**Working principle of deformable mirror based 4-f compressor**   An unfolded, so called 4-f zero-dispersion stretcher/compressor does not accumulate a spectral phase $\Phi(\omega)$ of an order higher than linear [Mar87], i.e. does not modify the pulse duration according to Equation 3.10. In this work a different approach was realised by a folded geometry [Zee99], which is schematically displayed in Figure 3.7 a). The uncompressed WLC pulse enters at the right hand side, is dispersed at a grating (600 g/mm plane ruled grating with 8.6° blaze angle) and the individual spectral components are focused by a spherical mirror (SM, $f = 250$ mm) onto a deformable mirror (DM), which is placed in the Fourier plane. The DM [Bon06] (supplier: ADAPTICA, Italy) acts as a folding mirror from which the indicated rays traverse back at a slightly downward angle (i.e. into the plane of the sketch), to be picked by a planar mirror (M). When the DM is switched off, the accumulated phase of a transmitted laser pulse is due to the specific geometric arrangement (indicated red, green and blue paths do not have the exact same length) and a residual deformation of the mirror. This is the reason for the particular temporal profile of the GD measured in the previous paragraph.

To operate the compressor, i.e. to add a certain phase to the transmitted pulse, the reflecting membrane of the deformable mirror (light blue) is deformed. The deformation/displacement is a change in path length for the frequency component $\omega$ that hits

---

[15]The pulse shape is already modified in comparison to the initial WLC pulse after generation, as the geometric arrangement of the compressor already introduces phase shift, even when switched off.
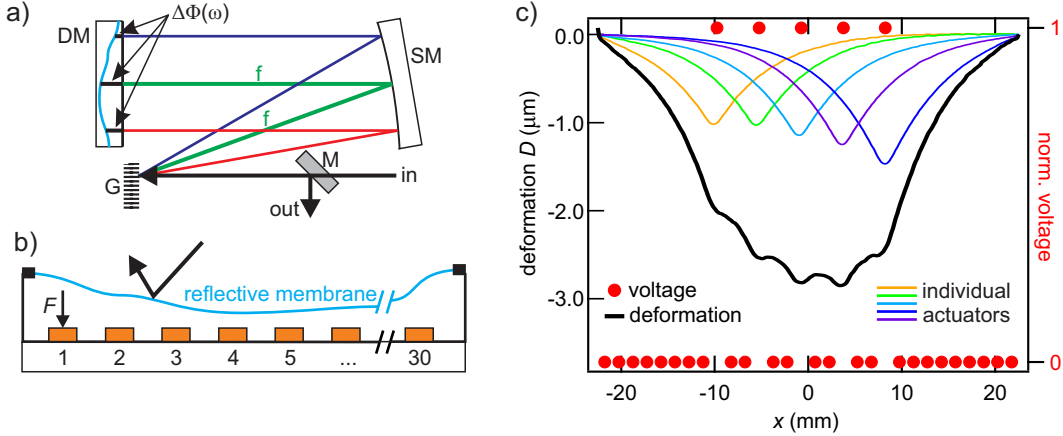
**Figure 3.7:** The folded 4-f-compressor arrangement for WLC compression is shown schematically in a). Different spectral components are focused onto the deformable mirror (DM). A spectral phase shift is introduced by DM's membrane (blue), which can be deformed by 30 electrostatic actuators as sketched in b). An exemplary, rather extreme, deformation is shown in c) for five fully activated actuators. The overall deformation (black) is the sum of the deformations generated by the individual actuators (coloured curves).

the mirror at the displaced location. This displacement $D(\omega)$ translates into a phase change via [Zee99]

$$\Phi(\omega) = \frac{2\omega}{c} D(\omega) \tag{3.12}$$

In Figure 3.7 b), a schematic representation of the DM is shown. 30 electrodes (orange) behind a reflective (i.e. metal-coated) membrane (blue) are used to pull back the reflective surface via electrostatic force (F). Applying appropriate voltages to the individual electrodes results in smoothly shaped deformation of the mirror surface. The individual deformation due to each electrode was calibrated via interferometric measurements. It is then assumed that the overall deformation is just a linear combination of the effect of each electrode. In c), the exemplary calculated deformation, (black line) due to applying the maximum voltage (indicated by the red dots) to 5 individual electrodes, is the sum of the individual deformations (orange, green, blue, violet and blue lines). A National Instruments LabView interface is used to apply normalised voltages to the device.

**Adaptive compression algorithm and resulting pulse** The compression algorithm is described by the flow chart in Figure 3.8 a):

The group delay of the WLC pulse is measured via transient reflectivity changes of LSMO and from that the phase is calculated. If the pulse is not compressed, the measured phase is stored for later use and the total phase is used to calculate the deformation needed to compensate for it (linear phase in $\omega$ can be arbitrarily added to minimise overall deformation). A calibration is performed routinely, which maps frequencies $\omega$ to physical positions $x$ on the DM by using a slit aperture and a spectrometer. The deformation is then translated from $D(\omega)$ to $D(x)$. Voltages are calculated by fitting
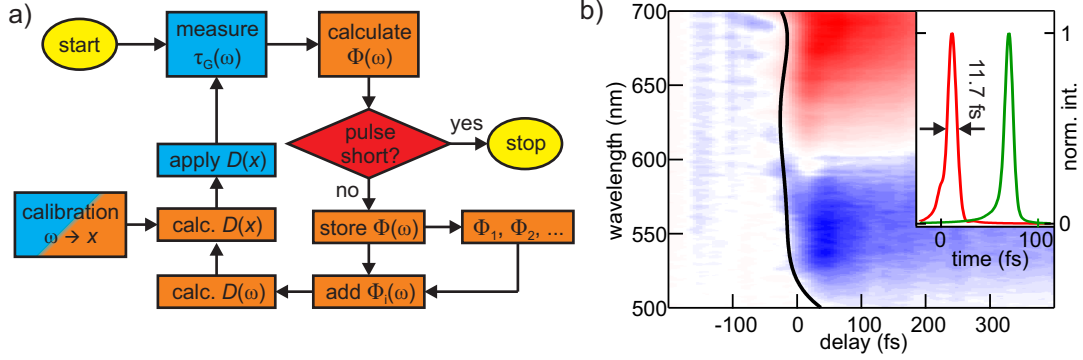
**Figure 3.8:** a) Flow chart for adaptive compression algorithm: the orange colour indicates calculations implemented in IGOR pro, blue steps are performed in National Instruments Lab-View. b) Transient reflectivity change in LSMO for compressed pulse. Pulse shapes in the inset: 11.7 fs FWHM was achieved (red curve). Calculated transform limited pulse (green) with FWHM of 10.5 fs for comparison.

the total deformation from Figure 3.7 c) to the calculated deformation $D(x)$, with the individual voltages as fit parameters. Finally these voltages given by the fitting routine, are applied to the deformable mirror. The resulting WLC pulses are characterised again. This process is iterated a few times (usually 2-4) to optimise the pulse duration.

Figure 3.8 b) shows the transient spectral reflectivity of LSMO after 2 iterative rounds through the compression algorithm. The black line indicates the group delay. The group delay spans a substantially smaller temporal range as compared to the group delay of the uncompressed pulse (see Figure 3.5), indicating a well compressed pulse. Fourier transformation again yields the temporal shape of the WLC pulse after compression (red curve in the inset). The pulses have a FWHM of 11.7 fs, very close to the 10.5 fs of the calculated transform limited pulse (green curve for comparison).

The adaptive compression scheme, employing a deformable mirror at the Fourier plane of a folded 4-f geometry, presented in this section, is able to compress broadband WLC pulses close to their transform limit (in our case sub-12 fs). The pulse is characterised in-situ in a optical pump-probe setup and therefore minimises errors due to separate setups for characterisation and actual measurement. Pulse compression is achievable on a regular basis (at the beginning of each lab-day), as it usually takes less than 1 h. This constitutes a prerequisite for reliable, cutting-edge ultrafast spectroscopic experiments.

## 3.2   Photoelectron spectroscopy

While optical spectroscopy probes the dielectric function, which is uniquely defined by the band structure, a direct access to the latter on an absolute energy scale is often desired. The most immediate access to the electronic band structure of a system is provided by photoelectron (or photoemission) spectroscopy. According to the photoelectric effect [Her87, Ein05] (on metals) a photoelectron can be emitted by absorption of a single photon if the work function $\Phi$ is smaller than the photon energy $h\nu$. If the photon energy is known, the measured quantities - the kinetic energy of the photoelectron and its emission angle relative to the surface - give insights into the binding energy of the initial state of the electron as well as its wave-vector component parallel to the emission surface.

Knowledge about the photon energy $h\nu$ and the kinetic energy $E_{\mathrm{kin}}$ of the emitted photoelectron allows for calculation of the binding energy of the electron in its ground state. According to Figure 3.9(a) energy conservation directly leads to:

$$h\nu - \Phi - E_{\mathrm{kin}} = E_{\mathrm{B}} - E_{\mathrm{F}} \qquad (3.13)$$

More precisely, the measured binding energy corresponds to the difference between the initial state energy of the $N$-electron system and the final state energy of the (N-1)-electron system left behind after the photoemission process. Under the assumption that the single electron wave functions in the $N$- and the $(N-1)$-electron system stay the same, Koopmans concluded that the eigenenergies of the $N$-electron system and the binding energies $E_{\mathrm{B}}$ of a single photo-electron are equal [Koo34]. In other words it is assumed that the photoexcitation and -emission happens instantaneously, before the $(N-1)$ system relaxes to its ground state, and that the photoelectron does not interact with the $(N-1)$ particle system left behind ('sudden approximation').
If photoelectrons are not excited very far above the photoionisation potential (i.e. vacuum level), e.g. because low photon energies are employed, effects beyond the sudden approximation might have to be considered. Deviations are connected to e.g. interactions between photoelectron and the photohole and other correlation effects beyond the single particle picture. In metals such interactions are screened by the large amount of conduction electrons [Tam13], but they can play a role in insulators and strongly correlated materials. For low-energy photoelectrons ($E_{\mathrm{kin}} < 15$ eV), and adiabatic evolution from ground state to photoexcited state is possible, as the photoelectron leaves the system on a slow time-scale [Tam13, Kor06].

In Figure 3.9 b) the mean free path of electrons in various materials is shown as a function of kinetic energy with respect to the Fermi energy. Although the cross-section for electron-electron scattering

$$\frac{\mathrm{d}^2\sigma}{\mathrm{d}\Omega\mathrm{d}\omega} = \frac{\hbar^2}{(\pi e a_0 q)^2}\mathrm{Im}\left(\frac{-1}{\epsilon(\mathbf{q},\omega)}\right) \qquad (3.14)$$

depends on the materials dielectric function $\epsilon(\mathbf{q},\omega)$, the mean free path is quite universal for different material, at decently high kinetic energies [Hüf10]. This is because at higher energies, the electrons are considered as quasi-free and their plasma frequency determines the loss function. The mean electron-electron distance, which is close to constant for a wide range of materials, in turn determines the plasma frequency, hence
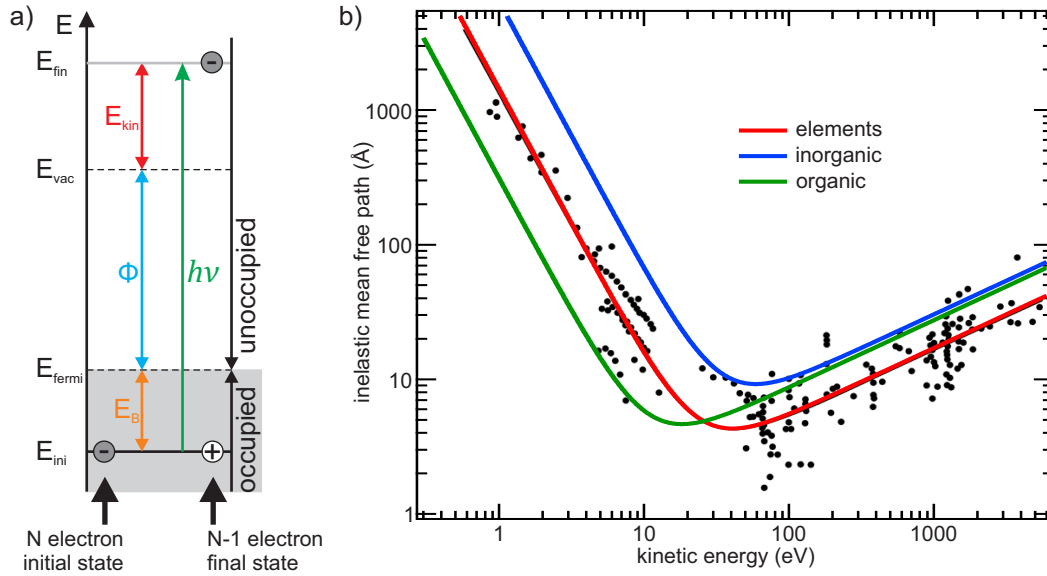
**Figure 3.9:** a) Energy conservation in photoemission process: A photon with energy $h\nu$ is absorbed. The binding energy of the photoelectron in respect to the vacuum level $(E_B + \Phi)$ has to be overcome. The photoelectron originating from initial state $E_{ini}$ has a kinetic energy in respect to the vacuum level of $E_{kin} = h\nu - \Phi - E_B$. b) Electron mean free path for elements (data) and universal curves for elements, organic and inorganic compounds according to [Sea79] and [Dam04].

the observed 'universality'. The universal curve is in general used as an argument for the surface sensitivity of photoemission spectroscopy (using photon energies on the order of tens and hundreds of eV), as unscattered electrons are mainly emitted from the surface region.

In the first of the following sections the 'three-step model' and the 'one-step model' of photoemission are described in more detail. The conservation of the parallel component of the electrons wave vector $k$ (relative to the emitting surface) is reflected by the emission angle of the photoelectron. Therefore, angle-resolved photoemission spectroscopy (ARPES) and its capability to map band structures is discussed in the subsequent section. Thereafter, two-photon-photoemission (2PPE) allowing for spectroscopic access to the unoccupied electronic band structure and time-resolving pump-probe schemes for 2PPE and ARPES are discussed.

A comprehensive description of photoelectron spectroscopy is for example found in the book 'Photoelectron Spectroscopy - Principles and Applications' by Stefan Hüfner [Hüf10].

### 3.2.1    One- and three-step-model of photoemission

The photoemission process is easily described in terms of the so called 'three-step-model' of photoemission. While the splitting of the photoemission process into three steps is arbitrary (phenomenological) and not exact, it is able to describe photoemission in a very intuitive and often sufficiently correct manner. The three steps involved are

depicted in Figure 3.10 a) and explained as follows:
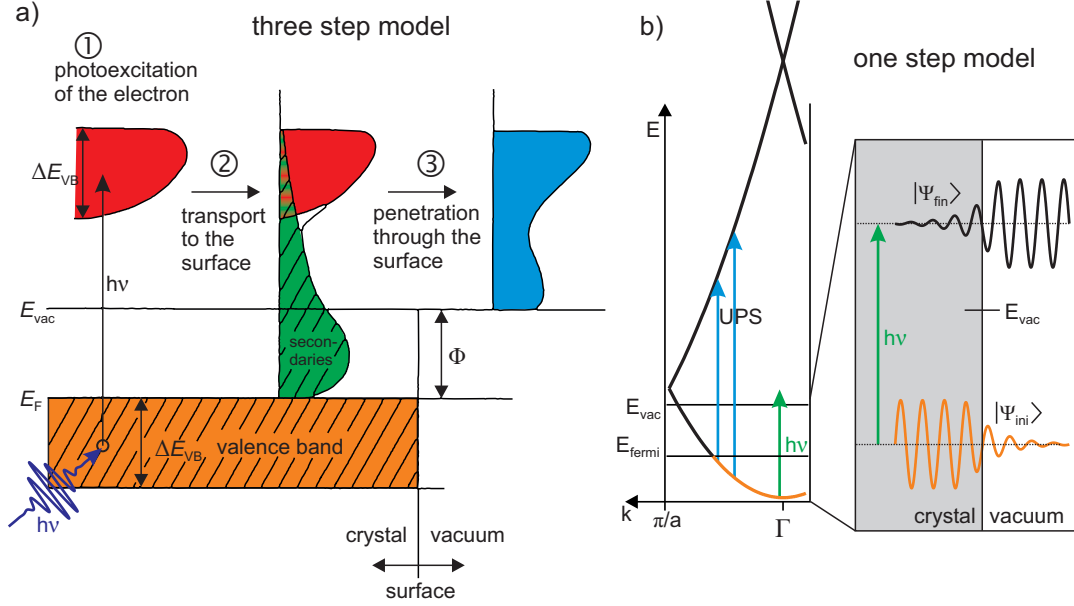


**Figure 3.10:** a) Three-step model of photoemission: ① an electron is excited from occupied states (below the Fermi energy $E_F$, orange) into final states (red) by photons with energy $h\nu = \frac{\hbar\omega}{2\pi}$. ② While they travel to the surface, they potentially undergo scattering events, generating secondary electrons at lower energies (green). ③ Only electrons that overcome the work function of the sample are emitted. Modified from [Hüf10]. b) One-step model, real final states are considered (inverse LEED states), especially when final Bloch states in the solid can not be excited.

① Local photoionisation: an electron-hole pair is created by absorption of a photon. This corresponds to an excitation between two Bloch states inside the solid. The transition probability from initial state $|\Psi_{\text{ini}}\rangle$ to final state $|\Psi_{\text{fin}}\rangle$ according to Fermi's Golden Rule within the dipole approximation is given by

$$|\langle\Psi_{\text{fin}}|\,\mathbf{A}(\mathbf{r})\cdot\mathbf{p}\,|\Psi_{\text{i}}\rangle|^2\,\delta(E_{\text{fin}} - E_{\text{ini}} - h\nu) \qquad (3.15)$$

The delta function ensures energy conservation. Momentum transfer from the photon to the excited electron is neglected and the excitation is considered 'vertical' in the band structure, because the momentum of the a UV photon of 200 nm wavelength corresponds to only 0.2% of the Brillouin zone size in Copper. A separate discussion of selection rules and matrix elements

$$M_{\text{if}} = |\langle\Psi_{\text{fin}}|\,\mathbf{A}(\mathbf{r})\cdot\mathbf{p}\,|\Psi_{\text{ini}}\rangle| \qquad (3.16)$$

follows below.

② Propagation of the photoelectron towards the sample surface. Depending on the mean free path and point of origin of the photoelectron, scattering occurs,

which can be described by a complex wave vector component perpendicular to the surface ($k_\perp = k_\perp^{(1)} + i k_\perp^{(2)}$). The imaginary part corresponds to a damping term of a plane wave travelling to the surface.

③ Emission of scattered (secondary) and unscattered electrons from the sample surface into the vacuum. Only photoelectrons that overcome the work function $\Phi$ are emitted. The binding energy can only be calculated following Equation 3.13 for unscattered electrons, which therefore constitute the signal of interest in the photoemission experiment. The scattered 'secondary' electrons appear as a background that has lost information of its energetic origin.

Especially for the low photon energies ($h\nu_{\mathrm{max}} = 6.2$ eV) used in the context of this work, final state effects have to be considered. The '1-step-model' of photoemission treats the whole photoemission process as a single coherent step, considering the exact initial and final state wave functions. The final state then is a so called 'inverse LEED state', which looks like a free electron state in the vacuum, but is connected to the electron wave function of the solid, depending on its intrinsic electronic structure.

In Figure 3.10 b) such a situation is depicted. While for higher photon energies (UPS with tens of eV, blue arrows), a transition between initial (orange) and final free-electron-like states (black curve) is energetically possible, this does not necessarily apply for lower photon energies (on the order of 6 eV, green arrow). Wave function overlap of initial state wave function $|\Psi_{\mathrm{ini}}\rangle$ (orange) and final state wave function $|\Psi_{\mathrm{fin}}\rangle$ (black) can be reduced to the surface region, as both decay towards opposite half-spaces. Whether this argument holds depends of course on the specific final state wave function, which is not necessarily known.

Photoemission spectroscopy can be quite surface sensitive for different reasons. For certain energies the electron mean free path is very short and in addition the specific surface electronic structure plays an important role. Nevertheless, bulk contributions might very well be probed.

Comparison with high-photon energy (i.e. $h\nu > 20$ eV) UPS data [Per06], where surface sensitivity is more established and the sudden approximation is likely to hold, allows for safe interpretation of data acquired employing low photon energies.

### 3.2.2   Angle-resolved photoemission spectroscopy (ARPES)

The electron momentum component parallel to the photoemission surface is conserved for the photoemission process [Hüf10]. If photoemission angle $\alpha$ and kinetic energy $E_{\mathrm{kin}}$ of the photoelectron are measured simultaneously, one can determine the momentum component of the photoemitted electron parallel to the emission surface $p_\parallel = \hbar k_\parallel$ via simple trigonometric consideration based on $k_\parallel = |\mathbf{k}| \cdot \sin \alpha$ and using $E_{\mathrm{kin}} = \hbar^2 |\mathbf{k}|^2 / 2m_e$. This allows the calculate of the electron wave vector component $k_\parallel$ prior to photoemission via:

$$k_\parallel = \frac{1}{\hbar} \sqrt{2 m_e E_{\mathrm{kin}}} \sin \alpha \tag{3.17}$$

$$= 0.512 \mathring{\mathrm{A}}^{-1} \mathrm{eV}^{-1/2} \cdot \sqrt{E_{\mathrm{kin}}} \sin \alpha \tag{3.18}$$

37
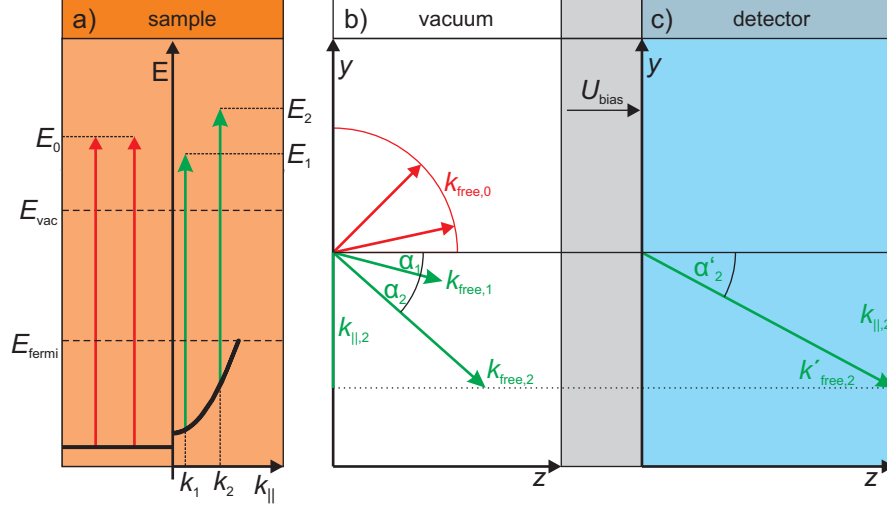
**Figure 3.11:** Angle resolved photoemission: a) non-dispersing state (left) and state with parabolic dispersion (right) are excited to final state energies $E_0$, $E_1$ and $E_2$. The electron momentum parallel to the surface ($k_\parallel$) is conserved upon transmission out of the sample surface. If a plate capacitor geometry between sample and analyser is employed, a potential difference ($U_{\mathrm{bias}}$) does not alter this parallel momentum component. Detected quantities are kinetic energy $E_{\mathrm{kin}} \propto k_{\mathrm{free},2}^2$ and emission angle $\alpha_2'$. See main text for further details.

In normal direction with respect to the surface, the crystal potential and work function have to be overcome. The perpendicular wave-vector/momentum component $k_\perp$ is therefore not conserved and can only be determined via measurements on different crystal faces or photon energy dependent measurements, under the assumption, that the final state dispersion is known.

The situation for localised (i.e. non-dispersing) and delocalised (dispersing) states is illustrated in Figure 3.11: a) depicts the band structure in reciprocal space. A non dispersing state is photoexcited (left) to a final state energy $E_0$ (red arrows) and a dispersing state (right) is excited to exemplary final state energies $E_1$ and $E_2$, depending on the initial momentum/energy position in the band.

In b) the electron momentum in free space after emission is shown. The length of momentum vectors from non-dispersing state (red) is constant, while in the dispersing case the length of the vectors (green) differs due to the different final state energies.

When electrons are accelerated homogeneously towards the detector by a bias voltage $U_{\mathrm{bias}}$, $k_\parallel$ can still be determined, as shown in c) using the example of $k_{\mathrm{free},2}$. As the accelerations only changes $k_\perp$, $k_\parallel$ is still conserved. Angle and total momentum change from $\alpha_2$ to $\alpha_2'$ and $k_{\mathrm{free},2}$ and $k_{\mathrm{free},2}'$, but $k_\parallel$ can still be calculated from Equation 3.18. If the sample is tilted (i.e. the surface normal is not directed towards the detector), or electrons are accelerated inhomogeneously, the simple calculation of $k_\parallel$ is not possible any more.

A fundamental limitation of such a band structure mapping via angle resolved photoelectron spectroscopy is given by the photon energy itself. The available kinetic excess energy after the photoexcitation has to be split in terms of momentum between
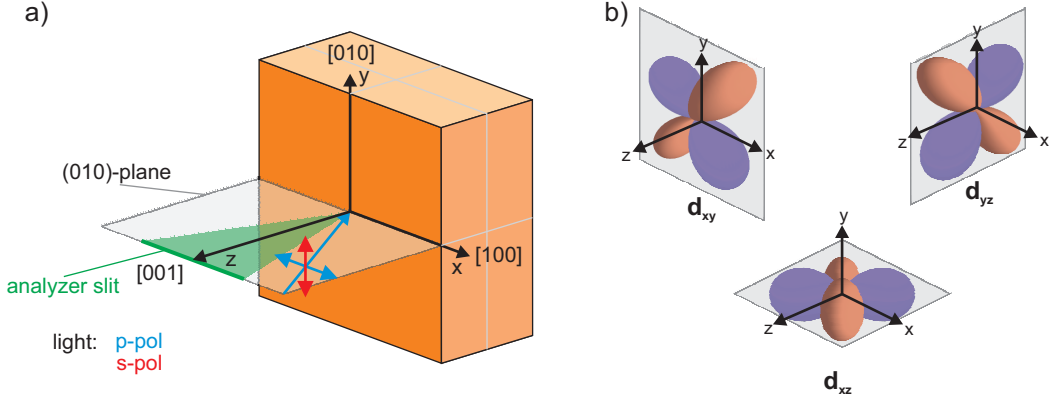
**Figure 3.12:** Symmetry considerations: a) light impinges onto the sample at the origin of the Cartesian coordinate system. The analyser slit, defining the direction of detected emission angles is shown in green. Photoelectrons that are emitted in the (010) plane are detected with respect to their angle (green shaded area) and kinetic energy. Direction of E-field vectors for p-polarised (blue) and s-polarised (red) are indicated by the arrows. b) The orientation of the $t_{2g}$ manifold ($d_{xy}$, $d_{xz}$ and $d_{yz}$) of 3d orbitals are shown using the same coordinate system as in a).

$k_\perp$ and $k_\parallel$. Electrons with $k_\perp \sim 0$ have the maximum possible parallel momentum, which can be detected. This maximum value for $k_\parallel$ is set by the kinetic energy of the photoelectron after emission. According to Equation 3.18 a photoelectron with $E_{\mathrm{kin}} = 1$ eV kinetic excess energy has $k_\parallel \sim 0.5\mathrm{\mathring{A}}^{-1}$. The accessible range of momenta $k_\parallel$ shrinks to a fraction of the Brillouin zone size for low photon energies.

### 3.2.3 Matrix elements and selection rules

As indicated by Equation 3.15 and Equation 3.16, dipole selection rules apply to initial-to-final state transitions (in both the three- and one-step-model). To calculate exact values for the matrix elements $M_{\mathrm{if}} = |\langle \Psi_{\mathrm{fin}}| \mathbf{A}(\mathbf{r}) \cdot \mathbf{p} |\Psi_{\mathrm{ini}}\rangle|$ the wave-functions of initial and final state have to be known, but even without this knowledge one can tell, if $M_{\mathrm{if}}$ vanishes or not via symmetry arguments only:

In Figure 3.12 the sample (orange), incident light (p-polarised: blue, s-polarised: red) and the (010)-high-symmetry-plane in which the photoelectrons are detected (along the analyser slit indicated by the green line) are shown. The symmetries are all given with respect to this (010)-plane:

- If the final state $|\Psi_{\mathrm{fin}}\rangle$ was odd with respect to the (010)-plane, there would be a node on this plane resulting in zero detection probability. Therefore the final state wave function $|\Psi_{\mathrm{fin}}\rangle$ has to be even.

- The whole matrix element $M_{\mathrm{if}}$ has to be even as well, otherwise integration would lead to a value of zero.

- Operator $\mathbf{A} \cdot \mathbf{p} = A_x \partial_x + A_y \partial_y + A_z \partial_z$ is odd for s-polarised light ($A_x = A_z = 0$),

as $\partial_y$ changes the symmetry with respect to the mirror plane. $|\Psi_{\mathrm{ini}}\rangle$ must also be odd.

- p-polarised light ($A_y = 0$) does not change the symmetry with respect to the mirror plane, i.e. it is even. The initial state must be even, too.

As an example, the 3d $t_{2\mathrm{g}}$ manifold of $\mathrm{d}_{xy}$, $\mathrm{d}_{xz}$ and $\mathrm{d}_{yz}$ orbitals is displayed in Figure 3.12 b). Only the $\mathrm{d}_{xz}$-orbital is even with respect to the (010)-plane. Its signal should be most intense, when probed by p-polarised light. If s-polarised light is used, the major part of the photo-current should stem from the other two orbitals ($\mathrm{d}_{xy}$ and $\mathrm{d}_{yz}$).

### 3.2.4   Unoccupied band structure and excited state dynamics

Photoelectron spectroscopy, employing photon energies larger than the work function of the investigated sample ($h\nu > \Phi$), is mainly sensitive to occupied states, i.e. the equilibrium band structure. To investigate the dynamics of a system upon perturbation, two slightly different approaches have been chosen:

- **Two-photon-photoemission (2PPE)** The photon energy is smaller than the work function of the investigated system. Single photon processes are therefore prohibited and only second (or higher) order processes can be detected, which involve intermediate unoccupied states. Dynamics are directly probed in the time domain by employing a pump-probe scheme.

- **Time-resolved and angle-resolved photoelectron spectroscopy (TR-ARPES)** The system is still probed in a single photon scheme, but a, potentially very strong, pump pulse is used to drive the system far out of equilibrium. The out-of-equilibrium situation and subsequent relaxation dynamics can be observed.

Both techniques need sufficiently high optical field strengths, as 2PPE is a second order nonlinear type of spectroscopy with a 4 orders of magnitude lower cross section than single photon photoemission [Fau94] and for TR-ARPES the pump-pulse has to be able to substantially drive the system out of equilibrium (e.g. even trigger a phase transition), to generate enough contrast with respect to the equilibrium situation. More specific details are given in the following sections.

### 3.2.5   Two-photon photoemission

If photon energies are used that are smaller than the work function of the system $h\nu < \Phi$, two (or more) photons are needed for photoemission of an electron. The possible excitation mechanisms are summed up in Figure 3.13 a):

Mechanism ①: A photon of energy $h\nu_1$ excites an electron resonantly from an initial state (ini) into a real intermediate state (int). A second photon of photon energy $h\nu_2$ excites the electron into a final state (fin), i.e. into a continuum of free electron states. In fact the two photon energies can be equal, the two photons can even be irradiated via the exact same pulse.

Mechanism ②: An intermediate state is populated non-resonantly, i.e. the excited electron has to undergo a scattering event (e.g. with another electron, a defect or
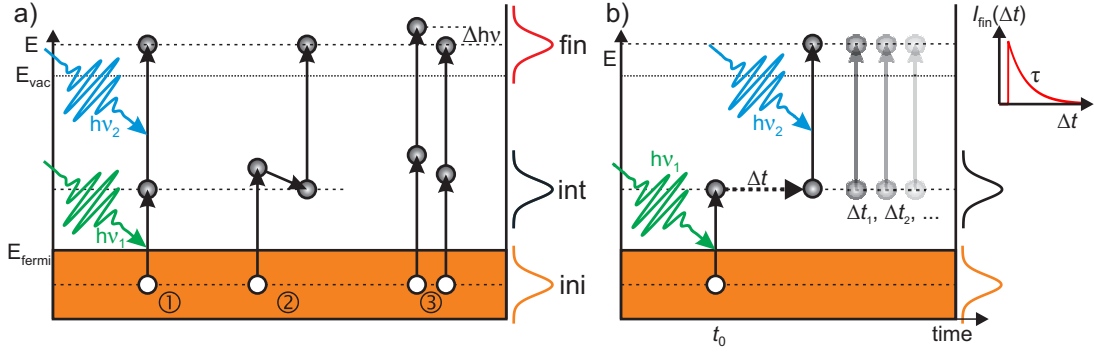
**Figure 3.13:** a) Different static 2PPE excitation schemes: ① resonant emission from initial state (ini) via real intermediate state (int) into final state (fin). ② non-resonant 2PPE via inelastic scattering. ③ 2PPE via virtual intermediate state. b) Illustration of time-resolved 2PPE scheme. A first laser pulse ($h\nu_1$) populates a real intermediate state at time $t_0$. The population of the intermediate state is then probed subsequently by a time-delayed (by $\Delta t$) pulse.

a phonon) so that energy and/or momentum conservation allows occupation of the intermediate state, which is probed by a second photon as in ①.

Mechanism ③: If there is no intermediate state in resonance with the photon energy $h\nu_{1/2}$ two-photon-absorption still allows for transitions between initial and final states. Photoemission via virtual intermediate states is connected to the second order polarisation due to the strong fields of the involved laser pulses.

To discriminate between different excitation mechanisms, photon energies can be varied. A variation of $h\nu_1$ would for example not change the final state energy in ①, but would shift the final state energy of ③ by the change in photon energy $\Delta h\nu$. For a real system the band structure can complicate such arguments and has to be carefully considered.

**Time-resolved 2PPE scheme**   The population and relaxation dynamics of unoccupied states are initiated and probed easily by a two-pulse experiment. As Figure 3.13 b) shows, the two photons with energy $h\nu_1$ and $h\nu_2$ arrive at different times. First $h\nu_1$ populates the real intermediate state (int) at time $t_0$. A second pulse with photon energy $h\nu_2$ then photoemits (i.e. excites above the vacuum level) electrons from that state after a time delay $\Delta t$, and thereby probes the population of the intermediate state at time $t_0 + \Delta t$. The experiment is repeated for different time delays[16] to acquire the population decay of the intermediate state via the time-dependent photoemission intensity $I_{\text{fin}}(\Delta t)$.

For negative $\Delta t$ (i.e. pulse $h\nu_2$ arrives first), the excitation scheme is inverted. The temporal direction in which a state shows finite lifetime thereby reveals the excitation mechanism. As the photoemission intensity is recorded with respect to energy $E$, emission angle $\alpha$ and time delay $\Delta t$, a three-dimensional dataset of the evolving

---

[16]Realised by variation of the path length via a computer controlled delay stage with a precision on the order of fs.
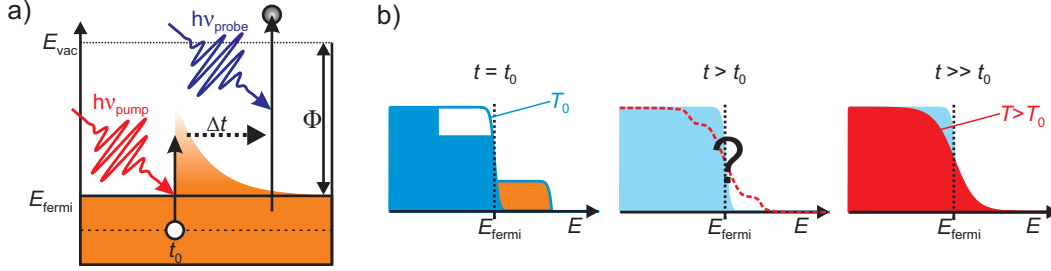
**Figure 3.14:** Time-resolved ARPES: a) Strong (e.g. infrared) pump pulse ($h\nu_{\mathrm{pump}}$) perturbs the system. A time-delayed probe pulse ($h\nu_{\mathrm{probe}} > \Phi$) is used to probe the transient evolution of the material band structure and its population upon pump excitation. In b) different temporal snapshots are illustrated. $t = t_0$: equilibrium band structure (Fermi-Dirac distribution with temperature $T_0$) is perturbed by pump pulse. $t > t_0$: Relaxation and transient changes depend on coupling of internal degrees of freedom. ($t \gg t_0$): Thermal equilibration results in increased temperature $T > T_0$ at late delays. Modified from [Kir09].

photoemission intensity $I(E, \alpha, \Delta t)$ upon photoexcitation is recorded.

## 3.2.6   Time- and angle-resolved photoelectron spectroscopy

Time resolved 2PPE spectroscopy is exclusively sensitive to the dynamics of unoccupied states, as only unoccupied states are probed with single photon energies below the work function. If one is interested in the potentially important energetic region around the Fermi-surface of a material (including occupied states), time-resolved ARPES measurements can be performed. The photon energy above the sample work function probes both occupied states and equilibrium-unoccupied states, which are transiently occupied by pump pulse excitation.

The experimental scheme is illustrated in Figure 3.14 a): A relatively strong pump pulse with photon energy $h\nu_{\mathrm{pump}}$ is employed to perturb the system significantly (several percent of electrons in the vicinity of the Fermi energy are excited [Kir09]). The pump induced dynamic evolution and thermalisation is probed after a time delay $\Delta t$ by UV photons with photon energies larger than the work function ($h\nu_{\mathrm{probe}} > \Phi$). Both occupied and unoccupied state population is therefore photoemitted. In Figure 3.14 b) snapshots of the transient population at different delay times $\Delta t$ are illustrated for a metallic sample. When the pump pulse arrives at the sample ($t = t_0$), electrons are photoexcited from occupied to unoccupied states, perturbing the occupation of states from an initial Fermi-Dirac distribution (blue) at temperature $T_0$ to a non-thermal situation (orange). At later times ($t > t_0$) the photoexcited electrons relax by undergoing scattering processes with each other, phonons, other quasiparticles or defects. The specific relaxation timescales in this regime are defined by the coupling strength between the degrees of freedom (electrons, lattice, spins) of the system, giving insights about its fundamental microscopic properties. At even later delay times ($t \gg t_0$) the system is in thermal equilibrium at an increased temperature $T > T_0$ (red) as compared to the equilibrium case (light blue).

In addition to observations of population changes (e.g. hot electron dynamics in
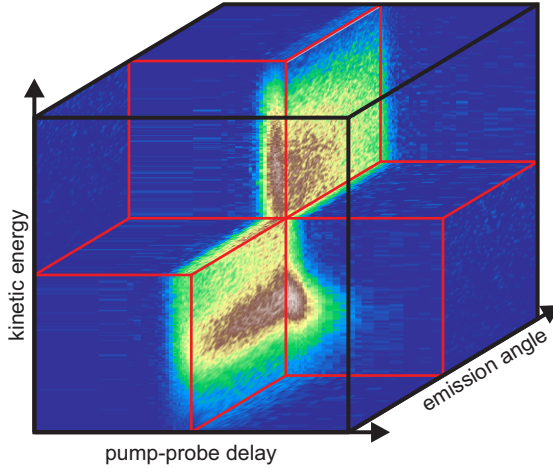
**Figure 3.15:**   3D-dataset generated by time-resolved photoemission experiment: The photoemission intensity is encoded in a false colour scale with respect to kinetic energy (vertical), pump-probe delay (horizontal) and emission angle. Cuts along centred planes are shown.

metals [Fan92, Ret02]) more complex excited state dynamics [Sob12] and phase transitions [Per06] can be observed by time resolved ARPES.

### 3.2.7   Data analysis

Both time-resolved 2PPE and ARPES measurements yield a diverse and complex dataset of photoemission intensity with respect to kinetic energy $E$, emission angle $\alpha$ and time delay $\Delta t$:

$$I_{\text{PE}}(E, \alpha, \Delta t) \tag{3.19}$$

A CCD camera acquires photoemission intensity with respect to energy and emission angle in a single shot, after photoelectrons pass the hemispherical analyser[17]. The time dependence is generated by repeating the measurement for various pump-probe delays. This section provides an overview over basic data treatment and evaluation schemes. In Figure 3.15 a) an attempt was made to depict the 3-dimensional dataset. Several 2-dimensional cuts along $E$, $\alpha$ and $\Delta t$ direction show the respective photoemission intensity on a false colour scale. The representations of photoemission intensity with respect to the variables $E$, $\alpha$ and $\Delta t$ and the related accessible physical information are discussed in the following.

**Kinetic energy**   After averaging the 3D-dataset over a certain range of angles $\Delta \alpha$ and delays $\Delta t$, a photoemission spectrum, i.e. photoemission intensity with respect to energy, remains. In Figure 3.16 a) the energetic situation and key quantities are described. The detected photoelectron energy $E_{\text{det}}$ (green) is the kinetic energy with respect to the vacuum level of the analyser. It differs from the kinetic energy after photoemission $E_{\text{kin}}$ (red) by the energetic difference between the vacuum levels of sample and analyser, which is determined by the sum of a bias voltage $eU_{\text{bias}}$ and the work function difference of sample and analyser $(\Phi - \Phi_{\text{spec}})$.

$$E_{\text{kin}} = E_{\text{det}} - \Delta E_{\text{vac}} \tag{3.20}$$

$$= E_{\text{det}} - eU_{\text{bias}} + (\Phi - \Phi_{\text{spec}}) \tag{3.21}$$

---

[17]Further details are given in Section B
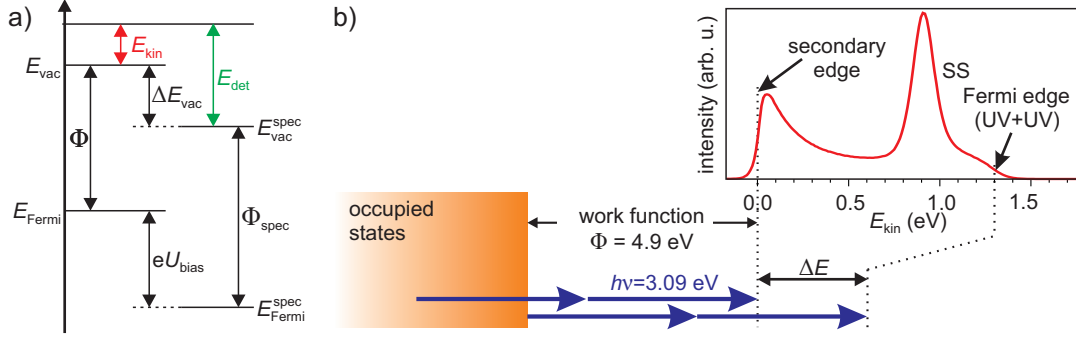
**Figure 3.16:** Energy consideration for PES: a) Illustrates the energy level alignment of sample vacuum- and Fermi-level ($E_{vac}$, $E_{Fermi}$), analyser vacuum- and Fermi-level ($E_{vac}^{spec}$, $E_{Fermi}^{spec}$) and applied bias voltage $U_{bias}$ between sample and analyser. b) Shows an exemplary 2PPE spectrum of the Cu(111) single crystal surface and the connection between low- and high-energy cut-off and sample work function $\Phi$. See text for details. Modified from [Mey11].

Both work function of sample and analyser need to be known, to calculate the respective kinetic energies. To avoid systematic errors, the energetic reference can also be performed via spectroscopic features of the measured spectra, as shown in Figure 3.16 b):

The Cu(111) surface is examined by 2PPE spectroscopy using a photon energy of $n\nu = 3.09$ eV as an example. The spectrum is cut-off at the lower energy side by the 'secondary edge' at $E_{sec}$, because only photoelectrons are emitted that overcome the work function of the sample. This energy coincides with the vacuum level of the sample and thus allows for a shift of energy axis, as displayed. The electrons with the lowest binding energy in a metal sit at the Fermi level. Photoemitting those will result in the high-energy cut-off of the spectrum at $E_{Fermi}$, approximately shaped like a Fermi-Dirac distribution[18]. For the depicted two-photon probing this means that the work function is easily calculated via photon energy $h\nu$ and width of the spectrum $\Delta E = E_{Fermi} - E_{sec}$:

$$\Phi = 2h\nu - \Delta E = 2h\nu - E_{Fermi} + E_{sec} \tag{3.22}$$

Thereby all information is available to reference the kinetic energy of photoelectrons to the sample vacuum- or Fermi-level. Depending on the probing mechanism, the energetic location of relevant states before photoemission can be determined by subtracting the respective probe photon energy $h\nu$ for intermediate (equilibrium-unoccupied) or $2h\nu$ for initial (equilibrium occupied) states.

When probing with single photons (TR-ARPES) obviously the probe photon energy has to be subtracted only once in order to access the initial state energy.

**Emission angle**   As discussed in section 3.2.2, each value pair of kinetic energy (now with respect to the analyser vacuum level, i.e. as-measured) and emission angle allows

---

[18]In reality, the underlying density of states is not necessarily constant and broadening due to the finite experimental resolution has to be considered. Both can modify shape and apparent position of the edge shape.
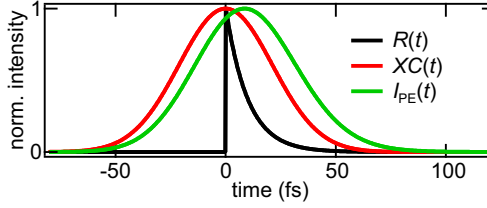
**Figure 3.17:** Exemplary photoemission intensity with respect to pump-probe delay $I_{\mathrm{PE}}(\Delta t)$ obtained via convolution of intermediate state response $R(t)$ (single exponential decay, $\tau = 10$ fs) with Gaussian laser pulse cross-correlation $XC(t)$ (FWHM = 50 fs)

for calculation of parallel electron momentum/wave-vector $k_{\parallel}$ via Equation 3.18.[19]

**Time delay**   By variation of the pump-probe delay $\Delta t$ population dynamics and transient changes of the band structure can be monitored. An exact quantum mechanical calculation for a three-level system (initial, intermediate and final state) is possible via optical Bloch equations [Lou00]. Exact knowledge of dephasing parameters needed for such a treatment is not easily accessible. Non-resonant excitation on the other hand can be described by a set of classical rate equations [Kir09], and the photoemission intensity then is

$$I_{\mathrm{PE}}(\Delta t) = \int \int I_1(t)R(t'-t)I_2(t'-\Delta t)\mathrm{d}t\mathrm{d}t' \tag{3.23}$$

$$= \int XC(t-\Delta t)R(t)\mathrm{d}t \tag{3.24}$$

with the intermediate state response function $R(t)$ and the cross-correlation function $XC(\tau)$ of the intensity envelopes $I_1(t)$ and $I_2(t)$ of pump and probe laser pulse

$$XC(t) = \int I_1(t)I_2(t-t')\mathrm{d}t' \tag{3.25}$$

The cross-correlation function can either be measured ex-situ (via nonlinear optical pulse characterisation) or determined from suitable energetic regions in the time-resolved photoemission data: If the intermediate state is virtual (or has sub-resolution lifetime), the response $R(t)$ is a delta function and $XC(t)$ is directly measured. Depending in the investigated system, a certain response function has to be assumed. In Figure 3.17 a single exponential decay has been used:

$$R(t) = e^{-t/\tau} \tag{3.26}$$

The convolution of $R(t)$ ($\tau = 10$ fs, black) and a Gaussian cross-correlation function (FWHM = 50 fs, red) yields the green curve. It is broadened and its maximum is shifted towards the exponentially decaying response, i.e. positive time delays. Such a model can be used to numerically perform least-mean-square fitting including the convolution from Equation 3.24. The fact that the measured trace is shifted with respect to the pure cross-correlation increases the time resolution of such an evaluation substantially below the employed pulse durations. The time resolution is approximately on the order of 1/10 of the pulse duration [Mey11].

---

[19]The transformation between non-energy-dispersive axis on the acquired camera image and emission angle is described in section 3.2.8.

### 3.2.8   Experimental setup for TR photoemission spectroscopy

The setup for photoemission experiments is based on a versatile ultrahigh vacuum (UHV) system for sample preparation and spectroscopy. The latter is performed with a *Phoibos 100* hemispherical analyser (SPECS) including a CCD-camera based, two-dimensional detector for simultaneous energy and angle resolved measurements. The overall setup is described in [Dei11] and presented in Appendix B in more detail. A similar UHV setup was used for example in [Gah04, Stä07b, Mey11] and is described in the respective sources. The sample transfer system is adopted from [Hag09] and also presented in Appendix B.

# 3.3 Optical pump-probe spectroscopy

Comparably low-energy excitations of valence electrons, excitons, lattice vibrations (phonons), etc. define the optical response of a solid. Electronic inter- and intraband transitions around the Fermi energy are the main excitations in the range of photon energies corresponding to visible light. The dielectric function $\epsilon(\omega, \boldsymbol{k})$ determines the response of the solid to the electromagnetic field of the light as a function of frequency $\omega$ and wavevector $\boldsymbol{k}$. Therefore the optical properties of a material give indirect access to the band structure via its dielectric function. The broader the accessible frequency range in the experiment, the more complete is the resulting view into the excitation spectrum of the investigated object.

The use of ultrashort laser pulses gives access to the ultrafast relaxation dynamics of such excitations on the order of the laser pulse duration, when applied in a pump-probe scheme, similar to time resolved ARPES 3.2.6, but instead of probing by photoemission the transient optical response is monitored. Studying the relaxation dynamics of a system, which strongly depend on the coupling between its internal degrees of freedom, allows for a deeper understanding of the fundamental properties of the system.

In the following sections a more detailed description of the outlined processes will be given.

## 3.3.1 Optical response, dielectric function and band structure

The electric field $E$ of light acts as a force upon free (metals) and bound (dielectrics, metals) charges, leading to a polarization $P$ of the illuminated medium[20]. If the electron (of mass $m$ and charge $e$) is bound in a harmonic potential its equation of motion corresponds to the one of a damped harmonic oscillator with eigenfrequency $\omega_0$ and damping rate $\gamma$, including the driving electric field $\mathbf{E}$ as an external force:

$$m[\ddot{\mathbf{x}} + \gamma\dot{\mathbf{x}} + \omega_0^2\mathbf{x}] = -e\mathbf{E} \tag{3.27}$$

The solution for a harmonic field $E(\mathbf{x}) = E_0 e^{-i\omega t}$ is leading to the following expression for the dipole moment of such a charge:

$$\mathbf{p} = -e\mathbf{x} = \frac{e^2}{m}\frac{\mathbf{E}}{\omega_0^2 - \omega^2 - i\gamma\omega} \tag{3.28}$$

The sum over all induced dipole moments will give the polarisation $P$ of the illuminated medium. In (linear) optics the macroscopic quantity connecting field and polarization ($\mathbf{P} = \epsilon_0\chi^{(1)}\mathbf{E}$) is called (linear) susceptibility and can be written as the sum of dipole contributions:

$$\chi^{(1)} = \frac{e^2}{\epsilon_0 m}\sum_{j=0}\frac{f_j}{\omega_j^2 - \omega^2 - i\gamma_j\omega}, \tag{3.29}$$

with individual oscillator strengths $f_j$. A term with $\omega_j = 0$ corresponds to the absence of a restoring force in Equation 3.27 and thereby describes free electron behaviour

---

[20]This section is compiled using various standard text books e.g. [Jac02, Ash76, Kop07]

in metals. With $\epsilon = 1 + \chi$ the complex permittivity is defined:

$$\epsilon(\omega) = (n(\omega) + i\kappa(\omega))^2 = 1 + \frac{e^2}{\epsilon_0 m} \sum_{j=1} \frac{f_j}{\omega_j^2 - \omega^2 - i\gamma_j\omega} + i\frac{e^2}{\epsilon_0 m} \frac{f_0}{\omega(\gamma_0 - i\omega)} \qquad (3.30)$$

The last term of Equation 3.30 is separated from the summation and can be identified by the complex conductivity $\sigma(\omega)$:

$$\sigma(\omega) = \frac{f_0 e^2}{m(\gamma_0 - i\omega)} \qquad (3.31)$$

Considering boundary conditions for electric and magnetic field components at a sample surface, one finds the Fresnel equations [Jac02] for reflection, depending on the complex refractive index $\tilde{n} = (n + i\kappa)$:

$$r_\perp = \frac{\cos\theta - \sqrt{\tilde{n}^2 - \sin^2\theta}}{\cos\theta + \sqrt{\tilde{n}^2 - \sin^2\theta}} \qquad (3.32)$$

$$r_\parallel = \frac{\tilde{n}^2 \cos\theta - \sqrt{\tilde{n}^2 - \sin^2\theta}}{\tilde{n}^2 \cos\theta + \sqrt{\tilde{n}^2 - sin^2\theta}} \qquad (3.33)$$

For a given complex permittivity it seems trivial to calculate the expected optical response. The inverse problem is not as easily solved. To find real and imaginary part of the dielectric constant from the measured reflectivity additional information is needed. Two approaches are commonly used:

1. Real $n(\omega)$ and imaginary $\kappa(\omega)$ part of the refractive index are related by the Kramers-Kronig-relation. To carry out the needed integration reflectivity measurements have to be conducted over a wide frequency range (extrapolation over 'all' frequencies)

2. Angle dependent measurements give additional sets of Fresnels equations that allow for extraction of $n$ and $\kappa$

Expanding **P** with respect to the source field **E** generally results in a term that is linear ($P_\mathrm{L}$) and higher order nonlinear terms ($P_\mathrm{NL}$) formally setting the frontier between linear and nonlinear optics. Nonlinear optical phenomena are explained in more detail in Appendix C.

### 3.3.2   Transient reflectivity upon photo-excitation

To get insights into the dynamics of material properties we use time-resolved pump-probe experiments to directly investigate the evolution of the system in the time-domain after a perturbation. Ultrashort laser pulses are used in a pump-probe scheme to first excite (pump) the system (i.e. photoexcite electrons from equilibrium occupied to unoccupied states in the solid) and thereby trigger an ultrafast dynamical response. The excited-state evolution and relaxation is probed via the optical response using a time-delayed ($\Delta t$) probe pulse, which is reflected from (transmitted through) the

sample of interest.  By scanning the time delay $\Delta t$, the transient evolution of the response $R(t)$ can be monitored over a wide range of timescales.  The time-resolution of such experiments is limited by the pulse durations of the applied laser pulses, as the detected signal is usually a convolution of material response $R(t)$ and cross correlation $XC(t)$ of pump and probe pulses (see Equation 3.24).

The reason for transient changes of the dielectric function upon optical excitation can be manifold.  Photoinduced charge transfer can lead to optical weight shifts [Oga01, Wal11, DC12a], photoexcited hot electrons increase the quasi-equilibrium temperature and thermalise with the lattice [DF00, Bon00], collective excitation like phonons, plasmons or charge density waves affect the dielectric function [Zei92, Kut92, Dem02, Has05, Ish06] and finally the whole band structure might be affected on a more fundamental level, e.g. when a phase transition is photoinduced [Roa71, Lys06, Tob08].  The temporal response will depend strongly on the coupling of internal degrees of freedom and energy dissipation mechanisms inside the solid, and can therefore give access to fundamental properties of the investigated system.

### 3.3.3   Coherent phonon generation and detection

A phonon is the quantum of a collective vibrational lattice excitation in a solid.  Exciting many of these quanta on a timescale shorter than their inverse eigenfrequency will lock their phase relation and a coherent phonon is generated.  As they can modulate the dielectric function, one can detect coherent phonon vibrations by optical spectroscopy.

The coherent phonon excitation mechanism depends on the nature of the driving force, that is inflicted on the lattice.  Initially light (in the near-UV, visible and near-IR regime) couples to the valence electrons of the solid, photoexciting them into previously unoccupied states.  Such a photoexcitation can generate a force onto the lattice, which can be anything between purely impulsive (delta-like) and persistent (step-like).  The classical equation of motion for the atomic displacement along the phonon coordinate $q(t)$ is:

$$\ddot{q} + 2\xi\omega\dot{q} + \omega_0^2 q = \alpha F(t)/m^* \tag{3.34}$$

$\xi$ is the damping factor, $\omega_0$ the phonon eigenfrequency and $m^*$ the effective mass of the atom in the lattice.  $\alpha$ is a coupling constant between force and specific normal mode.

Figure 3.18 shows, how the temporal shape of the force $F(t)$ affects the coherent phonon response.  In a) a purely impulsive mechanism is assumed.  The force (grey) therefore follows the laser intensity profile (red).  The resulting solution of Equation 3.34 is numerically calculated for a weakly damped ($\xi = 0.01$, blue), a critically damped ($\xi = 1$, green) and an overdamped ($\xi = 100$, yellow) case.  As the force acts instantaneously at $t = 0$ the displacement starts at the equilibrium displacement $Q_0$, i.e. it is sine-like, and subsequently oscillates around $Q_0$ in the weakly damped case.

Figure 3.18 c) depicts the other extreme case for a persistent force: The potential energy landscape is shifted according to the step-like force.  The oscillation crosses its new equilibrium position $Q_1$ after 1/4 oscillation period and therefore looks cosine-like. An intermediate case is depicted in b) with an exponentially decaying force (time constant: 500 fs), resulting in an oscillatory behaviour situated between the two extremes, both of which can be described in the theoretical framework of non-resonant and resonant Raman scattering [Gar96].  Careful analysis of the coherent phonon phase with
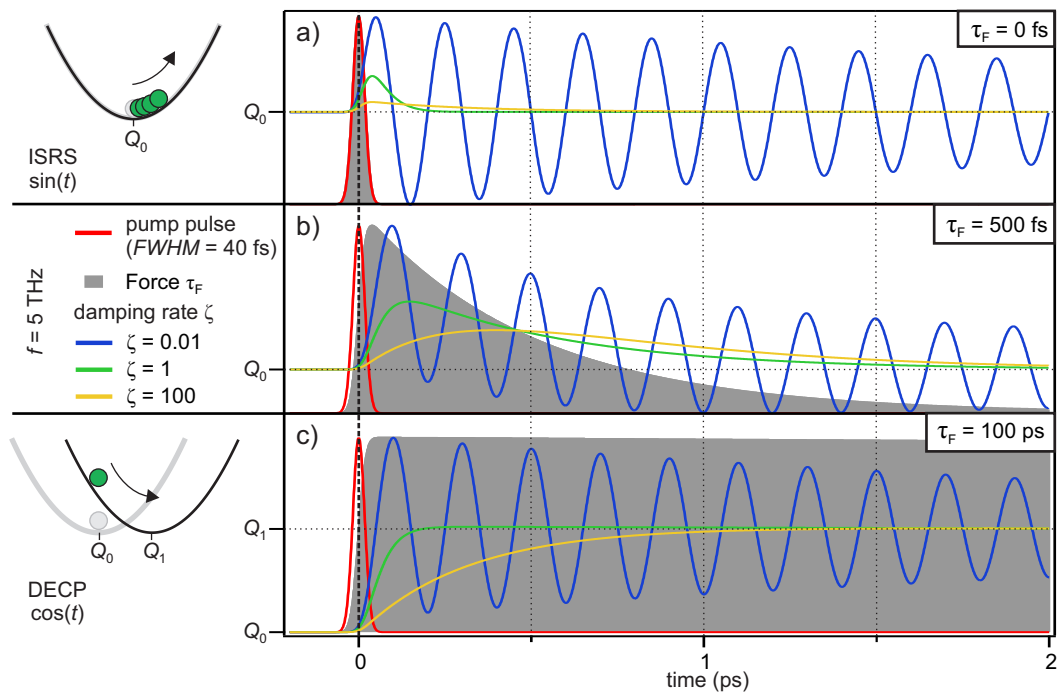
**Figure 3.18:** Coherent phonon generation: a) Impulsive stimulated Raman scattering (ISRS): Impulsive force (grey) follows laser pulse intensity (red), leading to a sine-like phonon phase. b) Intermediate case between impulsive and persistent force (grey). c) Displacive excitation of coherent phonons (DECP): Persistent force due to real electronic population, leading to a shift in the potential energy landscape. The ion oscillates around its new (excited-state) quasi-equilibrium position $Q_1$ in a cosine-like fashion.

respect to the excitation pulse, can lead to conclusion with respect to the excitation mechanism.

To optically probe coherent lattice vibrations, one can exploit the fact that coherent lattice vibration can modulate the dielectric function and thereby directly affect optical properties [Kut92]. The change of the reflectivity directly follows the lattice oscillation around its equilibrium positions [Zei92]:

$$\Delta R(t, \lambda) = \frac{\partial R(\lambda)}{\partial q} q(t) \tag{3.35}$$

The damping behaviour with respect to experimental parameters (i.e. temperature,
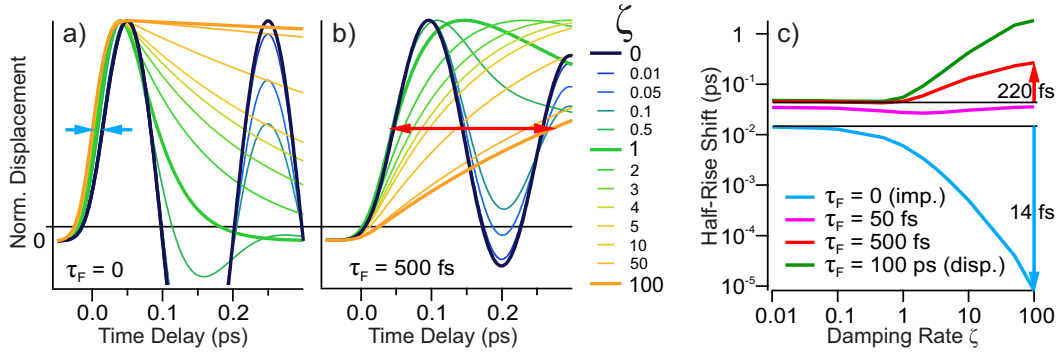


**Figure 3.19:** Initial coherent phonon response, depending on exciting force and damping: a) Impulsive force (40 fs laser pulse excitation) for various damping rates $\xi$. Increase of $\xi$ shifts initial response to earlier times. b) Semi-persistent force (time constant: 500 fs). Initial response is delayed to later times when damping rate $\xi$ increases. c) Comparison of half-rise-times on $\xi$ for different decay times of the driving force. Maximum shift between undamped ($\xi = 0$) and strongly overdamped ($\xi = 100$) case indicated by the arrows in a), b) and c).

excitation fluence, etc.) often changes e.g. towards phase transition [Har98, Sco74]. A closer look at the initial response with respect to a change of damping is depicted in Figure 3.19 a) for a purely impulsive force and in b) for a force decay constant of 500 fs. An increase in damping (cold to warm colours) surprisingly not always leads to a delay of the initial rise. For a purely impulsive force ($\tau_F$), the half rise point shifts to earlier times, as indicated by the blue arrows in a) and the blue curve in c). The effect is small ($\sim$ 14 fs) and vanishes for more persistent forces with $\tau_F \gg 0$, as shown in b) and c) (red arrow).

**Coherent control**   Coherent phonons can be controlled very similar to kicking a pendulum in- or out-of-phase to increase or decrease its oscillation amplitude. A three pulse experiment has to be performed to observe such behaviour [Dek93, Has96]. A first pump pulse initially excites coherent phonon oscillations. A second pump pulse is used to control the amplitude by simply adding to the initial effect.

If same and constant amplitudes are assumed, the combined response then becomes

$$R(t, \phi) = A \cdot \sin(t) + A \cdot \sin(t + \phi), \tag{3.36}$$

which has zero amplitude for $\phi = \pi, 3\pi, 5\pi, \dots$, i.e. the phase is an odd multiple of $\pi$ and amplitude $2A$ for even multiples, corresponding to out-of-phase cancellation and in-phase enhancement of the overall coherent lattice response.

# 4 Instantaneous band gap collapse in VO$_2$: Photoinduced change of screening

The phase transition of VO$_2$ from a monoclinic insulator to a rutile metal has intrigued scientists for decades, and the discovery of the ultrafast light-induced phase transition increased the attention even further. This chapter presents studies of non-equilibrium dynamics of the two equilibrium phases (insulating and metallic), as well as of the transient metallic phase after strong photoexcitation in VO$_2$, in order to clarify the driving force for the ultrafast transition and the nature of the transient phase. To achieve this knowledge, two complementary pump-probe spectroscopic methods are used to observe the dynamics directly in the time domain.

The structural phase transition is determined by the evolution of the potential energy landscape for the atoms. Here, this is studied by making use of the coherent phonon response of VO$_2$, which is also determined by the lattice potential energy landscape (Section 4.1). Using coherent phonon mode amplitudes as an order parameter, it is found that after strong photoexcitation a *transient* phase is entered, which has instantly lost the initial monoclinic lattice potential symmetry while the atoms are still in their monoclinic positions.

To get a comprehensive understanding of the *electronic* insulator-to-metal phase transition on the other hand it is self-evident to directly probe the electronic structure in the vicinity of the Fermi energy, as the presence of a Fermi surface is evidence for metallicity. This is achieved using time-resolved one- and two-photon photoelectron spectroscopy (Section 4.2). Strong photoexcitation instantaneously results in the appearance of DOS in the band-gap of insulating VO$_2$, meaning that the insulator-to-metal transition is directly driven by the photoexcitation. Furthermore, hot carriers within the collapsed monoclinic band-gap are observed that decay on timescales on the order of 100 fs.

This study gives novel insight into the driving mechanism of the PIPT and the properties of the transient phase: An instantaneous metallisation is observed, as a direct consequence of the photoexcitation. The photoinduced, transient phase is characterised as metallic with the monoclinic real space lattice structure, while the lattice potential is already raised above the monoclinic symmetry. Theoretical calculations confirm the purely electronic driving mechanism for the initial metallisation, by showing that photoexcitation (i.e. primarily hole doping) strongly modifies screening in VO$_2$, enough to completely renormalise its band structure.

## 4.1 Probing the potential energy landscape of VO$_2$

In this chapter, VO$_2$ is comprehensively studied by means of time-resolved broadband optical spectroscopy [21]. Figure 4.1 gives a schematic overview of the different aspects of

---

[21]The experiments have been performed in collaboration with Simon Wall, who was working as a PostDoc, and Laura Foglia, who was a diploma student in the group. The pump-probe experiments, using 800 nm probe light, were evaluated and presented to some extent in Laura Foglia's diploma thesis
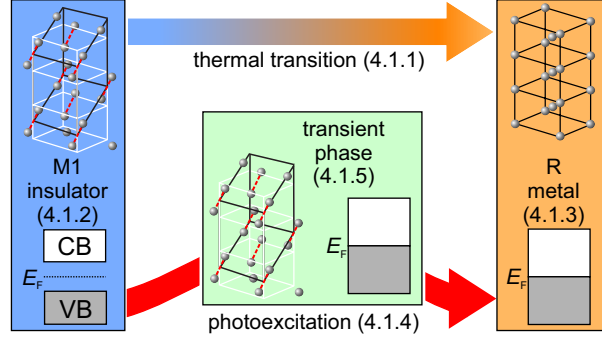
**Figure 4.1:** Schematic overview of performed studies of VO$_2$: Monoclinic insulating (blue),
rutile metallic (orange) and transient (green) phases of VO$_2$ are investigated along different
excitation pathways (top, bottom). Section

these studies. First the optical properties during the thermal transition are monitored
to characterise the sample (Section 4.1.1). The two equilibrium phases are investigated
after weak perturbation (i.e. without driving the PIPT) by a laser pulse, to expose
a phase-specific coherent phonon response: In the insulating monoclinic (M1, blue)
phase coherent phonon oscillations are detected (Section 4.1.2), which vanish in the
metallic rutile (R, orange) phase (Section 4.1.3). Their amplitude can be used as an
order parameter for the phase transition.

Strong perturbation (red arrow, Section 4.1.4), on the other hand, drives the system
out of the monoclinic into a transient phase (green). To probe the coherent phonon
response *of* this transient phase, a three pulse experiment is used (Section 4.1.5): A
first laser pulse drives the transition and a second, weaker pulse perturbs it in the
transient phase.

### 4.1.1 Temperature induced phase transition in VO$_2$/Si(100)

Vanadiumoxides exist in many stoichiometries and mixed oxidation states [Rie07]. The
VO$_2$ thin film samples used in this work were fabricated in the group of Richard Haglund
(Vanderbilt University). For the optical spectroscopy experiments a 200 nm VO$_2$ thin
film was grown by pulsed laser deposition (PLD) on *n*-doped Si(100) [Suh04]. This
results in a polycrystalline non-epitaxial film.

To characterise the sample and its switchability, temperature-dependent reflectivity
measurements ($\lambda_{\mathrm{probe}}$ = 800 nm) were performed. Figure 4.2 a) shows a measured
hysteresis loop together with the corresponding crystal structures. Upon heating across
the phase transition temperature the reflectivity at 800 nm drops by ∼70%. The
transition temperature (upon heating) is 344 K (71 °C)[22] and the hysteresis width is
11.8 ± 0.2 K.

Comparison of the width and shape of the measured hysteresis with the findings

---

(*Transient reflectivity and coherent phonon excitation: An ultrafast probe of the metal-to-insulator
transition in VO$_2$* at the Freie Universität Berlin) [Fog11].

[22] The deviation of the transition temperature by 5 K in respect to reference [Suh04] is very well
covered by a possible systematic error in sample temperature measurement (temperature gradient
between heater, thermosensor and probed region of the sample).
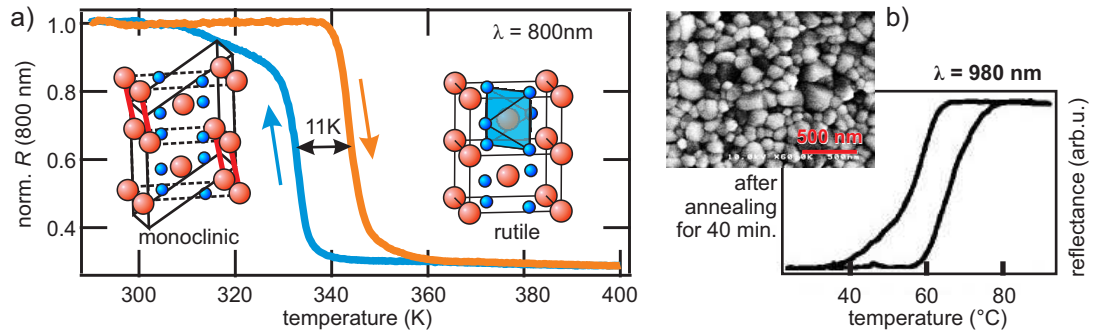
**Figure 4.2:** a) Reflectivity hysteresis (T$_C$ = 344 K) probed by 800 nm light upon crossing the insulator-to-metal transition in VO$_2$ with corresponding low-temperature monoclinic and high-temperature rutile crystal structure. b) Scanning electron micrographs and hysteresis (probed by 980 nm light) taken from reference [Suh04] for comparison.
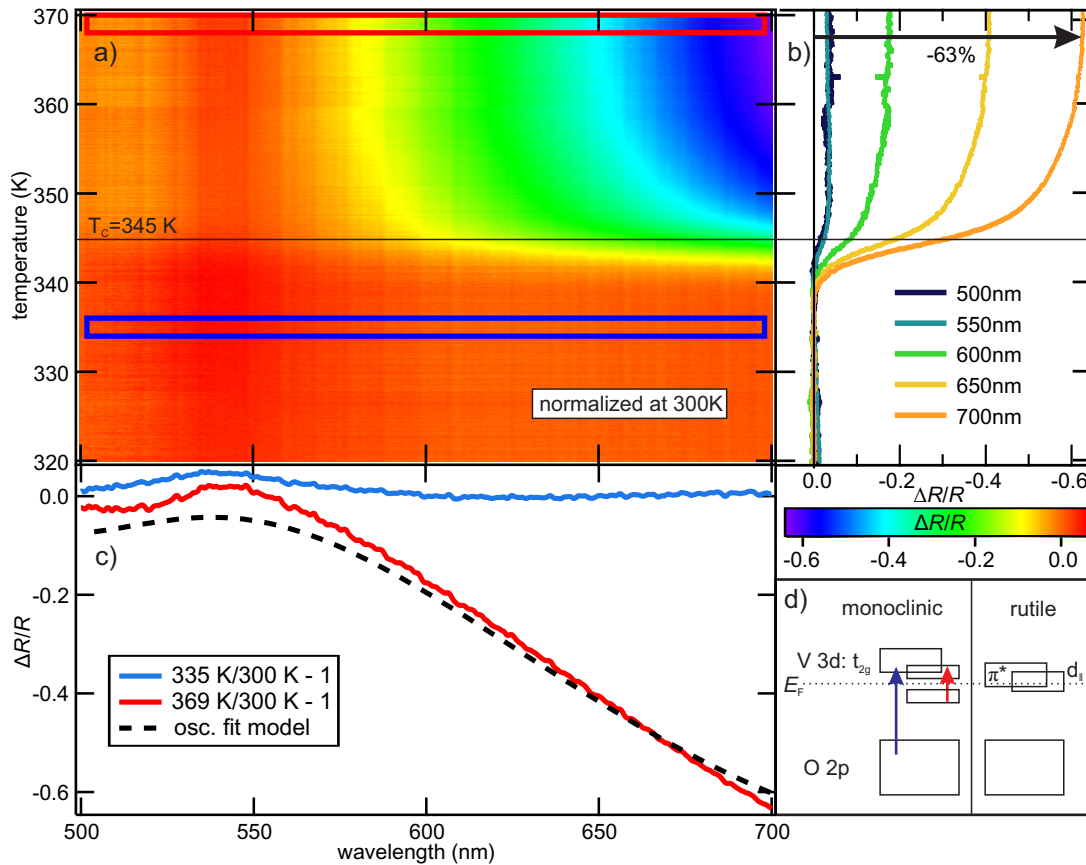


**Figure 4.3:** a) Temperature-dependent change of reflectivity in VO$_2$ probed using a WLC between 500 and 700 nm, normalised to measured reflectivity of the insulating phase at 300 K. b) Relative change in reflectivity for selected wavelengths normalised directly below the critical temperature, to only include changes connected to the phase transition. c) Lineouts at indicated positions in a) (red and blue box) with comparison to model from Ref. [Ver68] (dashed line). d) Sketch of VO$_2$ band structure change. Modified from [Wal13].

in a morphology dependent study [Suh04] (depicted in Figure 4.2 b)), suggests rather large crystallites with a diameter on the order of hundreds of nm.

The increased width of the hysteresis loop as compared to VO$_2$ single crystals (2-3 K) is due to averaging over an ensemble of many crystallites (grains) each showing slightly different transition temperatures. A competition between reduced amount of nucleating defects, crystallite size, stress and boundary effects determines the exact transition temperature of each crystallite and therefore influences the hysteresis width [Kli02, Lop02, Suh04].

The asymmetry between heating and cooling branch of the hysteresis has been observed before [Kli02, Suh04, Lea13]. Varying hysteresis widths with transition temperature, different distributions of nanocrystals for both branches or asymmetric conditions for superheating and supercooling[23] [Fan11] can explain such an asymmetric behaviour.

To extend the probing bandwidth, WLC pulses are used to monitor the temperature dependent changes in reflectivity over the whole visible wavelength range. The heating arm of a hysteresis curve is shown in Figure 4.3 a) for probe wavelengths between 500 and 700 nm (bottom axis). The left axis displays the sample temperature. Before crossing the transition temperature, the reflectivity increases slightly with temperature at wavelengths below 600 nm, while above 600 nm it stays constant. When crossing the critical temperature, the reflectivity drops at *all* probed wavelengths. This decrease can be seen in Figure 4.3 b), where lineouts at distinct wavelengths are shown, which are normalised to the reflectivity at 335 K - right before the transition temperature is reached - to exclude changes in reflectivity not connected to the phase transition.

Figure 4.3 c) shows two lineouts from Figure 4.3 a) to illustrate the wavelength dependence. The biggest change is observed at larger wavelengths (63 % at 700 nm) and the change decreases linearly towards 580 nm. At lower wavelengths than 580 nm it stays small (< 10 %).

To explain this behaviour, a sketch of the change in the VO$_2$ band structure is shown in Figure 4.3 d): Large wavelengths (lower photon energies, red arrow) probe transitions between the V 3d$_\parallel$ bands, which change strongly with the phase transition. On the other hand small wavelengths (higher photon energies, blue arrow) probe transitions from O 2p to V 3d states and are therefore less affected by the change in band-structure in the vicinity of the Fermi energy [Ver68].

### 4.1.2  Non-equilibrium dynamics of the insulating monoclinic phase

Exciting the system with laser pulses centred at around 800 nm constitutes an above band-gap excitation of the insulating phase of VO$_2$. The transient change of reflectivity, measured at room temperature, is shown in Figure 4.4 a) for a pump fluence of 1.7 mJ cm$^{-2}$, i.e. well below the photoinduced phase transition threshold. A relatively large sudden drop of reflectivity at the probe wavelength followed by a slow recovery is superimposed to beating phonon oscillations.

To analyse the coherent phonon oscillation, the incoherent (i.e. due to electronic excitation, thermal effects or incoherent lattice dynamics) part has to be subtracted.

---

[23]twin-walls and point defects act as selective, phase-dependent, nucleation seeds
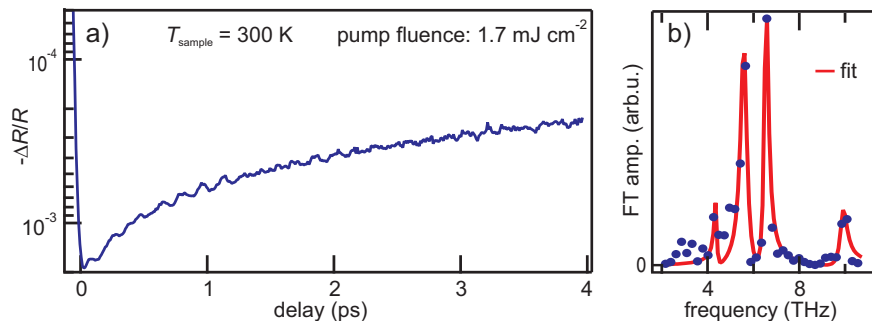
**Figure 4.4:** a) Reflectivity transient of VO$_2$ at room temperature upon weak excitation. After background subtraction a FFT yields the phonon spectrum b). Modified from [Wal12].

An empirical fit of the form

$$\Delta R(t)/R = (\mathrm{erf}(t/\tau_\mathrm{p}) + 1) \times (A_1\exp(-t/\tau_1) + A_2\exp(-t/\tau_2)), \qquad (4.37)$$

was used for background subtraction of this incoherent part. The error function $\mathrm{erf}(t/\tau_\mathrm{p}) + 1$) is used to model the rising edge. Its width ($\tau_\mathrm{p}$) is determined by the pump pulse duration. $A_1$ and $A_2$ are the two amplitudes and $\tau_1$ and $\tau_2$ the decay time constants of the initial recovery of the reflectivity change.

The remaining coherent part is then Fourier transformed for spectral analysis and yields the frequency spectrum shown in Figure 4.4 b). By fitting this spectrum with four Lorentzian line-shapes, the frequencies of the phonon modes are found to be 4.4, 5.7, 6.7 and 10.2 THz. Those eigenfrequencies agree very well with the four strongest Raman active phonon modes of the insulating phase measured by Raman spectroscopy in Ref. [Sch02] at 4.47, 5.97, 6.75 and 10.16 THz[24]. An even better match for two of the measured frequencies is found in Ref. [Par90]: 5.73 and 6.69 THz. Deviation from the exact values found in literature is either due to the slightly different stoichiometry of the VO$_2$ sample (Oxygen deficiency is known to change the phonon spectrum [Par90]) or strain effects due to the inhomogeneous nature of the thin film sample.

Probing the transient dynamics with broadband WLC pulses extends the amount of retrievable information. A transient trace (following weak excitation) is shown in Figure 4.5 a) with respect to pump-probe delay and probe wavelength. Again coherent phonon oscillations can be seen on top of a strong incoherent change of reflectivity following photoexcitation. The strongest incoherent contribution is observed at large wavelengths, as these are closest to the pumping wavelength of 800 nm, i.e. where the dielectric function is initially perturbed strongest. In contrast to that, the incoherent contribution is close to zero for wavelengths further away from the pump wavelength (i.e. at higher energies).

To analyse the phonon spectrum over the whole probing range, lineouts have been taken between 500 and 780 nm (not shown). The integration range was $\pm10$ nm around the central wavelength. Spectra resulting from FFT (without background subtraction, but employing a Hanning window function) of these lineouts are shown in Figure 4.5 b)

---

[24]Other strong modes with higher frequencies cannot be coherently excited/resolved because of the pulse duration of pump and probe laser pulses on the order of 40 fs.
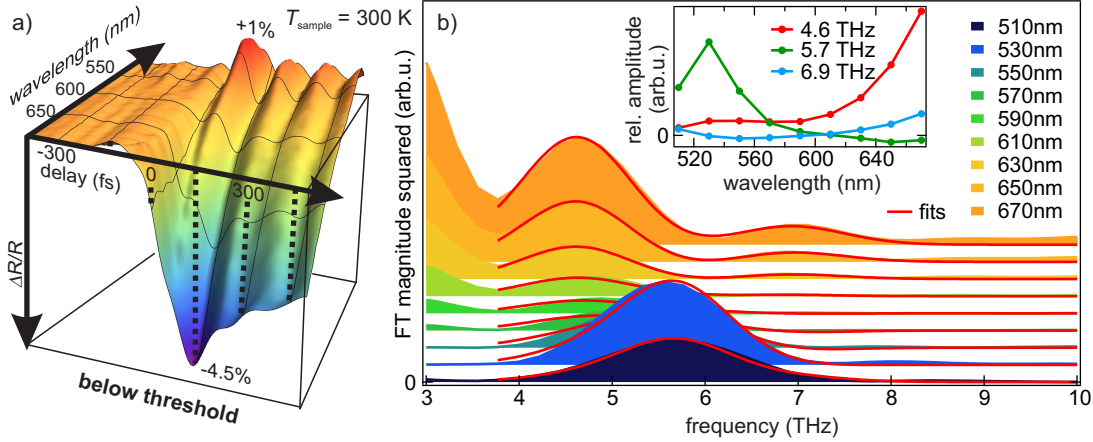
**Figure 4.5:** a) Broadband reflectivity change upon pump excitation at room temperature and below phase transition threshold fluence. b) FFTs of linouts at indicated wavelengths of a) ($\pm 10$ nm) and Gaussian fits to three detected phonon oscillations (curves are offset for clarity). Relative phonon amplitude with respect to probe wavelength is shown in the inset. Mind the opposite ordering of wavelengths in a) and b).

together with Gaussian[25] line-shaped fits at 4.6, 5.7 and 6.9 THz, in good agreement with the 800 nm probe data. However, the highest frequency (10.2 THz) is not observed. This might be due to a too long (>50 fs) pump-pulse. In addition to these modes, the FFT exposes increased intensity around 3 THz. This could, e.g. result from an artefact, due to a non-zero incoherent background.

Even though the FFT analysis over such a limited number of oscillation periods can only have a preliminary or supporting character an additional important observation is made: The relative amplitude of the modes and the ratio between coherent oscillations and incoherent background depends on probing wavelength! This is quantified in the inset of Figure 4.5 b). There, the relative intensity (fit amplitude) of the three visible phonon modes with respect to the probe wavelength are shown. Clearly different wavelength regions (i.e. parts of the dielectric function) are affected more or less strongly by the different phonon modes. This is due to different coupling strength between the distinct phonon modes and parts of the dielectric function.

The fact that at smaller wavelengths (around 520 nm) the incoherent background is close to zero and only one coherent phonon mode (at 5.7 THz) dominates the spectrum, qualifies especially this wavelength region for studies of the phonon as a marker of the monoclinic phase symmetry during the temperature- and photo induced phase transition of VO$_2$. However, before focusing on the *transient* metallic phase (upon photo inducing the phase transition), the differences of the equilibrium (high-temperature) metallic phase of VO$_2$ in comparison with the (low-temperature) insulating phase are characterised in the next paragraph.

---

[25]significant broadening due to the rather short range of delays (700 fs) available in this measurement.
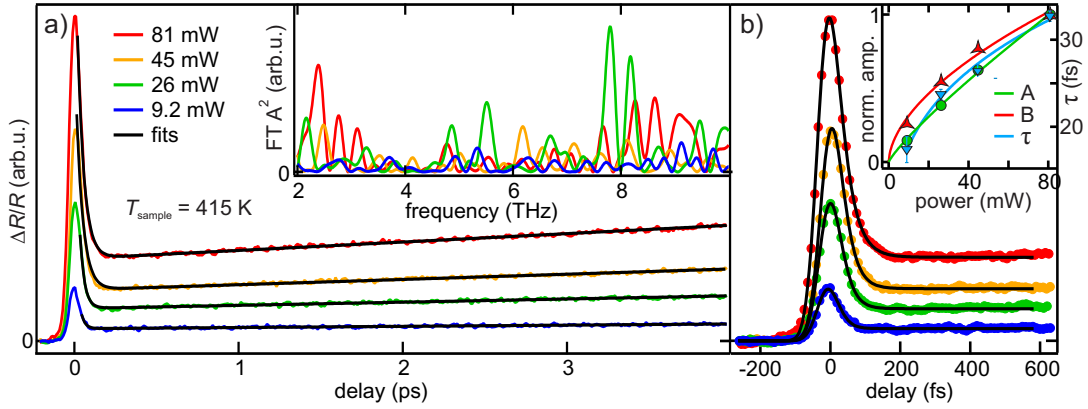
**Figure 4.6:** a) Pump-induced reflectivity change in metallic ($T = 415$ K) VO$_2$ probed by 800 nm pulses for different pump-power and empirical fits starting right after peak-like structure. Fourier transforms (after background subtraction using the fits) of the transients are shown in the inset. To capture the initial dynamics, a different fit for early delays ((4.39)) is shown in b). The inset displays pump-power dependencies of resulting fit parameters: Step amplitude A, peak amplitude B and decay time constant $\tau$.

### 4.1.3 Non-equilibrium dynamics of the rutile metallic phase

Heating the sample above the phase transition temperature allows to perform pump-probe measurements of the transient optical response of the equilibrium metallic rutile phase and compare them to the ones previously described for the low temperature phase.

Pump-induced reflectivity changes at a sample temperature of 415 K probed with 800 nm light for different pump fluences are shown in Figure 4.6 a). One characteristic difference to the insulating, low temperature phase is the sign of the transient, which is now positive (reflectivity increase upon pump excitation). A spike-like initial response is followed by a slow transient reflectivity increase. To perform Fourier transformations in the region after the initial spike up to late delays ($> 3$ ps) an empirical background consisting of an exponential decay and a increasing linear slope has been subtracted:

$$\Delta R(t)/R = A \cdot \exp(-t/\tau) + m \cdot t + c \qquad (4.38)$$

The resulting Fourier transforms are shown in the inset of Figure 4.6 a). There are no distinguished intensities visible in all of four exemplary traces. Furthermore, comparison with Raman data suggests that the frequency spectra shown, consist of noise only.[26]

To quantify the initial dynamics right after excitation, a more complex fit function than (4.38) has to be applied, while the slow transient reflectivity increase for later delays, covered by Equation 4.38, is neglected to minimise the amount of free fit parameters. The fit function consists of the sample response (sum of a step-function

---

[26]The high-frequency oscillations visible in Figure 4.6 a) do not show up as a consistent peak in the Fourier spectrum and do not behave like coherent phonon oscillations, e.g. they increase in amplitude with delay as late as three ps. They are therefore attributed to an artefact, e.g. due to periodic fluctuations in laser power or temperature oscillations in the sample heater feedback loop.

$(\text{erf}(t)+1)$ and an exponential decay), convolved ($*$) with the laser pulse XC temporal shape:

$$\Delta R(t)/R = (\text{response} * \text{pulse})(t) \tag{4.39}$$
$$\text{response} = (\text{erf}(t) + 1)(A + B \cdot \exp(-t/\tau)) \tag{4.40}$$
$$\text{pulse} = \exp(-t^2/\sigma^2) \tag{4.41}$$

Figure 4.6 b) shows the a close-up view of the data displayed in a) for the fitted delay region (coloured circles) and the respective fits (black curves). Assuming a laser pulse duration of 45 fs (which on average produced the best fit, when kept as a free fitting parameter) the fit generates decay times $\tau$ of the spike-like structure on the order of tens of fs with a growing trend with power. The power dependence of decay time $\tau$, normalised step amplitude A and normalised peak amplitude B is shown in the inset of Figure 4.6 b) (markers), together with power-law ($\propto x^p$) fits (solid lines). The step amplitude A is close to linear with pump-power ($p = 0.85 \pm 0.03$) while the amplitude B of the initial spike has a lower power dependence ($p = 0.56 \pm 0.05$) and the decay time grows with a power of ($p = 0.3 \pm 0.02$).

As the material is already in the high-temperature phase, no phase transition occurs any more upon pumping the system with light, which explains the linear power dependence of the step amplitude A of the slowly changing background. There are two probable causes for the spike-like structure right after photoexcitation:

① the initial spike is directly connected to photoexcitation of the electronic system. The dielectric function can be modified by the generation of hot electrons in various ways (via intraband and interband excitation, modification of plasma frequency, etc.) and the increase of the time constant $\tau$ can be explained in the framework of Fermi liquid theory by a transient increase of carrier screening or decrease of phase-space for e-e-scattering. Also electron-phonon scattering rates are known to change with excitation fluence.

② the initial spike is a modulation due to overdamped phonons of the equilibrium metallic phase, as the solution for an overdamped oscillation is a decaying exponential:

$$\text{q}(t) \propto \exp(-\alpha t) \tag{4.42}$$

The increasing decay constant would indicate a slight increase in damping rate with fluence. Although the onset of reflectivity change would shift in time with changes of the damping rate (Section 3.3.3), experimentally no conclusions can be drawn from that fact, as the exact temporal relation between pump and probe pulse is not fixed over the course of the different measurements.

Altogether there are too many possible explanations and too little information in the time domain, to give a conclusive answer regarding the nature of the spike-like feature.

In the previous section (4.1.2), the coherent response and incoherent background was disentangled via the probing wavelength. Therefore the transient reflectivity change of VO$_2$ at 400 K probed by WLC pulses is shown in Figure 4.7 a). The general shape is very similar to the response probed at 800 nm. The sign of the reflectivity change is positive at all wavelengths. The peak amplitude as well as the transient background
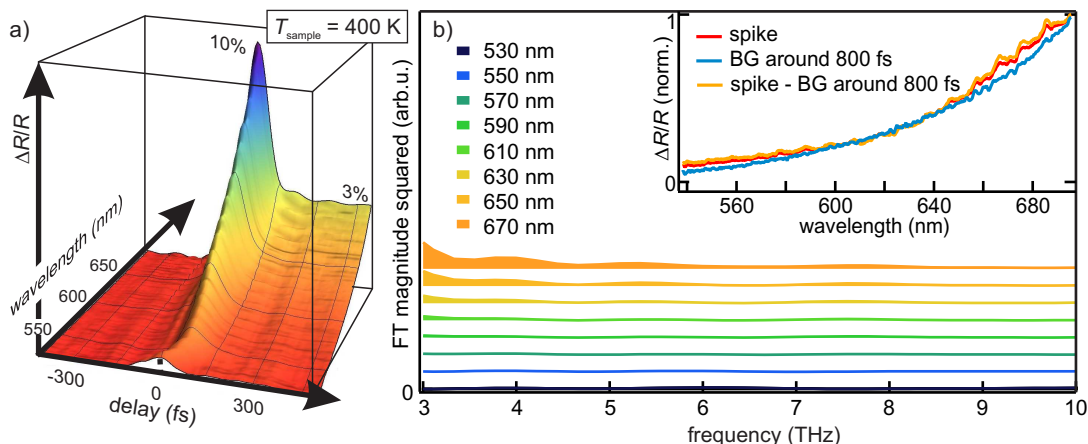
**Figure 4.7:** a) Broadband probing of the photoinduced dynamics of metallic VO$_2$ at T = 400 K. b) Fourier transforms of lineouts ±10 nm around the indicated wavelengths. To compare with the insulating phase response, the Fourier transforms have been scaled by the same amount as in Figure 4.4. The inset compares normalised lineouts directly at the spike and at late delays.

are strongest at long wavelengths and decrease towards shorter wavelengths. Again the dielectric function is affected most strongly close to the pump wavelength.

The Fourier transforms (starting right after the spike-like structure) of lineouts around indicated wavelengths are shown in Figure 4.7 b). The integration range was again ±10 nm. The scale (y-axis) of the Fourier transforms squared magnitude is chosen to be the same as in Figure 4.5, so one can directly compare intensities in the spectra. Clearly, there are no features with comparable amplitudes in the case of metallic VO$_2$. The phonon amplitude can therefore be used as a marker for the monoclinic phase symmetry and as an *order parameter* for the phase transition of the lattice potential symmetry in VO$_2$.

Especially at 530 nm, where the 5.7 THz phonon mode was the only dominant feature in the insulating case, neither oscillations nor significant incoherent response affect the signal. Hence this wavelength region will be the wavelength of choice to do high dynamic-range measurements with a lock-in amplifier to monitor the dynamic changes in phonon response when inducing the photo-induced phase transition (See next section 4.1.4).

In order to shed light on the nature of the spike-like feature, the wavelength dependence of the slow transient and the spike-intensity are compared in the inset of Figure 4.7 b). Lineouts (normalised to their maximum intensity) taken on top of the spike as well as between 700 and 900 fs (slow transient) after excitation are shown. The third curve results from subtracting the slow transient from the spike as a background before normalizing. The very similar shape of all three curves suggests a similar physical cause. Arguments for both, overdamped phonon and electronic origin, can be found:

① If the spike-like feature is a critically damped coherent phonon, the incoherent background could result from e.g. thermal expansion of the lattice, both structural phenomena.

② If electronic excitation is directly responsible for the spike, the incoherent background could be generated by the increased electronic temperature after electron thermalisation.

The optical measurements are not able to give a conclusive answer regarding the nature of the initial reflectivity response in the equilibrium metallic phase of VO$_2$, especially as also the effect of phonon oscillations on the reflectivity might have changed due to the different electronic band structure in the metallic phase. The photoemission experiments presented in section 4.2, on the other hand, will show hot electron lifetimes on the order of 200 fs. Therefore a structurally dominated response seems more likely, as the optically measured decay constant of 20 fs is one order of magnitude smaller as the hot electron lifetime, but very well compatible with a critically damped oscillation of the lowest energy phonon mode of rutile VO$_2$ at 7.2 THz [Sch02].[27] Independent of the exact origin, the distinct shape and sign of reflectivity change will be used to track the evolution towards the equilibrium metallic phase response after the photoinduced phase transition in section 4.1.5.

### 4.1.4 Strong photoexcitation

After describing the ultrafast response of the two equilibrium phases to weak excitation, the photoinduced phase transition is investigated by gradually increasing the pump-power, while staying at room temperature. When increasing the fluence across a critical fluence threshold ($F_{TH}$), distinct changes in electronic and lattice response are observed.

**800 nm probe**  Excitation fluence-dependent measurements, using 40 fs short laser pulses centred at 800 nm for both pumping and probing, have been performed over a wide range of fluences as shown in Figure 4.8 a). In line with previous investigations [Bau07, Küb07] a threshold fluence $F_{TH} = 6.9$ mJ cm$^{-2}$ is defined at the value where the response amplitude an arbitrary time delay of 1 ps is starting to become nonlinear with fluence (see Section 2.2 for details). A steep decrease of reflectivity, which grows in magnitude upon increasing the fluence is observed. The signal then recovers (double exponentially) with time constants that increase with fluence. Before discussing the incoherent response in more detail, coherent phonon oscillations are analysed by FFT:

The transients for below threshold excitation (blue) show coherent phonon oscillations, which vanish when exciting above the phase transition threshold. This is clear from Figure 4.8 b) where Fourier transforms (magnitude squared) of the traces in a) after background subtraction[28] are shown in a false colour representation on a logarithmic scale. Each of the Fourier spectra are normalised to fluence so that effects scaling linear with pump excitation density are removed. The black arrows at the top indicate the eigenfrequencies of the four strongest accessible Raman active phonon modes of the monoclinic, insulating, low-temperature phase of VO$_2$, which have been already discussed in section 4.1.2. Those eigenfrequencies can be seen in the Fourier spectra

---

[27]The other Raman active phonon modes are not excited coherently as their frequency is too high.

[28]Without background subtraction the large incoherent offset in the transients leads to a large intensity in the Fourier transforms at zero frequency. To remove this incoherent background, a strongly smoothed (binomial smoothing) replica of each dataset was subtracted. This corresponds to high-pass filtering in frequency space.
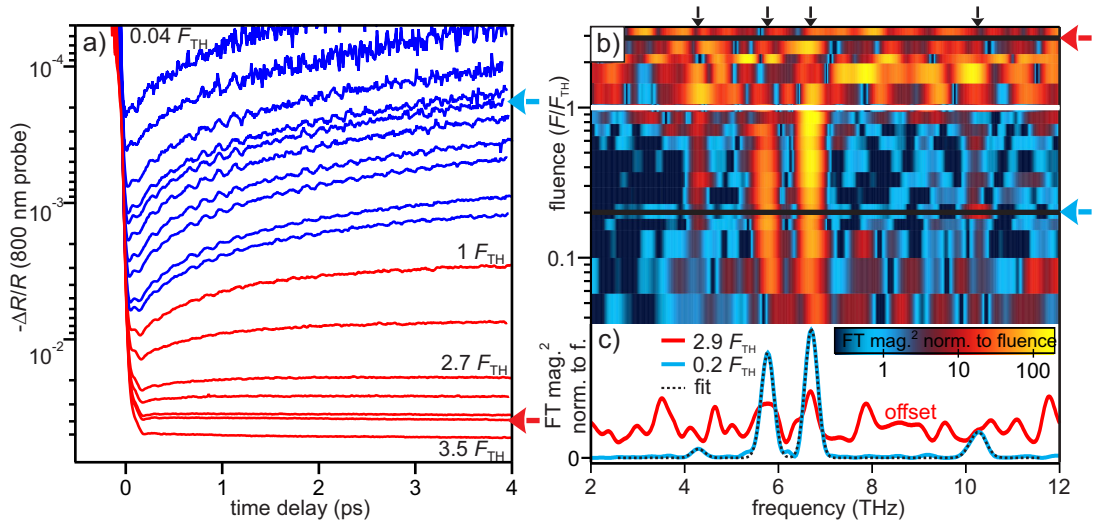
**Figure 4.8:** a) Photoinduced reflectivity changes pumped and probed by 800 nm (40 fs pulse duration) laser pulses for various excitation fluences below (blue) and above (red) the phase transition threshold $F_{\mathrm{TH}} = 6.9$ mJ cm$^{-2}$ ranging from 0.25 mJ cm$^{-2}$ (0.04 $F_{\mathrm{TH}}$) to 24 mJ cm$^{-2}$ (3.5 $F_{\mathrm{TH}}$). b) False colour plot of Fourier transforms of the transients in a) after background subtraction (described in the text) with respect to fluence normalised to $F_{\mathrm{TH}}$. The intensity has been normalised to the respective pump fluence. c) Fourier transforms for two distinct transients below (blue) and above (red) threshold. The respective positions are indicated by the coloured arrows in a) and b). Fitting with 4 Gaussian peaks yields dotted black curve in c).

as four distinct peaks when pumping below threshold ($F_{\mathrm{TH}}$ is indicated by the white line). At fluences above $F_{\mathrm{TH}}$ on the other hand, those eigenmodes vanish and cannot be observed any more, indicating a significant change in the response.

Selected Fourier transforms below (blue) and above (red) threshold in Figure 4.8 c) verify the vanishing of the coherent phonon modes upon driving the phase transition. The respective transients in a) and position in b) are indicated by the red and blue arrows. At 0.2 $F_{\mathrm{TH}}$ pump fluence, four clear peaks are observed centred at 4.29, 5.77, 6.7 and 10.26 THz, as discussed in section 4.1.2. Those can be seen for all fluences below threshold[29] but not for fluences above threshold, for example at 2.9 $F_{\mathrm{TH}}$ (red curve, offset for clarity), where only noise is visible in the spectrum. This resembles exactly the coherent response of the metallic rutile phase, where none of the monoclinic phonon modes could be excited (See Section 4.1.3).

**The disappearance of *all* of these phonon modes suggests the loss of the monoclinic lattice potential symmetry.** It will be shown that the phonon mode amplitudes can be used as an order parameter for this phase transition in terms of the lattice potential. However, first, the following paragraphs will exclude dephasing/damping as an alternative explanation for the loss of the phonon modes.

**525 nm probe**   As discussed in Section 4.1.2, the wavelength region around 520 nm qualifies for a systematic analysis of the PIPT, as the incoherent 'background' part of the transient, seen at longer wavelengths, is comparatively low in intensity, while the phonon mode centred at 5.7 THz dominates the phonon spectrum. To achieve a superior signal to noise ratio as compared to broadband measurements employing an optical spectrometer, lock-in detection was used after filtering the reflected WLC probe at 525 nm (bandwidth: 5 nm), therefore keeping the temporal shape of the WLC pulse intact at the time of probing.

The resulting pump-induced transients ($\lambda_{\mathrm{pump}} = 800$ nm) are shown in Figure 4.9 a). As the incoherent background amplitude is a smaller than in the previous paragraph, the y-axis is scaled linearly as opposed to in Figure 4.8 a) where it is logarithmic. The phase transition threshold has been determined again (independent of the 800 nm probe dataset) at the point where the transient response at 1 ps time delay starts to be non-linear with fluence. This yields a slightly different fluence threshold ($F_{\mathrm{TH}} = 4.93$ mJ cm$^{-2}$) for 525 nm probing than for 800 nm probing, mainly due to different systematic errors in fluence determination (a detailed discussion follows in the next paragraph).

Below threshold (blue curves) coherent phonon oscillations dominate the transients without any significant background intensity. Above threshold (orange) the coherent phonon signatures start to vanish and a slow transient background increases with fluence. This background increase occurs on a much smaller scale then when probing with 800 nm (compare to Figure 4.8). As higher fluences (up to $5.5 \times F_{\mathrm{TH}}$) could be achieved[30], a saturation regime (red) was accessible. Before conducting detailed fitting procedures of the transients based on a phenomenological model, the changes of phonon spectra with respect to pump fluence allow for the following qualitative discussion:

---

[29]In the transient with the lowest pump-fluence the phonons are barely visible, due to the low signal to noise ratio

[30]Reduction of the laser repetition rate allowed for higher pulse energies and therefore higher fluences.
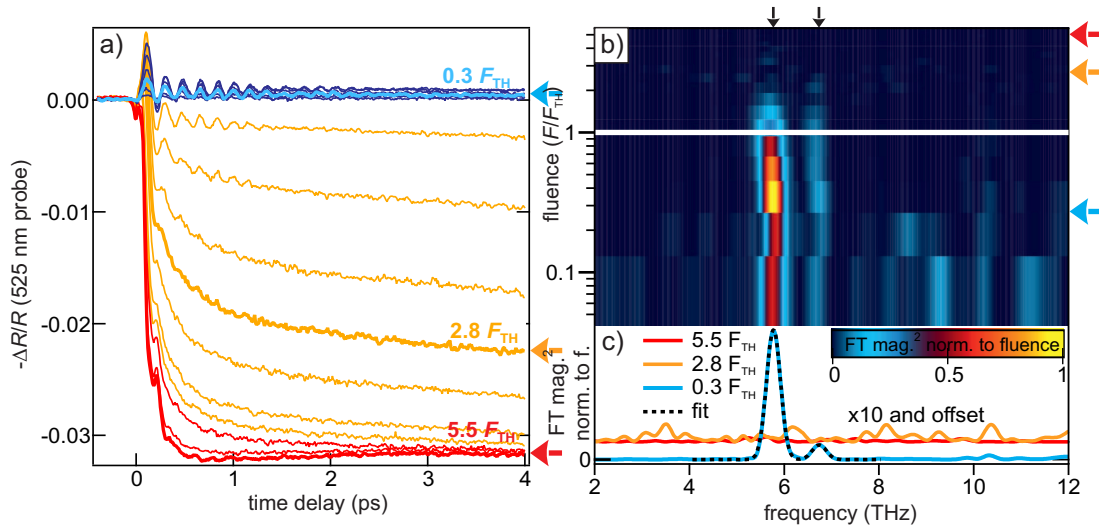
**Figure 4.9:** a) Photoinduced reflectivity changes probed by 525 nm part of WLC pulses for various excitation fluences ($\lambda_{\mathrm{pump}} = 800$ nm) below (blue) and above (orange) the phase transition threshold $F_{\mathrm{TH}}$ and in saturation regime (red). b) False colour plot of Fourier transforms of the transients in a) after background subtraction (same method as in Figure 4.8) with respect to normalised fluence. The intensity has been normalised to the respective pump fluence. c) Fourier transforms for three distinct transients representing the three regimes: below (blue) and above (orange) threshold and in saturation (red). The respective positions are indicated by the coloured arrows in a) and b). Fitting with two Gaussian peaks yields dotted black curve in c).

The Fourier transforms (magnitude squared) of the transients from Figure 4.9 a) (after background subtraction as described in the previous paragraph [28]) are shown in b) for increasing pump fluences. The Fourier transforms are normalised to pump fluence to remove any signatures that depend linearly on excitation density. The threshold is indicated by the white line. Clearly, there are at least two peaks in the phonon spectrum below $F_{TH}$, corresponding to the 5.7 and 6.7 THz modes of the insulating, monoclinic phase of VO$_2$. When the fluence is increased above threshold, these modes vanish quickly and no distinct features can be accounted for any more To illustrate this further, Figure 4.9 c) shows three distinct phonon spectra, representative of the three regimes (blue: below threshold, orange: above threshold, red: in saturation). The orange and red curves have been scaled up by a factor of ten and offset for clarity. A fit (two Gaussian peaks) to the phonon spectrum of the transient pumped below threshold, yields a strong mode at 5.8 THz and a weaker one at 6.7 THz in good agreement to the data shown in Figure 4.5 b).

A slight softening of the 5.7 THz mode is observed before it disappears, which will be quantified further by fitting the transients in section 4.1.4. The gradual decrease above threshold, seen in b), is due to inhomogeneous probing of a distribution of differently strongly pumped regions due to the Gaussian laser beam shapes. Clearly at $2.8 \times F_{TH}$ no phonon modes are visible any more, indicating homogeneous above threshold pumping of the whole probed area. The situation does not change with respect to the phonon modes when pumping in the saturation regime ($5.5 \times F_{TH}$).

**The photoinduced phase transition threshold**   The transient reflectivity probed both with 800 and 525 nm light is now analysed in detail, starting with the threshold fluence for the photoinduced phase transition for both wavelengths independently.

In Figure 4.10 a) the fluence dependence of the transient reflectivity change at 1 ps (filled circle) and 3.5 ps (open circle) pump-probe delay is shown for probing with 800 (red) and 525 nm (green) light. The integration range on each transient was 190 fs, corresponding to one phonon period, to average over reflectivity changes due to the phonon oscillation. Analogous to the literature [Bau07, Küb07] (as detailed in 2.2), the threshold fluence has been determined for each series of measurements as the point where the transient reflectivity at 1 ps starts to show a non-linear behaviour with fluence. The fluence axis has been normalised accordingly. The corresponding kink is therefore visible at $F/F_{TH} = 1$ (dashed line) for both pump-probe delays (1 and 3.5 ps). Determining the fluence threshold separately reduces systematic errors that are different for the two series of experiments. These errors include determination of spot-sizes, different incidence angles and absorption properties of the two wavelengths.

For 800 nm probing the threshold fluence is $F_{TH\text{-}800} = 6.9$ mJ cm$^{-2}$ and for 525 nm $F_{TH\text{-}525} = 4.9$ mJ cm$^{-2}$, yielding an average fluence of $F_{TH\text{-}avg} = 5.9 \pm 1.0$ mJ cm$^{-2}$. This is in good agreement with previously published values between 6 and 7 mJ/cm$^{-2}$ [Cav01, Bau07, Küb07, Hil07].

For the experiments using 525 nm probe wavelength higher maximum fluences could be achieved, because a lower repetition rate setting of the laser allowed for higher pulse energies. Therefore, a saturation regime could be entered as indicated by a second dashed line at around $4 \times F_{TH} \simeq 20$ mJ cm$^{-2}$. This saturation is indicative for a homogeneous non-thermal photo-induced phase transition over the whole probed
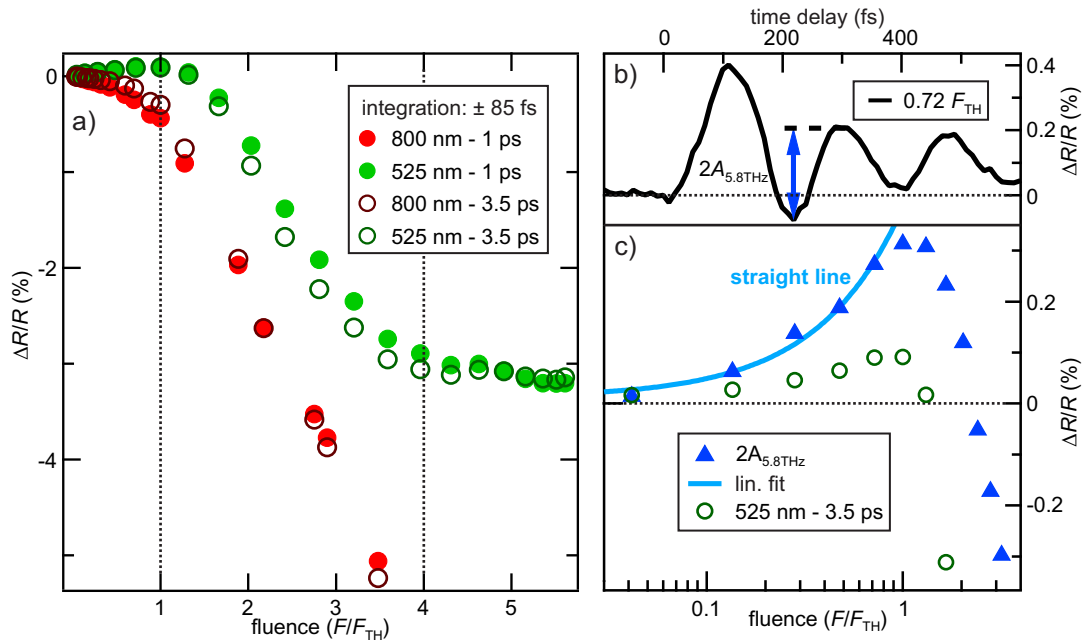
**Figure 4.10:** a) Fluence dependence of transient reflectivity probed by 800 nm (red) and 525 nm (green) light at 1 ps (filled circles) and 3.5 ps (open circles) pump-probe delay. The fluence axis is normalised to the respective threshold fluence. b) Detailed view on a below-threshold transient, probed with 525 nm to illustrate determination of phonon double-amplitude $2A_{5.8THz}$. c) Fluence dependence (logarithmic scale) of double-amplitude $2A_{5.8THz}$ in comparison to transient reflectivity change at 525 nm. The solid curve is a linear fit to below threshold points of $2A_{5.8THz}$.

volume. Time resolved diffraction experiments show a similar factor between threshold for the photoinduced transition of the lattice structure and saturation fluence [Mor14]. There, a threshold value of $F_{\text{TH}} = 9\,\text{mJ cm}^{-2}$ and saturation at $4.8 \times F_{\text{TH}} = 43\,\text{mJ cm}^{-2}$ were observed.

Using the nonlinearity of the reflectivity at 1 ps or 3.5 ps is of course an arbitrary choice. Reflectivity changes are not exclusively determined by changes of the electronic band structure and even if they would be, they do not necessarily probe a Fermi surface. In contrast, the phonon amplitude of monoclinic phase phonon modes are suggested as an order parameter for the phase transition of the crystal potential symmetry in VO$_2$.

A first quantification of the 5.8 THz phonon mode amplitude is done by finding the position of first trough and the following maximum of the phonon oscillation in a below threshold transient, as depicted in Figure 4.10 b) and extracting the difference $2A_{5.8\text{THz}}$ between both of these two points (yielding approximately two times the phonon amplitude). The fluence dependence of $2A_{5.8\text{THz}}$ is shown in Figure 4.10 c) together with the transient change in reflectivity probed with 525 nm at 3.5 ps (already shown in a)) on a logarithmic fluence axis. The phonon amplitude starts to deviate from the expected linear fluence dependence (indicated by the solid line) at the phase transition threshold $F_{\text{TH}}$, following the same trend as the transient reflectivity change. A complete loss of the phonon mode is observed, when its amplitude becomes negative, indicating that the phase transition of the lattice potential in VO$_2$ is completed homogeneously over the probed volume. This happens at $2 \times F_{\text{TH}}$ in contrast to the intensity at 1 and 3 ps, shown in a), which saturates at $4 \times F_{\text{TH}}$. It is not surprising that the phonon disappears at a lower fluence, because its signal is one order of magnitude smaller than the incoherent reflectivity change. It could simply be too small to be detected between 2 and $4 \times F_{\text{TH}}$.

To clarify the behaviour of the phonon amplitude as an order parameter, detailed fitting of transients for various fluences below, across and above the phase transition threshold are presented in the next paragraph.

**Detailed fitting of the transients below, across and above $F_{\text{TH}}$** To track the most prominent phonon modes close to the photoinduced phase transition, a complex fitting model, including the transient background due to electronic excitation and heating, has to be applied[31]. As discussed in Section 4.1.2, if the force exerted on the lattice is small and the phase transition is not driven (below threshold), the lattice dynamics (i.e. coherent phonon oscillations) will modulate the total reflectivity $R$ with a contribution according to the monoclinic phases normal modes:

$$\Delta R_{\text{Q}}(\lambda, t) = \sum_i A_i(\lambda) q_i(t), \tag{4.43}$$

as described in Section 3.3.3 by Equation 3.35 with the wavelength-dependent amplitude $A_i(\lambda) = \frac{\partial R(\lambda)}{\partial q_i}$. The time dependence of the phonon oscillation is therefore independent of wavelength, while its contribution to the reflectivity change is not. The phonon displacement $q_i(t)$ of the normal modes follows a forced, damped oscillation and is determined by damping constant $\xi_i$, eigenfrequency $\omega_i$ and generating force $F(t)$.

---

[31] The fitting model has been developed and applied by Simon Wall, who was working as a post doc in the group [Wal13].

To determine whether the force is impulsive, step-like or has some intermediate shape (i.e. a finite time constant $\tau_F$), several observations can be made, when looking at the below-threshold transients probed at 525 nm in Figure 4.9 a):

① there is no significant offset (on the order of the phonon amplitude).

② there is no exponential decay in the equilibrium position around which the phonon oscillates.

③ to determine the phase of the oscillation, timezero can be determined from the high fluence data.

An impulsive (or quickly decaying) force on the lattice generates a sine-like oscillation around the atomic equilibrium position, while a persistent (displacive) force results in cosine-like oscillations around a new (displaced) position (See Section 3.3.3 for details). Therefore, observation ① and ② hint towards a rather fast decay time constant for the force (more impulsive than step-like). Precise determination of timezero (③) is tricky, but assuming that it can be determined from the high fluence data and that it is not changed when changing the fluence[32] (due to experimental errors) the best fit for all fluences was achieved for $\tau_F = 50$ fs.

In addition to the coherent lattice response, e.g. carrier dynamics and heating effects lead to incoherent transient reflectivity changes, which are especially prominent when probing with 800 nm. When probing with 525 nm, only a constant offset is needed to describe the incoherent part of the transients:

$$\Delta R_{\rm K}(\lambda, t) = \Theta(t) K(\lambda) \tag{4.44}$$

$K(\lambda)$ describes the transient change, that appears constant with time in the accessible pump-probe delay range. The rising edge of the pump-induced change is modelled by the sigmoid function $\Theta(t) = (1 + \exp[-(t - \tau_{1/2})/w])^{-1}$, which has a width $w$ corresponding to the pump-pulse duration and a timezero/delayed-rise parameter $\tau_{1/2}$.

Above the phase transition threshold, the phonon modes are lost or become over-damped. Therefore, the previous description of the lattice response has to be modified, because eigenfrequency and damping ratio loose their meaning, when the phonon mode amplitude is zero, or are strongly coupled in case of an overdamped oscillation. The oscillatory contribution $\Delta R_{\rm Q}(\lambda, t)$ is then gradually replaced by:

$$\Delta R_{\rm S}(\lambda, t) = \Theta(t) \left[ \sum_{i=1,2} C_i e^{-t/\tau_{C_i}} \right]. \tag{4.45}$$

The overall change of the reflectivity is simply the sum of the contributions discussed above, but when increasing the fluence and moving through the 3 regimes (below threshold, above threshold and in saturation) different parts of the fitting model have to be switched off and on manually:

$$\Delta R(\lambda, t) = \Delta R_{\rm Q}(\lambda, t) + \Delta R_{\rm K}(\lambda, t) + \Delta R_{\rm S}(\lambda, t). \tag{4.46}$$

---

[32]attenuating the beam was done by a combination of 1/2-waveplate and polariser, therefore path-length differences are minimised.
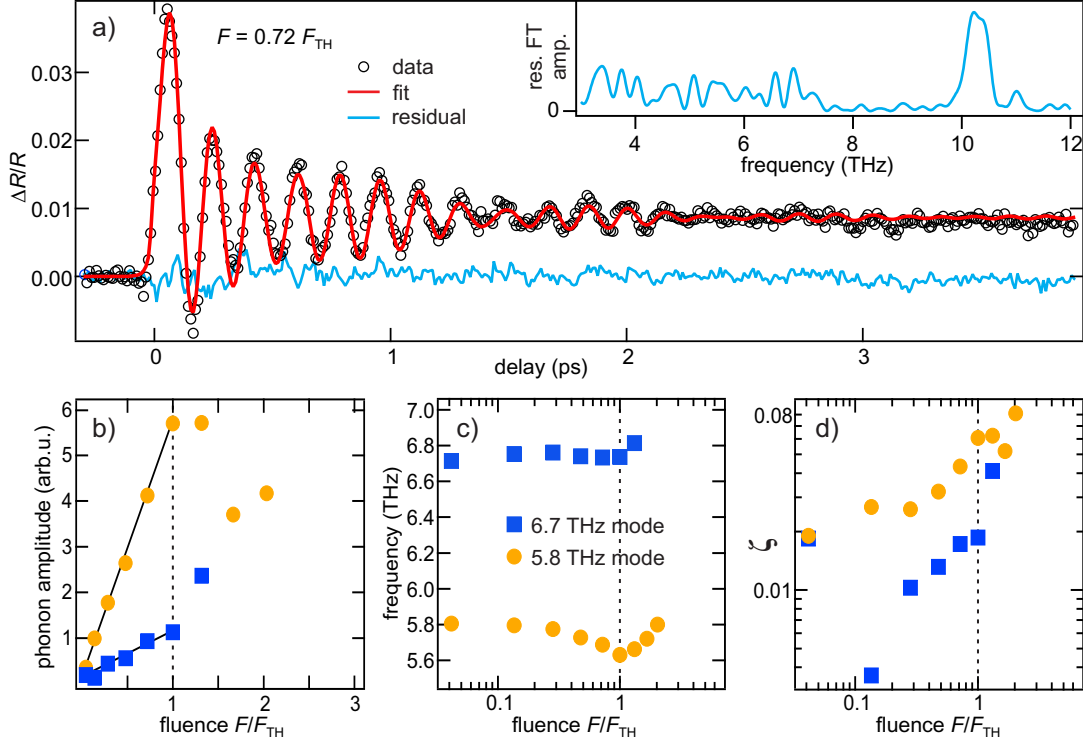
**Figure 4.11:** a) Exemplary transient response probed with 525 nm (pumped below $F_{TH}$) together with the fit described in the text and its residual. The inset shows the Fourier transform amplitude of the residual where the 10.2 THz mode, which is not included in the fitting model, can be seen. The fluence dependence of: b) the phonon amplitude, c) the phonon eigenfrequency and d) the phonon damping rate are shown for the 5.8 THz and the 6.7 THz modes of insulating VO$_2$. Modified from [Wal13].

The complete fit is then done by the Levenberg-Marquardt least-squares method and includes solving the differential equation determining the coherent phonon oscillations (see 3.3.3), when $\Delta R_Q(\lambda, t)$ is included.

**Below threshold fit results** A first round of fitting using $\Delta R_Q(\lambda, t)$ and $\Delta R_K(\lambda, t)$ yielded constant results for the electronic decay time constants $\tau_{C_i}$, which were therefore held fixed for a second run of fits at $\tau_{C_1} = 250$ fs and $\tau_{C_2} = 1.42$ ps to convert random errors due to fluctuations to systematic errors and yield more consistent results.

Only fits of transients probed with 525 nm are shown and analysed, as probing with 800 nm yields little additional information, because any of the monoclinic phonon amplitudes can be used as an order parameter for the phase transition with respect to the lattice symmetry. The number of free parameters on the other hand, is reduced due to the absence of a transiently changing incoherent background and two of the four phonon modes. A transient including its fit is shown in Figure 4.11 a). The model includes the two strongest phonon modes at 5.8 and 6.7 THz. Also shown is the fit residual (light blue) and in the inset its frequency spectrum calculated by FFT. Only a tiny residual oscillation of the 10.2 THz mode, which is not included in the fit model

can be seen.

The amplitudes of the two phonon oscillations are displayed in Figure 4.11 b) as a function of normalised fluence $F/F_{\mathrm{TH}}$. Both grow linear with fluence (indicated by the black lines) up to the threshold fluence, in agreement with the direct extraction of the phonon amplitudes in Figure 4.10 c).

The fluence dependence of the phonon eigenfrequency in Figure 4.11 c) shows, that the 5.8 THz mode seems to go slightly softer (the eigenfrequency is decreased) towards the photoinduced phase transition, a behaviour, which is not observed when thermally driving the transition [Kim06]. This photoinduced change of the connected force constant, can be assessed as an indication for a stronger coupling of the 5.8 THz mode to the electronic (photo-)excitation than to thermal driving mechanism. The increase of its frequency back to the initial value, when pumping above the threshold fluence could be an artefact, due to inhomogeneously exciting the VO$_2$ thin-film sample: As the reflectivity drops, when the immediate surface region, where pump-light is absorbed most, is driven across the phase transition, the backside of the film, which is still in the insulating phase is probed to a larger extend. Therefore, the phonon is probed more prominently at the backside of the film, where its frequency has not gone soft, as that region is not so strongly excited.

Finally the damping rates $\xi_i$ in ( Figure 4.10 d)) do increase with fluence, but stay $\ll 1$ for all fluences up across the threshold, and therefore the phonons never get close to a critical or overdamped regime.


**Above threshold fit results**   For fitting the transition region just above threshold, all components of the fitting model have to be switched on, as a distribution of regions where the fluence is below and above the threshold fluence is probed and residual oscillations are visible in the transients.

When the oscillations clearly vanish, $\Delta R_{\mathrm{Q}}(\lambda, t)$ is manually excluded from the fitting model. An exemplary above threshold transient ($F = 4.7F_{\mathrm{TH}}$) in the saturation regime, the corresponding fit and the fit residual (offset for clarity) are shown in Figure 4.12 a). The inset shows Fourier transform (magnitude squared) of the fit residual for pump-probe time delays smaller (red) and larger (blue) than 300 fs. At earlier delays than 300 fs there are still frequency components, that would be compatible with the 5.8 and 6.7 THz modes (indicated by the dashed lines). It has to be noted that there is FFT intensity on the same order of magnitude also at around 2 THz, which is clearly due to an artefact as it stems from a single oscillation *before timezero* and which is symmetric to the oscillation after timezero. At the high employed excitation intensities, wings in the temporal profile of the pump laser pulse might also play a significant role and could lead to the observed oscillations around timezero. After a delay of 300 fs there is certainly no oscillatory component at the phonon eigenfrequencies visible above noise level.

There are numerous potential explanations for the Fourier spectrum before 300 fs:

① temporal feature of the pump-laser pulse

② residual monoclinic lattice response contribution of weakly pumped region
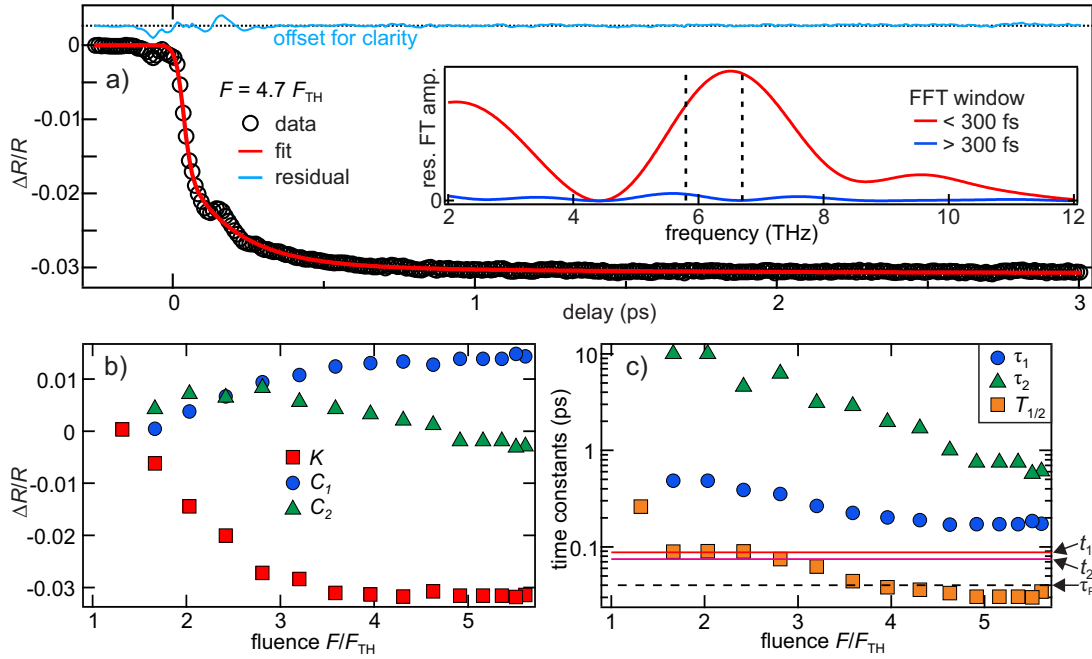
**Figure 4.12:** a) Pump induced transient reflectivity change above threshold in the saturation regime ($F = 4.7F_{\mathrm{TH}}$), fit (red) described in the text and its residual (light blue, offset for clarity). Fourier transforms of the residual for delay times smaller than 300 fs (red) and larger than 300 fs (blue) are shown in the inset. Dependence of constant offset $K$ (red squares) and amplitudes in Equation 4.45 ($C_1$: blue circles and $C_2$: green triangles) on fluence is shown in b). In c) the corresponding time constants $\tau_{C_1}$ and $\tau_{C_2}$ as well as the half rise position of the sigmoid function $T_{1/2}$ (orange squares) are shown with respect to normalised pump fluence. The solid lines at $t_1$ and $t_2$ correspond to the half-periods of the 5.8 and 6.7 THz phonon modes and the dashed line, labeled $\tau_P$ to the estimated laser pulse duration. Adopted from [Wal13].

③ strongly damped phonon of the photoexcited phase similar to the one postulated in [Pas11]

④ a 'coherent artefact', common in broadband pump-probe measurements [Kov99]

Taking into account the similarity to the oscillation before timezero, an artefact (choice ① or ②) is the more likely explanation. In any case it is very clear already from this analysis that at delays later than 300 fs, there is no phonon mode of the monoclinic phase visible any more Further discussion of the other fit parameters and investigation of the dynamics of the photoexcited state (4.1.5) will extend this statement to pump-probe delays before 300 fs in the following.

The dependency of various fit parameters on fluence (above threshold) is shown in Figure 4.12 b) and c). In b) the amplitudes of the two decaying exponentials $C_1$ and $C_2$ are shown together with the constant offset $K$. In c) the respective time constants and the half-rise time of the sigmoid function used in (4.44) and (4.45) are displayed.

The offset amplitude $K$ rises linearly with fluence and starts to saturate above $3F_{TH}$. Not surprisingly this resembles the extracted response at 1 ps shown in Figure 4.10. The decay constants $\tau_{1/2}$ (see discussion of Equation 4.45) could one one hand describe incoherent dynamics, but on the other hand also resemble strongly overdamped coherent phonon oscillations. The amplitude of the faster exponential decay (order of several 100 fs) $C_1$ (blue) grows and stays constant in the saturation regime. As its time constant $\tau_1$ shown in c) decreases form 500 to 200 fs upon increasing the fluence, an increasingly overdamped phonon of the monoclinic phase can be excluded. In the case of an overdamped phonon the time constant should increase, not decrease (or for a strictly impulsive excitation force decrease on a much smaller timescale, compare section 3.3.3). As it will be shown later (Section 4.1.5 and Chapter 4.2), the final value of time constant $\tau_1 \sim 200$ fs can be connected to hot electron thermalisation in the photoexcited metallic phase.

The slower exponential decay's amplitude $C_2$ grows first and decreases again in the saturation regime. As its time constant $\tau_2$ is on the order of 1 to 10 ps it could result from the thermal growth of metallic phase domains inside the probed volume. If pumped in saturation the whole probed volume is driven non-thermally into the metallic phase, hence $C_2$ decreases again.

The fluence dependence of the half-rise position $T_{1/2}$ of the sigmoid function ((4.44)) and (4.45)) is also displayed in Figure 4.12 c) (orange squares). Below saturation it is similar to the half-periods $t_1$ and $t_2$ of the 5.8 and 6.7 THz phonon oscillations (i.e. 74 and 86 fs, indicated by the solid lines) and might be connected to the 'structural bottleneck' timescale reported in [Cav04]. There the 'transition time' showed a minimum value of 80 fs, even when photoexciting the system with far shorter laser pulses down to 15 fs (as described in Section 2.2). Such a bottleneck cannot be retrieved from Figure 4.12, as the half-rise position $T_{1/2}$ decreases even below the pump pulse duration (i.e. $< 40$ fs indicated by the dashed line and labeled $\tau_P$) upon increasing the fluence in the saturation regime. **This on the contrary indicates, that the non-thermal phase transition out of the equilibrium monoclinic phase can be driven *arbitrarily fast*, faster than the pump pulses temporal envelope**.

Even without knowing about the exact nature of the different timescales presented in this paragraph, a subsequent softening of phonon modes of the monoclinic phase of
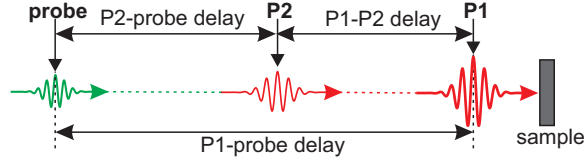
**Figure 4.13:** Pump-Pump-Probe scheme employed to investigate the dynamics of the transient phase in VO$_2$: First pump pulse P$_1$ (red, bold) drives the system into an excited state, or even into the transient phase (depending on fluence). A second, time delayed (by P1-P2 delay), weak pump pulse P$_2$ (red, narrow) perturbs the *excited* state. When arriving after P$_2$, the probe pulse (green) monitors the response of the *excited state* following photoexcitation.

VO$_2$ with increasing fluence can be excluded, as all of the timescales become *faster* with fluence. Therefore the amplitude of a monoclinic phase phonon mode does in fact act as an order parameter, that becomes zero when the system is driven out of the monoclinic phase crystal potential symmetry. It is known that the crystallographic phase transition and ionic movements following strong photo-excitation are only completed on various, much longer, timescale up to ns [Bau07, Had10, Had11]. In harsh contrast to that, the vanishing order parameter on an ultrafast timescale indicates that **the symmetry of the monoclinic phase potential landscape is lost *immediately* after above-threshold photo-excitation**.

To elucidate the nature of this strongly photo-excited, *transient* phase, which is far from either equilibrium phases, pump-probe measurements *in* this transient phase are presented in the following paragraph.

### 4.1.5 The dynamics of the photoexcited state

In line with the investigations of the transient response in the equilibrium insulating and metallic phases of VO$_2$, presented in section 4.1.2 and 4.1.3, the transient response following weak perturbation of the *photoexcited* state (below threshold) or transient phase (above threshold) is investigated in this paragraph.

As mentioned in the introduction of Chapter 4.1, a three pulse scheme, as depicted in Figure 4.13, has to be employed to monitor dynamics of already photoexcited VO$_2$ (and not just the excitation dynamics). There, a first laser pulse P1 is used to excite the system (below and above threshold, depending on its fluence) while a second, time-delayed, low intensity pump pulse P$_2$ acts as a weak perturbation[33], triggering dynamics *of* the *photoexcited* state. These dynamics are monitored by a probe pulse, with varying time delay with respect to P1 (and P2). This scheme is performed below and above the photoinduced phase transition threshold fluence, to elucidate the nature of the state after photoexcitation. The evaluation will be focusing on the coherent-phonon responses.

Below threshold, the photoexcited insulating phase is probed. Here, the most prominent dynamic features are modulations of the reflectivity due to oscillations of coherent phonons of the monoclinic symmetry. A coherent phonon, which has been excited by a first laser pulse and is less than critically damped, can be coherently controlled by a

---

[33]The fluence was kept below threshold to ensure that P2 does *not* drive the transition
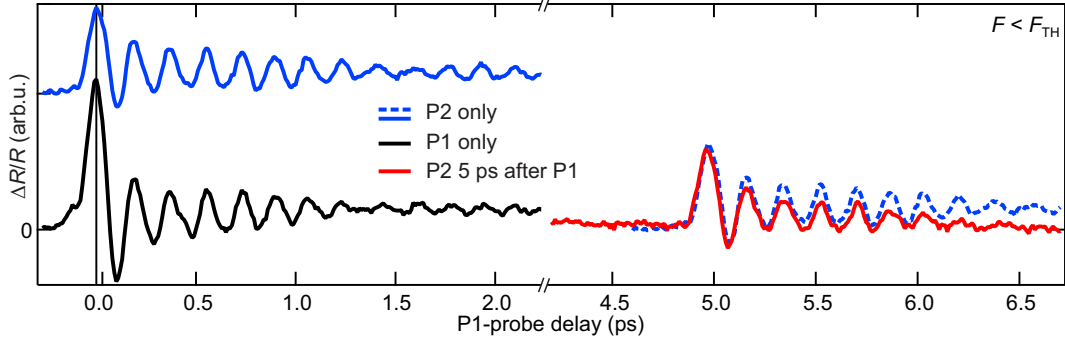
**Figure 4.14:** Transient reflectivity changes after below-threshold photoexcitation by pump pulse P1 (black) and second pump pulse P2 (blue) individually (left) show the response of the monoclinic phase of VO$_2$. On the right hand side the transient change due to a second photoexcitation by P2, 5 ps after P1, is shown, which exhibits no significant difference to the response of the equilibrium state (dashed blue). The delay axis is plotted with respect to the delay between P1 and the probe pulse (P1-probe delay).

second laser pulse as described in section 3.3.3. Trivially, it can also be excited again after the first phonon excitation has decayed/dephased. As the coherent phonon oscillation is characteristic for the symmetry of the system it can only be excited, if this symmetry persists.

The clearest results in terms of a coherent control experiment are achieved when only a single phonon mode is probed. Therefore only reflectivity transients probed at 525 nm, where the 5.7 THz phonon mode dominates the phonon spectrum, are discussed in the following section.

Starting with the trivial case, it is tested whether monoclinic phase phonons can be excited after a previously excited phonon signal has decayed: Figure 4.14 displays the transient reflectivity changes induced by a pump pulse P1 (black) and another pump pulse P2 alone (blue, offset for clarity). The temporal pump-probe overlap (P1-probe delay = 0) is displayed with respect to the initial excitation P1. Both transients show clear below-threshold behaviour: The 5.7 THz phonon oscillation of the monoclinic phase is the only significant feature. The phonon has decayed/dephased completely after 2-3 ps. Therefore it should be possible to excite it again with a second laser pulse independent of the relative phase of the excited phonons. This is shown on the right hand side of Figure 4.14: 5 ps after the initial excitation (black) by P1, the coherent phonon can still be generated by P2 (red transient). The only significant difference to the dynamics induced by P2 alone (dashed blue line, offset) are found in slow changes of the background intensity due to electronic and/or heating effects. *The monoclinic phase symmetry therefore clearly persists after below-threshold excitation.*

For the coherent control experiments the time delay between P1 and P2 has to be tuned in- and out-of-phase with respect to the 5.7 THz coherent phonon period. For this mode, out-of-phase ($\phi = \pi, 3\pi, \dots$) corresponds to a delay between the two exciting pulses P1 and P2 of $\sim 88$ fs and in-phase ($\phi = 2\pi, 4\pi, \dots$) corresponds to $\sim 175$ fs. The transient responses for a total pump fluence below threshold ($F_{P1} = 4.4$ mJ cm$^{-2}$, $F_{P2} = 1.7$ mJ cm$^{-2}$, $F_{P1} + F_{P1} < F_{TH}$) is summarised in Figure 4.15 for different P1-P2
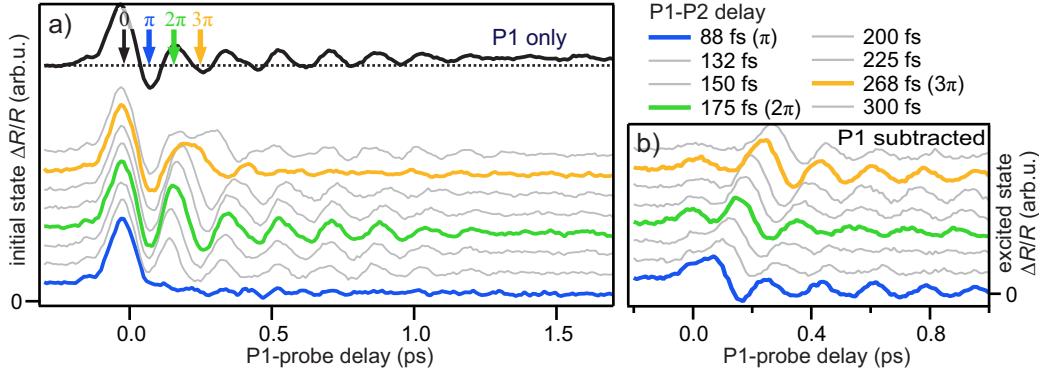
**Figure 4.15:** Coherent control of the 5.7 THz phonon mode in the monoclinic phase of VO$_2$: Transient response induced by P1 alone (below threshold) and probed by the 525 nm region of WLC pulses are shown at the top of a) (black). Below, in addition the transient reflectivity changes following a second excitation by P2 are shown for different P1-P2 time delays corresponding to tuning between in-phase and out-of-phase excitation. The arrival time of P2 is indicated by the arrows at the top. In b) the response due to P1 alone (black curve in a)) has been subtracted to show the changes induced by P2 alone.

delays:

The black curve in a) shows the transient reflectivity change due to P1 alone. The delay axis is plotted with respect to the temporal overlap between probe and P1. The coloured arrows indicate the temporal positions for in- and out-of phase excitation with a second pulse P2. The transients after double excitation, are colour coded to match the arrows at the top. They show, that for out-of-phase excitation the phonon amplitude is minimised (blue and yellow thick line), while in-phase excitation yields an amplified phonon amplitude (green thick line).

When subtracting the response of P1 alone, the transient P2-induced dynamics in the photoexcited state remain, as shown in Figure 4.15 b). The transients look essentially the same as the one excited by a single pump pulse (e.g. P1 only), but shifted in time by the respective P1-P2 delay. The pump-probe response *of* the below-threshold photoexcited state is therefore exactly the same as the one of the equilibrium monoclinic phase, meaning that the monoclinic symmetry in all cases determines the coherent phonon response.

**Photoinduced metallic phase** The situation is entirely different when driving the photo-induced phase transition within the first pump pulse P1: It will be shown that monoclinic phase phonons can neither be excited nor coherently controlled any more, substantiating the previous result that the monoclinic phase symmetry has been lost instantly after photoexcitation into this transient photoexcited phase.

The first excitation by pump pulse P1 is now done with a fluence above the photo-induced phase transition threshold ($F_{P1} = 10$ mJ cm$^{-2}$), while the second pump pulse P2 has a fluence that is still below threshold ($F_{P2} = 3$ mJ cm$^{-2}$). This scheme represents a weak perturbation by P2 of the *transient photo-induced phase*, created by P1. It is comparable to the investigation of the response of the equilibrium phases upon weak
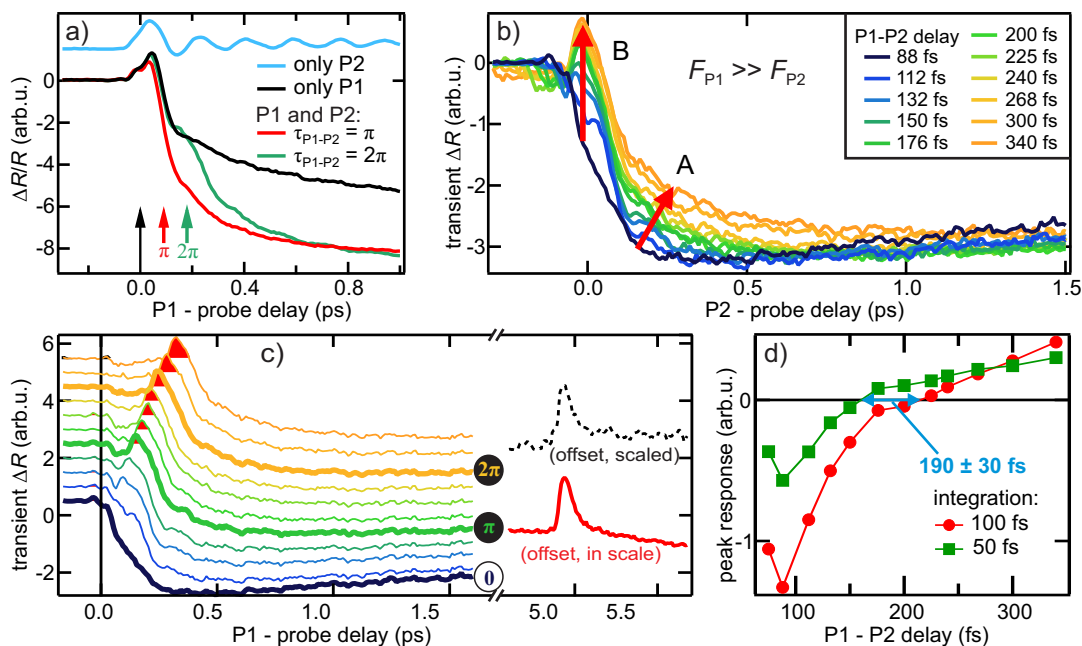
**Figure 4.16:** Probing the transient dynamics of the strongly photo-excited, transient phase: a) shows the response on weak, below threshold, perturbation by P2 alone (light blue), the response after inducing the PIPT (black) by pump P1 alone and the perturbation (by P2) of the transient phase (created by P1) in- (green) and out-of-phase (red) with respect to the 5.7 THz phonon oscillation. Subtracting the response due to P1 alone yields the response of the transient phase shown in b) with respect to the arrival time of P2 for different P1-P2 delays. Arrows indicate changes with P1-P2 delay. In c), the same data as in b) is displayed, but with with respect to the arrival time of P1. For comparison the transient phase response at long P1-P2 delays (5 ps, red curve) and the response of the equilibrium metallic phase (dashed black curve) is also shown in c). The evolution of feature B in b) with respect to P1-P2 delay is quantified in d).

perturbation in sections 4.1.2 and 4.1.3.

The transient reflectivity change due to P1 and P2 separately is shown in Figure 4.16 a): The below-threshold pump P2 (light blue) excites coherent phonon oscillations, as the monoclinic phase symmetry is not lost. The pump pulse P1 has a sufficient fluence to drive the transition, therefore coherent phonon oscillations are not present (black). Also, further transient reflectivity changes are shown: First exciting with P1 and later, after a P1-P2 delay of 88 (red) and 156 fs (green), weakly perturbing the transiently excited phase with P2. The two delays correspond to out-of-phase ($\pi$) and in-phase ($2\pi$) excitation with respect to the monoclinic phase 5.7 THz phonon mode and are indicated by the red arrows. The reflectivity drops further after excitation by the second pump pulse P2 and reaches a similar level around 800 fs after the first excitation by P1. The onset of the additional drop is obviously delayed by the P1-P2 delay, but no phonon oscillation is visible after the second, weak pump pulse P2.

The delay between P1 and P2 is now varied systematically to probe the dynamics of the transient phase at different times after its creation: Transient reflectivity changes initiated by P2[34] are shown first with respect to the arrival of the second pump pulse (P2) in Figure 4.16 b) for direct comparison. At timezero (corresponding to P2's arrival time) the falling edge, marked with a red arrow and the letter A, looses its steepness with increasing P1-P2 delay. When both pump pulses arrive shortly after each other, the non-thermal character of the phase transition is enhanced. Increasing the delay between the two excitations, regions in the transient phase are excited by P2 to an increasing extent, leading to a superposition of the response characteristic for the PIPT itself and the response of VO$_2$ in the transient phase.

Simultaneously a peak-like structure, marked with a red arrow and the letter B, starts to develop and increases with increasing P1-P2 delay. It will be shown that this feature very likely corresponds to metallic phase dynamics, initiated by P2, which that are superimposed to the initial dynamics due to P1. To further analyse the evolution of feature B, the transients from b) are displayed in c) with respect to the arrival of the initial pump P1 and offset along the $\Delta R$ axis. The regions where the signal becomes positive are marked in red and in-phase and out-of-phase P1-P2 delays are indicated by the thick lines and the markers ($\pi$ and $2\pi$). On the right hand side of c) the response induced by P2 is shown for a P1-P2 delay of $\sim$ 5 ps (red curve), where it clearly resembles the shape of the pump induced response of the *equilibrium* metallic phase at high temperatures, a positive peak (dashed black curve, scaled and offset).

A quantitative analysis of the appearance of the peak-like (i.e. equilibrium metallic phase-like) response with respect to the P1-P2 delay is shown in Figure 4.16 d): Integration of the transients in c) over a 50 fs window, centred around the arrival time of P2, yields the peak response of feature B (green curve). The integrated intensity is first negative and starts to get positive at a P1-P2 delay time of 160 fs. The positive sign is used as a marker for the appearance of a response that is similar to the one in the equilibrium metallic phase. An additional integration window of 100 fs width (red curve)[35] centred around the arrival time of P2 has been employed to show the robustness of this analysis. Qualitatively the two integration windows generate very similar curves (red and green), but the P1-P2 delay at which the sign change is observed is larger for the larger integration window (red curve). The fact that the probe pulse probes a superposition of P1 and P2 induced changes explains this observation: As the transient change still mainly consists of a reduction of reflectivity (initiated by P1) superimposed to the positive spike (generated by P2), for longer integration windows the negative trend decreases the integrated value, i.e. the sign change shifts to later P1-P2 delays. From both curves in d) an average value of $190 \pm 30$ fs is found at which the sign change occurs. As photoemission studies in the next chapter will show, this corresponds well to hot electron/hole relaxation times in the transient metallic phase. It has to be noted, that for much longer P1-P2 delay times and only after several ps, there is nearly no negative component in the transient reflectivity change left (red curve

---

[34]The P1-only transient, shown in Figure 4.16 a) has been subtracted from the raw data leaving only the changes created by P2.

[35]The pump pulse (P2) duration was estimated to be 50 fs. To make sure, that a wrong estimate does not change the resulting analysis, integration windows of one and two times the P2 duration were employed. The latter can be seen as a worst case estimate.
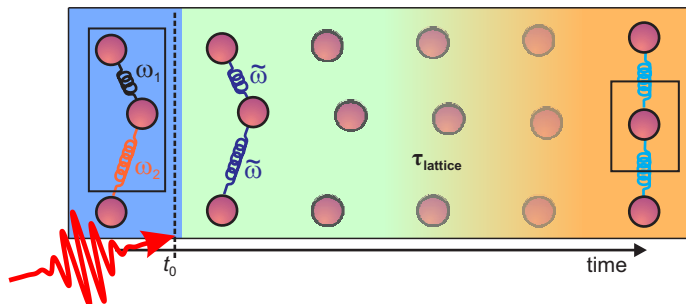
**Figure 4.17:** Illustration of the ultrafast symmetry loss of monoclinic VO$_2$: The lower symmetry monoclinic phase (blue) is photoexcited at $t_0$. The lattice potential changes its symmetry immediately, i.e. monoclinic phonon modes vanish. Starting at this highly non-equilibrium transient phase (green), the positions of the atoms (red circles), i.e. the actual crystallographic structure progresses on a much slower timescale $\tau_{lattice} \gg \tau_{pot}$ until it stabilises the metallic rutile phase (orange).

in c)) and the overall response resembles the shape of the one of the equilibrium metallic phase (dashed black curve in c)).

The dynamics *in* the transient phase after strong photo-excitation are fundamentally different from the ones in the equilibrium monoclinic and rutile phases. Features A and B, shown in Figure 4.16 change continuously with P1-P2 delay, in sharp contrast to the observations for the below threshold coherent control experiments shown in the preceding section, where in- and out-of-phase pumping by P2 lead to an oscillating control of one of the monoclinic coherent phonon mode amplitude. This observation confirms that **the monoclinic insulating phase of VO$_2$ is lost on an ultrafast timescale as its symmetry and thereby characteristic underdamped phonon modes have vanished.**

On the other hand, the transient response only slowly starts to resemble that of the equilibrium rutile phase after hundreds of fs and is only comparable in shape after picoseconds have passed, a time after excitation when the atoms are still far from their rutile atomic positions. This suggests that initially, right after P1 drives the system out of the monoclinic phase, a non-thermal state far from equilibrium is reached, that only starts to resemble the response of the equilibrium metallic phase after a certain relaxation time.

### 4.1.6 Conclusion: Ultrafast symmetry loss of monoclinic VO$_2$

This chapter has presented the effects of photo-excitation on the dielectric function and coherent lattice response of VO$_2$ for various excitation densities. The results are illustrated in Figure 4.17:

The amplitude of coherent phonon oscillations (visualised by the black and red springs and frequencies $\omega_{1/2}$) that are characteristic for the monoclinic phase symmetry have been established as an order parameter for the monoclinic phase (blue). Following strong photo-excitation at time $t_0$ (red arrow), above a threshold fluence of $F_{TH\text{-}avg} = 5.9 \pm 1.0$ mJ cm$^{-2}$, this order parameter reduces and reaches zero before

a saturation fluence of $4 \times F_{\text{TH-avg}}$, indicating the loss of monoclinic phase symmetry (the higher symmetry potential is indicated by the dark blue springs). Together with a detailed analysis of the ultrafast change of reflectivity it is concluded that this happens on a timescale $\tau_{\text{pot}}$, shorter than the laser pulse driving the transition at sufficiently high fluences. This means that the symmetry of the initial monoclinic phase is lost *immediately* when entering the transient photo-excited phase (green, higher symmetry lattice potential is indicated by the dark blue springs). On the other hand, the optical response starts to resemble that of the equilibrium rutile phase after 200 fs and shows a similar transient shape after several ps only, long before the atoms have reached the rutile phase (orange, high symmetry, but possibly further changed lattice potential is indicated by the light blue springs) equilibrium positions ($\tau_{\text{lattice}} \gg \tau_{\text{pot}}$) according to diffraction experiments [Bau07, Had10, Had11].

The transient phase[36] is a new, highly non-equilibrium state of the system, that is already remarkably different from the initial monoclinic phase, but still needs a long time to 'relax' into the high temperature rutile phase. In the next chapter it will be shown, that one additional essential feature of this transient phase is the appearance of electronic density of states at the Fermi energy, meaning that the transient phase has metallic properties right from the beginning.

---

[36]The term 'Phase' is not supposed to suggest thermal equilibrium, but is used nevertheless to distinguish from ordinary photo-excited states, where the potential energy landscape has not significantly changed.
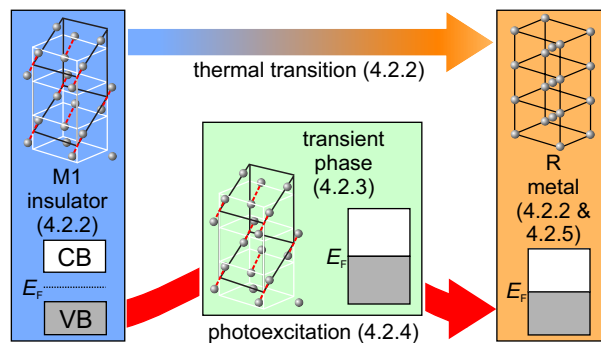
**Figure 4.18:** Schematic overview over photoemission studies of VO$_2$:

## 4.2   Ultrafast metallisation of VO$_2$

While time-resolved optical pump-probe measurements have revealed changes in electron and lattice response and the loss of monoclinic phase symmetry on an ultrafast time-scale, they lack an absolute energy scale in terms of electronic states and do not directly probe the metallicity. To get this direct insight into the phase transition and its electronic structure dynamics on an absolute energy scale, time-resolved photoemission experiments are performed.

Figure 4.18 presents a schematic overview of the performed experiments. At first, markers for the different phases in thermodynamic equilibrium (monoclinic insulating, M1, blue and rutile metallic, R, orange) are established via temperature-dependent investigations (Section 4.2.2): The appearance of density of states (DOS) at the Fermi energy is observed upon heating the VO$_2$ thin-film sample, providing a solid indicator for the insulator-to-metal transition.

Based on this observation, the instantaneous appearance of density of states at the Fermi energy (in the band gap region of insulating VO$_2$) after strong photoexcitation (transient phase, green, Section 4.2.3 and 4.2.4) shows a quasi-instantaneous photo-induced metallisation (coincidental with the instantaneous loss of monoclinic lattice symmetry presented in the previous chapter). This observation is consolidated by theoretical calculations that were performed in close collaboration with the Nano-Bio Spectroscopy Group in San Sebastian[37]. These calculations explain the band gap collapse with the generation of photoholes at the top of the valence band of VO$_2$ *in* the monoclinic crystallographic structure, i.e. show that *no structural component is needed* to describe a transient metallic phase with monoclinic crystallographic structure (but non-monoclinic lattice potential) after photoexcitation. Finally, hot electron dynamics of the metallic phase (orange) are investigated via two-photon photoemission spectroscopy (Section 4.2.5).

### 4.2.1   VO$_2$/Al$_2$O$_3$(0001) sample for photoelectron spectroscopy

The sample used for photoelectron spectroscopy was a 45 nm thin film grown on c-cut sapphire (Al$_2$O$_3$(0001) surface) by pulsed laser deposition. The lattice mismatch with

---

[37]Many thanks to Angel Rubio, Lede Xian, Matteo Gatti and Pierluigi Cudazzo!
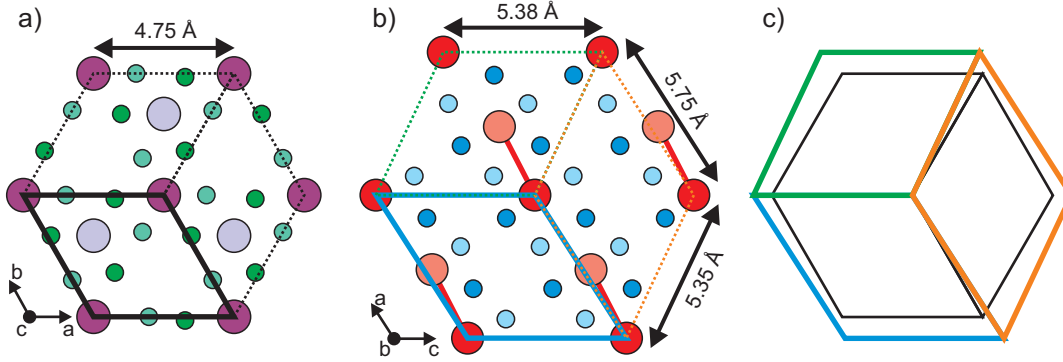
**Figure 4.19:** a) View onto the Al$_2$O$_3$(0001) substrate surface, on which the VO$_2$ thin-film was grown. The projection of the hexagonal unit cell (of the trigonal lattice system) along the c-axis is shown as thick black box. The threefold symmetry is indicated by the two other possible equivalent unit cell orientations (dashed lines), forming a hexagon. b) The corresponding interface plane, the (010)-surface of monoclinic VO$_2$, is shown together with three possible unit cells, forming a quasi-hexagonal entity. In c) the magnitude and geometry of the lattice mismatch is shown.

respect to the substrate is quite large (13-21 % depending on the direction) as can be seen when comparing the corresponding surface/interface structures in Figure 4.19 a) and b). Although the projection of the unit cells of substrate and thin film onto the interface look similar in shape, the unit cell angle is slightly different and VO$_2$ has substantially larger area of the projected unit cell. The lattice mismatch is sketched in Figure 4.19 c) where the distorted and slightly larger unit cell of VO$_2$ becomes obvious. According to reference [Nag08] it has nevertheless been used as the standard substrate for epitaxial VO$_2$ thin films for reasons of tradition, availability of the substrate, its stability at high temperatures and its low reactivity. Not surprisingly such thin films consist of many small crystallites. Their preferential orientation is with their (010)-axis along the substrates c-axis, while the Figure 4.19 c) directly illustrates the twinned structure with 120° domain walls reported in [Wu98], because of the threefold symmetry of the depicted combination of unit cells.

The growth method at room-temperature with subsequent annealing [Nag11] yields smooth films, suitable for surface sensitive photoemission spectroscopy. The sample was characterised in the group of Richard Haglund by measuring the hysteresis loop optically and checking the surface structure via SEM. A summary is given in Figure 4.20: In a) the transmission of a broadband light source through two different locations on the thin film is measured with respect to sample temperature. A typical hysteresis showing a drop in relative transmission by 30% is shown. To analyse the hysteresis further in b) the derivative with respect to temperature is displayed. Fitting two Gaussian line shapes allows for easy quantification of the hysteresis. The critical temperature upon heating is 330 K (57° C) and the hysteresis width between heating and cooling branch is 6 K. The transition between insulating and metallic phase is approximately 8 K wide in both cases.

From the deviation between the two curves in a) just above 300 K it can be concluded, that the sample is not perfectly homogeneous. This can also be qualitatively
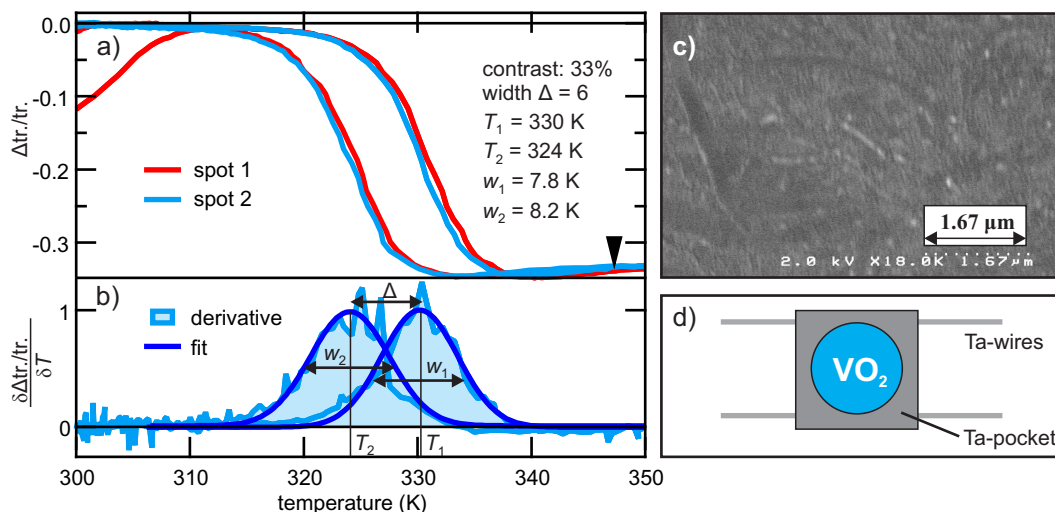
**Figure 4.20:** Characterisation of 45 nm VO$_2$ thin-film grown on Al$_2$O$_3$. a) Change in transmission of a broadband whitelight source upon heating across the phase transition temperature for 2 different spots on the sample (Data has been kindly provided by Christina McGahan, who made the samples in the group of Richard Haglund). b) Normalised derivative of data measured on spot 2 in a), together with Gaussian line shape fits to characterise transition upon heating and cooling. c) SEM image of the sample surface. d) scheme of sample mounted in tantalum pocket.

deduced from the SEM image shown in Figure 4.20 c).

To ensure electrical contact for photoemission experiments and uniform heating, the sample was mounted in a tantalum pocket as shown in Figure 4.20 d), which was spot-welded onto two tantalum wires. A hole of $\sim$ 5 mm diameter in the pocket guaranteed access to the thin film for the laser beam and for photoemission. A spot-welded thermocouple pair (Type K) was clamped between tantalum pocket and sample for temperature measurements. The sample was transferred into the UHV chamber[38], using the sample transfer system described in Section 3.2.8 and Appendix B.

The sample surface was cleaned from adsorbates by repeated annealing at 600 K for 30 minutes, while providing a background O$_2$ pressure of $10^{-4}$ mbar. The oxygen-background pressure was employed to prevent oxygen to diffuse out of the thin-film into the vacuum and therefore to keep the sample stoichiometric. The surface quality was checked by monitoring charging effects and detecting a characteristic hysteresis loop in-situ using photoemission spectroscopy, as presented in the next section (4.2.2).

### 4.2.2 Thermal insulator-to-metal transition

In the following, (single-photon) photoemission (PE) spectra at different sample temperatures are investigated in detail, to characterise insulating and metallic phase of VO$_2$. As a reminder, Figure 4.21 a) and b) show energy diagrams that illustrate the photoemission process for both cases. In a), a metallic sample with work function $\Phi$

---

[38]care was taken to keep the sample close to room temperature while transfer to avoid oxygen deficiency
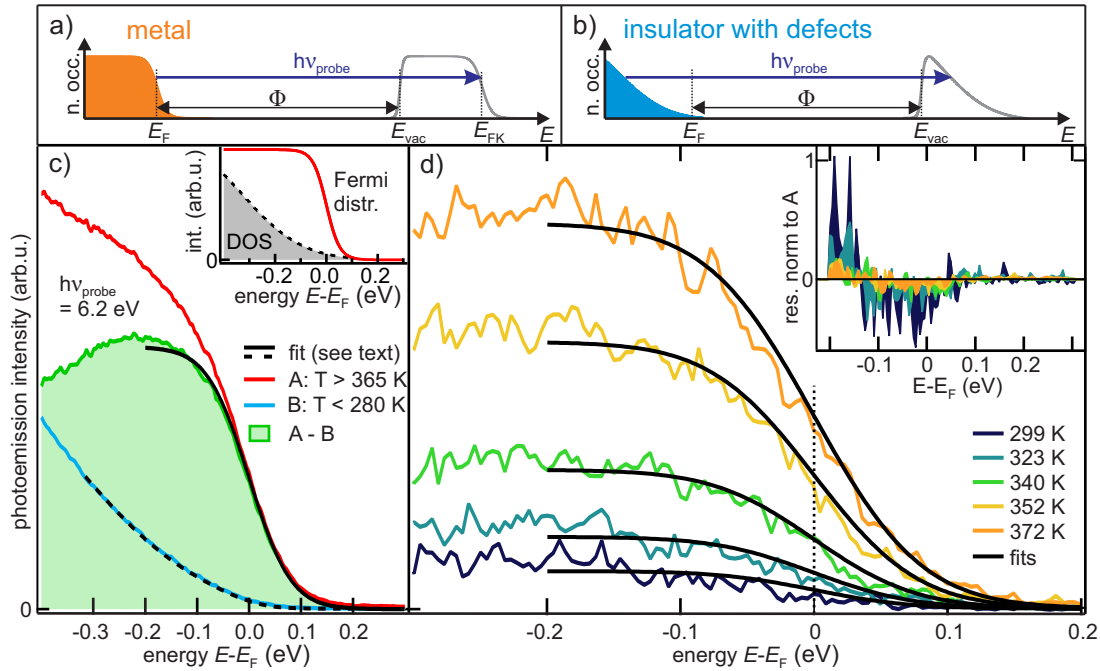
**Figure 4.21:** Detailed analysis of photoemission spectra of VO$_2$ at different temperatures: a) and b) illustrate the single-photon photoemission process and resulting photoelectron spectra for metallic and insulating sample (with defects), respectively. c) PES spectra for temperatures below 280 K (blue) and above 365 K (red) representing the insulating and metallic phase of VO$_2$. The temperature-induced change of photoemission signal (green) is fitted well by a Fermi distribution function (solid black) and a constant DOS (see main text). The DOS needed to fit (dashed black) the low temperature, insulating spectrum (blue) is shown in the inset. d) Shows background subtracted spectra at different temperatures, when crossing the phase transition temperature upon heating. Fit results (black) are generated by fitting with only one free parameter (amplitude). Fit residuals normalised to the respective amplitude are shown in the inset.

is investigated, using a photon energy h$\nu_{\text{probe}} > \Phi$. In a first approximation (neglecting e.g. transition matrix elements and scattering processes), the occupied density of states (DOS, orange) is projected from its initial energy onto final states above the sample vacuum level $E_{\text{vac}}$ in the continuum[39]. The detected photoemission intensity is indicated by the grey curve and exhibits a low energy cut-off (also called secondary edge) at $E_{\text{vac}}$, due to the sample vacuum level and a high energy cut-off (also called Fermi edge) at $E_{\text{FK}}$, because initial states are only occupied up to the Fermi energy $E_{\text{F}}$ (Thermal occupation is given by the Fermi-Dirac distribution function).

b) Shows a schematic representation of a similar situation for an 'insulator with defects' instead of a metal. Defect states are indicated by the occupation (blue) that decays towards the Fermi energy. No clear Fermi edge is visible, as there is no DOS at the Fermi energy. In contrast to the metal, the insulator does not exhibit a Fermi surface!

In the case of VO$_2$, the employed photon energy of $h\nu = 6.2$ eV is able to probe weakly bound ($\sim 600$ meV with respect to the Fermi energy) states, as the work function of VO$_2$ is on the order of 5.6 eV. Figure 4.21 a) shows photoemission spectra generated by $h\nu = 6.2$ eV photons of insulating (blue) and metallic (red) VO$_2$. For the spectrum representing the insulating and metallic phase, spectra below 280 K and above 365 K were integrated, respectively, clearly outside of the transition region. The difference is striking: the metallic phase spectrum shows a high photoemission intensity at the Fermi energy ($E - E_{\text{F}} = 0$), in contrast to the spectrum of the insulating phase, where the intensity at this energy is close to zero. Under the assumption that the PE intensity in the region of the band gap of insulating VO$_2$ (blue) is due to photoemission from defect states and does not change significantly with temperature, it can be subtracted from the high-temperature data to yield the *additional* density of states created by the thermal phase transition in VO$_2$ (green filled curve). To quantify this difference spectrum further in the region around the Fermi energy, the following fit function was used:

$$f(E) = (A \cdot F(E,T) \cdot \text{DOS}(E)) * G(E,\sigma), \tag{4.47}$$

$F(E,T)$ is the Fermi distribution function, which is multiplied by the density of states $\text{DOS}(E)$. This product is convolved with a Gaussian function $G(E,\sigma)$, representing the experimental resolution. To determine the experimental broadening $\sigma$, the width of the low energy cut-off of the photoemission spectra (secondary edge) was convolved with the laser bandwidth, which yields a value of 85 meV. The relative position of the Fermi energy was determined independently by a reference measurement on the gold-plated part of the sample holder and the temperature $T$ was directly measured via a type-K thermocouple pair attached to the sample.

To fit the low temperature data, shown in Figure 4.21 a) (blue curve), a non-constant density of states, decaying towards $E_{\text{F}}$, has to be assumed (shown in the inset). In absence of a better knowledge about the DOS, a Gaussian function was used, producing the displayed exponential tail towards the Fermi energy. This tail (in agreement with e.g. the exponential Urbach tail, observed in optical spectroscopy of amorphous semiconductors) is due to defect states in the band gap of *insulating* VO$_2$,

---

[39]For a more detailed description including the energetics of the photoelectron analyser, see Section 3.2

but does not resemble significant metallic DOS at the Fermi energy.

In contrast to that, fitting of the temperature-induced change (green curve) was performed, assuming a *constant* DOS across the Fermi energy, close to the expected situation for a metallic system[40]. It is noteworthy, that the only free fit parameter left is the amplitude $A$. Nevertheless the fit result describes the data remarkably well. At high temperatures, the density of states becomes much more homogeneous (constant) across the Fermi energy. This is the equivalent to the formation of a Fermi surface, characteristic for a *metal*.

The evolution of the system upon heating, is illustrated by spectra at intermediate temperatures in Figure 4.21 b). They are background subtracted and fitted (black lines) analogous to the difference spectrum (green) in a), described previously. The inset shows the residuals of the fit that have been normalised to the amplitude $A$, as a measure of the fit quality. Apart from the noise that is slightly amplified by the normalisation, only fits for the two lowest temperatures (299 and 323 K) have a significant residual. At these temperatures the sample is still (at least to a large extent) in the insulating phase and the slight increase in photoemission intensity cannot clearly be attributed to increased metallicity. To capture this small change in insulating PES signature that is likely mixed with the emergence of metallic DOS, a more complex fit function would be necessary. This is not feasible, because of the signal-to-noise and rather unspecific shape in these two spectra, and thus neglected.

This analysis shows, that the integrated photoemission intensity below the Fermi energy directly probes the metallicity of the VO$_2$ sample and therefore can be used as a marker for the insulator to metal phase transition. It also constitutes the most direct and natural marker of metallicity of a solid, which is defined by DOS crossing the Fermi energy (i.e. the existence o a Fermi surface).

To verify further that the photoemission experiment is sensitive to the insulator-to-metal transition observed via optical properties (see e.g. static transmittivity hysteresis in Section 4.2.1), the PE intensity in the energetic region below the Fermi energy is used to measure a hysteresis loop. Therefore photoemission spectra were recorded continuously while heating the sample from the insulating to the metallic phase. Figure 4.22 a) displays normalised photoemission intensity, encoded in a false colour scale with respect to energy $E - E_F$ and real time, recorded during a heating and subsequent cooling cycle. The simultaneously recorded sample temperature is shown below (black curve). Without further analysis it is clear that the photoemission intensity directly below the Fermi energy (red box) is larger at high temperature ($>320$ K), as characterised before in Figure 4.21.

Integration of the PE intensity over the energetic window indicated by the red box (i.e. between zero and 200 meV binding energy) in Figure 4.22 a) yields the intensity that is shown in b) with respect to sample temperature. Clearly the shape of a hysteresis loop is visible. This intensity *directly* indicates the metallicity of the sample during the heating and cooling cycle.

To quantify this hysteresis loop, a binned (20-fold) replica of the data (black curve in b)) is used to numerically calculate its derivative with respect to temperature $dI/dT$.

---

[40]A strictly constant DOS would be observed in an ideal 2D free-electron metal. In the present case, the real metallic DOS is approximated sufficiently well by a constant, due to the limited energy window and resolution of this analysis.
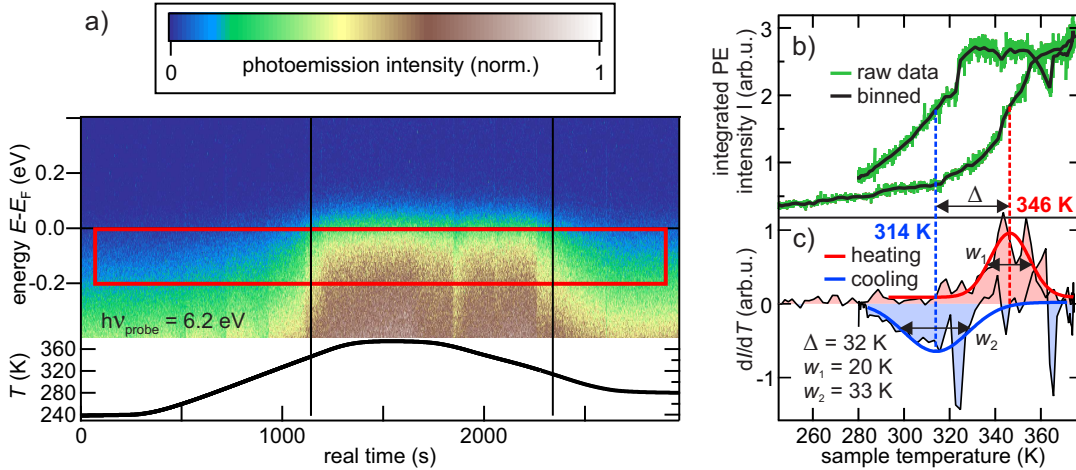
**Figure 4.22:** The hysteresis in VO$_2$ probed by photoemission spectroscopy: a) PE intensity, probed by ($h\nu = 6.2$ eV), is recorded upon heating the sample and displayed with respect to real time of the measurement and energy (top). Sample temperature is varied between 240 and 375 K (bottom). b) Integrated intensity over an energy window indicated by red box in a) is shown as well as binned ($\times20$) data. c) Derivative of the binned data in b) with respect to temperature and Gaussian fits to quantify transition temperatures of heating and cooling branch.

This derivative is shown in c). The increasing and decreasing branches of the hysteresis in b) are therefore converted to a positive (red) and negative (blue) peak in c), respectively. The heating branch has its maximum slope (peak maximum) at a higher temperature (346 K) than the cooling branch (314 K), as expected for a hysteresis.

| run | 1 | 2 | 3 | 4 | mean | $\sigma$ |
|---|---|---|---|---|---|---|
| T$_{heat}$ (K) | 347 | 346 | 338 | 345 | 344 | 4 |
| T$_{cool}$ (K) | 317 | - | 314 | 332 | 321 | 10 |

**Table 4.1:** Overview of phase transition temperatures extracted from four temperature dependent photoemission spectroscopy measurements performed at various days.

The positions and widths of the hysteresis branches are characterised by Gaussian fits. Similar temperature dependent measurements and data analyses have been performed after repeated sample preparations and most probably at different positions[41] on the sample, which yield the critical temperatures summarised in table 4.1. On average the critical temperature upon heating (cooling) is $344 \pm 4$ K ($321 \pm 10$), yielding a hysteresis width of 23 K. The increased width of the hysteresis of 23 K in comparison to the optically measured one (6 K) and also the width of the single branches shown in Figure 4.22 (20 and 33 K as compared to 7.8 and 8.2 K measured optically) measured at the same sample can be explained by an increased surface sensitivity due to

---

[41]Even with a reproducibility of sample positioning on the order of 100 $\mu$m on a day to day basis, using a probe-laser spot size smaller than 50 $\mu$m does not guarantee probing at the exact same location on the sample.

photoemission probing combined with an increased inhomogeneity of the surface, or minor sample ageing. Nevertheless the qualitative agreement and the previous analysis of photoemission spectra (Figure 4.21) leaves not doubt that **the photoemission experiment is sensitive to the insulator-to-metal transition in VO$_2$ by directly probing the relevant property: The spectroscopic appearance of a Fermi surface.**

### 4.2.3   Photo-induced change of electronic density of states

After characterising the differences between the equilibrium insulating and metallic phase of VO$_2$ in photoemission spectroscopy (using low-energy photons), *photo-induced* changes are investigated. The photo-excitation was performed using laser pulses centred at a wavelength of around 800 nm, in analogy to the optical experiments presented in the previous chapter and most of the earlier work involving time-resolved spectroscopy on VO$_2$ (see Section 2.2). The fluence was chosen as high as possible ($F = 6.7 \pm 0.8$ mJ/cm$^{-2}$ - see Appendix D for details), without charging the sample via the photoemission process or creating significant average heating effects[42]. Fluences above the photo-induced phase transition (PIPT) threshold fluence, determined by the optical experiments, ($F_{\mathrm{TH}} = 5.9 \pm 1.0$) could nevertheless be achieved.

As a starting point, the photo-induced change for a time delay $\tau > 2$ ps is analysed in order to characterise the transient phase in this temporal regime, which was used for PIPT threshold determination in previous studies [Küb07, Pas11, Wal13] as discussed in Section 2.2. To quantify photo-induced changes, averaged photoelectron spectra before (between -20 to -1 ps) and after (between 2 and 100 ps)[43] strong photo-excitation, measured at a sample temperature of 270 K, are shown in Figure 4.23 a). Both do not exhibit the characteristic shape of a Fermi-distribution function, but merely the onset of the valence band of insulating VO$_2$ and a secondary electron background created by the pump-light alone (the non-zero intensity above the Fermi-energy). The photo-induced *change*, i.e. the difference of the two curves in a), is displayed in Figure 4.23 b) after ten-fold binning (red curve). It compares very well with the *temperature induced* change, already shown in Figure 4.21 a) (green) and its Fermi-distribution fit after normalisation. **This means that the pump-pulse has induced an ultrafast metallisation of parts of the illuminated area and is a direct observation of the photo-induced *insulator-to-metal* transition in VO$_2$.**

The photo-induced signal is about a factor of 20 smaller, although a direct comparison of absolute intensities is not feasible, as slightly different probe fluences were used. The reasons for the reduced intensity as compared to the temperature-induced phase transition can be explained as follows: the pump-fluence of 6.7 mJ/cm$^{-2}$ is still well below the saturation regime, presented in the previous chapter (compare Figure 4.10 a). At such fluences in the close vicinity of the phase transition threshold, the

---

[42]Heat dissipation into the vacuum is only possible via radiation and therefore significantly lower in experiments performed in UHV as compared to optical experiments under atmosphere. To keep the illuminated spot below the critical temperature for the phase transition, the sample had to be cooled. This was only possible in a limited range, as charging effects due to the insulating/semiconducting character of the surrounding of the illuminated spot become more likely at low temperatures.

[43]No significant change is apparent in this time interval, it was therefore integrated to improve the signal-to-noise ratio
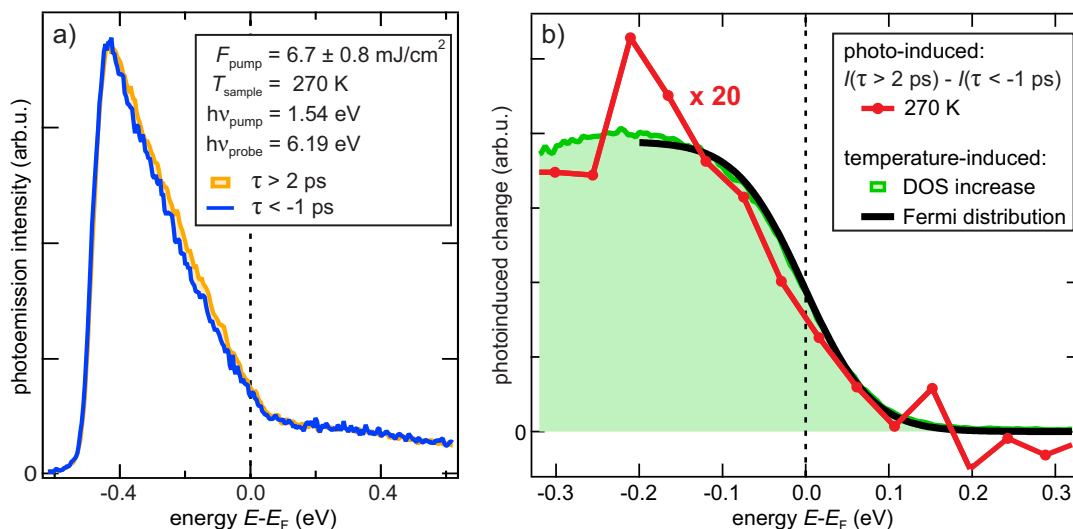
**Figure 4.23:** Photo-induced changes of DOS probed by time resolved PES: In a) averaged data between 20 and 1 ps before and between 2 and 100 ps after photo-excitation using a fluence of 6.7 mJ/cm$^2$ is shown for a sample temperature of 270 K. Subtracting the data before excitation ($<$ -1 ps) from data after photoexcitation ($>$ 2 ps), i.e. blue curve from orange curve, yields the photo-induced change (binning: ×10) of photoemission intensity displayed in b). This is compared to the temperature induced change (filled green curve) from Figure 4.21 and its Fermi-distribution fit (black) after normalisation.

photo-induced *reflectivity change* at 800 nm at 1 ps pump-probe delay is about 70 times smaller than the change in reflectivity upon thermally driving the phase transition. This is due to the inhomogeneous photo-excitation throughout the probed volume and explains the reduced change observed in photoemission as well.

In Figure 4.24 a) photoemission spectra including 800 nm pump, but at negative pump-probe delays, i.e. in the unpumped situation, are shown to illustrate the effect of equilibrium sample temperature plus average heating by the pump-laser. The increasing amount of metallicity, due to an increased equilibrium temperature, is clearly observed. However closer evaluation shows that it is shifted to lower sample temperatures compared to Figure 4.21, because the pump light elevates the local temperature at the illuminated spot: For example, comparison of the shape of a spectrum including pump-light at 320 K (orange curve) with a spectrum without pump-light (grey curve) at $>$ 365 K yields only marginal differences, indicating that the temperature in the illuminated area is on the order of 30 K higher than when the sample is not illuminated by pump-light.

In order to characterise the influence of temperature on the PIPT, Figure 4.24 b) shows pump induced change at different equilibrium sample temperatures. The data has been binned (×10) to reduce noise. Least-mean-squares fits (black lines) where performed using the amplitude as the only free parameter, while the sample temperature was fixed at the measured temperature[44] and an experimental broadening of 85 meV

---

[44]Laser induced average heating was not taken into account at this point, as the estimated difference of 30 K would not change the shape of the experimentally broadened Fermi-distribution function on a
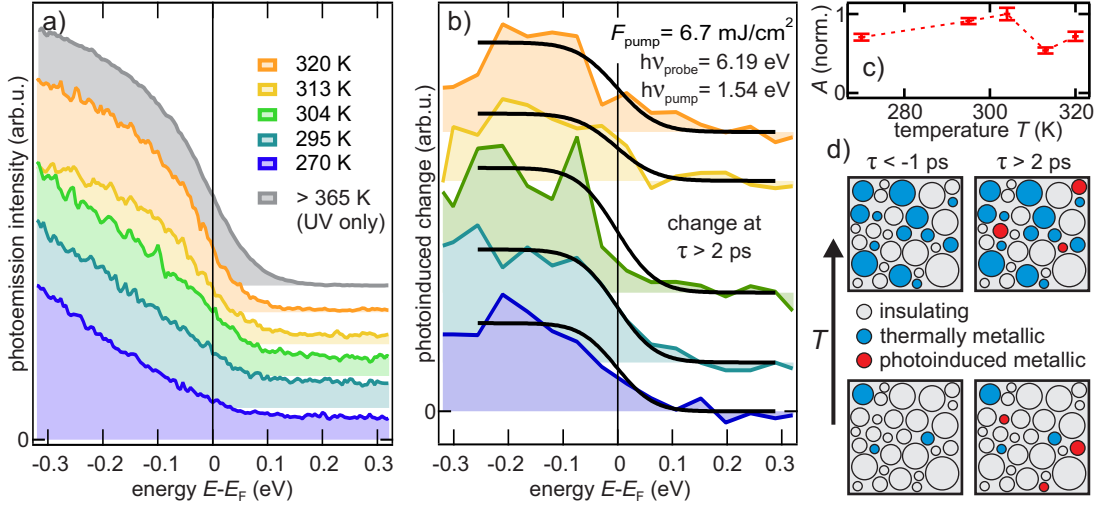
**Figure 4.24:** Probing photoinduced changes at different equilibrium temperatures: a) Photoemission spectra ($h\nu_{probe} = 6.19$ eV) before perturbation by pump pulse (i.e. at negative delays) for different sample temperatures (curves are offset for clarity). A spectrum without any pump light is shown (grey curve) for comparison. b) Photoinduced change at $\tau > 2$ ps for sample temperatures displayed in a) binned ($\times 10$). Fits with a broadened Fermi-distribution function for each curve (black curves) are generated using the amplitude $A$ as the only free parameter. This parameter is shown in c) with respect to sample temperature. d) Sketch of domains in VO$_2$ before and after strong photoexcitation for low and high sample temperature (see text).

was assumed. The energetic position of the Fermi energy was determined using the gold plated part of the sample-holder as a reference. The amplitude $A$ of the Fermi-Dirac-distribution function is shown in Figure 4.24 c) with respect to sample temperature and normalised to the maximum value of the series. Error bars indicate the standard deviations generated by the fit routine. **No clear trend can be observed, meaning that the amount of photo-induced metallisation does not depend on sample temperature in the range the measurements were performed in.** To illustrate the implications of this observation, a proposed VO$_2$ surface domain structure is shown in d). At low temperatures (bottom) only a limited amount of domains (circles) is thermally in the metallic phase (blue circles) and at moderate fluences around the phase transition threshold a certain subset is switched into the metallic state by the pump-light (red circles). At higher temperatures (top) the initial amount of metallic domains is larger, but still a different subset (exhibiting a higher phase transition temperature) of domains can be made metallic by photo-inducing the phase transition[45].

On the other hand, when the sample is uniformly in the temperature-induced metallic phase already ($T \gg T_c$), strong photo-excitation should not increase the metallicity of the sample. Such a behaviour is verified by monitoring the photo-induced spectral change while increasing sample temperature, as shown in Figure 4.25. To enhance

significant level.

[45]The inhomogeneous pump-profile due to the Gaussian laser beam shape can explain different subsets undergoing the phase transition at different temperature/fluence-combinations as well. The beam radius of the probe beam was chosen 2.3 times smaller than the pump beam to minimise such effects.
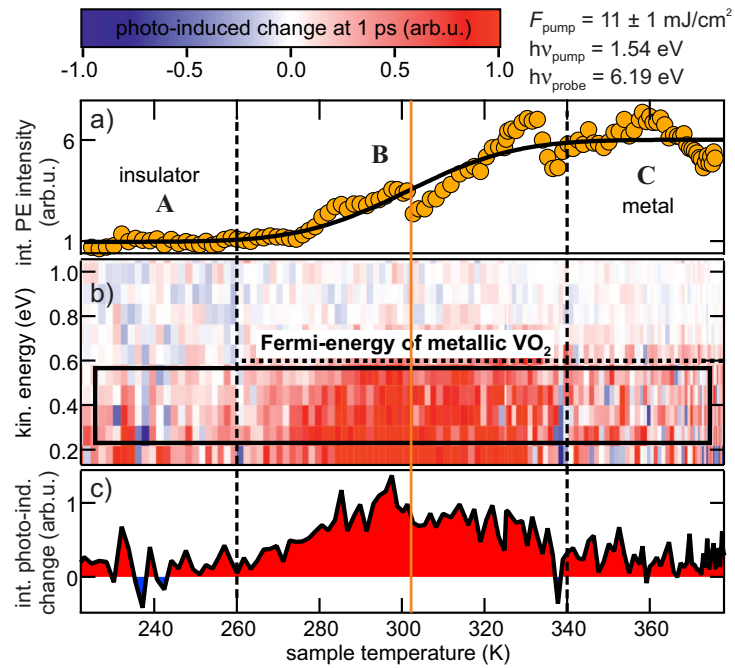
**Figure 4.25:** Temperature dependence of photoinduced changes at 1 ps pump-probe delay: a) Integrated PE intensity below the Fermi-energy. b) False colour plot of photo-induced changes due to strong photo-excitation ($11 \pm 1 \, \text{mJ/cm}^2$) with respect to sample temperature and kinetic energy of photoelectrons. Integrating the indicated area (black box) in b) yields the temperature dependence of photo-induced metallisation displayed in c).

signal-to-noise ratio and perform the temperature-dependent measurement in a reasonable time, the pump fluence ($h\nu = 1.54$ eV) was increased to $11 \pm 1$ mJ/cm$^2$. This raised the need for larger counter-cooling of the sample which created additional experimental difficulties: As the surrounding of the illuminated spot is now at a lower temperature, overall electrical conductivity is decreased while due to the higher fluence the photoemission process (for secondary electrons) is enhanced. These two processes lead to an increase in sample charging, reflected by transient shifts of the photoemission spectra. To cope with these charging effects, that are observed on a slow timescale on the order of seconds, two things had to be done:

① Long averaging times had to be omitted, so spectra influenced by a different amount of charging are not averaged over. Therefore spectra were recorded at a pump-probe delay of $\tau = -1$ ps and $\tau = +1$ ps alternately while slowly increasing the sample temperature. The integration time for each spectrum was set to 500 ms.

② A spectral signature had to be used to compensate for slower shifts. A Fermi-edge is not present in the insulating phase, therefore the low-energy cut-off of the spectra was used to compensate for charging *after* the photo-induced change was determined by subtracting spectra at $\tau = -1$ ps (unpumped) from spectra at $\tau = +1$ ps (pumped) for all temperatures separately. The fact that the spectra at negative and positive pump-probe delays were taken at different real times was accounted for by interpolating the intensities to a common point in time.[46]

A detailed description of the data treatment is given in Appendix E. Figure 4.25 a) shows the integrated photoemission intensity (below the Fermi-energy) of unpumped ($\tau = -1$ ps) VO$_2$. A clear increase corresponding to additional DOS due to the temperature induced phase transition is visible. The heating branch of the hysteresis is centred around 300 K (indicated by the orange line). The reason for the lowering of the apparent transition temperature by $\sim 40$ K in comparison to measurements where no pump-light was employed at all (Figure 4.22), is average heating of the illuminated region of the sample by the pump-light. Nevertheless three temperature regions can be identified corresponding to insulating **A** and metallic **C** VO$_2$ and the transition region in between **B**.

The photoinduced change (difference between spectra at plus and minus 1 ps pump-probe delay) is shown in Figure 4.25 b) with respect to kinetic energy and sample temperature. The low energy cut-off of the raw data at each temperature was used as an energetic reference for the presented data. The Fermi-energy of metallic VO$_2$ is at 0.6 eV on this kinetic energy scale. In the region between 0 and 400 meV below the Fermi-energy, a clear positive signal (red) is visible. A photo-induced decrease of PE intensity at lower energies (not shown, see Appendix E) corresponds to a photo-induced increase of the work function leading to a transient shift of the low energy cut-off to higher energies. A work function increase undergoing the phase transition from insulator to metal has been observed before [Ko11]. The observed intensity contrast

---

[46]Further systematic errors were excluded by confirming the observed effects without interpolation, but by either subtracting the background (at negative pump-probe delays) measured directly before and directly after the photo-excited (positive pump-probe delays) spectrum.

between positive and negative pump-probe delays is *not* compatible with a rigid shift of the spectrum (e.g. due to charging) or a pump-induced broadening effect (e.g. due to increased space charge effects). The pump-induced increase can therefore only be attributed to additional DOS due to the photo-induced phase transition.

To illustrate the temperature dependence of the photo-induced change, the integrated intensity below the Fermi-energy (black box in b)) is shown in Figure 4.25 c). The contrast is significantly positive, above noise level in the region between 270 and 340 K, which corresponds to the transition region, where insulating *and* metallic domains are present. At higher temperatures, the system is already uniformly metallic and strong photo-excitation cannot increase the metallicity any further. At temperatures below the transition region, the fluence ($F = 11 \pm 1$ mJ/cm$^2$, still far below saturation) is not high enough to induce the phase transition in a sufficiently large subset of domains to be detected. This is due to the moderate amount of averaging to avoid charging artefacts and therefore rather low signal-to-noise ratio.

**The preceding sections provide clear evidence, that the performed photoemission experiments are sensitive to both the temperature- and photoinduced insulator-to-metal transition in VO$_2$.** The metallisation in both cases manifests itself by additional density of states below the Fermi-energy exhibiting the shape of a Fermi-distribution function. To gain insights into the dynamics of the photoinduced phase transition, the next section presents the dynamical evolution of PE spectra upon strong photo-excitation.

### 4.2.4   The dynamics of the photo-induced insulator-to-metal transition

To investigate the electronic dynamics of photo-inducing the phase transition in VO$_2$, and thereby to expose its driving mechanism, time-resolved measurements have been performed. Figure 4.26 illustrates the goal of these experiments. The starting point is the monoclinic (M), insulating phase of VO$_2$ (blue), which is strongly photoexcited across the band gap by the pump pulse. If atomic movement is necessary (pathway A) to generate a metallic band structure, the gap-closing ($\tau_{\mathrm{gap}}$) would happen on a characteristic timescale of the lattice ($\tau_{\mathrm{lattice}}$), for example the famous structural bottleneck timescale of 80 fs, reported in [Cav04] (see Section 2.2).

If in contrast, a transient metallic phase is generated (green) due to the photoexcitation itself while the atoms are still in their monoclinic positions (pathway B), the gap closing should occur faster than typical lattice timescales ($\tau_{\mathrm{gap}} < \tau_{\mathrm{lattice}}$). Hot electron decay *inside* the band gap would in both cases only be observed when the gap is already closed. The quasi-equilibrated rutile (R), metallic phase (orange) is only reached after the whole system is thermalised and atoms have moved to their new quasi-equilibrium positions.

Experimentally, after strong photoexcitation (in the previously established threshold fluence region $F \simeq 7$mJ/cm$^2$) 6.2 eV photons were used to monitor the dynamics below the Fermi-energy of metallic VO$_2$ and directly follow the photo-induced metallisation and equilibration of VO$_2$. In addition, lower photon energies (below the work function of VO$_2$) were used to probe only the transiently occupied states above the Fermi-energy after photo-excitation and widen insights into hot electron dynamics of
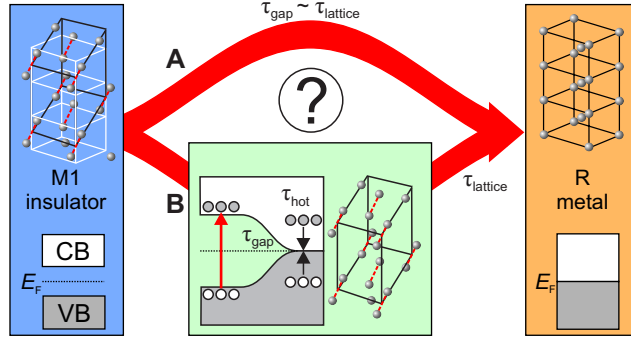
**Figure 4.26:** Timescales of the two supposed pathways for the photoinduced insulator-to-metal transition: **A** Structural changes are needed to generate a metallic density of states. The gap closing ($\tau_{\mathrm{gap}}$) would happen on a 'lattice timescale' ($\tau_{\mathrm{lattice}}$). **B** a transient metallic phase with monoclinic crystal structure is generated directly due to the photoexcitation, before any movement of the atoms ($\tau_{\mathrm{gap}} < \tau_{\mathrm{gap}}$). In both cases hot electron/hole decay ($\tau_{\mathrm{hot}}$) *inside* the gap can only be observed if the gap is closed.

the transient metallic phase.

**Metallisation Dynamics in VO$_2$**   The dynamics of the photo-induced phase transition is analysed in detail in this paragraph. A typical time- and energy-resolved photoemission spectroscopy dataset is shown in Figure 4.27 a). The equilibrium background has been extracted at negative pump-probe delays, therefore only the pump-induced change in photoemission intensity is displayed. At zero time delay between pump ($h\nu = 1.54$ eV) and probe ($h\nu = 6.19$ eV) pulse an intensity increase (red) is observed at all energies between -0.4 and 0.6 meV with respect to the Fermi energy. At positive pump-probe delays a photo-induced increase is detected at energies below the Fermi energy, that persists at least for hundreds of picoseconds[47].

The main part of intensity around timezero is interpreted as two-photon photoemission via virtual intermediate states in the band gap of unswitched, insulating VO$_2$, as observed in other systems previously [Kno95, Sch96]. The region indicated by the green box 400 to 600 meV above the Fermi energy is used to extract the cross correlation of pump and probe pulse displayed in b) (green filled curve). It is fitted with a Gaussian function (blue) yielding a XC-width (FWHM) on the order of 90 fs. It is also used to determine the exact temporal overlap between pump and probe pulse for further analysis. Together with displayed wavelength spectra of probe (left) and pump (right) their pulse duration can be estimated: The transform limited pulse duration is used both as a lower limit and also to estimate the upper limit of the respective other pulse together with the cross-correlation width $\tau_{\mathrm{XC}} \simeq 90$ fs via:

$$\tau_{\mathrm{XC}}^2 = \tau_{\mathrm{pump}}^2 + \tau_{\mathrm{probe}}^2 \qquad (4.48)$$

---

[47]A slight pump-induced decrease (blue) in photoemission intensity is observed at energies below -0.4 eV due to the dynamic work function increase as described in [Ko11]. It is a minor effect as compared to the increase (red) and not compatible with space-charge broadening of the spectrum or a rigid shift due to transient charging of the sample.
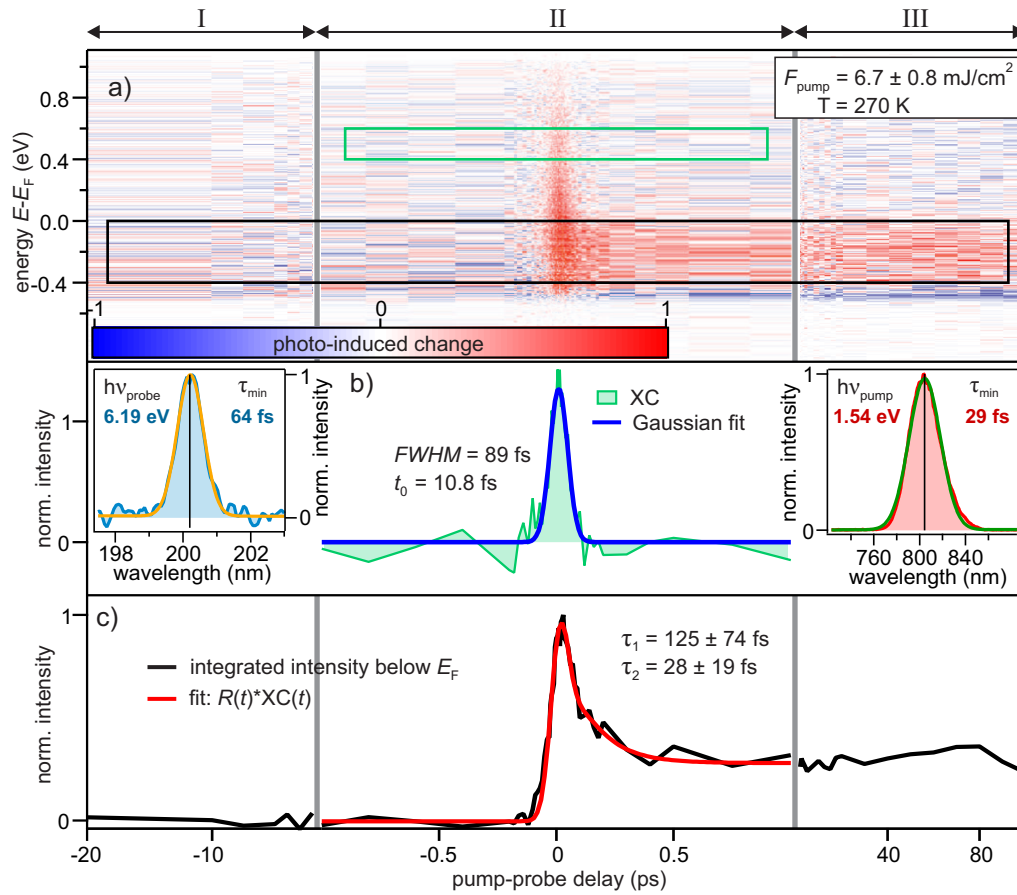
**Figure 4.27:** Overview over exemplary time-resolved PES dataset: a) shows the change in photoemission intensity induced by a $F = 7$ mJ/cm$^2$ pump pulse, centred at 1.54 eV photon energy, when probed by UV ($h\nu = 6.19$ eV) light. Region I ($< $ -1 ps) has been used for background subtraction of the uncorrelated signal. The XC of the employed laser pulses (green) taken from the region indicated by the green box and a Gaussian fit (blue) are displayed in b). The insets show laser spectra of probe (left) and pump (right) light. The transient evolution of DOS below the Fermi energy (region indicated by black box in a)) is shown in c). The fit with an empirical model (response $R(\Delta t)$ convolved with cross correlation from b)) yields the red curve.

Exploiting additional knowledge about the 800 nm pump-pulse duration ($\tau_{\mathrm{pump}} = 40$ fs, measured ex situ) that is realistically achievable the most likely pulse durations $\tilde{\tau}$ are given together with the limiting values in table 4.2 as to indicate an estimate of the time resolution of the experiment.

|        | $\tau_{\min}$ | $\tau_{\max}$ | $\tilde{\tau}$ |
|--------|---------------|---------------|----------------|
| pump   | 29 fs         | 63 fs         | 40 fs          |
| probe  | 64 fs         | 85 fs         | 81 fs          |

**Table 4.2:** Lower ($\tau_{\min}$) and upper ($\tau_{\max}$) limit for pump and probe pulse durations and estimated value $\tilde{\tau}$. Note that assuming the upper limit for the pump pulse implies the lower limit for the probe pulse and vice versa.

In Figure 4.27 c) the temporal evolution of the integrated energetic region between 0 and 400 meV *below* the Fermi energy (as indicated by the black box in a)) is shown (black curve). A contribution from two-photon photoemission via virtual intermediate states, exhibiting no lifetime, results in a peak at timezero. This peak appears asymmetric, as it is superimposed to a decaying intensity, that stabilises into a persisting increase at positive delays. Such a photo-induced increase of photoemission intensity *below* the Fermi energy is attributed to a change in DOS, i.e. the metallisation of parts of the sample as discussed before (section 4.2.3). It appears immediately after excitation and stays constant on the order of hundreds of picoseconds. This paragraph concentrates on the initial fast dynamics, while longer timescales are discussed later.

To analyse the transient change of photoemission intensity further, especially how fast it appears, a fit model has to be developed. Rate equations describing the appearance of DOS and on top of that quasiparticle relaxation dynamics turned out to be too complex (inhomogeneous quadratic differential equation with at least one time-dependent coefficient) to yield a robust fit function. Therefore a phenomenological model is used to quantify the timescales of the observed dynamics. The function used to describe the response $R(t)$ upon photo-excitation is as follows:

$$R(t) = \theta(t)\left(A_1 e^{-t/\tau_1} - A_2 e^{-t/\tau_2} + C\right) + D \cdot \delta(t) \tag{4.49}$$

The response consists of a positive exponential decay with amplitude $A_1$ and time-constant $\tau_1$, a negative exponential decay (i.e. rise) with amplitude $A_2$ and time constant $\tau_2$ and a constant offset $C = A_2 - A_1$ (fulfils initial condition $R(0) = 0$). The contribution, due to two-photon-photoemission via virtual intermediate states, is generated by the approximate delta-distribution $\delta(t)$ with amplitude $D$. The Heaviside function $\theta(t)$ ensures zero response before timezero. The response $R(t)$ is convolved with the the Gaussian function $XC(t)$, corresponding to the XC of the laser pulses extracted at high excess energies, as shown in Figure 4.27 b). The resulting curve is then fitted to the data by a least-mean-squares algorithm.

The global fit optimum is reached for values of $\tau_1 = 125 \pm 74$ fs for the decay and $\tau_2 = 28 \pm 19$ fs for the rise. As the large error bars already indicate, the fit is not entirely robust when none of the parameters in $R(t)$ is kept constant. The reason is, that for small $\delta\tau = \tau_2 - \tau_1$ the parameters, especially the two amplitudes, are not independent any more.
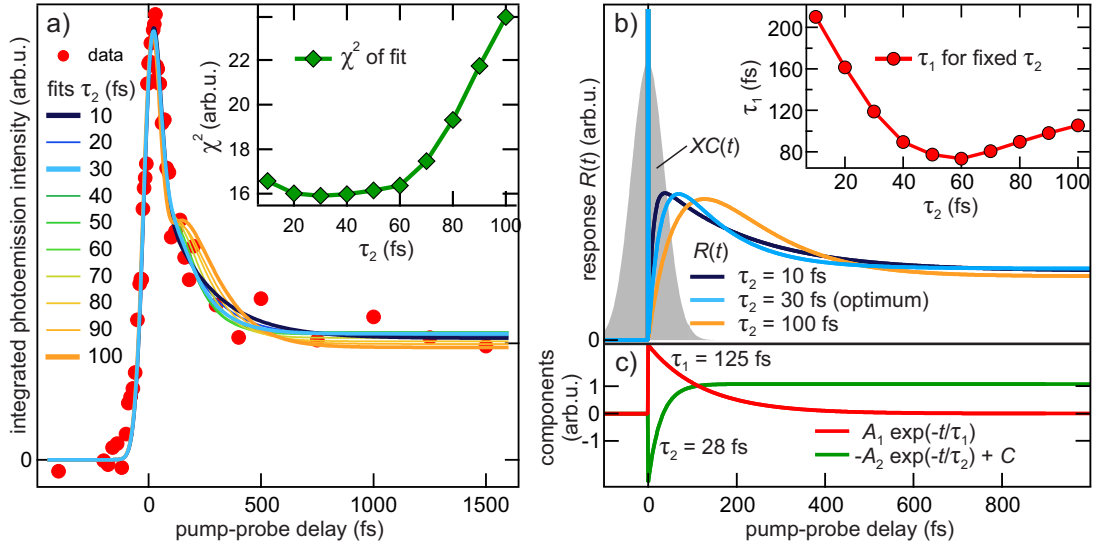
**Figure 4.28:** Exemplary fit results for transient metallisation of VO$_2$ below the Fermi energy: a) fits for various fixed rise times $\tau_2$. The inset shows the $\chi^2$-property of the fit with respect to the different values of $\tau_2$. In b) selected responses $R(t)$ are shown for $\tau_2 = 10$, $30$ and $100$ fs. The grey filled curve is a Gaussian function representing the XC of pump and probe pulse. The dependency of parameter $\tau_1$ as a fit result on the fixed $\tau_2$ is shown in the inset. Panel c) displays the rising (green) and decaying (red) part of the response for the free fit (none of the response-parameters are fixed).

To give an upper limit for the rise time, a trial and error method was employed: The fit was performed while the rise time constant $\tau_2$ was fixed at various values between 10 and 100 fs. An exemplary dataset and fit results for various $\tau_2$ are shown in Figure 4.28 a). As the $\tau_2$ is increased above 60 fs a secondary shoulder at 250 fs pump-probe delay develops that visually deviates from the data. To quantify the quality of the fit, the variable $\chi^2$, which follows the total deviation between data and fit, is displayed in the inset. The small value of $\chi^2$ between $\tau_2 = 10$ and $\tau_2 = 60$ fs indicates optimal fitting in that range. The significant increase of $\chi^2$ above $\tau_2 = 60$ fs signals a decrease in fit quality, already observed visually as the shoulder appearing in the fit results. It is therefore concluded that the rise time constant $\tau_2$ of the employed empirical mode cannot be larger than 60 fs. A clear global optimum is not observed as the fitting is more or less equally good for $\tau_2 < 60$ fs. This means that in this simplified model, a rise of intensity, interconnected to the creation of DOS, has to happen with a time constant of 60 fs or faster. The phase transition to the transient metallic phase happens on a timescale on the order of the time resolution of the experiment[48].

To clarify the problems of fitting with time constants $\tau_2 < 60$ fs the fitted response

---

[48]As discussed in Section 3.2.7, optical Bloch equations are omitted when modelling the temporal response, because dephasing times are not known. Using Bloch equations would in fact result in a delayed population [Her96, Ern04], with respect to the response generated by two-photon photoemission via virtual intermediate states (the delta peak, without real population). This alone could result in the observed, slightly delayed rise (30 fs) of the optimal fit. Because quantification is not possible, it can not be discussed further.

$R(t)$ for $\tau_2 = 10$, 30 and 100 fs is displayed in Figure 4.28 b) (the approximate delta-distribution $\delta(t)$ is not fully shown). The subtle changes for small $\tau_2$ in the region before 100 fs pump-probe delay are completely masked by the delta-peak amplitude after convolution with $XC(t)$ ($XC(t)$ is indicated by the grey solid curve in b)). Only for larger $\tau_2$ the region for larger delays than 100 fs is affected and results in significant deviation of fit result as the delta-peak does not affect this region. Increasing the time-resolution down to tens of fs would help to clarify the exact response at very small pump-probe delays. On the other hand cross-polarised pump- and probe-beams could reduce coherent contributions [Sch96], potentially simplifying data evaluation.

The interdependence of the two time constants $\tau_1$ and $\tau_2$ is displayed in the inset of Figure 4.28 b). In the region between 10 and 60 fs, for which the fit model works well, an inverse relationship between the two time-constants is observed. As $\tau_2$ increases up to 60 fs, $\tau_2$ decreases from 210 to 70 fs. The uncertainty in determining $\tau_2$ is well reflected on the results for $\tau_1$. Further investigation of quasiparticle decay dynamics is necessary and will be presented later, when discussing the dynamics above the Fermi energy, i.e. in unoccupied states of transient metallic VO$_2$.

A bottleneck behaviour [Cav04] is not observed within the temporal resolution of this experiment. **The transition from monoclinic insulating VO$_2$ to a highly excited transient metallic state is quasi-instantaneous ($\tau_2 = 30 \pm 30$ fs) and most likely not mediated by the crystal lattice.** This constitutes a very strong indication for an electronically driven band gap collapse, as the material is excited into a transient state with metallic properties on the timescale of the laser pulse durations[49]. **Hot carrier relaxation timescales on the order of 100 fs are observed in this transient metallic phase.** This agrees well with the timescale, it takes to observe a metallic-like, optical response after photoexcitation (see Section 4.1.5). To gain insight into whether the instantaneous band gap collapse is a reasonable scenario, the effect of photo-excited electrons on the electronic band structure of VO$_2$ can be investigated by theoretical calculations, as presented in the following paragraph.

**Band structure calculation of photoexcited monoclinic VO$_2$**  Theoretical investigations of VO$_2$ and its phase transition(s) are only recently able to reproduce a band gap in the equilibrium low temperature monoclinic phase [Gat07b, Eye11, Bie05]. The experimental observation of a quasi-instantaneous photo-induced band gap collapse in VO$_2$, which was presented in the previous paragraph, motivated theoretical investigations into the following scenario: Can such a band gap collapse be reproduced by electronic structure calculations *in* the monoclinic lattice structure, if electrons are promoted from valence to conduction band?

In close collaboration, such calculations were performed by Lede Xian (in the group of Angel Rubio, San Sebastián) and Matteo Gatti (École Polytechnique) using a first-principles Greens functions approach (the self energy $\Sigma$ is calculated in the $GW$ approximation (GWA), where $G$ is the single particle Green's function and $W$ the screened

---

[49]A timescale of 30 fs could be explained entirely by a response that is delayed with respect to the driving laser pulse, due to a coherence/polarisation build-up described correctly only in the framework of optical Bloch equations. This delay would be an effect of electronic population only and further confirm the electronic, instantaneous nature of the phase transition. As quantification is not possible, because dephasing times are unknown, this argument is neglected in the further discussion.
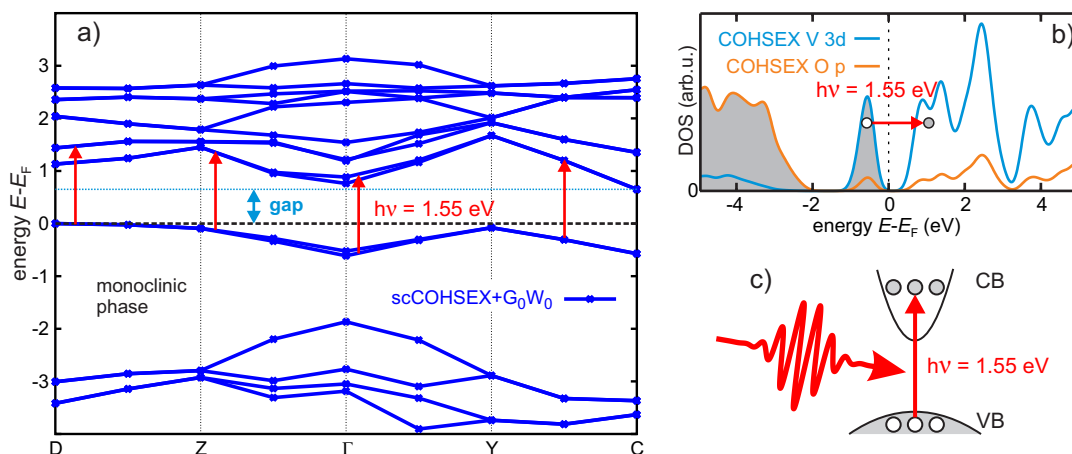
**Figure 4.29:** Calculations of the band structure a) and DOS b) of the monoclinic phase of VO$_2$. The calculations are done on a scCOHSEX level including perturbative GW correction. In a) a band gap of 0.65 eV is reproduced representing the insulating phase of VO$_2$ correctly. The red arrows indicate the excitation photon energy of 1.55 eV. The projected DOS onto V 3d (blue) and O 2p (orange) orbitals is shown in b). Occupied region (below the Fermi energy) is shaded in grey, the excitation photon energy of 1.55 eV is indicated by the red arrow. a) and b) are modified from [Gat07a] and [Gat07b].

Coulomb potential) in combination with DFT calculations. These calculations confirm a gap-closing by artificially promoting electrons from valence- to conduction-band of monoclinic phase VO$_2$ and are discussed in this paragraph.

To find the monoclinic ground state as a starting point for photoexcitation, the band structure is calculated by density functional theory (DFT) in the local density approximation (LDA) first. After that, 27 iterations of self-consistent COHSEX (COulomb Hole and Screened EXchange, a static approximation to GW) plus 9 iterations of perturbative $G_0W_0$[50] calculations are used [Gat07a, Gat07b].

Figure 4.29 a) shows the result of these monoclinic ground state calculations of the electronic band structure of monoclinic VO$_2$. The calculations correctly yield an indirect band gap of 0.65 eV, close the experimental value of 0.6 eV [Koe06], indicated by the light blue arrow. It is important to note that when self-consistency is obtained on the COHSEX level, screening is considered in a static approximation, leading to the correct opening of a band gap in these calculations. b) Shows the corresponding projected DOS onto V-3d (blue) and O-2p (orange) orbitals. Occupied (at T=0 K) states are indicated by the grey shading.

In analogy to the experiment, electrons have to be 'excited' from occupied states (below $E_F$) to unoccupied states (above $E_F$) in the calculation. Possible vertical[51] excitations in the calculated monoclinic band structure are indicated by the red arrows in a) and b). A schematic representation of the photoexcitation is also shown in c):

---

[50]In $G_0W_0$, the previously calculated eigenvalues and orbitals are recycled and self-energy corrections are evaluated

[51]The wave-vector of a photon $k = 2\pi/\lambda$ is small compared to the size of the Brillouin zone for the photon energies used.
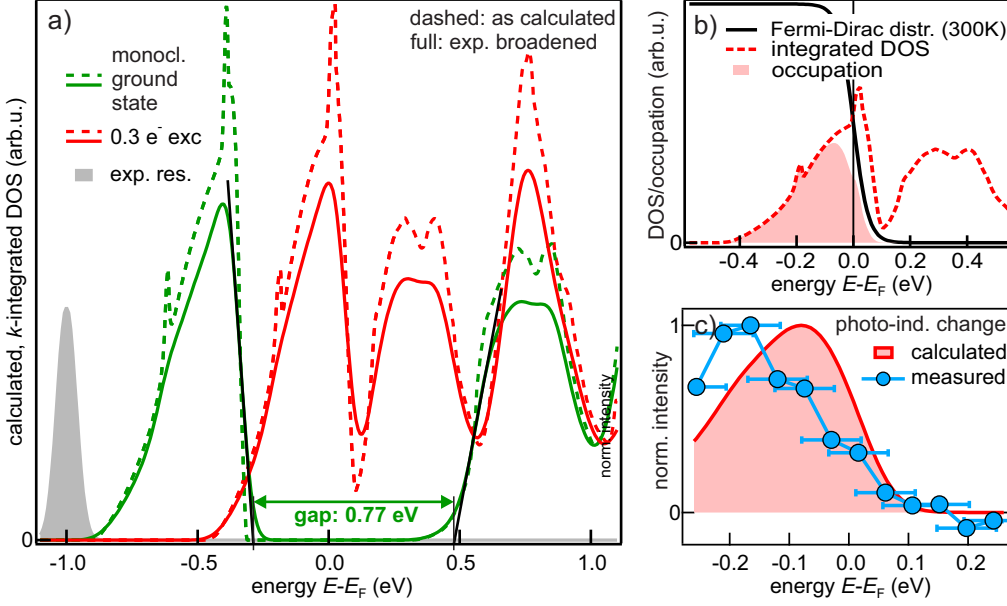
**Figure 4.30:** Comparison of experimental data with band structure calculations: a) Integrated DOS for equilibrium monoclinic phase (green). The broken lines are as calculated, the solid lines are broadened by the experimental resolution (85 meV - illustrated by grey shaded Gaussian). The red curve corresponds to the calculated DOS, when 0.3 electrons per monoclinic unit cell are promoted to the conduction band of monoclinic VO$_2$. In b) the DOS for the photoexcited system (broken red curve) and the occupation (solid red curve) is displayed assuming a Fermi distribution at 300 K (black curve). In c) the experimental data is compared to the experimentally broadened occupation from b). Error bars of $\pm 50$ meV are estimated. Modified from [Weg14].

Electrons (grey circles) are excited from valence band (VB) to conduction band (CB) by photoexcitation (red arrow) and leave behind holes (white circles). This means that the occupation in the VB is reduced and in CB increased by the same amount.

The band structure is then re-calculated in the framework of the $GW$ approximation. The photoexcitation is mimicked by modifications of the occupations. According to the calculated (maximum) excitation density of 0.075 electrons per vanadium atom (i.e. an incident fluence of 6.25 mJ/cm$^2$, see Appendix D for details), used in the experiment, the occupation numbers are reduced for occupied and increased for unoccupied states by the same amount (i.e. generating an equal amount of electrons and holes). This occupation change affects the screened Coulomb interaction $W$, and thus the band structure is re-calculated using this modified $W$.

Figure 4.30 a) shows the initial DOS[52] (green) and the re-calculated photo-excited DOS (red). The density of states is integrated over the Brillouin zone. Remarkably, this re-calculated band structure does not exhibit a gap for monoclinic VO$_2$. **This collapse of the calculated gap in the monoclinic lattice structure confirms**

---

[52]The monoclinic gap size of 0.77 eV slightly overestimates the experimental value, because the final $G_0W_0$-step has been omitted to reduce computational cost. Nevertheless, qualitatively the results remain valid.

**the experimental observation of an instantaneous metallisation in VO$_2$.** The difference between monoclinic ground state and photoexcited state DOS is entirely due to the difference in the screened Coulomb interaction $W$. Screening is enhanced, when electrons are promoted from VB to CB, mainly because intraband transitions *within* VB and CB are possible and allow low energy (smaller than the monoclinic gap size) excitations.

To compare the calculated band structure change with the experimentally observed one, in Figure 4.30 b), the calculated DOS (dashed red curve) is multiplied by a Fermi-Dirac distribution function at $T = 300$ K (black curve), which results in the occupation at room temperature (red shaded area). c) compares this calculated occupation to the measured photoemission spectrum presented earlier[53]. The qualitative agreement of measured data and calculations is very good. Deviations can be explained by systematic errors in the determination of a reference Fermi energy, as well as the fact that the experiment might very well not integrate over all k-space, in contrast to the calculated DOS. In fact, when ignoring scattering processes only parts of the band structure with small momenta (i.e. around the $\Gamma$-point) are probed with the low photon energies that have been used.

To gain additional insights into the microscopic origin of the band gap-collapse, different occupation distributions (with the same number of total electron-hole-pairs) are used and the results are compared. While a detailed analysis is presented in [Weg14], a summary of the findings is presented here: It is mainly the creation of holes in the top of the rather localised valence band (corresponding to the bonding orbitals of the V-dimers along the monoclinic c-axis) that leads to a dramatic change of low-energy excitations pathways. These *low* energy excitations are vital to allow for a energetically cheap charge redistribution that corresponds to effective screening of the Coulomb interaction. As a rough estimate of screening timescales in VO$_2$, the plasmon energy of $\sim 1.5$ eV [Bia81, Gat07b] of the metallic phase corresponds to an oscillation period of approx. 3 fs. Hence the term *instantaneous* band gap collapse is justified in the context of timescales of electron thermalisation or lattice dynamics.

The cartoon in Figure 4.31 a) concludes what has been learned in context of this work, about the initial steps of the photoinduced phase transition in VO$_2$ and its driving mechanism. The initial step is of course photoexcitation of electrons (grey circles) from VB to CB ①. The holes (white circle) in the VB and the electrons in the CB open up new intraband transitions ($\Delta E$) *within* VB and CB. Due to the higher joint density of states in the VB, there are more states available inside a smaller energy range. **These low-energy excitations, mainly due to holes in the VB, are precisely the reason for a photo-induced, strongly enhanced screening of the Coulomb interaction $W$ in VO$_2$ that leads to a massive band gap renormalisation and the transition from an insulating to a metallic band structure ②.** The calculated dielectric function in Figure 4.31 b), for initial insulating (blue) and transient metallic (red) electronic structure, exhibit a large change at low energies, corresponding to these intraband transitions.

The collapse of the gap happens on a screening timescale of a few femtoseconds. Only *after* the gap has closed, carriers thermalise within the energy region of the former

---

[53]Error bars are estimated to be $\pm 50$ meV, as for the determination of a reference Fermi energy (on the gold plated part of the sample holder), no DOS was considered.
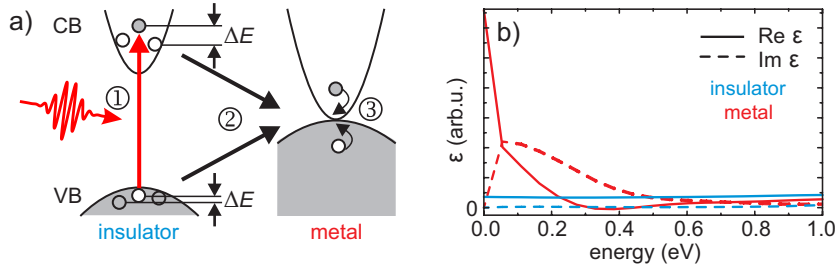
**Figure 4.31:** Mechanism of the instantaneous band gap collapse due to enhanced screening in VO$_2$ a): ① photoexcitation promotes electrons (grey circle) in the CB and leaves behind holes (white circle) in the VB. Intraband transitions increase the screening of the Coulomb interaction ② and thereby close the band gap before further thermalisation of carriers within the energetic region of the former gap ③. Real and imaginary part of the dielectric function $\epsilon$ are shown for initial insulating (blue) and transient metallic (red) phase. b) is adopted from [Weg14].

gap, inside the newly formed conduction band manifold ③. It is very likely that the time constant $\tau_1 = 125$ fs, from the experimental data shown in Figure 4.27 c) in fact corresponds to hot-hole thermalisation in this region.

The fact that the calculations have been performed in the monoclinic crystallographic structure means that no change in atomic positions (lattice contribution) is needed to explain this effect. This of course does not mean that the lattice will not respond quickly to this new electronic band structure. **In fact the optical experiments, presented in Chapter 4.1 have shown that the lattice potential, defined by the bonds, i.e. especially by the electronic valence band structure, is changed instantly, in perfect agreement with the observed instantaneous metallisation of VO$_2$.**

**Temperature dependence of the photo-induced phase transition**   After having established that the photo-induced insulator-to-metal-transition from the monoclinic insulating to the transient metallic phase happens instantaneously, the temperature dependence of the phase transition dynamics are investigated along the lines of the previously described empirical model (Equation 4.49).

Figure 4.32 a) shows integrated photo-induced change below the Fermi energy (black box in Figure 4.27 a)) for different sample temperatures between 270 and 320 K (The transients are offset for clarity). Qualitatively the transients look similar for all temperatures and are therefore fitted with the same model used for the detailed analysis two paragraphs earlier. Exact pump-probe overlap and FWHM of the laser pulse XC was determined for each temperature at high energies (green box in Figure 4.27 a)) and an average value was used. After a first round of fitting where all amplitudes $A_1$, $A_2$ and $D$ as well as the decay time constants were left free an average rise time $\tau_2 = 30 \pm 20$ fs was determined that showed no clear trend with temperature and is in good agreement with the previously determined value of 30 fs. To stabilise the fitting routine it was held fixed at 30 fs in a second round of fitting.

The resulting dependence of decay time $\tau_1$ on sample temperature is displayed in
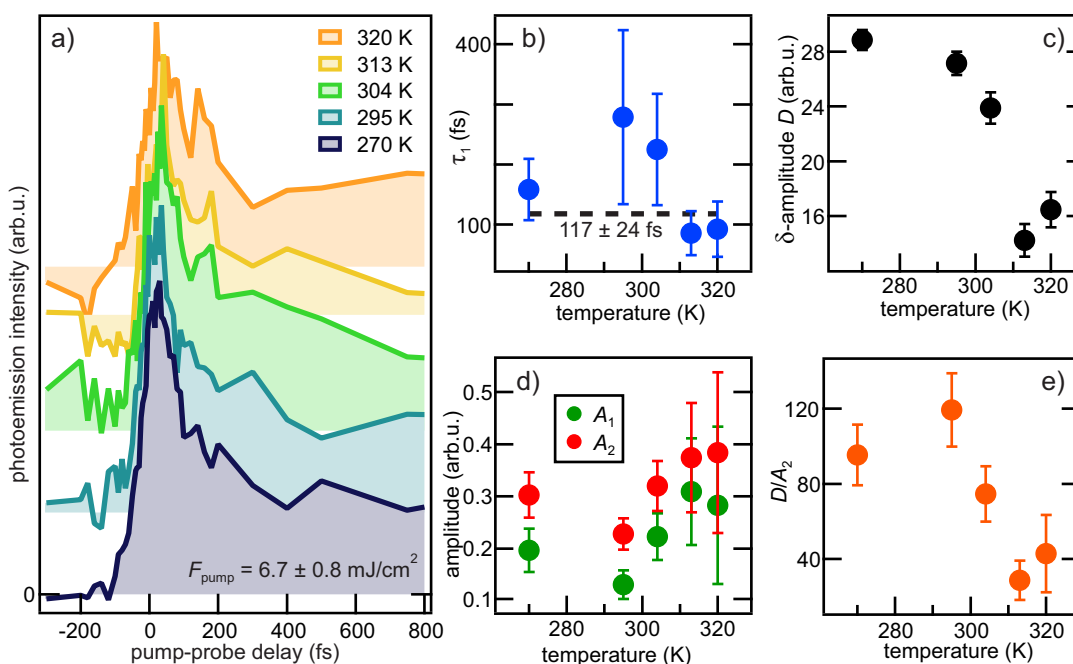
**Figure 4.32:** Temperature dependence of the photo-induced phase transition dynamics: a) Integrated PE intensity below the Fermi energy for different sample temperatures. Resulting fit parameters, when keeping $\tau_2 = 30$ fs fixed: b) decay constant $\tau_1$, c) $\delta$-distribution amplitude, d) amplitudes of rise- and decay-component and e) ratio between $\delta$-distribution amplitude and rise-amplitude. Error bars are standard deviations calculated by the fitting routine.
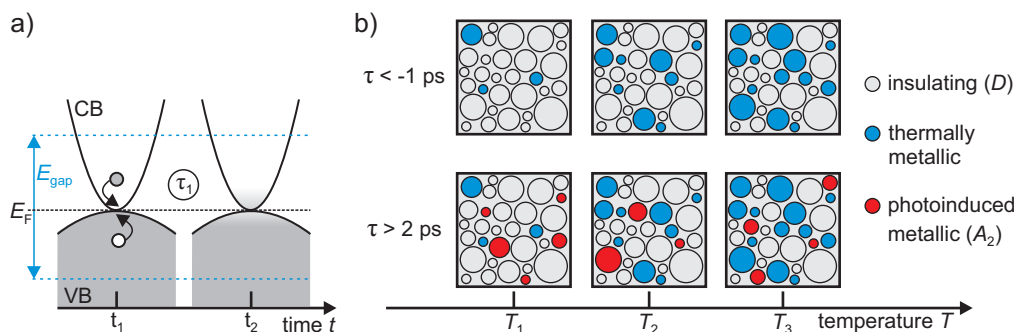


**Figure 4.33:** a) Explanation of decreasing PES intensity directly below the Fermi energy after photo-induced electronic phase transition. Thermalisation of holes reduces effectively reduces the occupation below $E_F$. b) Illustrates the photoinduced phase transition of different domains for increasing temperatures ($T_1 < T_2 < T_3$). PE signal from insulating region (grey) reduces with temperature, while signal from photo-induced metallic domains remains constant. See main text for details.

Figure 4.32 b) where no clear trend can be observed. Fitting to a constant value yields $117 \pm 24$ fs as an average decay time constant. In the context of the theoretical calculations (Figure 4.31 a) in the previous paragraph), this time constant can be interpreted as an average relaxation/thermalisation time for holes in the transient metallic phase. The reasoning is illustrated in Figure 4.33 a). After the photoinduced band gap collapse, at time $t_1$, a non-thermal distribution of electrons (grey circle) and holes (white circle) remain, as these carriers are not able to thermalise instantly (i.e. before or during the collapse). When those carriers subsequently relax towards the Fermi energy, a thermal distribution is reached at time $t_2$. In comparison with $t_1$ the occupations directly below the Fermi energy $E_\mathrm{F}$ and within the monoclinic phase gap (indicated by the blue dashed lines) is *reduced* at $t_2$. Therefore the photoemission intensity decreases slightly in this energetic region. This can only happen *after* the band gap has collapsed because otherwise there would be no DOS, confirming again the promptness of the electronic phase transition. Furthermore, a similar time constant has been observed in the optical experiments, described in Section 4.1.5: The average time it takes, until the photoinduced transient metallic phase exhibits a similar reflectivity response as the equilibrium metallic phase was $190 \pm 30$ fs, in qualitative agreement with the hot carrier relaxation time determined here. And of course it is reasonable that the optical response only starts to resemble the *equilibrium* metallic phase after hot carriers have thermalised.

Panel c) of Figure 4.32 shows the amplitude $D$ of the approximate $\delta$-distribution. A slight decrease with temperature is observed. At the same time the amplitudes $A_1$ and $A_2$ seem to increase slightly with temperature as shown in panel d), although due to the large error bars more or less constant amplitudes cannot be excluded. Panel e) shows the ratio between $D$ and $A_2$. This ratio decreases with temperature, following the trend of $D$. Figure 4.33 illustrates an explanation for this behaviour based on the domain structure of VO$_2$, already shown in Section 4.2.3. The grey circles indicate monoclinic VO$_2$ with existing band gap. These regions are responsible for the photoemission via virtual intermediate states, captured by the $\delta$-amplitude $D$. When heating from $T_1$ over $T_2$ to $T_3$, this grey portion reduces as more and more domains are thermally switched to the metallic phase, leading to the observed decrease of $D$.

The domains that change phase upon photoexcitation are indicated by the red circles (bottom row, after photoexcitation in contrast to the top row, before photoexcitation) and connected to the amplitude $A_{1/2}$. At the different temperatures $T_i$, the phase transition is induced in different subsets of domains, because of slight variations of the threshold due to the inhomogeneity of the sample. The amplitudes $A_{1/2}$ are therefore not affected by the increase in temperature (as long as not *all* domains are thermally in the metallic phase). The ratio $D/A_2$ that shows the same trend as $D$, shown in Figure 4.32 suggests that the trend in $D$ is not just due to random fluctuations. **The different subsets of domains seem to switch independently and with no significantly different dynamics.**

**The phase transition on longer timescales**  Figure 4.27 a) and c) have already shown that the signatures of the transient metallic state do not change over the course of 100 ps. In addition pump-probe photoemission experiments have been performed with significantly lower time resolution, but spanning a wider range of pump-probe delays
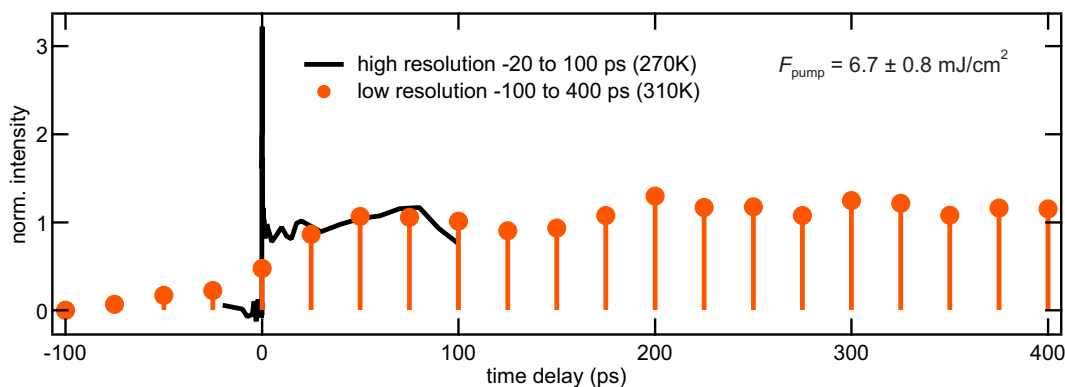
**Figure 4.34:** Transient change of DOS below the Fermi energy (interval of between -0.4 and 0 eV with respect to $E_F$) up to 400 ps: A low time resolution scan up to pump-probe delays of 400 ps (orange) is shown for an incident excitation fluence of $6.7 \pm 0.8$ mJ/cm$^2$. Data with better time resolution (black) from Figure 4.27 c) is displayed for comparison. Both datasets have been normalised to an average between 20 and 100 ps.

between -100 and 400 ps. The average photoinduced change in a 400 meV wide energy window directly below the Fermi energy is shown in Figure 4.34 (orange markers). The previously mentioned transient (black) is shown for comparison. No significant change for long delays (larger than 20 ps) is visible. **This means that the electronic structure does not change considerably after the initial ultrafast metallisation.** X-ray diffraction experiments performed with similar excitation densities (8.7 mJ/cm$^2$) have shown, that transformation of the atomic position to the high temperature rutile equilibrium positions is complete after 250 ps[Had10]. This structural transformation from the equilibrium monoclinic to the rutile phase on a timescale of 25 to 250 ps does not affect the electronic band structure further.

Of course the energy that is initially deposited in the electronic system by the photoexcitation dissipates with time, and electrons and lattice thermalise, most likely on a ps timescale. This leads to a transiently increased temperature in the illuminated spot. It has been shown that the threshold excitation density corresponds to a similar amount of energy as the one needed to thermally drive the phase transition [Pas11]. It is likely that after thermalisation a temperature is reached that stabilises the metallic rutile phase until the heat is effectively transported out of the excited region of the sample. The observed relaxation time back to the initial insulating monoclinic low temperature phase depends on how fast the thermal energy is carried away from the probed volume. In optical experiments in air, an incomplete recovery was observed (data not shown) at a laser repetition rate of 300 kHz, i.e. the sample does not relax completely within 3.3 $\mu$s. Optical experiments were therefore conducted at a lower repetition rate of 100 kHz, where complete recovery was observed. The photoemission experiments presented in the previous sections have been performed at even lower repetition rates of 40 kHz, because heat transport out of the probed volume was effectively reduced due to the in-vacuum measurements.
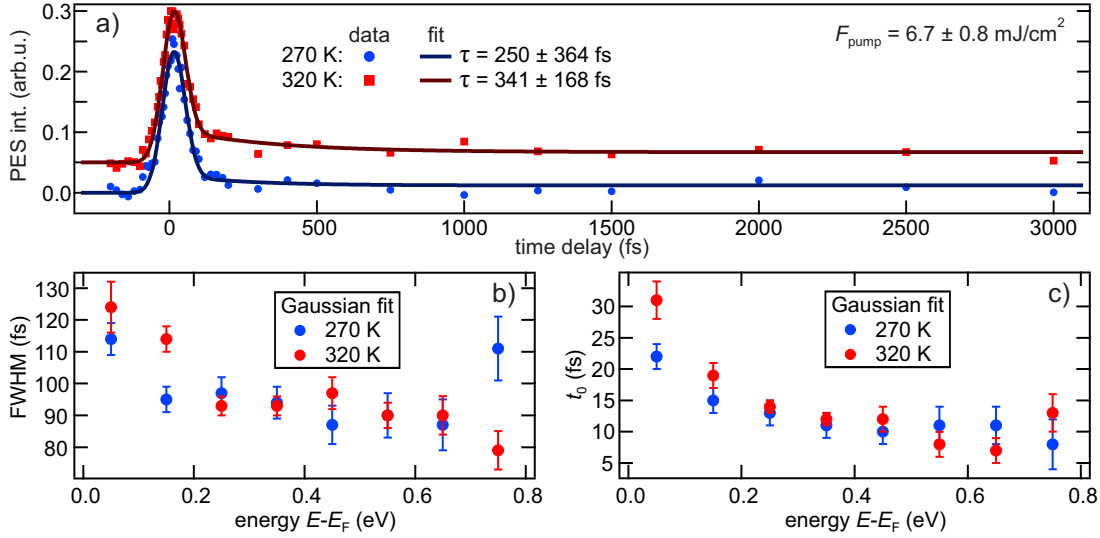
**Figure 4.35:** Pump-induced photoemission intensity change *above* the Fermi energy: a) integrated intensity in an energetic range between 0 and 400 meV above the Fermi energy for two sample temperatures and corresponding fits (The fit model is described in the main text). b) and c) show results of simplified fits by Gaussian functions for lineouts at various energies between 0 and 800 meV above $E_F$. In b) the FWHM and in c) the maximum position $t_0$ of the Gaussian function is displayed with respect to excess energy.

### 4.2.5 Relaxation dynamics in the transient metallic phase

In addition to the dynamics of the phase transition itself, i.e. the renormalisation of the bands leading to a closing of the insulating gap, the dynamics and relaxation of excited quasiparticle (electron) dynamics is investigated in this section. Therefore the focus is shifted from regions below to above the Fermi energy, where states are only occupied in a non-equilibrium situation or due to a Fermi-Dirac distribution at finite temperatures.

**Time-resolved 1PPE** Time-resolved photoemission data integrated over an energy interval between the Fermi-energy and 0.4 eV above (compare to Figure 4.27 a) for energetic reference) is shown in Figure 4.35 a) for sample temperatures of 270 K (blue) and 320 K (red). Least-mean-square-fitting has been performed to quantify average quasiparticle dynamics. The following response function was employed:

$$R(t) = D \cdot \delta(t) + \theta(t) \left( A \cdot e^{-t/\tau} + C \right) \tag{4.50}$$

The parameter $D$ is the amplitude of a delta-like distribution function capturing 2PPE via virtual intermediate states, $A$ is the amplitude of a decaying exponential and $C$ is a constant offset, due to occupied band structure changes leaking to energies slightly above the Fermi energy via the Fermi distribution function at finite temperatures. $\tau$ is the decay time constant of the exponential decay. Note, that a rising term is omitted, as including it prevents the fit from converging. This further confirms the instantaneous

nature of the gap collapse. $\theta(t)$ is a Heaviside function that ensures zero response before excitation. The fit is convolved with the laser pulses XC extracted at higher energies (see Figure 4.27 a)) to account for the time resolution of the experiment. The best fit is achieved for decay time constants $\tau$ of 250 fs (340 fs) for a sample temperature of 270 K (320 K). Unfortunately the standard deviations calculated by the fit routine are on the same order of magnitude. An average relaxation timescale on the order of hundreds of fs is therefore the only extractable information.

Performing these fits in an energy-resolved way (i.e. averaging over distinct, smaller energetic regions) is not possible, as the signal-to-noise ratio gets worse and prevents the fit algorithm from converging. To nevertheless catch a global trend, 100 meV wide energetic regions have been extracted and fitted with a simple Gaussian distribution function (Intensity $I(t) \propto e^{-(t-t_0)^2/\sigma^2}$). Lifetimes should shift the maximum position $t_0$ and increase the FWHM of the Gaussian curve.

The results for the fit parameters $t_0$ and FWHM are shown in Figure 4.35 b) and c). Again there is only a minor difference for measurements taken at temperatures of 270 K and 320 K. Both FWHM and $t_0$ increase with decreasing energy towards the Fermi energy. **This agrees with an increasing lifetime of quasiparticles (i.e. hot electrons), the smaller their excess energy with respect to the Fermi energy, compatible with e.g. Fermi liquid theory.** The minor difference for the two shown sample temperatures can be explained by the fact that in the band gap region of VO$_2$ the only *change* in photoemission signal is due to creation of the transient metallic phase. This corresponds to two different subsets of the sample showing slightly different transition temperatures, but exhibiting the same characteristic relaxation dynamics. This is in perfect agreement with the observed transition and hole relaxation dynamics below the Fermi energy, shown in the preceding Section (see Figure 4.33). The hot electron relaxation timescale is on the order of 100 fs, similar to the time constant for hole-equilibration and again in agreement with the appearance of equilibrium metallic response, which has been observed in reflectivity measurements (See Section 4.1.5).

**Time-resolved 2PPE**   To avoid intrinsically large background signal due to single photon photoemission, two-photon-photoemission experiments ($h\nu_{\text{probe}} < \Phi$) have been performed at a repetition rate of 200 kHz to investigate dynamics of unoccupied states explicitly. Average heating effects result in elevated sample temperatures at this repetition rate. Therefore, it has to be assumed that large sample portions are thermally metallic in these measurements. It will be shown that, although a pump pulse fluence of only 1 mJ/cm$^2$ (below threshold of the photo-induced phase transition) was used, signatures that can be related to the photo-induced phase transition are observed. A probable reason is the inhomogeneity of sample surface and photoexcited volume.

As a reminder Figure 4.36 b) shows a schematic energy diagram of the 2PPE process. Similar to the previous experiments, electrons are excited by an IR pulse ($h\nu_1$ = 1.55 eV, red arrow) from occupied (grey) states below to unoccupied (white) above the Fermi energy ($E_{\text{F}}$) of the metallic phase of VO$_2$. A time delayed (by $\tau$) UV pulse ($h\nu_2$ = 5.3 eV, blue arrow) probes the transient occupation of initially unoccupied states. Variation of $\tau$ captures the temporal evolution of this transient occupation.[54]

---

[54]See Section 3.2.5 for a detailed description.
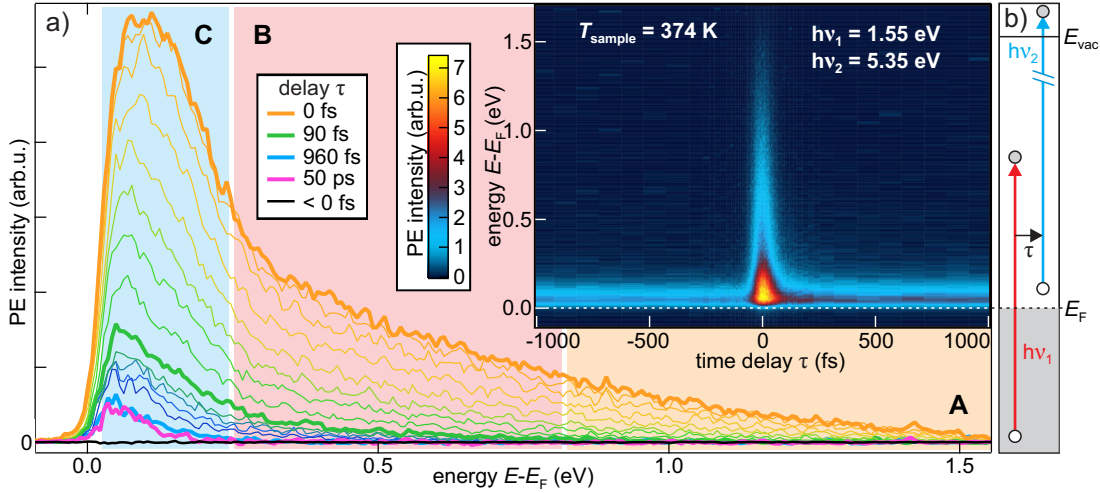
**Figure 4.36:** Time resolved 2PPE of unoccupied states in VO$_2$: a) The inset shows raw data. Vertical lineouts at different time delays are shown in the main figure. Regions **A**, **B** and **C** correspond to fast, intermediate and slow dynamics, respectively. b) Simplified pump-probe scheme for a). See main text for details.

The inset of Figure 4.36 a) shows the raw 2PPE data in a false colour scale on an intermediate energy scale and with respect to pump-probe delay $\tau$. The signal before $\tau = 0$ fs comes from thermally occupied states directly above the Fermi energy. This signal is constant for negative delays down to -50 ps and is integrated with respect to $\tau$ and used for background subtraction. The increased signal around $\tau = 0$ fs is due to hot electrons, excited in metallic VO$_2$. For positive delays the signal appears similar to the one before timezero, but slightly increased. Analysis in the time domain, i.e. of linouts along the delay axis, is not feasible, because the limited time resolution does not allow for robust fitting. Instead transient spectra at different delays $\tau$ are discussed in the following.

Figure 4.36 a) shows such spectra for various delays. At timezero (0 fs) the largest intensity is recorded, which decays for increasing $\tau$ on different timescales. The corresponding energetic windows are indicated by the coloured regions **A**, **B** and **C** (from right to left). In **A**, the intensity drops to zero after 90 fs already (thick green curve). The intensity in region **B** is zero before 960 fs (thick blue curve) and the intensity in the energetic window with the lowest excess energy persists on a significantly longer timescale, and does not even decay after 50 ps (thick pink curve).

The fast component at excess energies above 0.8 eV, which is not resolved in this specific experiment, either corresponds to very short hot electron lifetimes or residual 2PPE via virtual intermediate states in insulating parts of the sample[55]. Within the intermediate timescales, observed at excess energies between 0.25 to 2.75 eV, the 'lifetimes' increase gradually towards lower excess energies. **This trend agrees with the Fermi liquid theory prediction that quasiparticle lifetimes scale with the**

---

[55] Of course the elevated temperature of 374 K should guarantee a metallic sample, but deviations of stoichiometry and inhomogeneity can certainly lead to remaining semiconducting regions.

**inverse squared excess energy above $E_{\mathbf{F}}$, as expected for a metallic sample.**
The persistent increase in the direct vicinity of the Fermi energy could have various origins: Either it is due to residual photoinduced metallisation or at least an additional change of DOS within the metallic phase, or simply an increased temperature after electron thermalisation that leads to an increased Fermi tail, i.e. a change of thermal occupation above $E_{\mathrm{F}}$. The limited energy window and the limited knowledge about the shape of the DOS does not permit a further quantitative analysis of this Fermi tail.

**The time resolved spectroscopy of unoccupied states of VO$_2$ at elevated temperatures shows qualitative agreement with the expected metallic dynamics.**

### 4.2.6   Summary: Instantaneous band gap collapse in VO$_2$

Photoemission experiments have been performed to directly access the electronic band structure of VO$_2$. First, thermally induced changes were characterised to generate a baseline for the time-resolved studies of the photoinduced phase transition. A clear appearance of metallic density of states crossing the Fermi level is observed resulting in a Fermi-Dirac distribution-like high-energy cut-off.

When driving the PIPT, density of states is again generated in the band gap of the insulating phase within the pump laser pulse duration. This corresponds to an ultrafast photoinduced metallisation of VO$_2$, observed directly with unprecedented time resolution. An empirical model fit shows that the DOS is generated on a timescale of 30 fs, excluding a structural bottleneck timescale of 80 fs for the electronic transition. This is different to optical experiments in the saturation regime reported earlier [Cav04], which showed a structural bottleneck in the *dielectric* response.

Theoretical calculations confirm the idea of a purely electronic initial step for the phase transition: By promoting electrons from occupied to unoccupied states in the insulating monoclinic phase, similar to the initial photoexcitation in the experiment, a change of electronic structure is calculated that completely closes the band gap in VO$_2$, without any structural change. The origin of this band gap collapse is low-energy intraband transitions, mainly due to the photoholes in the valence-band that significantly increase the screening of the Coulomb interaction. This increased screening leads to a massive band gap renormalisation and a closure of the gap, a process that happens on electronic screening timescales of a few fs in the real system, in perfect agreement with the performed experiments.

Hot carrier relaxation (of electrons and holes) in the monoclinic band gap region confirm the instantaneous nature of the electronic phase transition further. The hot carriers decay on an average timescale of 100-200 fs. This corresponds to the time it takes after photo-inducing the phase transition, until the *optical response* (after additional photoexcitation, see Section 4.1.5) is similar to equilibrium-metallic phase. It also coincides with the timescale of incoherent conductivity changes, observed in [Pas11], which might originate from hot carriers in VO$_2$.

Further changes at later times after the photoinduced phase transition of the electronic band structure, i.e. due to changes in real space lattice structure are not observed.
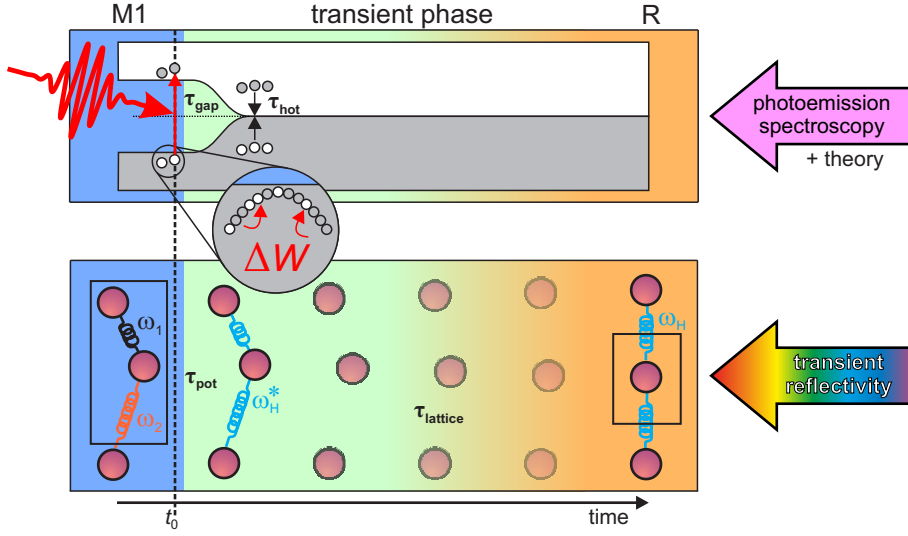
**Figure 4.37:** Ultrafast phase transition in VO$_2$, due to photoexcitation (at time $t_0$): band gap collapse on ultrafast screening timescales ($\tau_{\mathrm{gap}} \sim 3$ fs) and hot carrier thermalisation ($\tau_{\mathrm{hot}} \sim 100$ fs) is observed via photoelectron spectroscopy (top). Coherent phonon spectroscopy reveals (bottom) arbitrarily fast change in atomic potential energy landscape $\tau_{\mathrm{pot}} \to 0$ fs, long before the lattice reaches its equilibrium, high-temperature rutile structure ($\tau_{\mathrm{lattice}} <$ ns).

## 4.3 An new picture of the photo-induced, ultrafast phase transition in VO$_2$

VO$_2$, in spite of the simplicity of its chemical formula, represents a complex system with distinct peculiarities that concealed the nature of the underlying physics both experimentally and theoretically for nearly a century. Especially the photo-induced phase transition and its mechanism are subject of ongoing interest and discussion. The experimental and theoretical results, presented in the preceding chapters, help to clarify the nature of the initial steps after photoexcitation and therefore of the driving mechanism of the phase transition.

Figure 4.37 illustrates these findings: Strong photoexcitation (red arrow) in the monoclinic (M1) insulating phase at timezero ($t_0$) generates a transient non-equilibrium, metallic phase (green). Photoemission experiments (top part of the figure) show that the system undergoes a quasi-instantaneous ($\tau_{\mathrm{gap}}$) insulator-to metal transition upon laser excitation. Theoretical investigations reveal that especially the generation of holes at the top of the valence band (magnified in the circle), allows intraband transitions and changes the screening of the Coulomb interaction ($\Delta W$) to such an extent that the band structure is strongly renormalised. At excitation densities comparable to the photoemission experiments, the insulating gap in VO$_2$ is closed completely, turning the insulator into a metal. Therefore, screening timescales of a few femtoseconds define $\tau_{\mathrm{gap}}$. Subsequently hot electron and holes, within the energetic region of the collapsed monoclinic band gap, decay on an average timescale ($\tau_{\mathrm{hot}}$) on the order of hundreds of femtoseconds.

The all-optical experiments (bottom part of the figure) expose that the symmetry of the potential energy landscape that defines restoring forces on the ions, is changed upon photoexcitation and that this change happens increasingly early within the exciting laser pulse, when increasing the excitation density. Furthermore, the timescale at which the optical pump-probe response *of* the transient phase starts to get similar to the one of the equilibrium metallic phase coincides with the timescale of hot carrier decay $\tau_{\mathrm{hot}}$.

Combined, these results draw a comprehensive picture of the PIPT: The initial driving force is purely electronic, i.e. a photo-induced change of screening (magnified circle in Figure 4.37) is responsible for the electronic phase transition from insulator (blue) to metal (green). Contributions of the lattice structure to the initial photoinduced metallisation are neither needed (theoretically), nor observed (experimentally). At the same time, this change of the electronic structure, which defines the inter-atomic bonds, modifies the lattice potential and monoclinic symmetry (blue) is lost (green).

The optical excitation leads to an electronic band gap collapse and atomic potential symmetry change without a detour via the lattice structure, i.e. without a structural bottleneck. This of course does not mean that the lattice does not respond to the new potential energy landscape, both initially and on longer timescales. It is very likely that the lattice plays an important role in stabilising the metallic rutile phase, due to its increased temperature after thermalisation with the electronic subsystem. At later times ($\tau_{\mathrm{lattice}}$), the energy, deposited by strong laser excitation, is equilibrated throughout the system, which is then locked at the high temperature global potential minimum of the thermally rutile metallic phase (orange).

# 5 Screening and electron dynamics in two-dimensions: The SrTiO$_3$/vacuum interface

Recently, SrTiO$_3$ (STO) experienced attention in connection with the discovery of a two-dimensional electron gas (2DEG) at the interface of heterostructures with LaAlO$_3$ [Oht04]. This is remarkable, as both constituents are transparent insulators and nevertheless a high mobility 2DEG is formed at their interface.

The vacuum cleaved surface of STO also exhibits metallic states that are strongly localised in the surface normal direction, but delocalised within the surface plane. Such a 2DEG at the vacuum interface is easily accessible by photoemission spectroscopy [SS11, Mee11] and can act as a prototypical system to investigate effects of confinement and dimensionality on screening and carrier dynamics.

This work focusses on the *unoccupied* states at the STO surface and the carrier dynamics after optical excitation. Distinct final states are found with free electron like dispersion in the surface plane of STO. Excess energy-dependent electron scattering rates are extracted from time-resolved measurements that agree with 2D Fermi liquid theory predictions for the most part. Deviations are explained by the distinct band structure of the system. Furthermore, a transient photoinduced filling of the surface 2DEG via photoexcitation from in-gap states is observed and its temporal evolution is analysed. Such a control of the filling of the 2DEG by photoexcitation opens up new investigations into a system where the screening and thereby quasiparticle lifetimes could be transiently modified by light.

## 5.1 Vacuum cleaved and polished STO

Oxygen vacancies at the SrTiO$_3$ surface, acting as an effective electron donor into the Ti 3d manifold and leading to a downward band bending, are the most likely reason for the formation of the 2DEG [Aiu02]. Even at the vacuum-cleaved surface, Oxygen vacancies seem to be present in a sufficient amount, such that a 2DEG is generated. While cleaving or fracturing is a very convenient way of surface preparation, it does not produce a macroscopically flat surface of STO, due to the lack of a preferred cleaving-plane in its cubic crystal structure.

In Figure 5.1 a), a magnified optical image of the cleaved STO surface is shown. The sample height of 0.5 mm is indicated. Different regions reflecting light in various directions can be distinguished, indicative of varying surface orientations. Typical laser-spot diameters between 50 and 100 $\mu$m (FWHM) will therefore likely lead to photoemission spectra that average over a certain distribution of surface normal directions. This can potentially smear out angle-resolved measurements.

Another complication is the rather low speed of emitted photoelectrons, when using low photon energies. Electric fields are enhanced by the rather sharp edges of the cleaved sample, which seem to influence photoemission spectra. Especially at the low-energy cut-off, the photoemission spectra are strongly distorted.

To ensure comparability with previous high-resolution ARPES measurements [SS11,

**Figure 5.1:** Optical microscope image of the cleaved STO surface. Various facets and a slightly bent surface is visible at this particular sample. The fracturing is most inhomogeneous at the sample edges (dotted line). The sample height of 0.5 mm is indicated.
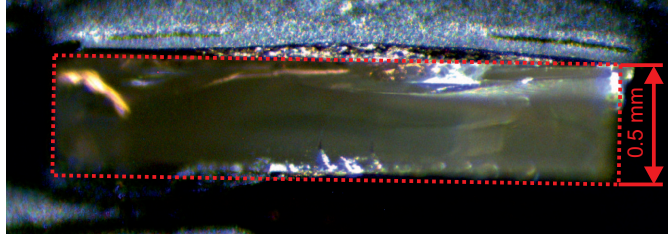


**Figure 5.2:** Spectroscopic signature of metallic 2DEG in different samples: polished (green) and exemplary cleaved (red, blue). For comparison a fit of a broadened Fermi-Dirac distribution to the green spectrum is shown (black dashed line).
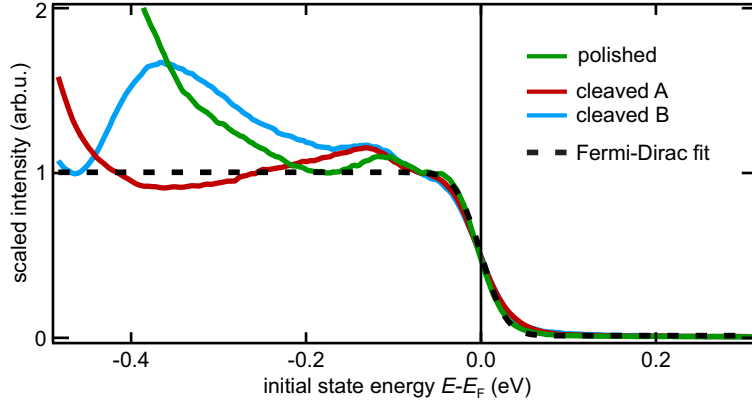


Mee11] and at the same time improve on the described problems, cleaved and polished samples (supplied by SurfaceNet GmbH) were compared by photoemission spectroscopy and low energy electron diffraction (LEED) measurements[56]. As the surface of polished STO samples is contaminated during polishing and storage, a cleaning procedure is performed. To generate a clean STO surface, showing similar properties as cleaved STO, the sample was kept at a temperature of 900 K for one hour until no charging (i.e. rigid shift of photoemission spectra with illumination time) was observed any more.

In Figure 5.2, angle-integrated photoemission spectra are compared for a polished (green) and two exemplary cleaved samples (red and blue). To compare the existence of the metallic 2DEG an energetic window around the Fermi energy is chosen. The spectra are normalised at -70 meV below the Fermi energy. The black dotted line is a least-mean-square fit to the green curve. Clearly a experimentally broadened Fermi-Dirac distribution describes the high energy cut-off of all the three spectra very well. The deviations in terms of density of states are most likely due to differing secondary electron background and possibly different amount of band bending due to a varying oxygen vacancy density. Nevertheless a metallic electronic structure is found in cleaved as well as polished and annealed STO surfaces.

To confirm the validity of treating polished and cleaved samples on even grounds further, the surface crystal structure has been compared via LEED. Electron diffraction patterns are shown in Figure 5.3 for a) cleaved and b) polished and annealed sample, using 92 eV primary electron energy. A qualitative analysis shows that the patterns

---

[56]In fact the most recent studies regarding the 2DEG on STO have used polished, etched and ex-situ annealed samples [SS14, Plu14]. Different surface treatments (annealing temperatures) did not affect the 2DEG-signatures [Plu14].
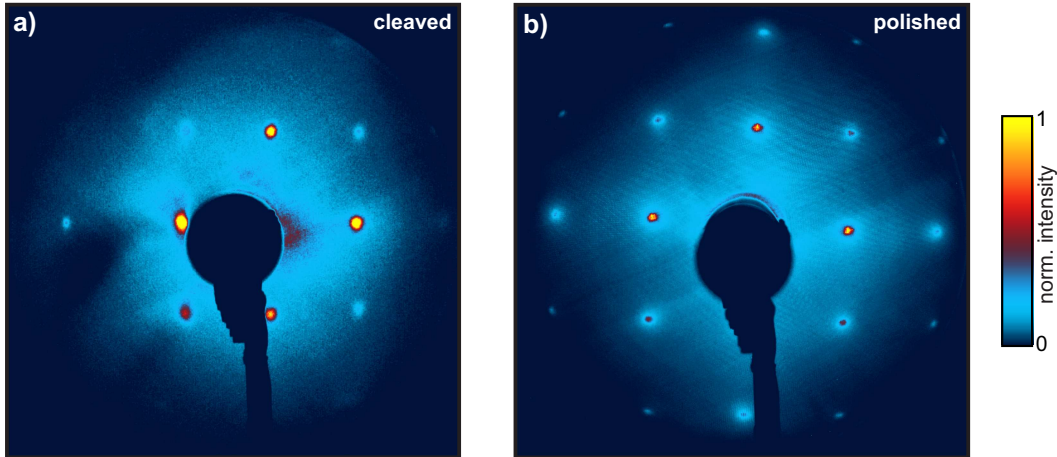
**Figure 5.3:** Qualitative comparison of LEED images for a) cleaved and b) polished and annealed STO surface: Diffraction spots exhibit expected cubic symmetry in both cases.

exhibit the same symmetry (cubic) and indicate the same lattice constant. The pattern originating from the polished and annealed sample exhibits sharper diffraction spots and less inelastic background intensity. Furthermore, higher diffraction orders are more clearly visible, than for the fractured surface.

The crystallinity of the polished sample seems to be homogeneous over a larger spatial extent, than of the fractured sample, as already suggested by the optical microscopy image. The employed electron energy of 92 eV leads to the shortest possible mean free path according to the fundamental curve (see Figure 3.9) and therefore is most surface sensitive. There is no indication for surface reconstruction [Shi12] in the presented LEED patterns.

Photoemission spectroscopy and LEED pattern show that both, lattice and electronic structure at the STO vacuum interface, do not significantly differ for cleaved and annealed samples. This is confirmed by the independence of the 2DEG electronic structure on different sample treatments (annealing temperature, oxygen background pressure) [Plu14] and different bulk dopings [SS11]. Most of the following evaluation has therefore been studied on the polished and annealed STO single crystal, as it is better suitable for low-energy photoemission spectroscopy.

## 5.2   Unoccupied states at the STO(001) surface

The clear metallic signature on insulating STO, already shown in Figure 5.2, confirms the presence of electrons close to $E_{\mathrm{F}}$. The following sections will first show that low photon energies are sensitive to unoccupied final states above the vacuum energy and that the structure of presented photoelectron spectra are dominated by those. After that, the dispersion of two distinct final state bands is analysed, yielding effective masses on the order of $m^* = 2m_e$.

As a first step towards the investigation of dynamics of the 2DEG at the STO surface, distinct changes of photoelectron spectra upon variation of the incident fluence are presented at the end of this section.
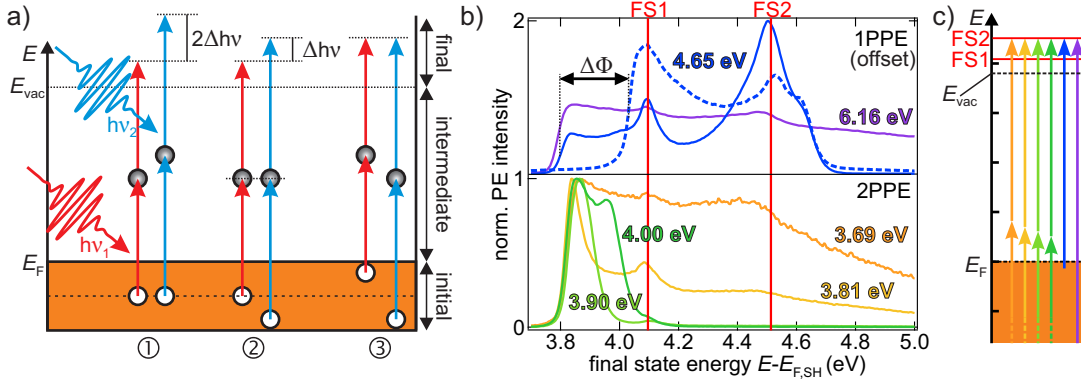
**Figure 5.4:** Final states in STO: a) different excitation schemes for ① initial, ② intermediate and ③ final states for different photon energies $h\nu_1/2$. b) Single colour one- and two-photon-photoemission spectra of STO with respect to final energy axis. Final states FS1 and FS2 are indicated by the red and blue solid lines. c) Single- and two-photon photoemission energetics of b): arrows correspond to the spectra in b) by their respective colour.

**Final state effects**  Photon energy dependent photoemission spectroscopy can distinguish between initial, intermediate and final state effects on spectral intensity distributions. As a reminder, a schematic representation of these three cases is shown in Figure 5.4 a) for single colour two-photon-photoemission with two different, exemplary photon energies $h\nu_1 < h\nu_2$. Initial states ① shift with twice the photon energy difference $\Delta h\nu$, as two photons probe the state via virtual intermediate states. Intermediate states ② are populated by one and probed by the second photon, therefore they shift with one times the photon energy difference $\Delta h\nu$. Final states ③, on the other hand, do not shift at all when varying the photon energy.

In Figure 5.4 b), photoemission spectra for various photon energies between 3.69 and 6.16 eV are shown. A final state energy axis is used with respect to the Fermi energy of the sample holder $E_{\mathrm{F,SH}}$. As the photon energy is tuned across the sample work function $\Phi = E_{\mathrm{vac}} - E_{\mathrm{F}}$ single- and two-photon photoemission (1PPE and 2PPE) spectra are recorded. 1PPE spectra are offset for clarity. Two states can clearly be identified in most of the spectra, indicated by the red vertical lines and denoted FS1 and FS2. They both appear at a constant energy on a final state energy axis, with slight deviations due to the change in secondary electron background intensity or minor shifts due to e.g. a voltage drop between sample holder and sample[57]. FS1 (FS2) resides approximately 4.1 eV (4.5 eV) above the Fermi energy.

For intermediate (initial) states, a shift of 310 meV (620 meV) would be expected, when changing the photon energy from 3.69 (orange) to 4.00 eV (dark green). This is clearly not the case, confirming the final state character of the observed spectral features. Furthermore, a change of work function due to anomalous preparation or ageing of the sample does not affect the final state energy position with respect to the Fermi-energy of the 2DEG. The two spectra probed with 4.65 eV (dashed and solid

---

[57]For discrete states, degenerate with bulk continuum bands quantum interference in the context of Fano's model [Fan61] might explain intensity variations that also might appear as shifts, when tuning across a resonance between 2DEG and final states [Eic11]. Due to the limited number of spectra and some uncertainty with respect to incident fluence a systematic analysis in this context is not possible.
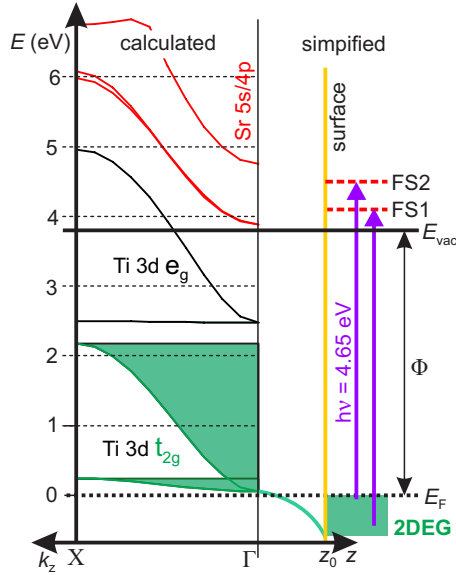
**Figure 5.5:** Resonant photoemission via final states: This illustration is based on bulk band structure calculations (DFT using hybrid functional HSE06 from [EM11]) between $\Gamma$ and X on the left. The simplified photoemission scheme from initial state 2DEG below the Fermi energy $E_F$ (green) and quantised final states (red) that lie energetically in the region of the Sr $5s$ bands. Resonant photoexcitation from initial 2DEG to these final states above the vacuum level $E_{vac}$ is achieved with a photon energy $h\nu = 4.65$ eV. Note the reciprocal and real space axes.

blue) for example, show a different low energy cut-off energy. The difference is due to a change in work function $\Delta\Phi > 300$ meV. Nevertheless the energetic positions of the two final states remain constant. **Two final states are found, which lie 4.1 and 4.5 eV above the Fermi level and are energetically pinned to it.**

The energetics of the photoemission process for the different photon energies are depicted in c), where the arrows correspond to spectra in b) by their respective colour. Clearly the 1PPE process (only one arrow) can be distinguished from the 2PPE process via intermediate states (two arrows) in this simplified energy diagram.

The enhanced appearance of the final state signatures for the photon energy of $h\nu = 4.65$ eV (blue spectra) can be explained by a resonance effect. This is illustrated in Figure 5.5. The calculated band structure from [EM11] in $\Gamma$-$X$ direction (see Section 2.3 for reference) is displayed on the left. In the middle, the surface band bending region is indicated by downward bent bands (sample surface at $z_0$). Below $E_F$, 2DEG states (blue) that are localised at the surface and originate from the Ti $3d$ $t_{2g}$ manifold are shown. Absorption of $h\nu = 4.65$ eV photons excites electrons above the vacuum level in the vicinity of Sr $5s$ bands, which are modified by the surface band bending as well. This modification could either result in quantised sub-bands, as proposed in [SS11, Mee11], or a lifted degeneracy of the Sr $5s$ bands at the $\Gamma$ point and thereby lead to the two distinct final states FS1 and FS2. Taking into account a certain uncertainty of the underlying band structure calculations with respect to absolute energies, the two bands could also stem from the two separated Sr band manifolds (red), or even be unrelated to these bulk bands.

The resonant character of this excitation at $h\nu = 4.65$ eV is a clear indication that these final state bands are localised at the surface, similar to the 2DEG, because if they were not, a dispersion in $k_z$ direction (perpendicular to the surface) would lead to a photon energy dependent shift of the resonance, i.e. of the final state energetic position.

For the other photon energies $h\nu$ (shown in Figure 5.4 c)) that are smaller than
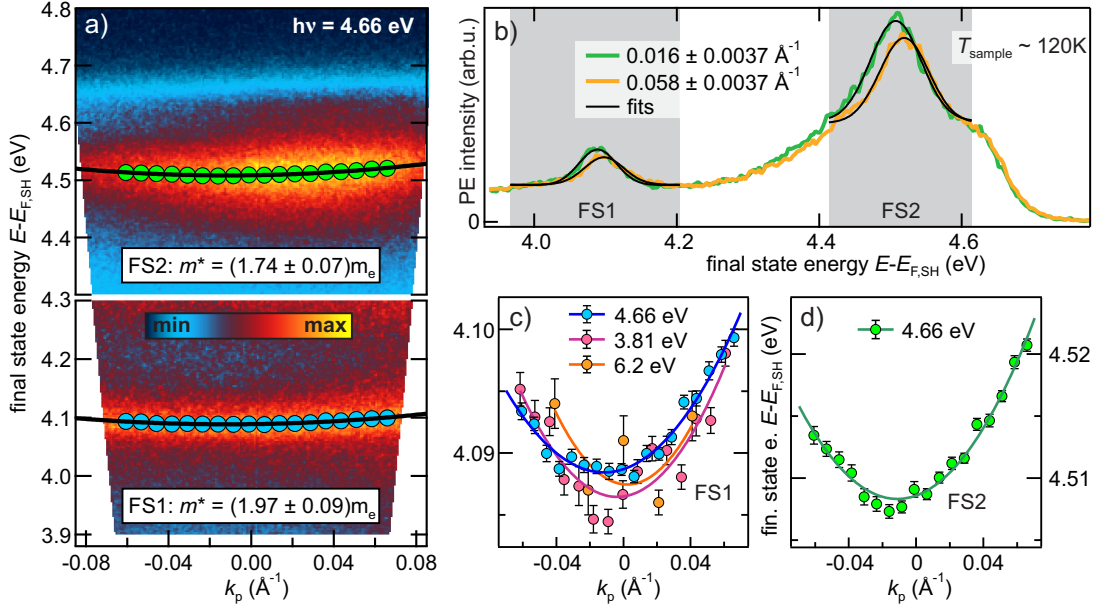
**Figure 5.6:** Dispersion of final state bands in STO: a) Photoemission intensity in false colours with respect to kinetic energy and $k_p$. Upper and lower portion of the Plot have different colour scales. b) Exemplary energy distribution curves (EDCs) from a), for a parallel component of electron wavevector $k_p = 0.016$ and $0.058$ $^{-1}$. Gaussian fits of states FS1/2 (black curves) and fit intervals (grey shaded area) are indicated. Peak position of FS1 from Gaussian fits of EDCs at various $k_p$ are shown in c), also for photon energies of 3.81 and 6.2 eV. d) shows FS2 peak positions. Parabolic fits (solid lines) yield effective masses $m^*$ indicated in a) and given in the main text.

the sample work function ($\Phi \sim 3.8$ eV) a non-resonant two-photon process and for $h\nu = 6.16$ eV a non-resonant one-photon process leads to photoemission at the final state energies, hence the lower peak-to-background ratio. The initial states are in both cases located in the band gap of STO, i.e are defect or in gap states, as mentioned in Section 2.3). In the following, the dispersion of the final states within the surface plane of STO is analysed in detail.

Figure 5.6 a) shows photoemission intensity with respect to final state energy $E - E_{F,SH}$[58] and momentum component parallel to the emitting surface $k_p$ (corresponds to the $\Gamma$-$X$ direction in the cubic Brillouin zone) encoded in a false colour scale. The photon energy for photoemission was $h\nu = 4.66$ eV. The high energy cut-off (at 4.66 eV) corresponds to the Fermi energy of the 2DEG, while two distinct dispersive final states, FS1 and FS2, are visible at lower energies. As determined in the previous section, the final states lie approximately at 4.1 (FS1) and 4.5 eV (FS2) above the reference Fermi energy at the $\Gamma$-point.

To analyse the dispersion of the two final state bands, energy distribution curves (EDCs, i.e. photoemission spectra) at various $k_p$ are extracted from a) and the energetic position of FS1 and FS2 is determined. Two exemplary EDCs (green and orange) and simple Gaussian peak fits for FS1 and FS2 (black lines) are shown in b). The

---

[58]The Fermi level of the sample holder $E_{F,SH}$ was used as a reference.

background is considered to be constant over the fit range to minimise systematic errors when fitting. Fits are performed only in the vicinity of the respective peaks, as indicated by the grey shaded regions. The centre position of FS1, as determined by those fits, are shown in c) (blue markers) with respect to the $k_p$ of the corresponding EDC. A similar analysis of peak positions has been performed for photon energies of 3.81 and 6.2 eV (pink and orange markers) for comparison. The analogue analysis of FS2 leads to the dispersion shown in d). The error bars in each case are the standard deviation of the Gaussian peak position, calculated by the fitting routine. To quantify the dispersion in a quasi-free electron model, a simple parabolic relation, corresponding to

$$E = \frac{\hbar^2 k_p^2}{2m^*} \tag{5.51}$$

is used to fit the data. $m^*$ is the effective electron mass, which is a measure for the localisation of the band. For $m^* = 1$ the dispersion corresponds to that of a free electron. The fit based on 4.66 eV data, i.e. the blue curve in c) and the green curve in d), yield $m^* = (1.97 \pm 0.09) \times m_e$ for FS1 and $m^* = (1.74 \pm 0.07) \times m_e$ for FS2 ($m_e$ is the free electron mass). The extracted peak positions from the other datasets (with $h\nu = 3.81$ and 6.2 eV) exhibit larger error bars and deviations from the parabolic fit, because the peak-to-background ratio in the corresponding EDCs was lower. Nevertheless the values of $m^* = (1.48 \pm 0.13) \times m_e$ (for $h\nu = 3.81$ eV) and $m^* = (1.2 \pm 0.8) \times m_e$ (for $h\nu = 6.2$ eV) agree well with the ones extracted from the 4.66 eV data.

For comparison, the free electron masses of the light 2DEG bands found in [SS11] are $0.7 \times m_e$ and in [Mee11] $0.5 \times m_e$. The final states observed here, are slightly less delocalised (in plane) than the 2DEG bands.

In conclusion, the final states FS1 and FS2 exhibit the following properties:

① they do not shift with photon energy

② they are resonantly excited from initial states (using $h\nu = 4.65$ eV photons) that are localised in $z$ direction (the 2DEG) or

③ they are non-resonantly (i.e. involving phonons) excited from initial states within the STO band gap (defect states or vacancy induced IGS), i.e. localised states.

④ they are delocalised in the surface plane and exhibit effective masses in the range of 1 to 2 times the free electron mass $m_e$

⑤ their energetic position is pinned to the Fermi energy rather than the vacuum level.

The resonant character and the fact that the final states do not shift with photon energy (① and ②) indicate that they are also localised in the z-direction, similar to the 2DEG in STO, because otherwise for different photon energies, different resonances between non-dispersive initial and dispersive final state would be observed [Dam04]. The effective masses are ($1$-$2m_e$), heavier than the 2DEG states but similar to the lightest bulk effective masses of $1$ $m_e$ [Mee11]. **In conclusion, two distinct final**
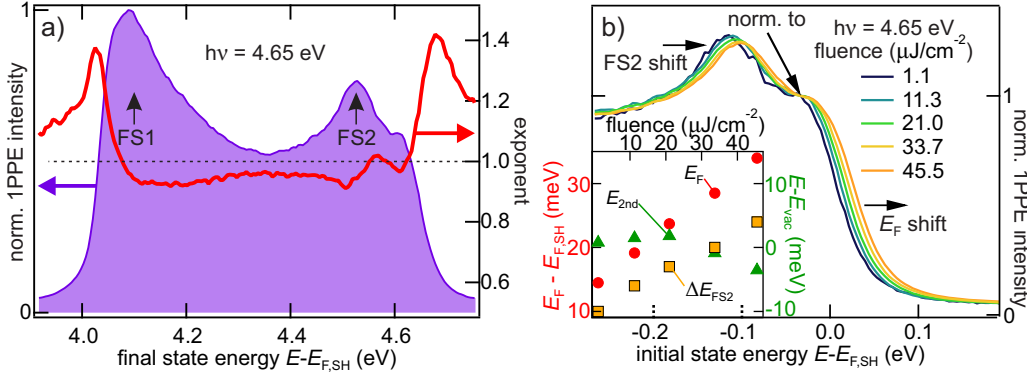
**Figure 5.7:** Fluence dependent 1PPE (h$\nu$ = 4.65 eV) on STO: a) Exemplary angle integrated 1PPE spectrum with final state FS2 (purple) and exponent of power law fit for each energy (red) from fluence dependent measurements. b) Fluence dependent shift of Fermi edge. The inset shows a linear increase of Fermi edge position (red circles) with fluence, while the low-energy cut-off (green triangles) of the spectra does not show a similar trend.

**states are found that are delocalised within the surface plane but are non-dispersive perpendicular to it. They are energetically pinned to the surface Fermi level.** Over the angular range of the the measurements ($\pm 7°$) the dispersion is energetically small ($\sim 10$ meV), therefore from now on angle integrated spectra are presented for simplicity.

Figure 5.7 shows the impact of the photon density on the photoemission spectra. An exemplary spectrum (purple) is displayed in a) on a final state energy axis, using the Fermi energy of the sample holder $E_{F,SH}$ as a reference. The low energy cut-off of the spectrum corresponds to the position of the vacuum level with respect to the reference Fermi energy. Therefore, the work function is $\Phi = 4.03 \pm 0.01$ eV, and FS1 is partially cut off by the low energy edge of the spectrum. As expected, FS2 is visible at an energy of $\sim 4.5$ eV above the Fermi energy.

Photoemission intensities $I$ for various incident fluences $F$ have been analysed in an energy resolved manner by a power law fit $I(F,E) \propto F^{x(E)}$. The extracted exponent $x(E)$ is the solid red line in a). It only deviates strongly from the expected linear power dependence (single photon photoemission process) at the edges of the spectrum. These deviations are due to changes of the shape, rather than the intensity, of the spectra with fluence.

The most prominent changes of spectral shape are found in the vicinity of the Fermi edge, as shown in Figure 5.7 b). When increasing the incident fluence from 1.1 to 45.5 $\mu$J/cm$^2$ the position of the Fermi edge shifts by $\sim 30$ meV. The results of a quantitative analysis of the edge positions, by finding the energetic position at half-maximum of the edge, and FS2 peak position, by fitting with a Gaussian, are displayed in the inset and compared with the low-energy cut-off position. The position of the Fermi edge $E_F$ is displayed with respect to the Fermi energy of the sample holder $E_{F,SH}$, measured separately. The low energy, or secondary electron cut-off position $E_{2nd}$ is displayed with respect to an average value $E_{vac}$ and the change in FS2 peak position $\Delta E - FS2$ is shifted to match the energy scales of $E_F$ and $E_{2nd}$. Clearly $E_F$ and $\Delta E_{FS2}$ exhibit a linear shift with fluence, whereas $E_{2nd}$ does not show any systematic trend,
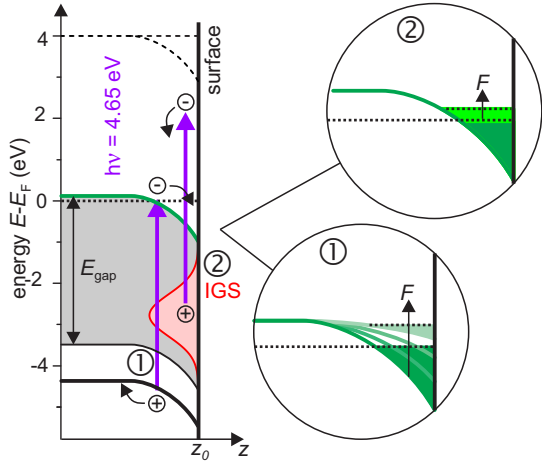
**Figure 5.8:** Possible origins of photon density dependent shifts in STO: Above band gap excitation (photon energy:  $h\nu$  =  4.65 eV) leads to surface photo voltage effect and counteracts band bending ①, effectively shifting the 2DEG Fermi level (and the entire PE spectrum) to higher energies. Photoexcitation from in gap states (IGS) into the 2DEG via intermediate excited states ② leads to a transient increased filling of the 2DEG, i.e. a Fermi level shift, without any effect on the over PE spectrum.

i.e. is constant within the experimental resolution. Linear fits yield shifts of $(305 \pm 15)$ and $(435 \pm 9))$ $\frac{\text{eV}}{\text{J/cm}^2}$ for FS2 and $E_F$ respectively.

To rationalise the origin of these shifts, several effects that are driven by 4.65 eV photons are discussed in the following and illustrated by Figure 5.8:

① a transient surface photo voltage (SPV) shift (Figure 5.8 ①): electron-hole pairs are generated via above band gap (grey region) excitation and are subsequently separated by the potential gradient in the surface band banding region. This counteracts the band-banding, leading to flat bands in the limiting case. The apparent Fermi energy of the surface 2DEG would thereby be shifted to higher energies with increasing light fluence $F$.

② a transient filling of the 2DEG from defect or in-gap states (IGS, red), localised at the surface (Figure 5.8 ②). As both 2DEG and IGS are localised at the surface no charge separation is expected. A transiently increased filling of the 2DEG would nevertheless up-shift the apparent Fermi level position with $F$ and possibly the final states, as they are pinned to $E_F$.

③ vacuum space charge effects would lead to an overall broadening of the photoemission spectrum that could be misinterpreted as an energetic shift.

Surface photo voltage effects (①), i.e. transient photoinduced relaxation of surface band-bending, usually result in a rigid shift of the photoemission spectrum [Ret12], which is clearly not observed here, because the low-energy cut-off does not shift.

Broadening and shift of a Fermi edge due to vacuum space charge effects (③) in laser based solid-state photoemission spectroscopy have been observed and characterised before [Gra10]. The lack of a clear shift of the low-energy edge on the same order of magnitude as that of the Fermi edge suggests a different origin. On the other hand it is not clear how vacuum space charge affects specific signatures in photoemission spectra. In [Hel09] detailed investigations have been performed and indicated that a complex interplay between different experimental parameters defines the character of the space charge broadening. Interestingly a stronger broadening and shift is predicted for electrons with larger kinetic energies, which would explain the observed difference between

low- and high-energy cut-off qualitatively. More detailed arguments and estimates of the number of photoemitted electrons are given in Appendix F for this specific case and summarised here:

The worst case scenario yields 1300 electrons per $\mu$J/cm$^2$, while a more realistic estimate yields 13 electrons per $\mu$J/cm$^2$. Assuming that the shift in Figure 5.7 b) is purely a vacuum space charge effect and comparison with [Gra10], yields 2000 emitted electrons per shot for the highest fluence of 45 $\mu$J/cm$^2$, i.e. 44 electrons per $\mu$J/cm$^2$. This is clearly less then the unrealistic worst case, but slightly higher than the more optimistic estimate. Space charge broadening can therefore not be excluded as a possible reason of the observed shifts.

A transient photoinduced filling of the 2DEG from defect or IGS (②) would increase the effective Fermi energy position, but not affect the work function. This is due to the lack of charge separation, because electron hole pairs are generated and stay within the surface region (The surface oxygen vacancy induced IGSs are located at the surface).

While it is not possible to decide whether vacuum space charge effects ③ or a transient filling ② lead to the observed phenomena (a mixture of both is also possible), the lack of a shift of the low energy cut-off slightly favours the latter effect. Time-resolved data, presented later will confirm this assessment.

In the following, time-resolved photoelectron spectroscopy is used to shed light on this question. Two-photon photoemission experiments yield a higher contrast between uncorrelated background signal and transiently populated electronic states, as energetically only the latter ones are probed. The overall electron yield is usually a lot smaller than for 1PPE [Fau94]. Vacuum space charge effects are therefore not expected to affect those measurements significantly at the employed fluences.

## 5.3 Hot electron dynamics in STO

Usually hot electron decay in metals, due to electron-electron scattering with rate $\Gamma_{\text{e-e}}$, can be approximated fairly well by Fermi liquid theory (FLT) [Her96, Kno96, Oga96, Oga02]. Predicted electron scattering rates scale with the quadratic excess energy with respect to the Fermi level: $\Gamma_{\text{e-e}} \propto (E - E_{\text{Fermi}})^2$ [Pin66, Qia05] (compare Equation 2.2). A quantitative deviation from this scaling law in real systems is expected, as screening and phase space is modified by the band structure of real solids. For example d-bands enhance screening and thereby increase lifetimes in Cu [Cam99], while they provide increased phase space for scattering in the vicinity of the Fermi level in Ta, resulting in shorter quasiparticle lifetimes [Kno96].

Fermi liquid theory also predicts a deviation of this scaling law for two-dimensional systems. Due to the competition of lower phase space for scattering (decreased scattering rate) and less efficient screening of the Coulomb interaction (increased scattering rate) a small, logarithmic correction is added.[Giu82, Qia05] (compare Equation 2.4).

In this section, effective hot electron lifetimes at the STO/vacuum interface are analysed and compared to FLT. In Figure 5.9 a), time- and energy-resolved 2PPE data of the annealed STO surface, recorded at a sample temperature of $T < 120$ K, is shown. As illustrated in b), electrons of the 2DEG and in-gap states are excited by $h\nu_{\text{pump}} = 1.54$ eV photons (red arrows) and populate unoccupied states. The population is probed by photons with energy $h\nu_{\text{probe}} = 3.86$ eV (blue arrow) and
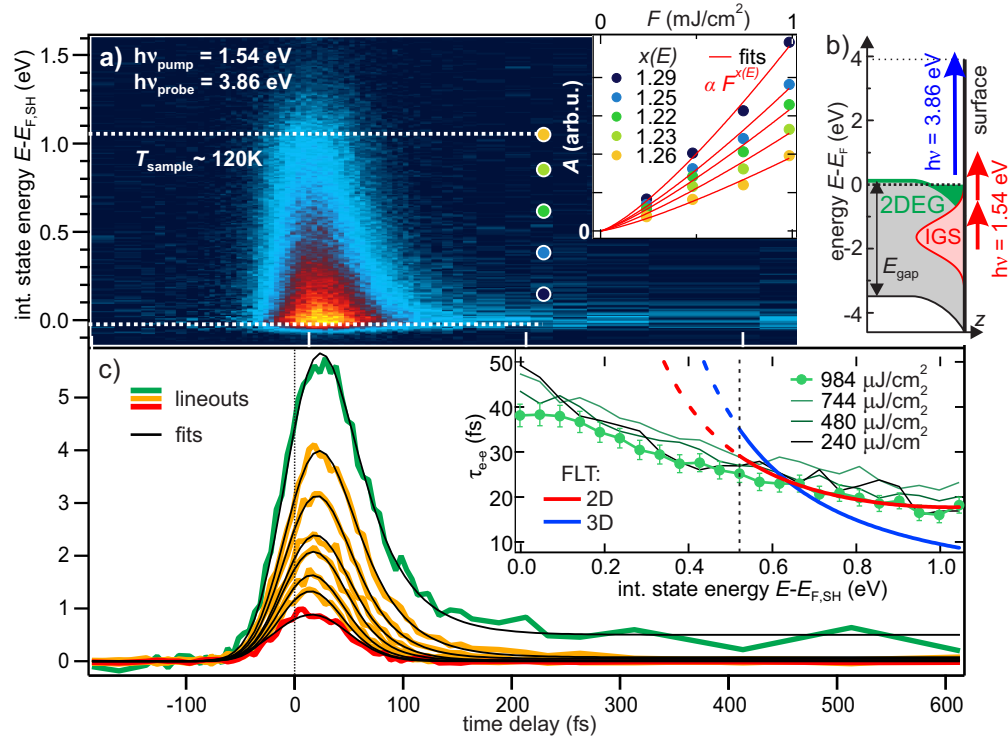
**Figure 5.9:** 2PPE intensity with respect to time delay and intermediate state energy is encoded in a false colour scale in a) and pump-fluence dependence of photoemission intensity is displayed in the inset. The diagram in b) illustrates energetics of photoexcitation ($h\nu = 1.54$ eV) and probing ($h\nu = 3.86$ eV) (see main text for details). Exemplary lineouts and corresponding fits (described in the main text) are shown in c). The resulting effective hot electron lifetimes with respect to excess energy (green) and fits are displayed in the inset of c).

decays towards positive delay times. The asymmetric shape in a) indicates that the population is longer lived, the lower the excess energies with respect to the Fermi level gets, in qualitative agreement with FLT predictions. For further quantitative analysis, horizontal lineouts at various energy intervals in equidistant steps between the white dashed lines have been extracted and characterised by a fit model, based on simple rate equations. Exemplary lineouts are shown in Figure 5.9 b) with their respective fits (black). The fit model consists of the response function $R(t)$ convolved with a Gaussian pulse XC. The response function is assumed to be:

$$R(t) = \theta(t)(Ae^{-t/\tau_{\text{e-e}}} + C) \tag{5.52}$$

The single exponential decay with amplitude $A$ quantifies an effective electron lifetime $\tau_{\text{e-e}}$. This effective lifetime is an upper limit for the real quasiparticle lifetimes, which would require analysis via optical Bloch equations [Kir09]. The Heaviside-$\theta$ function prohibits response before timezero and the constant offset $C$ is necessary to capture a persistent signal increase directly above the Fermi energy, which will be discussed separately in Section 5.4.1.

Although the pulse duration and exact timezero (temporal overlap between both laser pulses) was not determined independently, fits of various lineouts with *all* fit parameters free (including the laser pulse width and timezero) yielded consistent values for timezero and a clear fit optimum for a laser pulse XC width of FWHM$_{\text{XC}} = (61.5 \pm 0.8)$ fs (i.e. an average pulse duration of 44 fs).

Before focusing on the quasiparticle lifetimes, the behaviour of the amplitude $A$ with respect to infrared-pump (IR-pump) fluence is evaluated: The exponent $x(E)$ of the power-law $A(F, E) \propto F^{x(E)}$ with fluence $F$ is characteristic for the order of the initial photoexcitation process into the unoccupied states ($E - E_{\text{F}} > 0$). To find the excitation order, the dataset from a) was recorded for three additional IR-pump fluences. Based on these, overall four, datasets, the inset in a) shows the fluence dependence of the fit amplitude $A$ for lineouts at energies indicated by round markers in a) with the respective colour. Power law fits (red) yield an exponent between 1.2 and 1.3 for all energetic positions. The non-integer exponent points to a mixture of single and two photon processes for the dominant IR-excitation pathway. As indicated by the red arrows in Figure 5.9 b), single and two photon processes correspond to excitation of electrons from initial states *within* the band gap (grey shaded), because one (1.54 eV) and two (3.08 eV) times the photon energy is both smaller than the indirect band gap of 3.25 eV (the direct gap is even larger with 3.75 eV). **This means that the initial states, which are photoexcited by the IR-pump pulse, originate from within the band gap of STO, i.e. from in-gap states (IGS) or the 2DEG.** Transient surface photovoltage shifts require above band gap excitation and are therefore never induced by these IR-pump pulses.

The inset of c) shows the effective lifetimes $\tau_{\text{e-e}}$ of hot electrons with respect to excess energy $E - E_{\text{F,SH}}$ for various incident pump fluences (green to black curves). Effective lifetimes do not significantly depend on excitation density, as there is no clear trend for the different fluences. For excess energies $> 0.5$ eV an adequate fit by 2D FLT (Equation 2.4, red curve) is possible (the start of the fitted interval is indicated by the dashed line), yielding electron density of $n_{\text{2D}} = 3.5 \times 10^{18}/\text{m}^2$ (as the *only* fit parameter). A fit with 3D FLT (Equation 2.2, blue curve) in the same energy interval
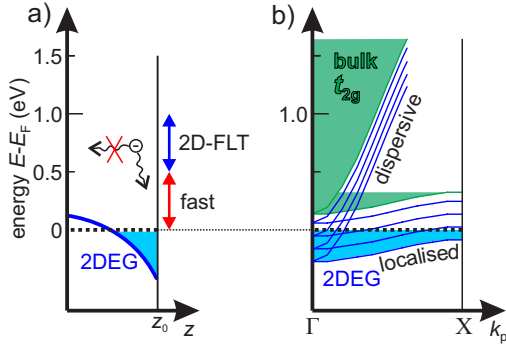
**Figure 5.10:** a) Different regimes of scattering rates: above $E - E_F > 0.5$ eV the rates are described well by 2D-FLT (blue). Increased rates below $E - E_F = 0.5$ eV deviate from 2D FLT, i.e. quasiparticles decay faster (red). b) Shows strongly dispersive and more localised components of bulk band-structure (green) and indicated bent $t_{2g}$ band of the 2DEG (blue) in order to explain this deviation (see main text for details).

does not agree well with the data. The extracted $n_{2D}$ from the 2D-fit agrees well with the value of $2 \times 10^{18}/\text{m}^2$ determined from the Fermi surface area in [SS11].

**The scattering rates of hot electrons at excess energies $> 0.5$ eV are explained well by electron-electron scattering in the framework of 2D-FLT**, even though the 2DEG bands are energetically degenerate with the bulk conduction band.

The deviation from FLT predicted curves (2D and 3D) at lower excess energies (i.e. $E - E_F < 0.5$ eV) is significant and discussed in the following. Figure 5.10 a) sums up the observations at the surface region of STO: Above $E - E_F = 0.5$ eV 2D FLT behaviour is observed (blue), while at lower energies deviations towards higher scattering rates ($\tau_{e\text{-}e} \sim 40$ fs) are observed (red).[59]

To explain the deviations at low excess energies, the band structure of STO is shown in Figure 5.10 b). The 2DEG (blue) originates from the bulk $t_{2g}$ manifold (green). The downward band bending towards the surface is indicated by the exemplary replica (dark blue curves). At high excess energies, only the strongly dispersive, free-electron like band contributes, resulting in the good agreement with 2D-FLT. At lower excess energies the less dispersive, more localised band contributes in addition. Therefore, the density of states is suddenly enhanced, which means that the phase space for scattering is increased within this energetic region. **This increased phase space for electron-electron scattering explains the observed increased scattering rates [Kno96] at low excess energies.** Electron-phonon scattering can, of course, also contribute, but is not necessary to explain the observed quasiparticle lifetimes in the 2DEG at the STO surface.

In summary, the investigation of hot electron population dynamics, directly probed by 2PPE, yields good agreement with 2D-FLT for excess energies $E - E_F$ above 0.5 eV. The deviation from FLT at lower excess energies can be described by the increased phase space for electron-electron scattering due to the more localised components of the Ti 3d-bands that generate the 2DEG. Therefore, the hot carrier dynamics of the 2DEG in STO have been evaluated and rationalised comprehensively with a focus on equilibrium unoccupied states. In the following section this focus is shifted towards occupied states and photoinduced changes therein, where a shift of the Fermi energy is directly observed.

---

[59]Not shown is the persistent increase $C$, directly above $E_F$. Its origin will be discussed separately in Section 5.4.1.
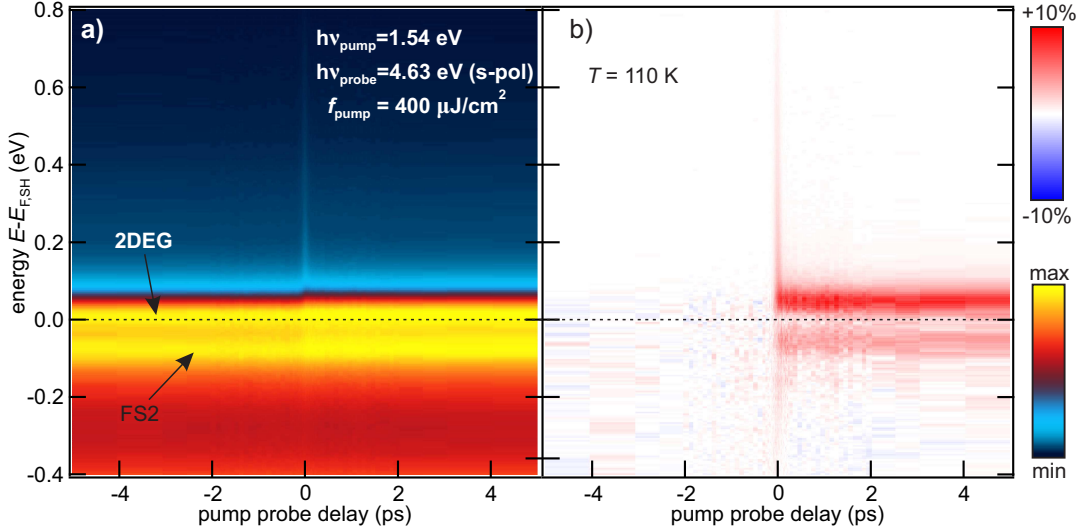
**Figure 5.11:** Time resolved PES of STO upon IR pump excitation: a) raw photoemission data with respect to energy and pump probe delay. The Fermi level of the sample holder is indicated by the dotted line. b) shows data from a) after background subtraction. Averaged spectra between -50 and -1 ps were employed as background.

## 5.4   Pump-induced dynamics of the occupied band structure

When using photon energies larger than the work function ($h\nu_{\text{probe}} > \Phi$) the occupied band structure is probed. Strong pump excitation can modify this band structure significantly (see Section 4) and trigger dynamic effects. In STO, a transient shift of the surface Fermi level is observed, as IR-pumping increases the filling of the 2DEG by photoexcitation from in-gap states (IGS).

A photon energy of $h\nu = 4.65$ eV probes the 2DEG in STO resonantly via final states, as presented earlier (Section 5.2). The result of an experiment, monitoring the band structure of STO before and after IR ($h\nu = 1.54$ eV) pump excitation in a time resolved manner is shown in Figure 5.11 a). The incident IR pump and probe fluences were 400 $\mu$J/cm$^2$ and 7$\mu$J/cm$^2$, respectively. No multiphoton signal from the IR pulses alone was observed at this excitation density, excluding transient vacuum space charge effects. The photoemission intensity is encoded in a false colour scale with respect to energy and pump probe delay. The energy axis is referenced to the Fermi level of the sample holder, which was in electrical contact with the STO surface. At negative delays, the UV pulse arrives before the IR pump pulse and probes the unperturbed system. The spectra expose a peak at $\sim -100$ meV, which results from the final state FS2, as discussed in Section 5.2, and a 2DEG band at the Fermi energy, both indicated by the arrows. The 2DEG band is prominently probed, because s-polarised UV light was used (see Section 3.2.3). At zero delay, a short-lived feature is visible in the unoccupied region of the band structure, corresponding to hot electron dynamics, which were discussed in the previous section.

In the occupied region of the band structure, the photoemission intensity changes
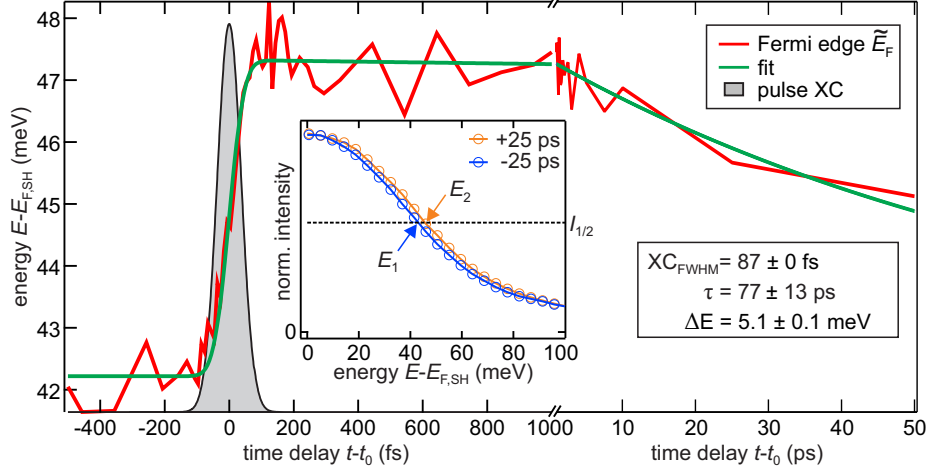
**Figure 5.12:** Transient Fermi level shift in STO: The inset shows exemplary extracted effective Fermi level positions $E_1$ and $E_2$ at fixed intensity $I_{1/2}$ before (blue) and after (orange) IR-pump photoexcitation (Spectra are lineouts from Figure 5.11 a)). The thereby extracted Fermi edge position (red) is fitted by a simple step-like response with slow exponential decay (green curve, see main text for details). The Gaussian XC function of pump and probe pulses is indicated by the grey shaded curve.

at positive delays, i.e. after IR-pumping. It will be shown in the following that the main reason for these intensity change is a transient shift of the Fermi level. After background[60] subtraction, the pump induced change, depicted in b) remains. At the energetic region of FS2 and 2DEG, photoemission intensity increases up to 10 % and then stays constant. To disentangle energetic shifts and 'real' intensity changes, the raw data (Figure 5.11 a)) is analysed further, instead of the background subtracted one.

The inset of Figure 5.12 shows two spectra (linouts from Figure 5.11 a)) in the energetic region of their Fermi edge, before (blue) and after (orange) IR-excitation. The Fermi edge of the spectrum after photoexcitation (orange) is clearly shifted to higher energies. To determine the transient evolution of this shift, spectra at each pump-probe delay were evaluated: The spectra were first normalised to the maximum intensity (this was only a minor correction) and then the half rise intensity $I_{1/2}$ (dashed line) of the Fermi edges was visually determined. Then, the energy at which $I_{1/2}$ is crossed ($E_1$ and $E_2$, indicated by the arrows) was found by linear interpolation between the two data points closest to $I_{1/2}$. Thereby the energetic position of the effective Fermi level $\tilde{E}_F$ was determined for each pump probe delay from Figure 5.11 a). The result of this analysis is shown by the red curve in Figure 5.12.

$\tilde{E}_F$ is constant for negative delays at approximately 40 meV higher energy than the reference Fermi level $E_{F,SH}$, measured at the sample holder. Photoexcitation leads to a fast increase of $\tilde{E}_F$ at $t - t_0 = 0$ fs by $\Delta E \simeq 5$ meV. This shift relaxes slightly towards its value before timezero on a timescale of many ps. It has to be noted that this photoinduced change corresponds to a shift rather than a transient increase in (electronic) temperature, as the Fermi edge shape is unchanged.

---

[60]Averaged spectra at negative delays were used as background.
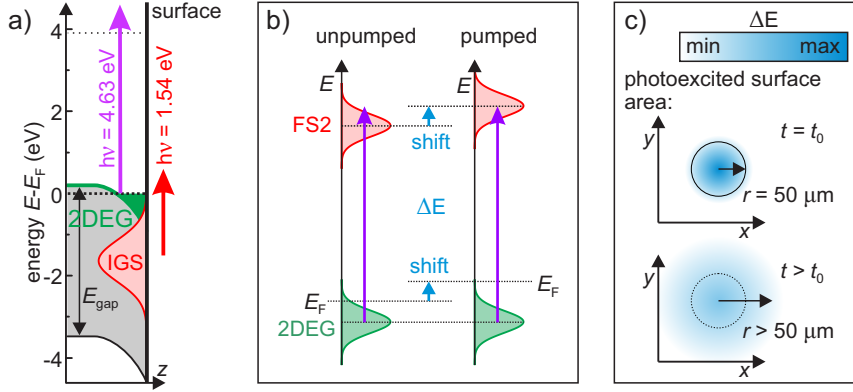
**Figure 5.13:** a) IR-photoexcitation (red arrow) at the STO surface is possible from IGSs (red) and the 2DEG (green), but not from the valence band (VB). b) Photoinduced shift (blue) of Fermi level ($E_\mathrm{F}$) and final state (FS2) enhances resonant probing from initial 2DEG states to FS2. c) Photoinduced Fermi level increase (blue) can equilibrate laterally (in the $x - y$ surface plane) within the STO 2DEG.

To quantify the temporal evolution of this effective Fermi level, a least mean squares fit was performed. The transient response $R(t)$ was modelled by a step (Heaviside-$\theta$) function multiplied by a single exponential decay:

$$R(t) = \theta(t - t_0)\left(\Delta E e^{-(t-t_0)/\tau}\right) + E_0 \tag{5.53}$$

Timezero $t_0$, a decay time constant $\tau$, a time-independent shift $E_0$ and the amplitude of the transient shift $\Delta E$ were the fit parameters. $R(t)$ was convolved with the cross-correlation function $\mathrm{XC}(t)$ of pump and probe pulse, which was determined ex-situ via difference frequency generation (DFG) in a thin BBO crystal[61]. The full-width at half-maximum was $\mathrm{FWHM_{XC}} = 87$ fs and held fixed for the fitting. The fit result (green curve) agrees very well with the data (red). The photoinduced shift of the Fermi level was $\Delta E = 5.1 \pm 0.1$ meV and the relaxation time constant $\tau = 77 \pm 13$ ps.

The constant shift $E_0$, visible even before pump excitation, is due to the UV-probe beam alone (as observed before: see Figure 5.7 in Section 5.2). In addition, the following pump-induced effects are observed:

① A quasi-instantaneous shift of the Fermi edge by 5 meV to higher energies.

② Slow relaxation of this change of the electronic structure on a timescale of 77 ps.

③ An increase of the photoemission intensity of FS2 that can not be explained by this shift alone (Figure 5.11 b), analysis not shown).

As mentioned before, transient space charge and surface photovoltage effects can be excluded, because there is no photoemission from the IR-pulses alone and no above-gap excitation is performed (the pump photon energy is significantly smaller than the band gap and no shift of the low-energy cut-off of the photoemission spectra is observed). The

---

[61]Care was taken that the DFG beam path exhibited the same dispersion as the path to the sample.

only remaining explanation has been suggested in Section 5.2: A transiently increased filling of the 2DEG due to photoexcitation. This mechanism is outlined in the following:

Figure 5.13 a) shows a sketch of the surface electronic structure of STO and photoexcitation pathways. Single photon photoemission probing via $h\nu = 4.63$ eV UV light is indicated by the purple arrow. Initial states for IR-excitation (red arrow) are exclusively in-gap states (IGS) or the 2DEG, because the IR-photon energy is not sufficient to excite from the valence band. Excitation from the 2DEG will not change the occupation within the 2DEG, but photoexcitation from localised IGSs *into* unoccupied 2DEG states can transiently increase the filling of the 2DEG. Because hot carriers above $E_F$ relax fast, within tens of fs (Section 5.3), the shift of the Fermi level appears quasi-instantaneously after photoexcitation (explaining ①). Final states are pinned to the (transient) surface Fermi energy, and therefore, a similar energetic shift is observed for FS2.

The *additional* intensity increase of the FS2 signature (③) can by rationalised by a resonant enhancement. Figure 5.13 b) illustrates such an effect via a simplified energy diagram, involving initial 2DEG states (green) and final state FS2 (red). Before pump excitation (left), the photon energy (purple arrow) excites slightly off-resonant between 2DEG and FS2. After IR excitation (right), the transient shift of Fermi level and final states (blue arrows), due to the increased filling of the 2DEG, enhance the resonance condition, and thereby the photoemission intensity of signature FS2 increases.

The remaining open question is regarding the stability of the transiently increased Fermi level. A system in equilibrium does only exhibit one chemical potential, i.e. the Fermi energy should be equal everywhere. The relaxation of the transiently shifted Fermi level can therefore either happen laterally within the 2DEG by equilibration with the unpumped region of the sample, or by recombination of electrons from the 2DEG and localised holes in the IGSs. Figure 5.13 c) illustrates the lateral equilibration in the 2DEG. The initial (at $t = t_0$) Fermi level shift follows most likely the intensity profile of the laser pulse, i.e. has a radius of approx. 50 $\mu$m. At a later time after photoexcitation ($t > t_0$) the additional electrons equilibrate laterally and the effectively raised Fermi level reduces and spreads spatially. To estimate a limiting timescale for such an equilibration, one can consider ballistic transport of electrons at the Fermi energy and the time it takes for those electrons to move from the middle of the excited area to its edge (i.e. by 50 $\mu$m). The Fermi velocity for a 2D carrier density $n^{(2D)}$ is:

$$v_F = \sqrt{\frac{2E_F}{m_e}} \tag{5.54}$$

with (for two dimensional systems)

$$E_F = \frac{\hbar^2 k_F^2}{2m_e} \quad \text{and} \quad k_F^{(2D)} = \sqrt{2\pi n^{(2D)}} \tag{5.55}$$

With the previously determined value $n^{(2D)} = 3.5 \times 10^{18}/\text{m}^2$ and using the free electron mass for $m_e$ this results in $v_F = 543465$ m/s. Therefore, the electrons need 92 ps to leave the photoexcited area. This is in very good agreement with the relaxation time constant $\tau = 77 \pm 13$ ps of the transient Fermi level shift. Diffusive electron transport would be even slower, but as also the recombination timescale with the photoholes

in the IGSs is unknown, further speculations are omitted. The shift of 5 meV itself corresponds to an increased carrier density of $2.1 \times 10^{16}/\text{m}^2$, i.e. is on the order of one percent of the initial 2DEG carrier density. This is a reasonable number, because the incident IR-pump fluence of $400\ \mu\text{J/cm}^2$ corresponds to $1.6 \times 10^{19}$ IR-photons per m$^2$ and is therefore larger. **The present analysis shows that the photoinduced shift of the Fermi edge is due to a transiently increased filling of the 2DEG with electrons from in-gap states by IR-photoexcitation.**

With this knowledge one open question with respect to the previously presented 2PPE experiments can finally be addressed: What is the reason for the 'constant' offset $C$ that was needed to fit hot electron transients at low excess energy (Section 5.3)? In the following section it will be shown that $C$ is a signature of the transient Fermi level shift as well.

### 5.4.1 Fermi level shift in 2PPE data

With the knowledge about the transient, photoinduced shift of the Fermi level from the previous section, one observation within the investigations of the unoccupied band structure by 2PPE (Section 5.3) can be explained now: An offset $C$ was necessary to model the low-excess energy transients of the hot electron population. In the following, the fluence dependence of this parameter is investigated and it is shown that it can be explained by a photoinduced shift of the Fermi level as well.

The underlying datasets (e.g. Figure 5.9 a)) have been background subtracted, using averaged spectra before timezero. Therefore, their intensity is the difference between the spectrum with equilibrium and transiently shifted Fermi edge. Figure 5.14 b) shows two exemplary Fermi-Dirac distributions with shifted Fermi edges (red and green) and the difference between the two (black, scaled by a factor of 15). Then, $C$ corresponds to the intensity *change* (black) at the excess energy with respect to $E_\text{F}$ of the respective lineout in Figure 5.9 a). This can be described mathematically by the difference of two Fermi-Dirac distribution functions, shifted with respect to each other and evaluated at energy $E$:

$$C(E, F) = A \left[ \frac{1}{e^{(E-E_\text{F}-\alpha \cdot F^\beta)/(k_\text{B}T)} + 1} - \frac{1}{e^{(E-E_\text{F})/(k_\text{B}T)} + 1} \right] \qquad (5.56)$$

The photoinduced energetic shift $\Delta E = \alpha \cdot F^\beta$ is a function of the fluence $F$ to the power $\beta$ multiplied by a scaling factor $\alpha$. Such a nonlinear scaling is expected, because the hot electron photoemission intensity scales scales nonlinearly with the IR-pump fluence $F$ (inset of Figure 5.9 a)). $A$ is an amplitude and $T$ the temperature of the Fermi-Dirac distribution.

Figure 5.14 a) shows the offset $C$ from the fits (according to Equation 5.52, as shown in Figure 5.9) with respect to excess energy for four different IR-pump fluences (coloured circles). The data point at $E - E_\text{F,SH} = 0.2$ eV has been manually inserted and set to zero, as no offset was needed to perform the fits at this energy.

A global fit, based on Equation 5.56, was used to model the four datasets simultaneously, using global values for most of the parameters: A single equilibrium Fermi
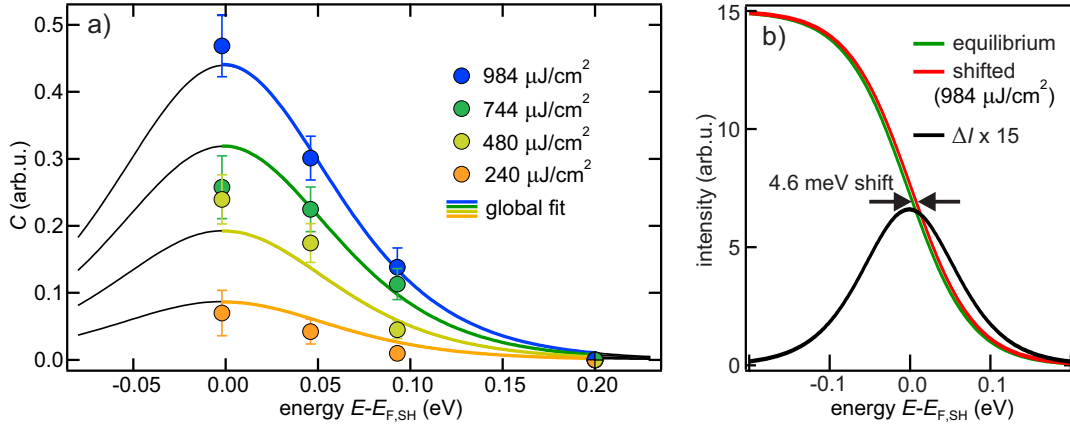
**Figure 5.14:** a) Energy dependence of fit parameter $C$ for different fluences and global fit (solid lines). The fit model is based on the difference between two Fermi-Dirac distributions that are slightly shifted with respect to each other (see main text). These Fermi-Dirac distributions and their difference $\Delta I$ are shown for the highest fluence ($984\ \mu\mathrm{J/cm}^2$) in b).

energy $E_{\mathrm{F}}$, scaling factor $\alpha$, exponent $\beta$ and effective temperature[62] $T$ have been used. Only the fluence was set constant to the respective measured value for each dataset. The amplitude $A$ was also kept constant, because for small energetic shifts $\Delta E$, the difference between two Fermi-Dirac distributions scales with $A$ and $\Delta E$ in a very similar way[63].

The global fit (Figure 5.14 a), solid lines) describes the data remarkably well. The exponent $\beta = (1.15 \pm 0.14)$ in the scaling law agrees nicely with the ones determined earlier (Section 5.3: $1.2 - 1.3$ in Figure 5.9 a)). The scaling factor $\alpha = (1.7 \pm 1.6)\frac{\mathrm{eV}}{\mathrm{J/cm}^2}$ is a hundred times smaller than for the static shift, induced by UV light (Section 5.2), but this is easily explained by the rather different experimental conditions: Only the transient photoinduced change is considered and a much lower photon energy is used here.

Figure 5.14 b) shows the equilibrium (green) and shifted (red) Fermi-Dirac distribution that results in the blue curve in a), to illustrate the magnitude of the photoinduced shift: **A photoinduced Fermi level shift of only 4.6 meV is able to describe the persistent offset C that was necessary to model the transient evolution of hot electrons in the 2DEG at the STO surface**. This value agrees very well with the 5 meV observed in time-resolved 1PPE measurements (previous Section 5.4), although the fluence there was smaller by a factor of two. Altogether a complete picture of the effects of photoexcitation within the 2DEG at the STO/vacuum interface can be drawn, as concluded in the following section.

---

[62] Neither experimental broadening nor real density of states was considered explicitly, therefore the temperature does not correspond to the real temperature.

[63] To find a reasonable value for $A$, a Fermi-Dirac distribution was fitted to raw data (without background subtraction, not shown) and the resulting fit amplitude was used.

**Figure 5.15:** Illustration of ultrafast electron dynamics in STO: near-IR photoexcitation (red arrows) from initial in-gap states (IGS) and the 2DEG generates hot carriers above the Fermi level. At high excess energies, those decay as predicted by Fermi liquid theory for two dimensions. At low excess energies the quasiparticle decay is faster than expected. Bulk valence and conduction bands are indicated (VB, CB). b) shows a transient increased filling of the 2DEG due to photoexcitation from IGSs.
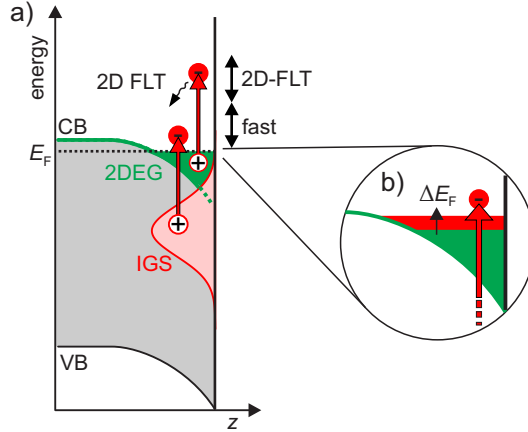
# 5.5   Summary & Conclusion: dynamic 2DEG at STO(100)/vacuum interface

Photoemission spectroscopy has been used to investigate the unoccupied electronic band structure of the SrTiO₃(100)/vacuum interface and ultrafast dynamics therein, after near-IR photoexcitation.

Distinct final states, pinned at 4.1 and 4.5 eV above the surface Fermi level, have been discovered. They exhibit a free electron like dispersion within the surface plane, but are localised perpendicular to it.

The nonequilibrium quasiparticle dynamics of the system after IR photoexcitation have been investigated extensively and yield the following picture: As illustrated in Figure 5.15 a), electrons are photoexcited (red arrows) from in gap states (IGS, red) and from the two-dimensional electron gas (2DEG, green), both localised at the sample surface, into unoccupied states above the Fermi energy. Lifetimes of quasiparticles with high excess energies (top double arrow) are described well by Fermi liquid theory for two dimensions (2D-FLT). When the excess energy is lower than 0.5 eV above the Fermi level, this situation changes drastically: An increased phase space for electron-electron scattering due to more localised bands within the 2DEG (originating from the bulk Ti $3d$ $t_{2g}$-bands) in this energetic region leads to an increased scattering rate, i.e. decreased hot electron lifetimes (bottom double arrow).

In addition, a second transient effect is observed and illustrated in Figure 5.15 b): The Fermi level shifts to higher energies after photoexcitation, due to a transiently increased filling of the 2DEG from initial in-gap states via near-IR excitation. This corresponds to an increase of charge density in the 2DEG on the order of one percent. The relaxation of this shift can be explained by ballistic transport of these excess electrons out of the photo-excited surface area, but diffusive transport or electron-hole recombination are also likely to play a role. Varying the excitation density could potentially be used to tune the carrier density in the 2DEG and thereby transiently modify the electron-electron scattering rates in this system.

The screening of the Coulomb interaction plays a more restrained role in the system: In two-dimensions, screening is less efficient than in three dimensions. The excess energy dependence of scattering rates for quasiparticles, predicted by Fermi liquid the-

ory, deviates from the ones in three dimensions, because of an interplay between this reduced screening and on the other hand a reduced phase space for scattering. At low excess energies, the latter effect is compensated for by additional, localised electronic bands. The decreased screening for two dimensions remains and results in the observed increased scattering rates.

# 6 Screened excess electrons in amorphous ice: Transmission, trapping and reactivity

The interaction between matter and excess electrons is important in various fields of physics and chemistry. Screening plays a stabilising role for excess charges in polar solvents like water. Instead of quasi-free carriers, as for example in metals, dipole moments of the solvent molecules screen the Coulomb interaction with the excess charge by structural reorientation.

In this work, amorphous solid water (ASW) is used as a exemplary polar environment to study various processes in connection with screened excess electrons. Those processes include the transmission of these electrons through the molecular adlayer (defined by the mean free path), stabilisation and trapping of the electrons. The extremely long residence times of these trapped electrons enhance possible electron-induced chemical reactions with the environment, like for example the so called bimolecular water reduction reaction [Bar11]:

$$(\mathrm{H_2O})_n^{-2} \longrightarrow (H_2O)_{n-2}(\mathrm{OH^-})_2 + \mathrm{H_2} \tag{6.57}$$
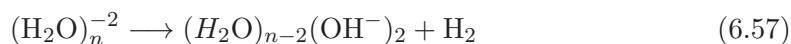
The build-up of hydroxide ($\mathrm{OH^-}$) at the surface leads to a change of work function that depends on the photon dose and therefore on the spatial profile of the laser beam. In Section 6.4.1 such a spatially dependent work function is directly observed and Appendix G describes the implications for low photon energy photoemission spectroscopy on such inhomogeneous systems, in general.

## 6.1 Preparation of $\mathrm{D_2O}$ Layers on Cu(111)

Well established recipes for cleaning the Cu single crystal (111) surface by repeated Ar-ion sputtering and annealing cycles and adsorbing amorphous $\mathrm{D_2O}$ films [Stä07b, Mey11] have been used in this work. The Cu(111) single crystal was placed in front of a sputter gun under a shallow angle. At an argon partial pressure of $2.2 \times 10^{-6}$ mbar Ar-ions (generated by a filament inside the sputter-gun) are accelerated towards the sample by a voltage of 0.7 kV for ten minutes. The ion current was on the order of 8 $\mu$A. The sample was annealed after each sputtering at a temperature of 800 K for 30 minutes in order to generate a smooth crystalline surface. The procedure was repeated until the signatures of the Cu(111) surface- and image-potential-states were the dominant features in the photo-electron spectra.

$\mathrm{D_2O}$ (supplier: Sigma Aldrich) was purified via freeze-pump-thaw cycles and dosed via a pinhole doser as described in [Dei11]. The sample was positioned in front of the pinhole doser and cooled down to 100 K for compact and below 50 K for porous ASW via a liquid Nitrogen/Helium cryostat. By variation of dosing pressure and dosing time the absolute dose and therefore $\mathrm{D_2O}$ coverage was adjusted in a controlled manner. The $\mathrm{D_2O}$ molecules form closed amorphous layers at such temperatures (below 110 K) in UHV [Stä07b]. The $\mathrm{D_2O}$ coverage has been determined independently by TPD spectroscopy, using a quadrupole mass spectrometer. Exemplary TPD spectra are shown
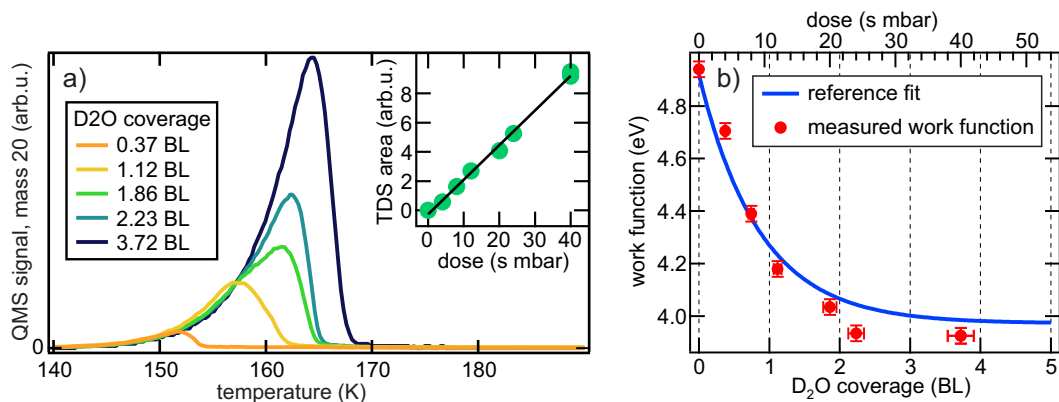
**Figure 6.1:** Characterisation of amorphous D2O-layers via TPD and work function: in a) TPD spectra for various $D_2O$-coverages are displayed. The inset confirms the linear relation between dose (dosing pressure times dosing time) and integrated TPD intensity. In b) a reference fit (blue) performed in [Dei11] is used to translate dose into coverage in BL, via the measured change in work function (red) of the system.

in Figure 6.1 a) for various coverages. Zero-order desorption sets in at a temperatures between 140 and 150 K, independent of $D_2O$ coverage. As the intermolecular binding strength is on the same order as to the metal surface no multilayer desorption cannot be distinguished from the first layer desorption. The dependence of the integrated QMS signal on dose (i.e. dosing time times $D_2O$-pressure) is shown in the inset (green circles). The expected linear behaviour is indicated by the solid line.

Without distinct mono- and multilayer features a direct determination of coverage from the TDP spectra is not possible. Instead the change of work function $\Phi$, measured via the spectral bandwidth in photoemission spectroscopy, is used to determine the coverage: One bilayer (BL) is initially defined by the ordered $\sqrt{3} \times \sqrt{3}$ structure of $D_2O/Ru(0001)$ [Hel95]. A calibration of work function change with coverage of $D_2O/Cu(111)$ in comparison of coverage in bilayers for $D_2O/Ru(0001)$ has been performed in [Bov03, Gah04]. This specific work function dependence was used to determine the $D_2O$ coverage on the Cu(111) surface, as shown in Figure 6.1 b). The reference curve (blue) is a fit with a decaying exponential performed in [Dei11][64]. Red markers indicate measured values of $\Phi$ with respect to the deposited dose.

## 6.2 Mean free path of low energy excess electrons in ASW

The interaction of secondary electrons (e.g. generated by ionising radiation) with water is an important field of research in radiation chemistry and highly relevant for biological systems. In this Section the mean free path, defined by such interactions, of low-

---

[64]It is assumed that the work function decreases linearly with the reduction of free substrate surface. A simple rate equation for the available binding sites on the metal surface leads to the exponentially decaying behaviour. Saturation is reached when a closed adsorbate layer is formed, i.e. between 2 and 3 BL [Gah02]
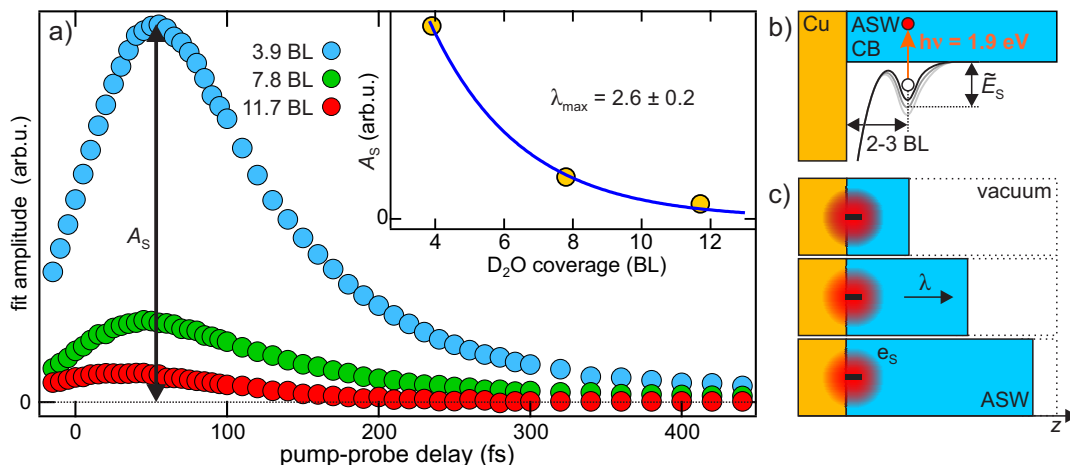
**Figure 6.2:** Coverage dependence of solvated electron signature: In line of the analysis described in context of Figure 2.9, the fit amplitude of the solvated electron signature with respect to pump-probe delay is shown for different $D_2O$-layer thicknesses in a). The mean free path $\lambda_{max} = 2.42 \pm 0.25$ BL is extracted from the thickness dependence of the fit amplitude from a) in the inset. In b) the binding site and changing situation for the respective layer thickness is illustrated.

energy excess electrons in ASW will be estimated. The inverse mean free path in semiconductors and insulators is proportional to the loss function $Im(1/\epsilon)$, which is usually small for energies below the band gap [Hüf10]. In ice, the band gap is on the order of 8 eV, therefore, a large large mean free path is predicted for low-energy electrons.

Solvated electrons in ASW layers, as presented in Section 2.4, reside at a constant distance to the metal substrate [Mey08]. Figure 6.2 b) illustrates this situation: Electrons, excited from the substrate, are solvated 2 to 3 BL from the substrate surface. Photoexcitation of these electrons by visible light (e.g. a photon energy of $h\nu = 1.9$ eV) turns them into low energy, 1.3 eV with respect to the conduction band minimum (CBM)[65], electrons that are photoemitted from this defined spatial and energetic location. On the way from this location to the ice/vacuum interface, their interaction with their surrounding defines their mean free path. An effective mean free path[66] $\lambda$ can be defined within

$$I(z) = I_0 e^{-z/\lambda} \tag{6.58}$$

The transmitted 'electron-intensity' $I(z)$ through a material, in this case ASW, of thickness $z$ decreases exponentially, with the characteristic length $\lambda$, i.e. the mean free path. Observing the intensity for different thicknesses $z$, therefore, allows to determine $\lambda$. Figure 6.2 c) illustrates the idea of the experiment: Solvated electrons (red) are used as a localised electron source for low energy electrons. Increasing the overall thickness

---

[65]Solvated electrons are energetically 0.6 eV below the CBM [Stä14]. Photoexcitation by 1.9 eV photons, thus, lifts them 1.3 eV above the CBM.

[66]Including elastic and inelastic contributions, see e.g. [Pow09] for detailed definition of the terminology.

of the ASW layer, then, corresponds to an increase of material, which the electrons have to be transmitted through, before photoemission and detection.

Figure 6.2 a) shows the transient evolution of photoemission intensity from solvated electrons, after photoexcitation, for a ASW coverage of 3.9 BL[67] (blue circles), as evaluated from pump-probe data earlier (Section 2.4). For increasing coverage (green and red circles) the intensity decreases as expected, but the dynamical evolution (rise and decay) do not change significantly. The peak amplitude $A_S$ is hence used for quantification of the transmitted electron intensity $I(z)$ (Equation 6.58). At coverages above 11.7 BL, no solvated electron signal was detected any more.

The inset of Figure 6.2 a) shows the change of amplitude $A_S$ with respect to the overall ASW coverage. A single exponential fit (Equation 6.58) yields a value of $\lambda_{max} = 2.6 \pm 0.2$ BL. It has to be noted that for an exact analysis, the laser fluences would need to be considered. These have not been recorded, but it is known that they were not decreased for increasing coverages. Hence it is possible that the photoemission signal decreases even faster with increasing coverage than shown here, but certainly not slower. The determined mean free path is therefore an upper limit, hence the term $\lambda_{max}$.

**The mean free path of low-energy (1.3 eV with respect to the CBM) electrons in compact ASW is remarkably short, i.e. 2.6 BL (approx. 10 Å).** As mentioned earlier, the mean free path (as a result of electron-electron scattering) of electrons with energies below the band gap of the material, they are transmitted through, is predicted to be long. The observed short mean free path of 10 Å must therefore stem from scattering with defects and phonons. Defect scattering is not unlikely in an amorphous system and by exciting OD stretch vibrations, 300 meV are transferred to the lattice [Ang84], explaining the small effective mean free path.

As mentioned before, photoelectrons, originating from this species of solvated electrons, are not observed for coverages above 11.7 BL (due to their short mean free path). Instead, a new species of *trapped* electrons is detected in thicker layers (i.e. for $\theta > 11.7$ BL). These will be subject of the following sections. They exhibit a remarkably long lifetime on the order of tens of seconds (14 orders of magnitude larger than for the previously discussed solvated electron species), similar to the species found at the vacuum interface of $D_2O$ crystallites [Bov09] that were introduced in Section 2.4.

## 6.3 Trapped electrons in thick ASW films

In ASW[68] layers, thicker than 11.7 BL, a new species of electrons is detected. Figure 6.3 shows characteristic signatures of this species: a) Shows a photoemission spectrum, generated by UV-light ($h\nu_{UV} = 4.62$ eV) with respect to an intermediate state energy axis. A very broad feature $e_T$ is assigned to this new species. It spans an energy

---

[67]The sample temperature while adsorbing $D_2O$ was 100 K in these experiments, therefore compact ASW layers were formed and the conversion from 1 BL to more common units of distance is estimated from lattice constants of crystalline ice, which are similar: 1 BL $\sim 3.9$ Å

[68]Porous amorphous water to be exact, as the $D_2O$ films were deposited at substrate temperatures of 40 K [Stä07b]. The trapped electrons have also been observed after heating the sample above 90 K, i.e. for compact ASW (data not shown).
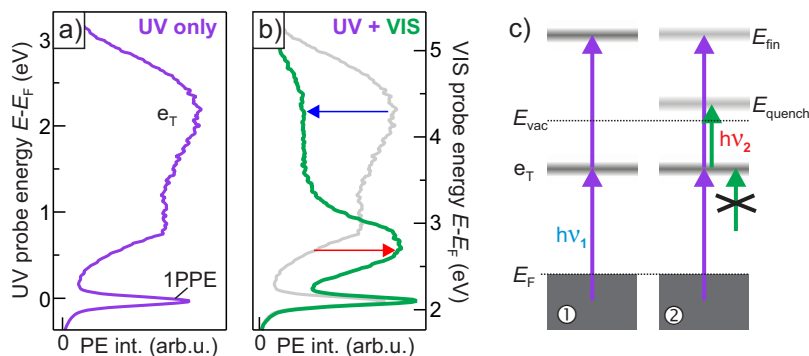
**Figure 6.3:** Electrons probed by UV and visible light: a) shows a photoemission spectrum generated by UV light irradiation ($h\nu_{UV} = 4.62$ eV). A new species of electrons are marked $e_T$. b) Shows a modified spectrum (green) when visible light ($h\nu_{vis} = 2.49$ eV) is added. The signal $e_T$ decreases (blue arrow) and at lower energies an increased intensity is detected (red arrow). c) Shows a schematic energy diagram of trapped electrons $e_T$ and probing pathways for UV (purple) and visible (green) light to explain these effects: UV light populates $e_T$ and at the same time photoemits electrons from it, which are detected at $E_{fin}$ (①). Visible light (②) cannot populate $e_T$ due to its lower photon energy, but can still photoemit electrons that are detected at a lower final state energy $E_{quench}$. This also reduces the intensity at $E_{fin}$.

window roughly between 1 eV and 3 eV above the substrate Fermi energy[69]. The peak-like structure at low energies stems from an onset of single-photon photoemission (1PPE) from parts of the sample with a low work function and is discussed in detail in Section 6.4 and Appendix G. When adding visible light the photoemission spectrum changes drastically. This is shown in b) (green curve) with the UV-only spectrum as a reference (grey curve), with respect to an intermediate state energy axis for visible light ($h\nu_{vis} = 2.49$ eV) probing. The $e_T$ signature has decreased significantly (blue arrow) and at lower energies an intensity increase is observed (red arrow).

To explain these changes, a simplified energy level scheme is depicted in Figure 6.3 c). In the UV-only (①) experiment, UV photons (purple arrows) populate a state $e_T$ by photoexcitation in the metal substrate and subsequent transfer of photoexcited electrons into the ASW film. At the same time these photons photoemit electrons from $e_T$ to the final state energy $E_{fin}$.

When adding visible photons (green arrows) a new photoemission pathway is opened, but the population channel stays unchanged, because the visible photons do not possess enough energy to populate $e_T$ from occupied substrate states. This results in a rise of photoemission intensity at lower energies $E_{quench}$ and at the same time reduces the photoemission intensity generated by the UV photons at $E_{fin}$.

This mechanism is confirmed by the energetics of the observed changes in b): The increase by visible light photoemission energetically starts below 3 eV (right axis) and is cut by the work function of the system at lower energies. This coincides with the $e_T$ signature probed by UV light, which also starts roughly at 3 eV (left axis) and extends further down to 1 eV (Binding energies that are too large for visible light photoemission).

---

[69]From now on 'Fermi energy' always refers to the Fermi energy of the metal substrate.
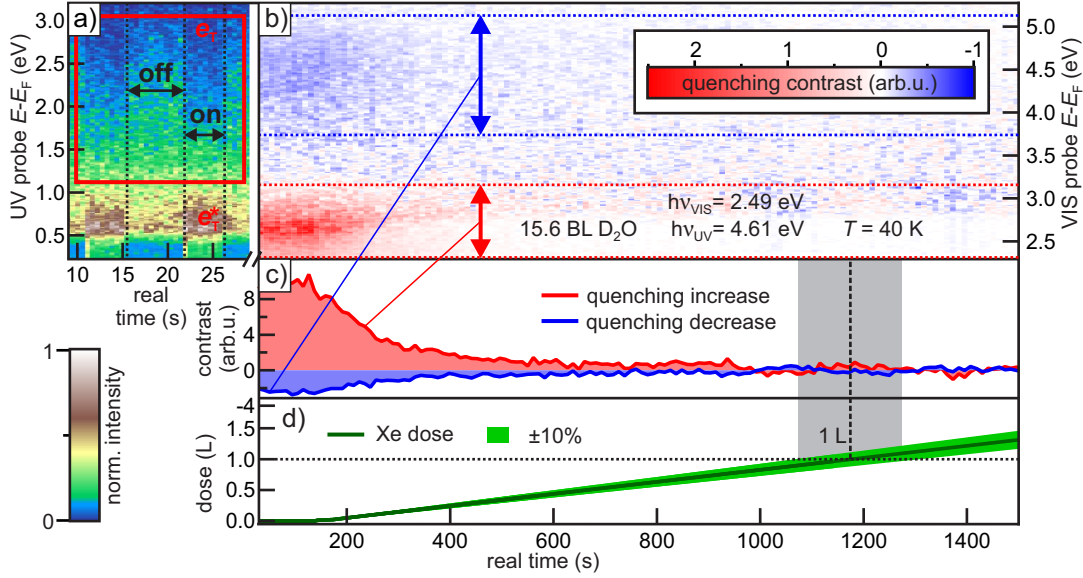
**Figure 6.4:** Xenon overlayer on top of ASW/CU(111). Intensity changes in photoemission upon UV plus VIS illumination (on) in contrast to UV-only illumination (off) are shown in a). The quenching contrast (on minus off) is shown in b) with respect to real time and energy upon xenon adsorption. Integrated increase and decrease (region of integration is indicated by the arrows) are shown in c). d) Shows the adsorbed amount of xenon.

This effect, i.e. the 'quenching contrast', does not depend on the temporal order of visible and UV pulses (not shown). The population of $e_T$ must therefore stay constant for at least the inverse repetition rate of the laser, i.e. 3.33 $\mu$s. Otherwise the contrast would be different when visible light pulses interact directly after UV-excitation or directly before (i.e. 3.33 $\mu$s after UV excitation). **The electrons remain in a quasi-stationary, excited state $e_T$ (1 eV to 3 eV above the Fermi energy) at least for the inverse repetition rate of the laser (3.33 $\mu$s).** It will be shown later that they in fact survive for tens of seconds in their trapping sites, and therefore, will be called *trapped electrons*. They are similar to the species of trapped electrons at the vacuum interface of $D_2O$ crystallites [Bov09]. Before investigating the timescales on which these electrons stay in an excited state in detail, the location of the trapping sites within the ASW film is determined in the next section.

### 6.3.1   Trapped electrons at ASW/vacuum interface

To determine whether the trapped electrons reside in the vicinity of the ASW/vacuum interface or within the bulk of the adsorbate, xenon overlayer experiments have been performed. The basic idea is the following (as shown in [Stä07a, Mey08]): An electronic state or trapping site close to the ice/vacuum interface will be strongly influenced by a coadsorbed overlayer of xenon, while bulk-ice states will not be affected strongly. Xenon as a rare gas will not interact chemically and therefore can be viewed as inert. It nevertheless acts as a polarisable overlayer that will change the dielectric environment at the vicinity of the ice/vacuum interface and thereby modify lifetimes and 'squeeze'

the wave function of excess electrons [Stä07a].

Figure 6.4 a) shows photoemission intensity encoded in a false colour scale with respect to intermediate state energy (for UV probed states) and real time, while switching the visible beam on and off. When the visible light is on, a clear intensity decrease is observed in the region of $e_T$ (red box), whereas at lower energies the intensity is increased due to photoemission from $e_T$ by the visible light (marked $e_T^*$). This was already shown in the previous section.

The difference between on and off yields the quenching contrast, shown in b). Blue corresponds to the decrease and red to the increase due to visible photons, which is displayed with respect to real time (bottom axis), while dosing Xe. The quenching contrast clearly decreases quickly with time. To emphasize this further, an integration was performed over the indicated energetic regions of increase and decrease (red and blue arrow) in b). c) Shows this integrated decrease (blue) and increase (red). In d) the xenon dose is displayed with respect to real time. It was calculated by integrating the partial Xe pressure in the vacuum chamber, which was measured by an ion gauge, with respect to time.[70]

The quenching contrast in c) stays constant when no Xe is adsorbed ($t < 180$ s), but decreases rapidly as soon as Xenon is dosed onto the system. Long before a dose of 1 L, indicated by the dashed line in c) and d), is reached, the contrast has completely vanished. Assuming a sticking coefficient of 1, which is a reasonable estimate at a sample temperature of 36 K, this means that at a coverage of 1 ML the trapped electron state has been substantially modified. **The massive influence of the Xe-overlayer on the trapped electron state $e_T$ shows that it resides at the ASW/vacuum interface.**

Defects at the ice-vacuum interface could e.g. act as pre-existing traps for electrons, leading to extraordinary long residence times, similar to the ones observed on crystalline ice [Bov09]. Such a species of long lived excess electrons at the vacuum interface has the great potential of enhancing (electron induced) chemical reactions there. Before observing the reactivity of this species directly, the residence times at the surface are investigated in more detail in the following section.

### 6.3.2   Relaxation dynamics of trapped electrons in ASW

When an excitation does not relax within the inverse repetition rate (i.e. temporal separation between two subsequent laser pulses on the order of $\mu$s) of the laser system, pump-probe experiments start to probe quasi-stationary contributions and the system is prevented from reaching its initial equilibrium state at all times. The evolution of the occupation $n(t)$ of trapped electron sites (maximum available sites shall be $N$) with

---

[70]The pressure reading from a Bayard-Alpert ion gauge is calculated from the ration of ion current $I_I$ and electron emission current $I_e$, including a sensitivity factor $S_g$ depending on the constituents of the measured gas pressure:

$$P = \frac{I_I}{S_g I_e} \tag{6.59}$$

Usually $S_g$ is at a value of 19 corresponding to $N_2$, for detection of air-like rest gas. For Xenon the correction is $S_g = 55$, due to a the lower ionisation cross-section. Therefore, the measured pressure has to be corrected by a factor of $\sim 2.9$.
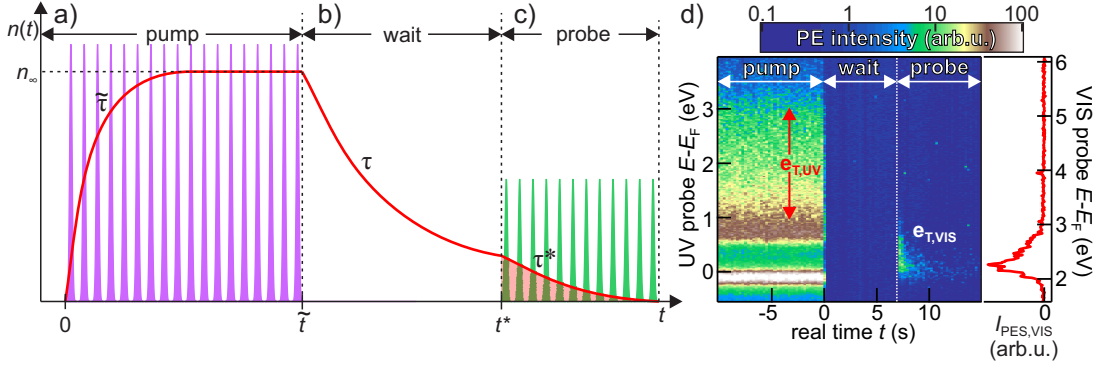
**Figure 6.5:** Trapped electron population during pump-wait-probe experiment:

time can then be described by the following rate equation [Gah04]:

$$\dot{n}(t) = a \cdot I(N - n(t)) - \frac{1}{\tau}n(t) - b \cdot I \cdot n(t) \tag{6.60}$$

The first term covers the population of the sites by the laser with intensity $I$ (single photon processes are assumed for population and depopulation) and cross section $a$. It is proportional to the number of sites that are not populated yet $(N - n(t))$.

The remaining terms describe the decrease of population $n(t)$ due to relaxation of the excited state on timescale $\tau$ and de-population by photoexcitation (i.e. photoemission) with cross section $b$. Both are proportional to the number of occupied sites. The solution of the differential equation (Equation 6.60), with boundary condition $n(0) = 0$, is:

$$n(t) = \frac{a \cdot I \cdot N}{1/\tau + I(a + b)} \left(1 - e^{-(1/\tau + I(a+b))t}\right) \tag{6.61}$$

Figure 6.5 a) illustrates how the population $n(t)$ reaches the quasi-equilibrium population $n_\infty$ on a timescale $\tilde{\tau} = (1/\tau + I(a + b))^{-1}$ under pulsed UV illumination. In the experiments, presented within this thesis, $\tilde{\tau}$ is short compared to the experimental resolution of $1/4$ s and the important quantity

$$n_\infty = \lim_{t,\tau \to \infty} n(t) = \frac{a \cdot N}{a + b} \tag{6.62}$$

depends only on population $(a)$ and depopulation $(b)$ cross sections and the total number of trapping sites $N$ for long relaxation times $\tau$.

Figure 6.5 b) displays the evolution of $n(t)$ when the light is switched off (i.e. $I = 0$) after reaching $n_\infty$. The system relaxes and $n(t)$ decays exponentially with time constant $\tau$.

Probing with lower energy, visible light pulses does not populate but only depopulate trapped electron states via photoemission, as indicated in the previous section. Figure 6.5 c) illustrates this situation: The population has reached a value $n(t^*)$ after relaxation in the dark and is depleted quickly by photoemission with visible pulses on a timescale of

$$\tau^* = \lim_{\tau \to \infty} (1/\tau + I \cdot b)^{-1} = 1/(I \cdot b). \tag{6.63}$$

142

The integrated photoemission intensity during visible light probing is proportional to the integrated population (red shaded area) and therefore to $n(t^*)$, the population at the end of the 'wait' interval:

$$I_{\text{PES,VIS}}(t^* - \tilde{t} = \Delta t) = I_{\text{VIS}} \cdot n_\infty \cdot b \cdot e^{-\Delta t/\tau} \tag{6.64}$$

A pump-wait-probe experiment (corresponding to a), b) and c) in Figure 6.5) can be used to find the intrinsic relaxation time $\tau$ by measuring $I_{\text{PES,VIS}}(t^*)$ for different wait-times $t^* - \tilde{t}$.

Figure 6.5 d) shows an exemplary pump-wait-probe dataset (with $\tilde{t} = 0$). Photoemission intensity is encoded in a false colour scale and shown with respect to intermediate state energy. The left axis corresponds to the energy for UV-probed ($h\nu = 4.62$ eV) states and the right one to the one for visible light ($h\nu = 2.49$ eV) probing relative to the Fermi energy. The quasistationary population is reached at negative delays. To make sure $n_\infty$ is reached, the sample is illuminated for 40 s with UV light only (pump) such that the signal is constant with time. The photoemission intensity during this time interval corresponds to the spectrum previously shown in Figure 6.3 a). The red arrows indicate the energetic region that corresponds to trapped electrons $e_{\text{T,UV}}$ between 1 and 3 eV (left axis).

After $t = 0$ the sample is left in the dark for a certain wait time ($\Delta t = 7$ s in this example), during which the system relaxes (wait). Obviously no photoemission intensity is recorded during that time.

In this case at $t = 7$ s, the visible (probe) beam is switched on[71] and photoemits from the trapped electron states generating the photoemission intensity $e_{\text{T,VIS}}$. Energetically the signature is lower in energy, because the photon energy is lower, than for UV light. The signal appears in an energetic window between 2 and 3 eV (right axis), which agrees well with the one for the UV-signal (1 to 3 eV), if one considers the fact that the work function determines the low energy cut off here[72]. The photoemission intensity vanishes with time, because trapped electrons are not re-populated by visible light. The red curve in d) corresponds to the integrated photoemission intensity probed by visible light $I_{\text{PES,VIS}}$.

According to Equation 6.64, this integrated as a function of wait time $\Delta t$ can be used to find the intrinsic relaxation time $\tau$ of the system: The inset of Figure 6.6 a) shows further analysis of $I_{\text{PES,VIS}}$: An asymmetric Gaussian fit with amplitude $A$ (red) and, alternatively, the integrated intensity $I$ (blue) were extracted from the data.

The experiment was repeated for various time delays $\Delta t$ between 1 and 180 s. The data analysis shown in the inset yields the red (fit amplitude $A$) and blue (integrated intensity $I$) markers in Figure 6.6 a). Both ways of extracting the photoemission signal intensity coincide very well (red and blue). A single exponential fit according to Equation 6.64 results in a time constant of $\tau = 24 \pm 3$ s ($\tau = 20 \pm 3$ s) based on the fit amplitudes $A$ (integrated peak area) from the inset. **The trapped electrons relax on a timescale on the order of 20 s, at least 14 orders of magnitude slower than solvated electrons at the ice-metal interface.**

---

[71]Computer controlled mechanical shutters were used to switch beams on and off.

[72]The signal appears within a region of an inhomogeneous work function distribution, as discussed in Section 6.4
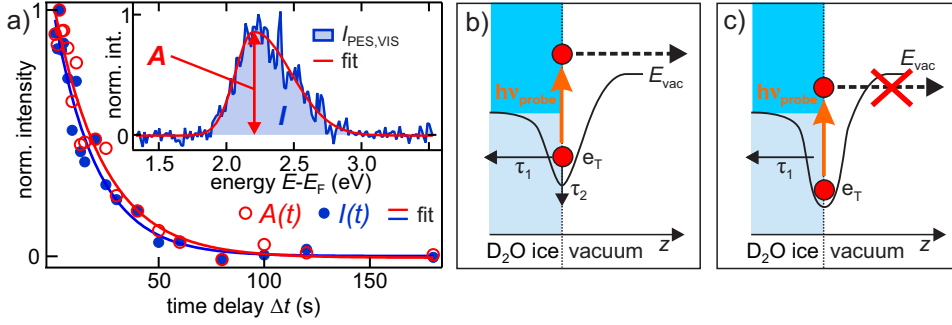
**Figure 6.6:** Trapped electron relaxation times: a) Trapped electron photoemission intensity at various times after injection. The data is fitted by a single exponential decay. The inset shows extraction of amplitude $A$ (red) and peak area (blue) from raw data. b) and c) illustrate the loss of photoemission signal from $e_T$, due to energetic relaxation (see main text for details).

Figure 6.6 b) illustrates the fact that this intrinsic *relaxation* time $\tau$ does not necessarily correspond to the *lifetime* of trapped electrons. In this simplified picture $\tau_1$ corresponds to the time it takes the trapped electron to relax back to the metal substrate, which would correspond to its lifetime in a sense that the system would relax back to its initial state via this route. In contrast, $\tau_2$ would correspond to further energetic stabilisation of the trapped electron. c) shows that this energetic relaxation at the surface region can also lead to a disappearing photoemission signal: The probe photon energy is not sufficient for photoemission (the final state is below the vacuum energy $E_{vac}$) if the trapped electron state stabilises too far towards the Fermi energy (i.e. gains too much binding energy). Also, further relaxation channels (e.g. laterally within the ice layer) are not considered, but might play a role. The low signal-to-noise ratio of the data does not allow to distinguish between these pathways, therefore, the effective relaxation time $\tau$ is not specified further.

**Film thickness dependence**

Because the trapped electrons reside at the ASW/vacuum interface, changing the adsorbed ASW coverage is equivalent to changing the distance of the trapped electron sites to their energetically most favourable relaxation channel, the metal substrate. To gain further insights into the main relaxation mechanism, pump-wait-probe measurements have been performed for ASW films between 15 and 30 BL thickness. The extracted trapped electron relaxation times $\tau$ with respect to $D_2O$ coverage are shown in Figure 6.7 a). $\tau$ has been extracted for each individual measurement (light blue circle), as discussed in the previous paragraph and shown in Figure 6.6 a). Average values are shown with error bars resulting from the spread of the data points (dark blue squares). **Within the error bars the relaxation time of trapped electrons is independent of their distance to the metal substrate.**

Figure 6.7 b) illustrates possible relaxation channels: Tunneling to the substrate as a rate limiting process is clearly excluded, because an exponential dependence on the barrier thickness (i.e. coverage) would be expected. Also wave function overlap with substrate states is improbable at these distances and a strong coverage dependence would be expected as well.
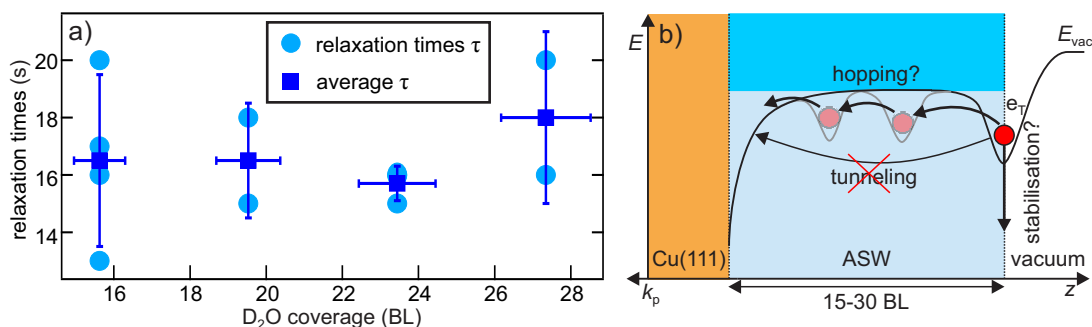
**Figure 6.7:** a) ASW layer thickness dependence of trapped electron relaxation times: Individually measured values lifetimes (light blue circles) and average value per thickness (dark blue squares). The y-error bars are extracted from the spread of measurements and the x-error bars correspond to the estimated error of 4.3 % due to the bilayer reference calibration. b) Illustration of various relaxation pathways. See main text for details.

Hopping via bulk defect states or energetic stabilisation within the ice/vacuum interface are two relaxation mechanisms that would show significantly less or no coverage dependence, as compared to e.g. tunneling. A mixture between both, on a similar timescale, might very well result in the observed effective relaxation times on the order of 20 s. This would also explain the large spread of the data in a): Exact preparation conditions (Temperature, dosing pressure, purity of $D_2O$, etc.) might influence the defect density and properties, which affect the relaxation times more strongly than the thickness of the ice layer.

Trapped excess electrons that ① reside $\sim 2$ eV above the substrate Fermi energy, ② are located at the ASW/vacuum interface and that ③ exhibit extraordinary long relaxation times on the order of 20 s, are extremely relevant for electron induced chemical reactions [Ber09, Stä12]. They have the potential to be highly reactive, because of their exposed location at the vacuum interface and the enhanced reaction probability due to their long residence times there.

In the next chapter their reactivity will be investigated further. A significant change of work function due to UV illumination of the system, not only results in peculiar photoemission spectra, but is explained by excess electron induced generation of $OH^-$ within the *dielectron hydrogen evolution reaction*.

## 6.4    Trapped electron induced chemistry at the ASW/vacuum interface

The possibility to efficiently localize and trap charges at the ASW-vacuum interface paves the way for investigations of interactions of these excess charges with their environment. Trapped electrons at ice-crystallites have been used before to trigger chemical reactions e.g. $CFCl_3$-dissociation [Ber09, Stä12]. Due to their extremely long residence times and location at the vacuum interface, the reaction cross section is enhanced.

In this chapter, it is shown that this is also the case for trapped electrons at the ASW/vacuum interface. Electron-induced chemistry is observed that modifies the sur-
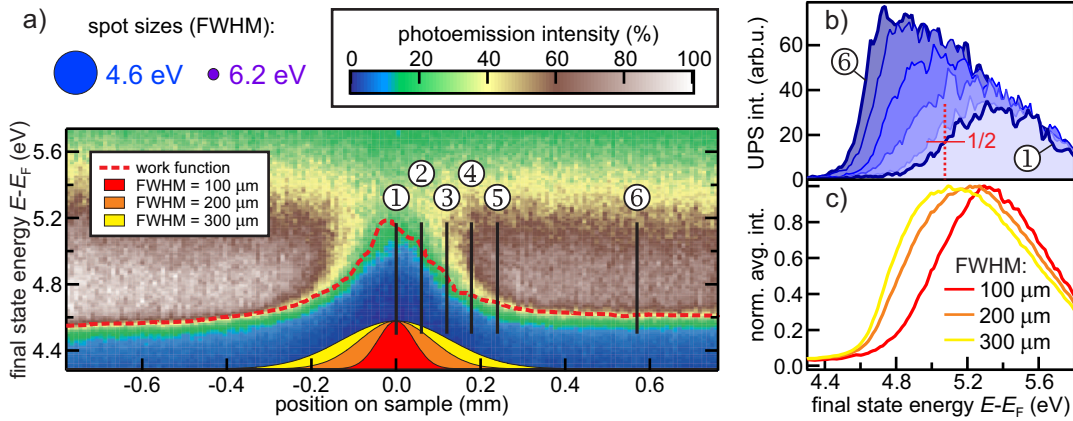
**Figure 6.8:** Photoinduced modification of the work function of $D_2O/Cu(111)$: a) The relative beam sizes of 4.6 and 6.2 eV beams used to modify and probe the work function of the sample, are indicated by the blue and violet circles. The low energy region of photoemission spectra are displayed in the 2D plot with respect to final state energy and probing position on the sample. The red curve shows the spatial progression of the extracted work function for this dataset. In b) lineouts from a) at the positions indicated by the black lines and numbers, are shown. The result of spatially averaging over various widths, indicated by the Gaussian curves at the bottom of a) is displayed in c). Adopted from [Weg13].

face chemical composition of the ice layer itself. This leads to significant changes of the vacuum potential: A photon dose dependent, persistent, work function change of up to 1 eV is the result of a modification of the surface electronic structure by the trapped electron species. The *dielectron hydrogen evolution reaction* [Bar11] is proposed, as the underlying mechanism for $OH^-$ generation that modifies the vacuum potential.

In addition, it is found that the change of work function affects the photoelectron spectra in a very distinct way for photon energies close to the sample work function. This effect is universal and is proposed to be observed in various photo(re)active systems. Their peculiar effect on photoemission spectra is described very well by a simple phenomenological model in Appendix G.

### 6.4.1 Spatially varying photoinduced work function change

The low-energy cut-off of spectra in photoemission spectroscopy is determined by the work function $\Phi$ of the investigated system, as the kinetic energy $E_{\text{kin}}$ of photoemitted electrons

$$E_{\text{kin}} = n \cdot h\nu + (E - E_{\text{F}}) - \Phi, \tag{6.65}$$

with the order of the emission process $n$ and photon energy $h\nu$, has to be positive. Even electrons with the lowest binding energies ($E = E_{\text{F}}$) are only emitted if the photon energy $h\nu$ (or for higher order photoemission its multiples) is larger than the work function $\Phi$. The low-energy cut-off can therefore be used to directly determine the work function of the investigated sample. A spatially dependent change of work function is observed as follows: A high power (1.3 mW average power), large diameter ((FWHM = 110 $\mu$m)) beam with $h\nu = 4.6$ eV is employed to populate trapped electron

sites for a duration on the order of 3 minutes, as presented in Section 6.3. The impact of those trapped electrons is then afterwards measured by spatially scanning over the previously illuminated area with a very weak (600 nW average power) and smaller (FWHM = 25 $\mu$m) beam with h$\nu$ = 6.2 eV photon energy. The relative beam sizes are indicated in Figure 6.8 a). In the false colour plot, photoemission intensity is shown with respect to final state energy $E - E_\mathrm{F}$ (i.e. the energetic position of the low energy cut-off corresponds to the work function with respect to the Fermi energy) and the sample position with respect to fixed laser beam and photo-electron analyser. The large diameter 4.6 eV beam was centred at zero position. The red dashed line indicates the local work function of the sample and is determined by analysing the low energy cut-off position for various line-outs[73]. The shape of this distribution qualitatively follows the 4.6 eV beam profile. The spatial resolution is on the order of the 6.2 eV probe spot size (25 $\mu$m).

Selected line-outs, as indicated by the black lines and numbers in a), are displayed in b). An exemplary half rise position is sketched (red lines). The lineouts show remarkably different low-energy cut-off positions and edge widths. ⑥ corresponds to a lineout that has not previously been illuminated by the 4.6 eV beam. A work function of $\Phi$ = 4.61 eV has been determined here. In the centre position of the 4.6 eV beam (at ①), the effective work function is $\Phi$ = 5.16 eV, thus the 4.6 eV illumination has increased the work function by more than 0.5 eV. The effect on averaged photoemission spectra is illustrated by integrating over distinct spatial extents (indicated by the red, orange and yellow Gaussian curves in a)) in c): Cut-off positions differ by 230 meV between 100 and 300 $\mu$m spot sizes and the edge width (20 % to 80 %) is not only comparably large, but also differs between 220 and 300 meV.
The importance of this observation is manifold:

- Such a spatially inhomogeneous work function distribution affects experimental procedures: referencing to the low energy cut-off becomes non-trivial as its position is only locally defined. Often, the low energy cut-off is used to determine the experimental energy resolution of photoemission experiments. The apparent resolution can therefore be underestimated due to a varying work function distribution, if the measurement averages spatially.

- A photoinduced change of work function is a strong indicator for significant changes in the surface electronic structure, which can be caused by photodesorption or other types of photochemistry. This means that the measurement process is highly invasive and modifies the system.

- Electron induced photochemistry at the vacuum interface can be exploited to enhance certain chemical reactions via the generation of trapped electrons.

A phenomenological model that describes the effect of such a spatially varying work function distribution on low-energy photoemission spectroscopy is presented in Appendix G.

In the following Section, the underlying mechanism for this work function change is addressed: The dielectron hydrogen evolution reaction is proposed to generate OH$^-$

---

[73]the half rise position was used as an effective edge position

that resides at the vacuum interface and thereby persistently changes the surface dipole,
i.e. the work function.

### 6.4.2  Mechanism of work function modification in $D_2O/Cu(111)$

To gain additional insights into the underlying mechanism of the persistent photo-
induced work function increase, observed in 15-30 BL amorphous $D_2O/Cu(111)$ at
low temperatures (40 K), the transient evolution (in real time) of the work function
change upon illumination is examined in detail. In experiments using only UV-light
with a photon energy $h\nu = 4.6$ eV, the work function is at the same time modified and
probed, as discussed in Appendix G. A microscopic model, explaining work function
change and decrease of trapped electron signal at the same time, is used to shed light
on the underlying mechanism in the following.
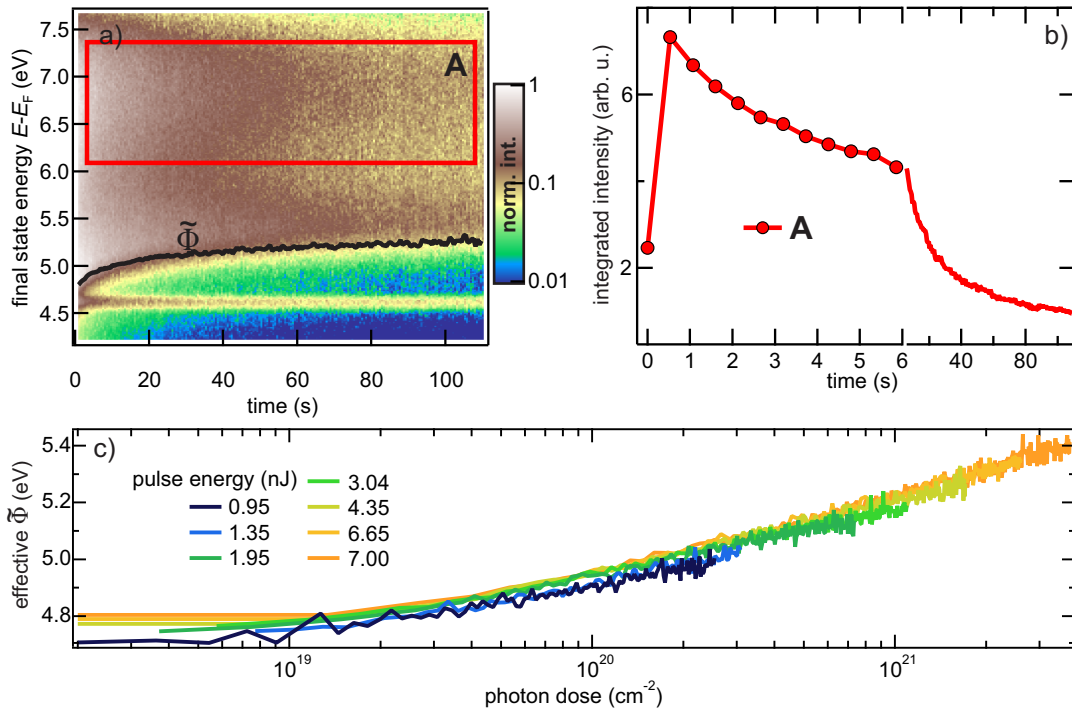


**Figure 6.9:** Transient changes of photoemission spectra under UV-illumination: a) Photoe-
mission intensity ($h\nu = 4.6$ eV) with respect to final state energy and illumination time encode
in a false colour scale. $\tilde{\Phi}$ is the effective work function extracted from the low-energy cut-off.
b) Shows integrated intensity in the energetic region indicated by the red box in a). The work
function change with respect to photon dose for indicated pulse energies is shown in c).

The spectral changes that happen upon illumination of a previously non-illuminated
spot on the sample are summarized in Figure 6.9: Photo-electron spectra with respect
to a final state energy $E - E_F$ and real time are shown in a 2D false colour plot in a).
The black line is the edge position (at half maximum amplitude) for the low energy
cut-off[74] of the 2PPE-part of the spectra and is a marker for the average/effective

---

[74]The feature at 4.6 eV is due to 1PPE from spatial areas with a work function lower than the photon

work function $\tilde{\Phi}$.[75] One can clearly observe that under illumination the effective work function increases with time.

Furthermore, the trapped electron state $e_T$, previously identified in the energetic region A, looses intensity. b) Shows the integrated intensity of this region with respect to real time: It decreases on a similar timescale as the work function increases.

Both, work function increase and intensity decrease, are persistent and do not relax back to their initial value, when the sample is left in the dark for hours. The trapped electrons with lifetimes of tens of seconds can therefore not only cause the observed changes by themselves, but must induce some permanent modification in the adsorbate.

To gain additional information about the driving force for the work function change, intensity-dependent measurements have been carried out, each on previously not illuminated spots on the sample, i.e. under the same initial conditions. When plotted with respect to the deposited photon dose $d = I \times t$ ($I$ = light intensity, $t$ = illumination time), the transient work function curves lie on top of each other, as shown in Figure 6.9 c). This means that the work function increase depends only on the photon dose, i.e. is a linear with light intensity. In summary the observations are:

① The amount of trapped electrons reduces.

② The work function increases on the same timescale.

③ The photon dose determines the total work function change.

In Section 6.3.2 it was shown that the population of trapped electrons within a quasi-stationary limit $n_\infty$ is (Equation 6.62):

$$n_\infty = \lim_{t,\tau \to \infty} n(t) = \frac{a \cdot N}{a + b} := N \cdot \beta \quad \text{with} \quad \beta = \frac{a}{a + b} \tag{6.66}$$

① demands that $n_\infty$ becomes dependent on illumination time: $n_\infty \to n_\infty(t)$. Under the assumption that the population and depopulation cross sections ($a$ and $b$) stay constant, this means that $N$ must change with illumination time: $N \to N(t)$

As the quasistationary population (Equation 6.66) is reached quickly, faster than the experimental resolution of 1/4 s, and the photoinduced change happens on a timescale of many seconds it can be assumed that (in contrast to a modification of the underlying rate equation 6.60)

$$n_\infty(t) = N(t) \cdot \beta, \tag{6.67}$$

i.e. the amount of occupied trapped electron sites $n_\infty(t)$ follows the change of the total amount of available sites $N(t)$. The expression is still independent of light intensity, contradicting ③: An increased fluence does speed up the observed changes. Hence, $N(t)$ must become a function of light intensity $I$[76].

---

energy and is discussed in detail in Appendix G

[75]The exact spatial work function distribution is neglected at this point, as it would complicate the analysis further. For details see sections 6.4.1 and G.

[76]The fact that the work function change depends on photon dose $d = I \cdot t$ implies directly that it is a function of $t \cdot I$

The work function of a system consists of at least two contributions: The crystal potential $\mu$ and the surface dipole barrier $D = -ep/\epsilon_0 = -e\mu_0\rho_{\text{dip}}/\epsilon_0$ [Leu03, Mon12]

$$\Phi = -\mu - \frac{e\mu_0\rho_{\text{dip}}}{\epsilon_0}. \tag{6.68}$$

The photo-induced change of work function is then most likely due to a modification of the latter surface dipole term, commonly observed when adsorbing atoms or molecules. Microscopic dipole moments are generated, due to charge transfer [Ger70], ordered adsorption of molecules with intrinsic dipole moment [Blu00, Duh08] or both [Cri11, All03]. To irreversibly change the surface dipole in $D_2O$/Cu(111) either some ordering of the intrinsic water dipoles, or a chemical reaction leading to a new species with modified dipole moment (e.g. $OD^-$) is needed.

Assuming that the change of work function is connected to the trapped electrons (②) it should have two contributions: 1. due to the negative charge of the trapped electrons at the surface themselves, which is proportional to their population $n_\infty(t)$ and 2. due to the amount of already modified trapping sites, proportional to $N_0 - N(t)$ (with $N_0$ the initial amount of potential trapped electron sites before illumination):

$$\Delta\Phi_{\text{tot}}(t) = A \cdot (N_0 - N(t)) + B \cdot n_\infty(t) \tag{6.69}$$
$$= A \cdot N_0 + N(t)\left[\beta B - A\right] \tag{6.70}$$

The individual contributions to the total work function change is unclear, as effective dipole moments are unknown. Parameters $A$ and $B$ are introduced that correspond to the effective weighting of both contributions.

The question then remains how the total amount of trapping sites is modified, i.e. what is the underlying mechanism or, mathematically speaking, how does the number of modified sites $N_0 - N(t)$ depend on time $t$?

One possible electron-induced chemical reaction is the so-called *dielectron hydrogen evolution reaction*[77] [Bar11]:

$$(D_2O)_n^{-2} \longrightarrow (D_2O)_{n-2}(OD^-)_2 + D_2 \tag{6.71}$$
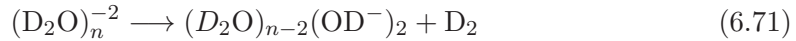
In a doubly charged cluster of $n$ water molecules, the two excess electrons induce two covalent bond breaks in adjacent water molecules. Thereby two hydroxide ions ($OD^-$) and one hydrogen molecule ($D_2$) are formed. If this reaction happens at the ASW/vacuum interface and the hydroxide ions remain at the ice surface, this could explain the observed permanent work function increase.

In line with this *dielectron hydrogen evolution reaction* (Equation 6.71) *two* electrons are involved in the reaction. At least one of them has to be in a trapped state to enhance the reaction, otherwise the work function change would be observed at any ASW coverage and not only in thicker adlayers. Also the change of trapped electron signal strongly indicates their involvement. Figure 6.10 illustrates three possible ways to realise such an electron 'pairing' for this reaction. The already trapped electron is

---

[77]As a possible candidate for the slightly less specific bimolecular water reduction reaction, also called hydrogen evolution disproportionation reaction or hydrated-electron bimolecular self-recombination [Bar11]. H is replaces by D, because heavy water was used in the present experiments. While reactions rates might change due to this replacement, no change of the general mechanism is expected.
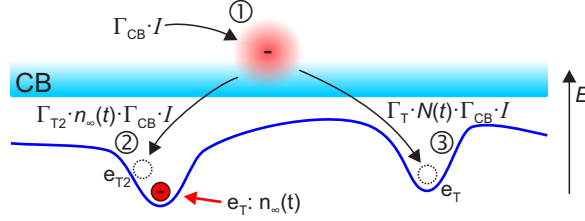
**Figure 6.10:** Dielectron hydrogen evolution reaction at the ASW surface. Possible scenarios, involving two electrons, are: One trapped electron (red arrow) interacts with: ① an electron in the ice conduction band (CB), ② a subsequently trapped electron $e_{T2}$ in the same trapping site or ③ a subsequently trapped electron in any trapping site. Transfer rates are indicated (see main text for details).

indicated by the red arrow. A second electron arrives at the surface, most likely via the ice conduction band (CB). Then, the already trapped electron and ...

① ... this second electron in the CB directly induce the reaction. The reaction rate then is proportional to the excitation probability into the CB ($\Gamma_{CB}$) and the laser intensity $I$, as well as the number of already trapped electrons ($n_\infty(t)$):

$$\dot{N}(t) = -\gamma \cdot \Gamma_{CB} \cdot I \cdot n_\infty(t) \qquad (6.72)$$

$$= -\gamma_1 \cdot I \cdot N(t) \qquad \text{with: } \gamma_1 = \gamma \cdot \Gamma_{CB} \cdot \beta \qquad (6.73)$$

$$\Rightarrow N(t) = C_1 e^{-\gamma_1 \cdot I \cdot t} \qquad (6.74)$$

The constants are combined with the reaction probability $\gamma$ into a single rate constant $\gamma_1$ and $C_1$ is determined by the initial conditions. Equation 6.67 was used to transform $n_\infty(t)$ to $N(t)$, the total amount of trapping sites.

② ... and an electron from the CB, subsequently trapped in *the same* site, induce the reaction. The reaction rate then is proportional to the excitation probability into the CB ($\Gamma_{CB}$) and the laser intensity $I$, as well as the trapping probability for a second electron ($\Gamma_{T2}$) and to the number of trapped electrons ($n_\infty(t)$) squared, i.e. once for the already trapped electrons and once for the trapping of the second electron:

$$\dot{N}(t) = -\gamma \cdot \Gamma_{T2} \cdot n_\infty(t) \cdot \Gamma_{CB} \cdot I \cdot n_\infty(t) \qquad (6.75)$$

$$= -\gamma_2 \cdot I \cdot N(t)^2 \qquad \text{with: } \gamma_2 = \gamma \cdot \Gamma_{T2} \cdot \Gamma_{CB} \cdot \beta^2 \qquad (6.76)$$

$$\Rightarrow N(t) = \frac{1}{\gamma_2 \cdot I \cdot t - C_2} \qquad (6.77)$$

The constants are combined with the reaction probability $\gamma$ into one constant $\gamma_2$ and initial conditions define $C_2$.

③ ... and an electron from the CB, subsequently trapped in *any* site, induce the reaction. The reaction rate then is the same as for ②, except that the second electrons trapping probability scales with all free sites $N(t)$ instead of only the

occupied sites $(n_\infty(t))$:

$$\dot{N}(t) = -\gamma \cdot \Gamma_T \cdot N(t) \cdot \Gamma_{CB} \cdot I \cdot n_\infty(t) \tag{6.78}$$

$$= -\gamma_3 \cdot I \cdot N(t)^2 \qquad \text{with: } \gamma_2 = \gamma \cdot \Gamma_T \cdot \Gamma_{CB} \cdot \beta \tag{6.79}$$

$$\Rightarrow N(t) = \frac{1}{\gamma_3 \cdot I \cdot t - C_3} \tag{6.80}$$

As before, the constants are combined with the reaction probability $\gamma$ into $\gamma_3$ and initial conditions define $C_3$.

The solution for ② and ③ yield the same analytical form for $N(t)$. With initial conditions $N(0) = N_0$, the constants are $C_1 = N_0$ and $C_2 = C_3 = -1/N_0$. Inserting the solution $N(t)$ into Equation 6.70 yields the expected change of work function with time. The photoemission intensity from trapped electrons is proportional to their number (Equation 6.67), also defined by $N(t)$. This means that one can fit both experimental observations with the function $X(t) = \tilde{A} + \tilde{B}N(t)$ with the respective $N(t)$, corresponding to model ①, ② and ③ and compare the results.
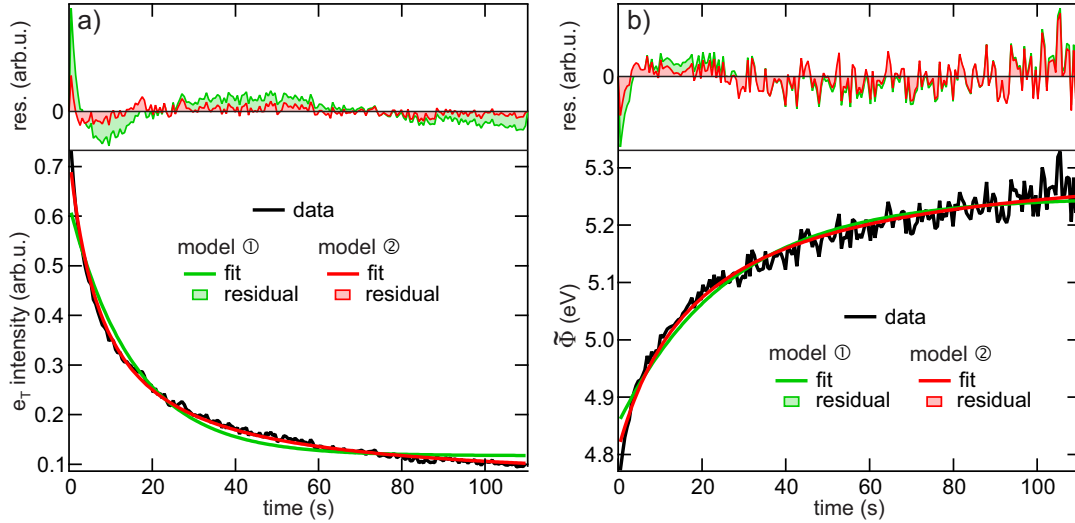


**Figure 6.11:** Comparison of two model fits for transient changes of the ASW/vacuum interface, based on the dielectron hydrogen evolution reaction (see main text for details). a) Shows the global fit to the decreasing trapped electron intensity and b) to the increasing effective work function. Model A (red) assumes one trapped electron and one that is simply 'flying by' initiates the reaction, whereas model B (blue) assumes both electrons are trapped. This analysis favours model B, because the fit residuals corresponding to B are smaller, i.e. the fits describe the data better.

Figure 6.11 shows a comparison of fits to experimental data based on the two functional dependencies (model ① and ②/③). a) Displays the decrease of signal from $e_T$ (black) and the fit with model ① in green and model ②/③ in red. The red curve (model ②/③) is able to describe the evolution of the measured signal better than the green one. This becomes clearer when considering the residuals of the fits (top part of

the graph). The difference between data and fit are shown in the respective colours. The residual is smaller for model ②/③ and constantly close to zero.

b) Shows the change of effective work function ($\tilde{\Phi}$) and fits according to the two models. Again the model corresponding to ②/③ (red) describes the data better than the one for ① (green), even though the difference is not as pronounced as in a), as evident from the fit residual shown at the top of the graph. The residual of the model ②/③ is only slightly smaller than the one of model ①.

Both fits favour the analytical function derived for model ② or ③ over the one for model ①. This means that the reaction is more likely to happen with two electrons that are both trapped. Model ③ also includes interactions between arbitrarily distant trapped electrons, hence ② might be the more reasonable choice. This is in agreement with investigations of liquid water clusters [Bar11], where also two electrons in one single solvation cavity induce this reaction. **The transient changes of photoemission spectra are described well by a consistent model, based on the dielectron hydrogen evolution reaction.** Pairs of trapped electrons at the ASW/vacuum interface react with pairs of $D_2O$ molecules, generating a pair of hydroxide ions and a hydrogen molecule. This blocks electron trapping sites and thereby reduces their total number $N(t)$, which leads to a reduced occupation $n_\infty(t)$ and therefore, a decrease of trapped electron photoemission signal. At the same time the hydroxide ions at the ASW/vacuum interface change the work function of the system.

# 6.5   Excess electrons in ASW: Long residence times enhance reactivity

Photoemission spectroscopy has been used to investigate various aspects and properties of excess electrons in amorphous solid water (ASW). Figure 6.12 summarises the findings. The large band gap ($\sim 8$ eV) of ASW allows for a selective excitation of electrons within the Cu substrate. A few of the exited electrons in the metal are transferred to the adsorbate layer, i.e. true excess electrons are generated.

Solvated electrons that are stabilised due to screening of the polar environment are used as a defined, local electron source, to investigate the mean free path (①) of low excess energy electrons in ASW. A maximum value of 10 Å is found, which must stem from effective scattering with phonons or defects, as electronic states are too well separated by the large band gap[78].

For thicker ice layers at coverages above 15 BL, a new species of stabilised electrons appears: Trapped electrons at the ice-vacuum interface (②) are observed for many seconds after photoexcitation. Most likely surface defects stabilise and screen these excess charges so efficiently that they can be observed for such long times. This is not without consequence:

An electron induced chemical reaction, probably the dielectron hydrogen evolution reaction, is observed at the ASW/vacuum interface, which transforms water molecules into hydroxide ions and hydrogen molecules with the help of a pair of trapped electrons

---

[78]Only a transient population of excess charges in the conduction band could provide electronic scattering partners.
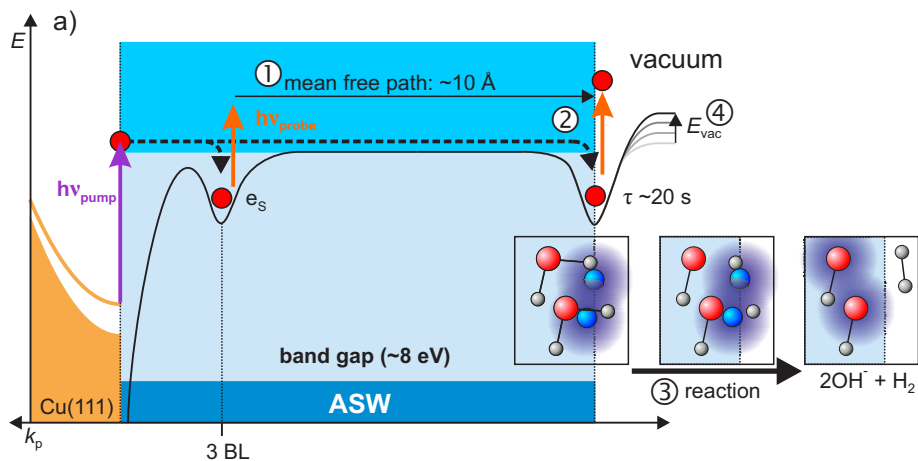
**Figure 6.12:** Summary of excess electron interactions within ASW: The mean free path of excess electrons ① is found to be 10 Å. At the vacuum interface excess electrons are efficiently trapped ② on a timescale of many seconds. This increases the reaction cross section and hydroxide is generated efficiently via the dielectron hydrogen evolution reaction ③. The surface electronic structure is modified by the accumulation of hydroxide at the surface ④.

(③). Such enhanced chemical reactivity is highly interesting in itself but also leads to a modification of the surface electronic structure of the system:

The work function increases (④) by up to 1 eV due to this reaction. This work function change depends on light intensity and is therefore spatially inhomogeneous, following the beam profile of the laser. This leads to specific and universal signatures in photoemission spectroscopy, described well by a phenomenological model (Appendix G).

# 7 Summary & Conclusion

The present work focuses on the ultrafast electron dynamics in solids and the respective role of screening of the Coulomb interaction. Screening is a collective response of charges that modifies the effective interaction between these charges. The questions how screening influences electron dynamics and how one can dynamically influence screening are addressed by investigating three model systems. The role of screening within these systems is outlined in the following, before a detailed description of all experimental findings is presented:

The (thermally and photoinduced) insulator-to-metal transition in Vanadiumdioxide ($VO_2$) has been studied by means of time-resolved optical and photoemission spectroscopy. A change in screening due to photoholes in the valence band of $VO_2$ is shown to lead to a band gap collapse in the insulating phase, turning the material into a metal, before its crystallographic structure changes.

The *modified* screening of the Coulomb interaction in two dimensions is investigated in the two-dimensional electron gas (2DEG) at the $SrTiO_3$/vacuum interface. Time resolved photoemission spectroscopy reveals modified quasiparticle scattering rates and distinct, two-dimensional, final states.

Dipolar screening of excess charges in a amorphous solid water (ASW, amorphous ice) has been exploited to trap electrons at the ASW/vacuum interface. Trapping for at least tens of seconds allows these electrons to enhance chemical reactivity at the surface of the ice layer.

While the screening of the Coulomb interaction is a universal effect that defines key properties in these three model systems, it is not the only interesting aspect to investigate. Hence, a more detailed overview of the results is given in the following:

**Instantaneous band gap collapse in $VO_2$: Photoinduced change of screening**
$VO_2$ exhibits a seemingly simultaneous electronic and crystallographic phase transition from insulating monoclinic to metallic rutile structure. This transition can, e.g., be driven by temperature or ultrashort light pulses.

Especially the driving mechanism behind the photoinduced insulator-to-metal transition in $VO_2$ is still debated. The seemingly simultaneous transition of the lattice structure raised the question which of both initiates the phase transition on an ultrafast timescale. This work contributes a significant amount of pieces to the puzzle: It is shown that the insulating phase loses its band gap and lattice potential symmetry instantaneously with photoexcitation. This happens with the atoms still in their initial monoclinic positions, i.e. is a purely electronic effect. In fact the role of screening is vital:

Photoexcitation across the insulators band gap generates photoelectrons and photoholes. Especially the latter open up intraband-transitions within the valence band that increase the screening of the Coulomb interaction to such an extent that the band gap collapses. This significant change in the valence electronic structure is likely to be responsible for the instantaneous symmetry loss of the lattice potential as well, because it defines the bonding between the atoms.

Further investigations would require a wider range of excitation densities, which were limited by the type of sample in this work. Single crystals on conducting sub-

strates would allow for stronger photoexcitation. This and the investigation of differently grown samples could clarify the large spread of measured quantities and proposed mechanisms in the literature regarding this intriguing system.

**Screening and electron dynamics in two-dimensions: The SrTiO$_3$/vacuum interface**

In two dimensions, electrons can screen the Coulomb interaction less efficiently, because their ability to 'move' is restricted in one spatial direction. This and the different phase space for electron-electron scattering in two dimensions modifies the lifetime of quasiparticles in such a system. How screening and phase space affect quasiparticle dynamics in the 2DEG at the SrTiO$_3$ (STO) surface has been investigated by time-resolved photoemission spectroscopy. Fermi-liquid theory predicts correct lifetimes as long as the electronic density of states (DOS) is constant. More localised bands at low excess energies lead to increased scattering rates with respect to those predictions.

Another aspect of the unoccupied electronic band structure of the STO surface, two distinct final states with the same two-dimensional character as the 2DEG, are discovered. Dynamically, a transiently increased filling of the 2DEG from localised in-gap states, was observed that relaxes on timescales of ballistic transport.

The screening in the 2DEG, and therefore the observed quasiparticle lifetimes depend on the carrier density. It would be interesting to vary this systematically (by changing the oxygen defect density) and find out if and at which carrier density Fermi liquid theory fails to predict quasiparticle lifetimes. Also, if the transient filling of the 2DEG could be increased even more, this could have a measurable effect on hot electron lifetimes. A three pulse experiment could be performed: 1. Strong near-IR excitation increases the filling of the 2DEG from in-gap states, 2. Hot carriers are generated by a second IR pump pulse and the hot carrier lifetimes after the second excitation could be investigated. As these lifetimes depend on the screening of the Coulomb interaction and, therefore, the carrier density, they could be 'tuned' by the excitation density of the first pulse.

**Screened excess electrons in amorphous ice: transmission, trapping and reactivity**

The idea of the last investigation was to use dipolar screening of excess charges in amorphous solid water (ASW) to stabilise them to such an extent that they enhance chemical reactivity. The electrons are literally trapped at the ice-vacuum interface for at least tens of seconds. There, they enhance a chemical reaction, most likely the dielectron hydrogen evolution reaction, resulting in the splitting of water molecules into hydroxide (OD$^-$) and hydrogen (D$_2$). The hydroxide ions stay at the surface and change the work function of the system dramatically.

Apart from this enhanced reactivity, the mean free path of low-energy electrons in ASW is estimated to be 10 Å at maximum. This is very short and indicates a strong interaction with defects and/or phonons, a result that is important in the field of radiation chemistry where interaction of secondary electrons with biological systems (that consist of water to a large extent) play an important role.

In the future, the study of the mean free path could be extended for different ice structures and sample temperatures. To substantiate the observation of the dielectron

hydrogen evolution reaction, an attempt could be made to detect the generated hydrogen.

These studies have contributed significantly to the understanding of electron dynamics considering the role of screening, and at the same time, open up new pathways for interesting future investigations. The initial driving mechanism of the photoinduced phase transition in $VO_2$ is found to be purely electronic, chemical reactions can be enhanced at the ASW/vacuum interface and the 2DEG at the STO surface shows interesting properties and its filling can be manipulated by light.

Given the conceivable concept of the general phenomenon of screening, its large impact on the properties of condensed matter is, in each particular system, intriguing and impressive.

# A    Screening of a point charge

The electrostatic potential $\Phi_0(\mathbf{r})$ of an electron obeys the Laplace equation $\Delta\Phi(\mathbf{r})$ and is

$$\Phi_0(\mathbf{r}) = \frac{e}{4\pi\varepsilon_0 \mathbf{r}}. \tag{A.81}$$

When additional mobile electrons with density $\rho(\mathbf{r})$ are present instead, The Poisson equation has to be solved:

$$\Delta\Phi(\mathbf{r}) = -\nabla\mathbf{E} = -\frac{\rho(\mathbf{r})}{\varepsilon_0} \tag{A.82}$$

Within Maxwell-Boltzmann statistics (ignoring the Fermionic character of electrons) the particle density of these additional electrons depends on potential energy $e\Phi(\mathbf{r})$, if $n_0$ is the density of the unperturbed system, without the excess charge:

$$n(\mathbf{r}) = n_0 e^{\frac{e\Phi(\mathbf{r})}{k_B T}} \tag{A.83}$$

The change in charge density is then $n_0 - n(\mathbf{r})$, generating a net *charge* density

$$\rho(\mathbf{r}) = -en_0\left[e^{\frac{e\Phi(\mathbf{r})}{k_B T}} - 1\right] \approx \frac{-e^2 n_\Phi(\mathbf{r})}{k_B T} \tag{A.84}$$

The first order linear approximation can be inserted into the Poisson equation in spherical coordinates A.82:

$$\Delta\Phi(r) = \frac{1}{r}\frac{\mathrm{d}^2(r\Phi)}{\mathrm{d}r^2} = \frac{-\rho(r)}{\varepsilon_0} = \frac{e^2 n_0}{\varepsilon_0 k_B T}\Phi(r) \tag{A.85}$$

With the Debye length $\lambda_\mathrm{D} = (\varepsilon_0 k_B T / n_0 e^2)^{1/2}$, this becomes:

$$\frac{\mathrm{d}^2(r\Phi(r))}{\mathrm{d}r^2} = \frac{r\Phi(r)}{\lambda_\mathrm{D}^2} \tag{A.86}$$

When considering the boundary conditions $\Phi(\infty) = 0$ and $\Phi(r \to 0) = \Phi_0(r)$ (Equation A.81), this becomes:

$$\Phi(r) = \frac{e}{4\pi\epsilon_0 r}e^{-r/\lambda_\mathrm{D}}, \tag{A.87}$$

which is the screened Coulomb potential of an electron (point charge) that has the form of a Yukawa potential. Using Maxwell-Boltzmann statistics is only correct for low electron densities, or far away from $E_F$ (i.e. in semiconductors). In the Thomas-Fermi approximation, which considers the fermionic nature of electrons, the Thomas-Fermi screening length $\lambda_\mathrm{TF}$ replaces the Debye length $\lambda_\mathrm{D}$:

$$\lambda_\mathrm{TF} = \sqrt{\frac{2\kappa\varepsilon_0 E_\mathrm{F}}{3n_0 e^2}} \tag{A.88}$$

For further quantum-mechanically correct treatments refer to [Cha99].
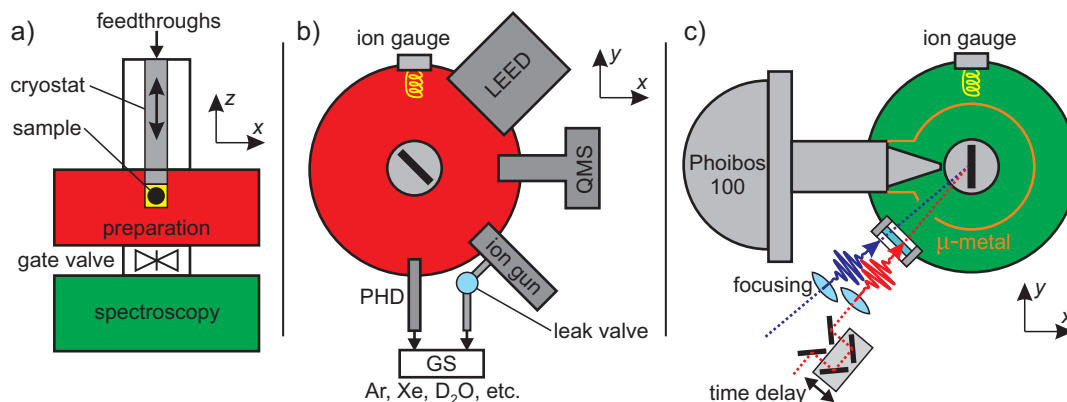
**Figure B.1:** UHV chamber: a) Sample is fixed on cryostat and can be moved (along $x$, $y$, $z$) and rotated (around $z$). UHV chamber for preparation (red) is separated from spectroscopy chamber (green) by a gate valve. Overview of preparation chamber is shown in b): LEED and QMS for characterisation, ion gun for single crystal surface preparation, PHD for $D_2O$ adsorbate dosing. The spectrometer part is displayed in c): Phoibos 100 electron analyser and incoupling window for focused laser pulses. Time delay control via linear translation stage is indicated. See text for details.

# B   Experimental setup for TR photoemission spectroscopy

Photoemission spectroscopy is performed inside an ultrahigh-vacuum (UHV) chamber to avoid contamination of the sample surface, which could significantly alter the photoemission signal due to the surface sensitivity of the technique. On the other hand, the sample surface has to be prepared by various procedures, sometimes involving comparably high background pressures (e.g. sputtering with Ar-ions, annealing under $O_2$-atmosphere and dosing of adsorbates). To separate spectroscopy from sample preparation the employed vacuum-chamber is divided into two parts, as shown in Figure B.1 a). Preparation (red) and spectroscopy (green) are separated by a gate valve. When the gate valve is open, the sample, which is attached to a liquid He/$N_2$-cryostat[79] (Cryovac), can be moved downwards (along $z$) from preparation to spectroscopy compartment. The linear movement along $x$-, $y$- and $z$-axis and rotation around $z$ is controlled by a motorised manipulator. Computer-controlled stepper motors outside of the UHV chamber move the cryostat and sample along with it.

A few key components installed in the preparation chamber are shown in b). A commercial LEED (low-energy electron diffraction) apparatus (SPECS) is used to characterise sample surface crystal structure. Residual gas analysis and thermal desorption spectroscopy (TDS) is performed using a quadrupole mass spectrometer (QMS, model: MKS satellite). The UHV pressure is monitored routinely via an ion-gauge.

For sample surface cleaning procedures (sputtering) an Ar-background pressure can

---

[79]Temperatures around 90 K are reached when cooling with liquid $N_2$, liquid He enables cooling down to 40 K.
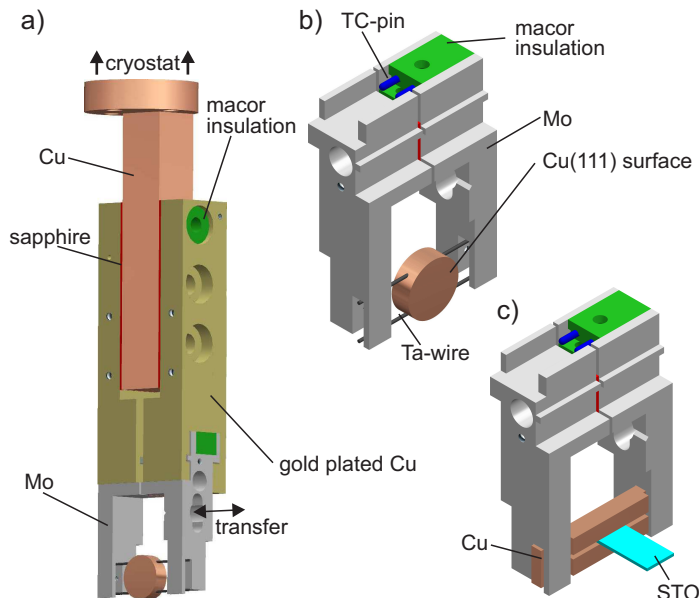
**Figure B.2:** a) Upper part of sample holder (Cu and gold plated Cu) is fixed at the cryostat. A transferable sample boat (Mo) is inserted along indicated direction and fixed via two screws at the back (not shown). Electrical insulation is done via macor® ceramics and sapphire pieces. b) Sample boat with Cu single crystal sample. Left and right side of boat act as electrodes for resistive heating via Ta-wires. Two thermocouple (TC) pins are used for temperature measurements. c) STO sample is glued into a grooved Cu-piece.

be set via a leak valve and an ion gun (SPECS) ionises and accelerates Ar-ions onto the sample. Light molecules and gases can be adsorbed on the sample via a home-built pinhole doser (PD). Gas enters the preparation chamber via a 5 $\mu$m diameter pinhole followed by a 22 mm long metal tube [Dei11]. The direct beam is blocked by a small piece of tantalum behind the pinhole. Collision of molecules with each other and the walls of the tube ensure a homogeneous molecular beam [Mey11]. The complex gas distribution system (GS), described in detail in [Dei11], is used to provide pure gases and adsorbates at defined pressures. It is thereby possible to adsorb distinct doses in a very reproducible manner.

A turbomolecular pump (Pfeiffer, HiPace 700, not shown) is used to keep the preparation chamber at a pressure in the range of $1 \times 10^{-10}$ mbar.

The spectroscopy part of the UHV system is routinely kept at a base pressure below $5 \times 10^{-11}$ mbar by additional ion- and Ti-sublimation-pumps, which easily keep such low pressures even when the gate valve is closed (i.e. the turbomolecular pump is disconnected from that part). A Phoibos 100 (SPECS) hemispherical electron energy analyser is used in this spectroscopy part to acquire photoemission spectra. Light is coupled in via a MgF$_2$ window. Focusing of pump and probe laser pulses with fused silica lenses[80] and temporal delay via a linear translation stage and retroreflecting arrangement of mirrors are set outside of the UHV system. The travel distance for photoelectrons is minimised by an extended analyser entrance nozzle reaching close (4 mm working distance) to the sample and is shielded from magnetic fields by a $\mu$-metal shielding.

**Sample holder and transfer** A versatile sample-holder, which allows sample-transfer into the UHV system, while providing controlled electrical contacts and allowing the use of temperature sensors, was needed to effectively investigate different types of sam-

---

[80]Custom broadband anti-reflection coatings (Laser Components) were employed to minimise losses.
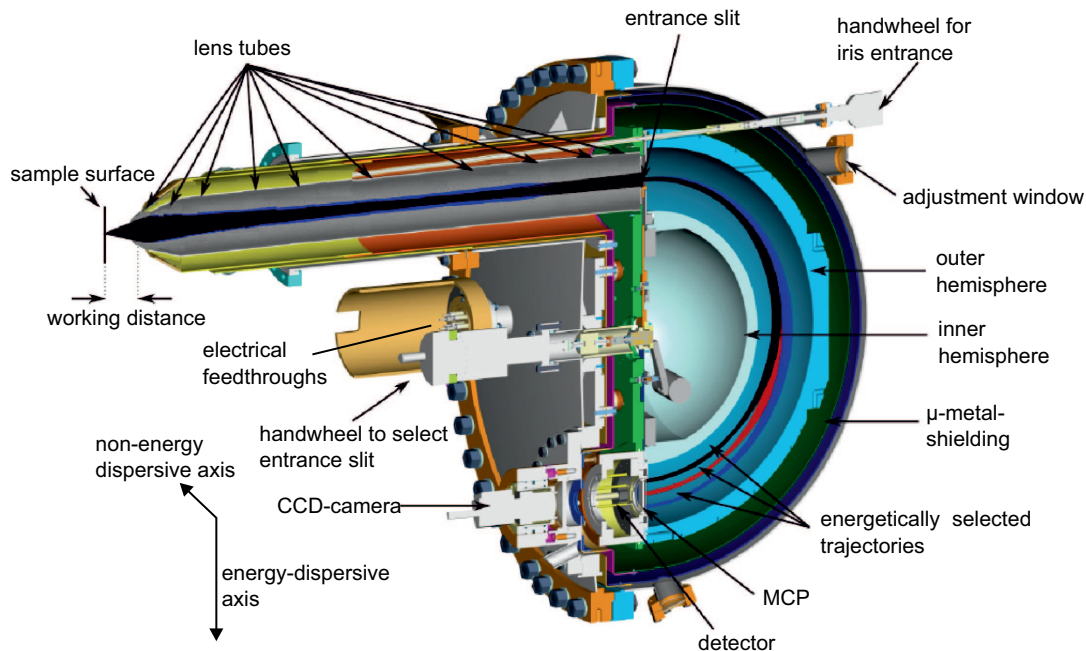
**Figure B.3:** Hemispherical electron analyser Phoibos 100: Photoelectrons enter the analyser through an adjustable lens system and entrance slit. Energy dispersion is introduced via two hemispheres along the vertical axis, while conserving the emission angle (horizontal, non-energy-dispersive axis). Analysed photoelectrons are amplified by a MCP and converted into photons via a phosphorous screen. A two-dimensional image is acquired by a sensitive CCD-camera (PCO sensicam QE), containing information about photoelectron energy on one, and emission angle on the other axis. Modified from [Dei11]).

ples. The sample-holder system described in [Hag09] fulfils those requirements and was therefore replicated.

A schematic drawing of the sample holder is displayed in Figure B.2 a): A central copper piece is fixed to the bottom of the cryostat. Two individually insulated (sapphire was used for high thermal conductivity instead of macor® ceramics) gold-plated Cu parts act as the slot for the transferable sample boat (which is crafted out of Molybdenum for better thermal endurance and to avoid fusing).

A detailed schematic of such a sample-boat is shown in Figure B.2 b). It consists of two electrically insulated Molybdenum parts, which thermally and electrically connect to the two gold-plated Copper pieces of the fixed sample holder in a). They act as electrodes for resistive sample heating via two Tantalum wires, which are used to fix the sample mechanically to the boat. Two thermocouple (TC) pins connect to two jacks on the bottom of the fixed part of the sample holder. The sample temperature can therefore be monitored over a wide range via thermocouple wires.

A differently mounted sample is shown in c): $SrTiO_3$ (STO) samples can be prepared for measurements by cleaving (i.e. breaking) them. Crashing the STO vertically into a fixed tool inside the UHV chamber exposes a clean surface for measurements. The sample therefore needs to be attached firmly to a Copper piece using conducting glue. Resistive heating is not possible in this case.

**Electron analyser Phoibos 100**   The probably most vital part of the setup is the electron energy analyser Phoibos 100 (SPECS), which allows analysis of photoelectron energy and emission angle simultaneously, via a two-dimensional detector. The system, currently in use, has been described and characterised in [Dei11].

A schematic view of the analyser is shown in Figure B.3. Photoelectrons, emitted from the sample surface, first enter a lens system consisting of several electrostatic lens tubes. The lens system can be used to manipulate the projection of the photoemitted electrons onto the entrance slit of the analyser, either conserving emission angle or spatial position of emission. More importantly the photoelectrons are accelerated in the lens system such that a certain moveable energetic window can be analysed.

The entrance slit size can be chosen via a magnetically coupled hand-wheel to adjust transmission versus energy resolution. The smallest possible slit (size: 200 $\mu$m) was selected for best energy resolution. The hemispheres act as a capacitor and generate a radial electric field $E(r)$:

$$E(r) = \frac{V_{\text{in}} - V_{\text{out}}}{r^2} \frac{R_{\text{in}} R_{\text{out}}}{R_{\text{out}} - R_{\text{in}}} \tag{B.89}$$

The field is defined by voltages $V_{\text{in/out}}$ and radii $R_{\text{in/out}}$ of of the inner and outer hemisphere and energetic dispersion is introduced along the radial direction, along $r$. The hemispherical geometry furthermore generates a focusing condition after passing 180° [Lüt01], such that an angular spread in $r$-direction behind the entrance slit does not affect the energy resolution. The energetically dispersed electrons are multiplied locally by a multi-channel plate (MCP of chevron type) and the electron bunches are subsequently converted into light on a phosphorous screen (type P43, time constant $\sim$ 1 ms) [SPEa]. A highly sensitive CCD camera (PCO sensicam QE) records this visual image of impinging electrons. The conversion from pixel $m_{\text{E}}$ to kinetic energies $E$ follows [SPEb]:

$$E = E_{\text{kin}} + De1 \cdot E_{\text{pass}} \cdot M \cdot Ps(m_{\text{E}} - \frac{M_{\text{E}}}{2}) \tag{B.90}$$

The parameters $E_{\text{kin}}$ and $E_{\text{pass}}$ define the energetic window that is simultaneously detected and can be set via the computer-controlled power supply (SPECS HSA3500). $De1$ is the energetic dispersion due to the hemispherical analyser, $M$ the magnification of the camera objective and $Ps$ the pixel size of the CCD chip. The latter three constants are saved in the windows operating system registry file. The total range of pixels $M_{\text{E}}$ along the energy dispersive axis is adjusted by the data acquisition software (National Instruments LabView), such that the acquired image is centred around the middle of the screen, i.e. centred around $E_{\text{kin}}$.[81]

The translation from pixel along the energetically non-dispersing direction $m_{\alpha}$ to emission angle $\alpha$ is slightly less trivial. Due to chromatic aberrations inside lens system and the hemispherical part of the analyser, the conversion is non-linear and depends on parameters $E_{\text{kin}}$ and $E_{\text{pass}}$.

Based on calculated electron trajectories, an image transformation (called unwarping) may nevertheless be performed. For a certain set of parameters, iso-angle lines can

---

[81]A removable slit aperture at the analyser exit plane is used for calibration.

**Figure B.4:**   a) Raw photoemission intensity image in false colours and exemplary iso-angle lines (red,orange,yellow). Magnified portion of a) is shown in b), as indicated by the black square. See text for details.
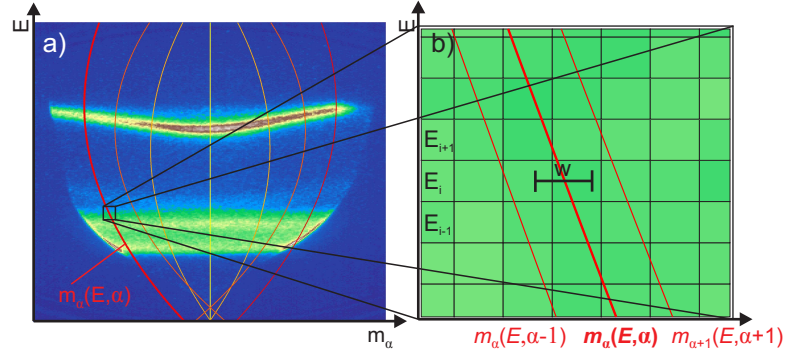
be calculated that describe how a constant emission angle looks after traversing the analyser. The pixel (number) $m_\alpha$ corresponding to the angle $\alpha$ at energy $E$ is given by the second order polynomial:

$$m_\alpha(E, r) = n_0(\alpha, r) + n_1(\alpha, r)E + n_2(\alpha, r)E^2 \tag{B.91}$$

The coefficients $n_i$ depend on the retarding ratio $r = E_{\text{kin}}/E_{\text{pass}}$ and are indirectly provided by SPECS via another polynomial expression and interpolation, as described in [SPEb]. Exemplary iso-angle lines are overlayed onto a raw-CCD image in Figure B.4 a). Clearly the iso-angle lines (red, orange, yellow) do not follow a constant pixel $m_\alpha$ along the angular direction.

One iso-angle line is calculated for each angle on the final image, to unwarp the image. An algorithm traverses one iso-angle line and for each energy $E_i$, the pixel intensities are averaged over in the horizontal direction $w$ between neighbouring iso-angle lines, as indicated in b). Proper weighting of intensities based on the local density of iso-angle lines is performed. Depending on the amount of angular distortion, which significantly depends on the projected angular range defined by the lens system, unwarping has to be performed before further data analysis.[82]

# C   Nonlinear optics

This section recapitulates the most important concepts of nonlinear optics that are used in this work. It is based on parts of the book 'nonlinear optics'[Boy08] and Â´Femtosecond Laser Pulses' [Rul05]. Quantities like electric fields and polarisations are treated as scalar and, if applicable, complex quantities for simplicity.

## C.1   Introduction

If the electric field strength $E(t)$ of electromagnetic radiation is on the order of the characteristic atomic field strength of $5 \times 10^{11}$ V/m[83], the nonlinear terms in $E(t)$ of

---

[82]In particular when angular dependence is discussed.

[83]While at the field-strength, mentioned above, strong photoionisation would make Equation C.93 invalid, already at lower light intensities nonlinear effects start to play a role[Boy08]

the induced polarisation of matter are on the same order of magnitude as the linear one:

$$P(t) = \epsilon_0 \left( \chi^{(1)} E(t) + \chi^{(2)} E^2(t) + \chi^{(3)} E^3(t) + \dots \right) \tag{C.92}$$

$$= P^{(1)}(t) + P^{(2)}(t) + P^{(3)}(t) + \dots, \tag{C.93}$$

The material response is now characterized also by higher order nonlinear optical susceptibilities $\chi^{(n \neq 1)}$. The resulting nonlinear order polarisation components $P^{(n \neq 1)}(t)$ act as a source term in the wave equation, adding new components of electromagnetic radiation:

$$\frac{d^2 E}{dz^2} - \frac{\epsilon(\omega)}{c^2} \frac{\partial^2 E}{\partial t^2} = \frac{1}{\epsilon_0 c^2} \frac{\partial^2 P^{(n \neq 1)}}{\partial t^2} \tag{C.94}$$

The second order polarisation $P^{(2)}(t)$ will generate new frequencies by mixing two fundamental frequency components $E_i(t) = e^{-i\omega_i t}$, due to the quadratic dependence on $E(t)$. There are three waves involved altogether, hence the name three-wave mixing. Higher orders of $P$ will subsequently add an additional wave component resulting for example in four-wave mixing etc.

## C.2   Second order effects and conservation laws

Inserting two plane wave components $E(x,t) = e^{-i\omega_1 t} + e^{-i\omega_2 t} + $ c.c. at a frequencies $\omega_{1/2}$ into the second order term of Equation C.93, immediately leads to polarisation contributions at the sum and difference frequency $\omega_3 = \omega_1 \pm \omega_2$, corresponding to sum and difference frequency generation (SFG and DFG). Also the second harmonic at $2\omega_{1/2}$ is generated (SHG). In a particle picture two photons of energy $\hbar\omega_1$ and $\hbar\omega_2$ create a single photon of energy $\hbar(\omega_1 \pm \omega_2)$, thereby fulfilling energy conservation.

The analogy to momentum conservation in nonlinear optics comes into play when considering the spatial dependence of the propagating plane wave. The amplitude of the newly generated components changes with propagation at the 'spatial frequency' $\Delta k = k_1 + k_2 - k_3$, which is called wavevector or momentum mismatch. Integrating over the full propagation distance $L$ yields an expression for the newly generated field component:

$$I_3 \propto I_1 I_2 L^2 sinc^2 \left( \frac{\Delta k L}{2} \right) \tag{C.95}$$

As shown in Figure C.1 a), this expression is only non-zero for small arguments $\Delta k L / 2$. As the intensity $I_3$ also scales with $L^2$, this implies small $\Delta k$ for effective an wave mixing process. In a particle picture this $\Delta k = 0$ corresponds to perfectly fulfilled momentum (wavevector) conservation. In terms of plane waves it corresponds to a situation where all waves included in the mixing process are in phase, hence the name phase-matching condition. As the refractive index $n(\omega)$ and therefore also the wavevector $k(\omega)$ usually increases with frequency (normal dispersion) in a non-resonant situation, the phase matching condition for SFG,

$$k_1 + k_2 = k_3 \tag{C.96}$$

$$n(\omega_1)\omega_1 + n(\omega_2)\omega_2 = n(\omega_3)\omega_3, \tag{C.97}$$

165
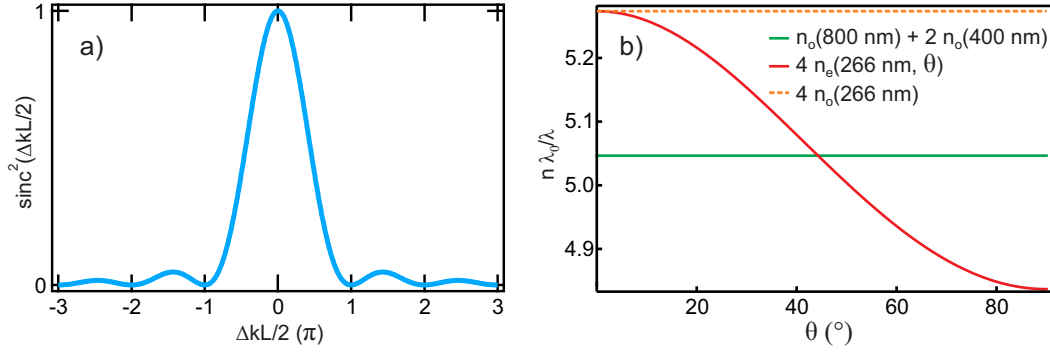
**Figure C.1:** a) Intensity dependence on wavevector mismatch according to Equation C.95. b) Phase matching condition in BBO for SFG of 800 nm and 400 nm photons, normalized to $\lambda_0 = 800$ nm: For the left hand side of Equation C.97 (green curve) the ordinary refractive index $n_0(\lambda)$ applies, as the polarisation of the fundamental waves at 800 and 400 nm is chosen perpendicular to the plane of propagation direction and optical axis. If the resulting sum frequency would also see the ordinary refractive index (dashed orange curve), the two curves would not intersect, meaning that the phase-matching condition cannot be fulfilled. If on the other hand the effective extraordinary refractive index, according to Equation C.98, (red curve) applies, the two curves cross at $\theta = 44.3\,^\circ$. This means that the resulting SFG photons will be polarized perpendicular to the two fundamentals.

can only be fulfilled by using mixed polarisations and birefringent non-linear optical crystals. Angle-tuning of the optical axis then changes the effective refractive index $n_{\text{eff}}(\theta, \lambda)$ at the angle between propagation direction and optical axis, $\theta$, according to

$$n_{\text{eff}}(\theta, \lambda) = \sqrt{\left( \frac{\cos^2 \theta}{n_{\text{o}}^2(\lambda)} + \frac{\sin^2 \theta}{n_{\text{e}}^2(\lambda)} \right)^{-1}} \tag{C.98}$$

Plotting the left- and right-hand side of Equation C.97 with respect to $\theta$ directly yields the phase matching angle at the point, where the two curves cross, as displayed in Figure C.1 b) for a BBO-crystal. The phase matching condition is met at an angle $\theta = 44.3\,^\circ$, if the fundamental (800 nm and 400 nm) beams are polarized perpendicular to the optical axis of the BBO, while the resulting SFG beam will be polarized perpendicular to the fundamental beams.

When leaving a collinear geometry, $k$ becomes a vector and the calculations get more complicated, but the overall concept remains the same. Using a non-collinear geometry is especially helpful for broadband optical-parametric amplification as described in [].

## C.3 Third order effects

According to Equation C.93, the induced polarisation in centrosymmetric media (i.e. $\chi^{(2)} = 0$) for a plane wave $E(t) = E(\omega)e^{-i\omega t}$+c.c. after dropping the complex conjugates

is:

$$\frac{P(t)}{\epsilon_0} = \chi^{(1)}E(\omega)e^{-i\omega t} + \chi^{(3)}\left(3E(\omega)^2 E^*(\omega)e^{-i\omega t} + E(\omega)^3 e^{-i3\omega t}\right) \tag{C.99}$$

$$= \left(\chi^{(1)} + 3|E(\omega)|^2\chi^{(3)}\right)E(\omega)e^{-i\omega t} + \chi^{(3)}E(\omega)^3 e^{-i3\omega t} \tag{C.100}$$

$$= \chi_{\text{eff}}E(\omega)e^{-i\omega t} + \chi^{(3)}E(\omega)^3 e^{-i3\omega t} \tag{C.101}$$

$$\text{with } \chi_{\text{eff}} = \chi^{(1)} + 3|E(\omega)|^2\chi^{(3)} \tag{C.102}$$

After dropping the third harmonic part (e.g. because phase-matching conditions are not fulfilled), identifying $|E(\omega)|^2 = I$, using $n^2 = 1 + \chi_{\text{eff}}$ and dropping some higher order contributions, linear ($n_0$) and nonlinear ($n_2$) parts of the refractive index

$$n_0 = \sqrt{1 + \chi^{(1)}} \tag{C.103}$$

$$n_2 = \frac{3\chi^{(3)}}{2n_0} \tag{C.104}$$

will justify the definition of an intensity dependent refractive index of the form

$$n(I) = n_0 + n_2 I. \tag{C.105}$$

Equation C.105 can then be used to explain several third order nonlinear effects, e.g. Kerr lens effect and self-phase-modulation.

## C.3.1   Kerr lens effect

The spatial intensity dependence of a laser beam can be assumed to be Gaussian $I(r) = I_0 e^{-\Gamma r^2}$. According to Equation C.105 this means that the refractive index in the centre of the beam is higher than in the wings and in fact follows the Gaussian intensity distribution. This has the same effect on the propagating wavefront as a convex lens, only that the optical path is increased towards the centre of the beam by the increasing refractive index $n(I)$ instead of the increased propagation distance through the medium (i.e. the centre part of the lens). The Kerr lens effect is also termed self-focusing.

## C.3.2   Self phase modulation

Self phase modulation can be understood in a similar fashion as the Kerr lens effect, but assuming a Gaussian intensity distribution of the laser pulse in time $I(t) = I_0 e^{-\Gamma t^2}$. An optical pulse propagating along the positive x axis, can be written as

$$E(x,t) = \sqrt{I(t)}e^{i(\omega_0 t - k(t)x)} \tag{C.106}$$

with

$$k(t) = \frac{\omega_0}{c}n(t) \tag{C.107}$$

$$\propto \tilde{n}_0 + \tilde{n}_2 I(t) \tag{C.108}$$
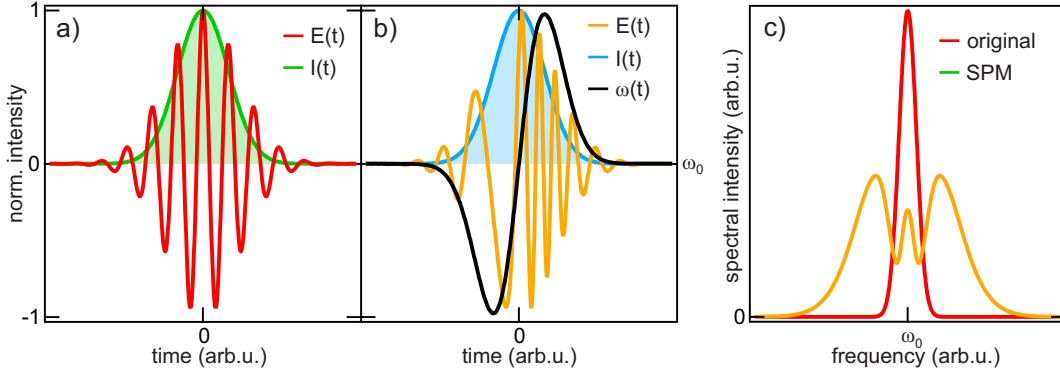
**Figure C.2:** Self phase modulation: a) Electric field (red) and intensity envelope (green) of a transform limited Gaussian laser pulse. b) Self phase modulation leads to a modification of the electric field waveform (orange), while leaving the intensity envelope (blue) intact. The instantaneous frequency (black) varies with time: the pulse is chirped. c) spectral intensity of original laser pulse (red) from a) and self phase modulated pulse (orange) from b).

The temporal phase of the oscillation becomes $\Phi(t) = \omega_0 t - \tilde{n}_0 x - \tilde{n}_2 I_0 e^{-\Gamma t^2}$ and from that the instantaneous frequency $\omega(t) = \partial \Phi(t)/\partial t$ can be calculated:

$$\omega(t) = \omega_0 + 2t\tilde{n}_2 I_0 e^{-\Gamma t^2} \tag{C.109}$$

A visualisation of the effect on pulse and spectrum is given in Figure C.2. A Gaussian laser pulse (oscillating electric field and intensity envelope) is displayed in a). Adding the effect of the intensity dependent refractive index leads to self phase modulation as depicted in b). When neglecting dispersion effects due to propagation the intensity envelope keeps its temporal shape. Fourier transforms of the pulses from a) and b) are displayed in c) and clearly show a spectral broadening due to self phase modulation.

# D   Excitation density in VO$_2$

Calculating excitation densities is no trivial task, not because the calculations are difficult, but because experimental parameters (e.g. spot size) possess rather large error margins and often it is unclear under which assumptions excitation densities are calculated. To minimize uncertainties the calculation for the excitation density in VO$_2$ is outlined here:

The absorbed light intensity $dI$ over a distance $dz$ is proportional to the incident intensity $I$, the absorption coefficient $\alpha$ and the distance $dz$ (yielding the Lambert-Beer law):

$$dI = -I \cdot \alpha \cdot dz \tag{D.110}$$

To calculate the amount of photons absorbed per unit cell $N$ in the surface layer of VO$_2$ the incident fluence in mJ/cm$^2$ is converted to number of photons [n] (800 nm or

1.55 eV) per unit cell [uc] and inserted in Equation D.110:

$$N \text{ [n/uc]} = \frac{6.25 \times 10^{15} \text{ [eV/mJ]}}{1.55 \text{ [eV/n]}} \times F \text{ [mJ/cm}^2\text{]} \times A \text{ [cm}^2\text{/uc]} \times \alpha \text{ [1/nm]} \times \mathrm{d}z \text{ [nm]}$$
(D.111)

For the (010) surface of $VO_2$, the monoclinic unit cell has a surface area of 26.05 $\text{Å}^2 =$ $26.05 \times 10^{-16}$ cm$^2$ [Eye02], the absorption coefficient at 800 nm is $\alpha = 0.01$ 1/nm [Gav72] and the unit cell dimension in surface normal direction is $\mathrm{d}z = 0.453$ nm [Eye02], therefore:

$$N \text{ [n/uc]} = 0.048 \text{ [cm}^2 \text{ n/mJ uc]} \times F \text{ [mJ/cm}^2\text{]}$$
(D.112)

As inhomogeneity of surface and interface effects do not allow for precise calculations of absorbed photons in the real system, the *incident* fluence is used as a maximum limit for calculated absorbed photon density. It is based on independent in-focus spot size (FWHM) measurements, using a CCD-camera (Ophir Spiricon SP620U with 4.4 $\mu$m pixel spacing), and incident power measurements, using a thermopile power detector (Newport). If the photon energy is sufficient to excite above gap, the number of absorbed photons is equal to the number of excited electrons in the conduction band. This approach allows for comparison with other experiments and yields an upper limit for the real deposited excitation density.

# E    Photoemission data treatment from Section 4.2.3

As mentioned in Section 4.2.3, great care was taken when analysing the photoinduced change of photoemission signal during the thermal phase transition in $VO_2$. This section describes the steps of data treatment that lead to Figure 4.25. As a clearest possible representation, the data (Figure E.1) is displayed with respect to the acquisition number of each photoemission spectrum.

The data was acquired continuously during heating (shown) and cooling (not shown) by measuring alternately at a delay $\tau = +1$ (pumped) and $\tau = -1$ ps (unpumped) for 500 ms each. 'Pumped' means that the probe pulse arrives 1 ps after the pump pulse and 'unpumped' the opposite order. The resulting raw data for the pumped case (same visual appearance as for the unpumped data set) is shown in Figure E.1 a) in a false colour scale with respect to acquisition number and kinetic energy (The energy axis is shifted arbitrarily at this point and will be fixed to a spectroscopic signature during later steps). Fluctuations of intensity (due to a thermally induced movement of the sample during heating) and charging (shift of the intensity along the energy axis) are observed.

The temporal ordering of pumped ($P_i$) and unpumped ($U_i$) acquisition cycles is precisely $P_1$, $U_1$, $P_2$, $U_2$, $P_3$, etc. during the measurement ($i$ is the number of acquisition cycles). To obtain the change induced by the pump pulse, unpumped spectra have to be subtracted from pumped spectra. Two obvious choices are possible *without* any raw data treatment: $P_i$ minus $U_i$ or the opposite way around $P_{i+1}$ minus $U_i$. The
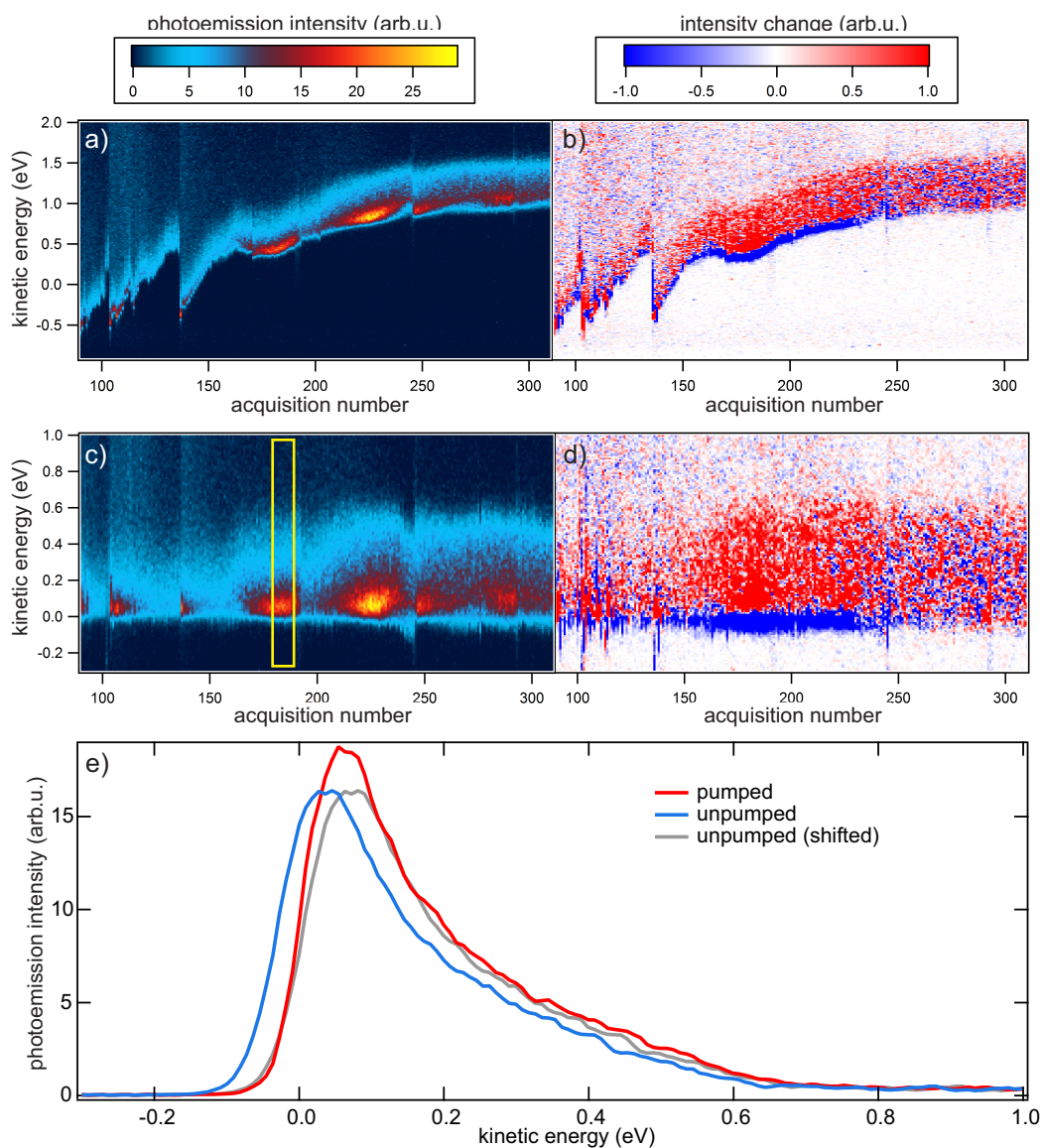
**Figure E.1:** Raw data treatment for Temperature dependence of photoinduced changes in VO$_2$: a) Shows raw data, b) shows photoinduced change after interpolating pumped and umpumped acquisition to a common point in time (see text for details). c) and d) shows datasets from a) and b) after correction for charging induced shifts. Averaged (over the region indicated by the yellow box in c)) spectra for unpumped (blue) and pumped (red) situation. The unpumped spectrum is shifted (grey) to indicate that such a rigid shift generate the red (pumped) spectrum.

first choice subtracts unpumped background, measured *after* the pumped spectrum, the second one *before* the pumped spectrum. Both choices result in *the same* contrast as shown in b): An intensity increase (red) at higher energies and a decrease (blue) at lower energies, at acquisition numbers between 160 and 250 (that is the thermal phase transition region, shown in Figure 4.25). The intensity change displayed in b) is in fact determined even more accurately by first interpolating $P_i$ and $U_i$ to an intermediate time between them. This is possible, because the exact time of measurement is recorded for each acquisition. Via this analysis and the fact that raw data subtraction for two different time orderings results qualitatively in the same photoinduced intensity change excludes shifts due to charging as a reason for the observed contrast (In the case of slow charging the sign of the contrast would change).

To correct for sample charging *after* this background subtraction procedure, the secondary edge (low-energy cut-off) was determined from one raw dataset at each acquisition. The raw data spectra in a) and also the intensity change spectra in b) were then shifted accordingly, based on this *single* value for each acquisition. These shifted datasets are shown in c) and d) respectively.

To further exclude rigid photoinduced shifts on a single acquisition timescale, pumped and unpumped raw data is averaged over 10 aquisitions (indicated by the yellow box in c)) and compared in e). The blue curve is from the unpumped dataset and the red one from the pumped one (both are interpolated to a common time, as described above). It is clear that the red curve is not just a rigidly shifted replica of the blue spectrum, but two distinct effects are observed: a change in secondary edge position (i.e. a work function change) and an photoinduced increase at higher energies (>0 eV). To illustrate this, a shifted replica of the blue (unpumped) curve is displayed (grey), such that the low-energy cut-off coincides with the red curve. Still the red (pumped) curve shows a higher intensity at most energies. This analysis clearly shows that the photoinduced increase *in the phase transition region* (see Section 4.2.3 for the actual temperature dependence) below the reference Fermi energy (at 0.6 eV in c) and d)) is a real increase of density of states, not just an artefact.

# F   Space charge effects

In photoemission spectroscopy, as soon as there is more than one electron emitted by an ultrashort laser pulse, the repulsive Coulomb interaction between emitted electrons has to be considered. While the proper treatment is a numerical simulation of electron trajectories, describing the real experimental conditions accurately, some qualitative aspects are considered here. Systematic experimental and theoretical investigations are for example presented in [Gra10, Hel12, Hel09].

Photoelectrons, emitted with kinetic energy $E_{\mathrm{kin0}}$, are accelerated by the potential difference, between sample and analyser work function, plus bias voltage $\Delta\Phi + U_{\mathrm{bias}}$, during their flight path of $\sim 4$ mm, before they enter the analyser. They are spatially densest, in the initial time after emission and disperse at later times, due to their different velocities. Only this initial region is therefore considered in a simplified plate-capacitor scheme. This is illustrated in Figure F.1 a):

A spatially thin disk of electrons (blue shaded ellipse) is emitted at time $t_1$, when
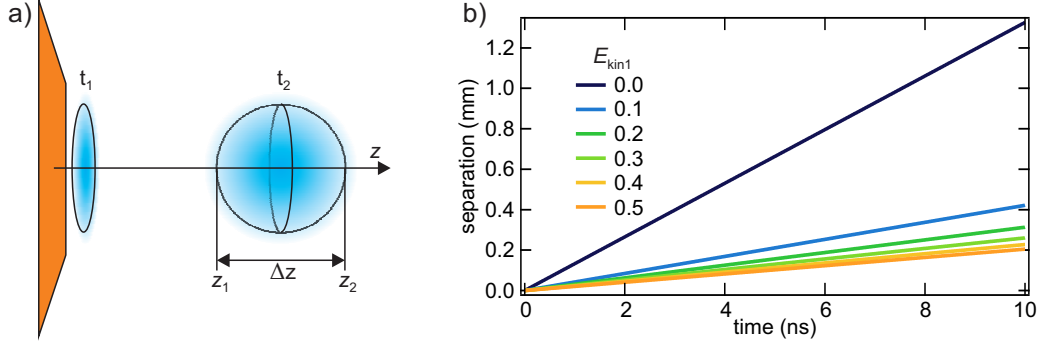
**Figure F.1:** .

space charge interaction is generally strongest. After propagation in vacuum at time $t_2$, the electrons have dispersed, due to their kinetic energy distribution and Coulomb repulsion. As a first extreme case, we start with no Coulomb interaction and consider the density of the electron cloud (in one dimension) to estimate the strength of space charge broadening. Textbook physics yield:

$$F = m \cdot a \tag{F.113}$$
$$= -\nabla V \tag{F.114}$$
$$= qE \tag{F.115}$$

Integration of the equation of motion and writing the electric field $E = -V/qd$ in terms of the potential drop $V$ over the distance $d$ gives the trajectory

$$x(t, E_{\text{kin0}}) = \frac{V}{2dm_e} \cdot t^2 + \sqrt{\frac{2E_{\text{kin0}}}{m_e}} \cdot t, \tag{F.116}$$

where the first term captures the acceleration by the potential V and is constant for all photoemitted electrons, and the second term captures the initial conditions (initial kinetic energy upon photoemission). The distance $\Delta x(t, \Delta E_{\text{kin}})$ between two photoemitted electrons, possessing an initial kinetic energy difference $\Delta E_{\text{kin}} = E_{\text{kin2}} - E_{\text{kin1}}$ is therefore:

$$\Delta x(t, E_{\text{kin1}}, \Delta E_{\text{kin}}) = \left( \sqrt{\frac{2(E_{\text{kin1}} + \Delta E_{\text{kin}})}{m_e}} - \sqrt{\frac{2E_{\text{kin1}}}{m_e}} \right) \cdot t \tag{F.117}$$

Assuming a spectral bandwidth of 1 eV for photoemitted electrons, a bias voltage of 1 eV over a sample-analyser distance of 4 mm and a emission spot size of 50 $\mu$ (FWHM), the total separation in $z$-direction is as large as the spot diameter (i.e. 50 $\mu$m) after $t_2 = 84$ ps. This confirms our initial assumption that only small times have to be considered. The photoelectrons starting with $E_{\text{kin}} = 0$ eV have then travelled to $z_1 = 0.2$ $\mu$m, while the fastest ones with $E_{\text{kin}} = 1$ eV are at $z_2 = 50.2$ $\mu$m.

In Figure F.1 b) the change of spatial separation with propagation time for pairs of electrons with kinetic energies of $E_{\text{kin1}}$ and $E_{\text{kin1}} + 50$ meV is displayed. Clearly low

initial energies lead to a large separation (i.e. lower density). From this consideration one can argue, that faster electrons are affected more strongly by vacuum space charge broadening than slower ones.

Of course switching off the Coulomb interactions might be considered a very crude approximation, especially when discussing an effect based on it. Therefore we now switch off the propagation and discuss the other extreme: The photoelectrons are space charge broadened only at time $t_1$, initially after emission. All electrons, no matter which initial kinetic energy they possess, will interact and repel each other. But no acceleration due to the bias voltage has happened yet, so the slowest electrons with $E_{kin} = 0$ eV could be pushed back an reabsorbed by the sample. Again space charge effects would only be visible at energies $E_{kin} > 0$. A decreased shift of the low-energy cut-off would be expected.

Reality probably is situated between those two extremes, but would only be accessible by means of complex numerical simulations including e.g. image charge effects. This is beyond the scope of this Appendix. Nevertheless qualitatively it seem that high energy features in photoemission spectra might be influenced more strongly by vacuum space charge effects, than e.g. the low energy cut-off.

For dynamic vacuum space charge effects observed in [Leu11], a characteristic timescale on the order of 100 fs has been reported at metal surfaces.

**Estimated detection efficiency of hemispherical analyser investigating STO**
In this paragraph an upper and lower estimate for emitted photoelectrons per laser pulse is given, for a specific experiment on STO (see Section 5.2). Two geometric considerations can reduce the ratio between detected and emitted electrons: If photoelectrons are emitted equally over a half solid angle $\Omega_0 = 2\pi$ (neglecting any band structure). The detection cone (in LAD analyser mode) with apex angle $2\theta = 16°\circ$ yields a solid angle of $\Omega_1 = 2\pi(1 - \cos(\theta))) = 0.061$ sr. The ratio between the two is $1 \times 10^{-2}$.

The employed analyser entrance slit has the dimensions of 20.2 mm$^2$, where the width of 20 mm corresponds to the apex angle of approx $\pm 8°$ and therefore restricts transmission further in one direction. This reduces the detection efficiency by a factor of $1.2 \times 10^{-2}$.

Combining both efficiencies in a worst case estimate yields $\gamma = 1.2 \times 10^{-4}$ detected electrons per emitted electron. A more optimistic estimate assumes uniform emission into the detection cone ($\pm 8°$), but no significant emission into the rest of the vacuum half-space. Only the reduction due to the slit of $\gamma = 1.2 \times 10^{-2}$ has to be considered then.

To translate this into meaningful numbers, for the investigations of the SrTiO$_3$ surface, a single electron counting algorithm was employed to analyse camera pictures, delivered by the 2D electron analyser (Phoibos 100 and SensiCam QE) in real time. For a moderate incident fluence of 1.7 $\mu$J/cm$^2$ (photon energy 4.6 eV, i.e. single photon photemission), 0.27 electrons per laser shot are detected on average. The worst case scenario then yields 2250 and the optimistic one 22.5 emitted electrons per shot. (Corresponding to 1300 and 13 emitted electrons per $\mu$J/cm$^2$).
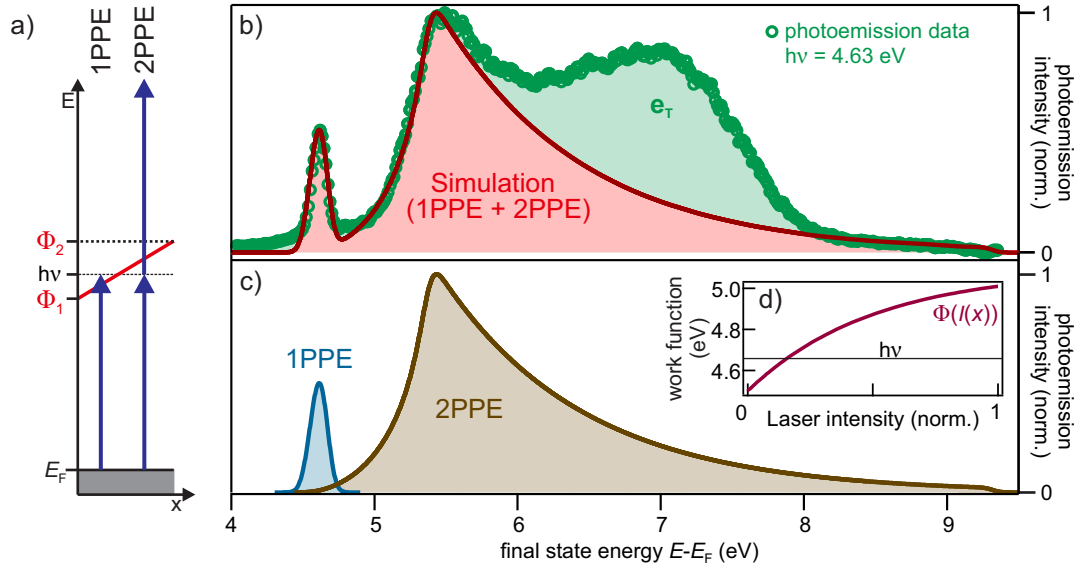
**Figure G.1:** a) Schematic view of a work function distribution (red) that crosses the photon energy (h$\nu$) and resulting in one- and two-photon-photoemission processes. b) Shows a measured photoemission spectrum (green markers, h$\nu$ = 4.63 eV) and the result of a model calculation (red curve, model described in the text) agree very well in the low energy region. Single- (blue) and two-photon (brown) contributions of the model are separately shown in c). The underlying work function distribution with respect to the laser intensity in the Gaussian beam profile is displayed in d). Adopted from [Weg13].

# G   Work function distribution and effect on photoemission spectroscopy

In Chapter 6 it has been shown that a spatial work function distribution leads to an effective shift and broadening of the low energy cut-off of photo-electron spectra, when photon energies are larger than the work function distribution (h$\nu$ > $\Phi$). For photon energies on the order of the work function distribution (h$\nu \sim \Phi$), the resulting photoemission spectra exhibit a very peculiar shape, as both single- and two-photon-processes can mix.[84] Such a situation is schematically shown in Figure G.1 a): At a position $x$, where $\Phi(x)$ is smaller than the photon energy h$\nu$, single photon photoemission (1PPE) is energetically possible, whereas at positions $x$, where $\Phi(x)$ > h$\nu$, two photons are needed to photoemit (2PPE) an electron even from the most weakly bound states (i.e. at the Fermi energy). A mixture of both processes is detected. The phenomenological model to describe such mixing and predict the resulting spectroscopy is simple:

- Under the assumption that the work function modification depends on photon dose or light intensity, a work function profile $\Phi(r)$ is calculated from the laser beam intensity profile $I(r)$. Different functional dependencies $f$ reflect different

---

[84]Short laser pulses, exhibiting high enough peak intensities and therefore supporting non-linear two-photon processes are a requirement for such a behaviour, which is usually met by time-resolved 2PPE and laser-based time-resolved ARPES sources.

underlying mechanisms: $\Phi(r) = f(I(r))$. An exemplary work function profile, calculated from an intensity profile $I$ of a 4.6 eV beam via

$$\Phi(I) = \Phi_0 + \Delta\Phi_{\text{max}}\frac{1 - e^{-\gamma I}}{1 - e^{-\gamma}}, \tag{G.118}$$

is shown in Figure G.1 d). In this case, $I$ is the normalized radial Gaussian light intensity $(I(r) = e^{-r^2/\beta})$ that generates a work function profile starting at $\Phi_0$ and saturating at $\Phi_0 + \Delta\Phi_{\text{max}}$.

- A density of initial states $DOS(E)$ and some photoemission cross section or transmission function $T(E)$ has to be assumed, reflecting the energy dependence of the emission process.

- The resulting 'spectrum' $DOS(E) \cdot T(E)$ is shifted up (i.e. to higher energies) from the initial state energy by the photon energy h$\nu$ for 1PPE$(E)$ and by two times h$\nu$ for 2PPE$(E)$, to get to the final state spectra.

- Both contributions are convolved separately with the energy bandwidth of the laser.

- For each work function $\Phi(r)$ the low-energy side of the spectra are cut at the respective position of $\Phi$, yielding 1PPE$(E, \Phi)$ and 2PPE$(E, \Phi)$.

- It is numerically integrated over $r$, assuming a linear intensity dependence for 1PPE and a quadratic one for 2PPE contributions. The global ratio $\xi$ between 1PPE and 2PPE is a free parameter and depends on various conditions (laser fluence, cross sections, etc.). The 2D character of the laser beam is accounted for by an additional weighting by the illuminated area, which is proportional to the radial position $r$.

- Finally the resulting spectrum is convolved by the energetic resolution of the detection apparatus.

Neglecting the mentioned convolutions for simplicity, the total yield $Y(E)$ is

$$Y(E) = \int_0^\infty \left[ 1\text{PPE}(E, \Phi(r))I(r) + \xi \cdot 2\text{PPE}(E, \Phi(r))I^2(r) \right] \cdot r \, \mathrm{d}r \tag{G.119}$$

For the case of the investigated system, $D_2O/Cu(111)$, a constant initial DOS multiplied by a Fermi distribution function (metal substrate) and an exponentially decaying transmission function $T(E) \propto e^{-E}$ was assumed. The latter is due to the transmission of secondary electrons, that constitute the signal at low energies, through the $\sim 20$ BL thick $D_2O$ layer and describes the typical shape of inelastically scattered electrons for low kinetic energies fairly well [All03]. Model calculation and experimental data are compared in Figure G.1 b): A remarkable agreement at the low energy side of the spectrum is achieved, in spite of the simplicity of the model. The deviation at higher energies is due to the trapped electron state $e_{\text{T}}$, discussed in the previous chapter, which is not included in the model.
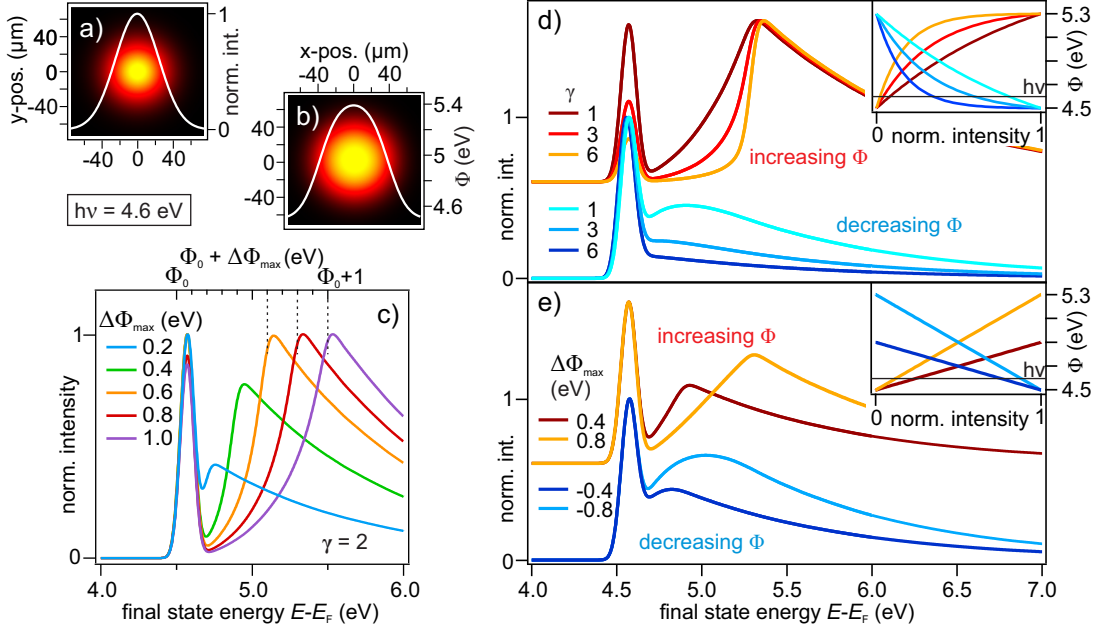
**Figure G.2:** Variation of model parameters: a) laser spot profile and resulting work function distribution for the functional dependence Equation G.118 b). c) shows calculated spectra for different maximum work function changes $\Delta\Phi_{max}$. In d) the parameter $\gamma$ is varied and resulting spectra are shown for a photoinduced increase and decrease of $\Phi$. A linear relationship between beam intensity profile and work function change yields qualitatively similar spectra, displayed in d). Adopted from [Weg13].

Figure G.1 shows the two contributions leading to the peculiar peak like structure at the low energy side of the spectrum: A small contribution, where $\Phi < h\nu$, generates a photoemission spectrum dominated by a narrow single photon contribution (1PPE). A more continuous spectrum, exhibiting a very broad low-energy edge, is generated via two-photon processes (2PPE). The exact shape of the work function distribution depends of course on the underlying mechanism of work function change, but a general peak-like structure below the broadened low energy cut-off is very robust against modifications.

This is verified by changing the functional dependence between laser intensity and work function change, while initial DOS and transmission function are kept fixed (as described in context of Figure G.1): Figure G.2 a) shows a calculated Gaussian intensity profile of the laser beam. Using Equation G.118, an exemplary spatial work function profile is calculated and displayed in b).

Variation of $\Delta\Phi_{max}$ tunes the gap between peak like structure (1PPE) and effective low-energy edge of continuum (2PPE), as can be seen in Figure G.2 c). The larger the maximum change of work function, the wider the gap. It is noteworthy that the maximum work function $(\Phi_0 + \Delta\Phi_{max})$ of the system is found at the top of the edge and not at the half-rise position, which is commonly used to determine the energetic position of the low-energy cut-off.

In d) the parameter $\gamma$ is varied, which tunes how quickly $\Phi$ saturates with laser

intensity. In addition to a photoinduced work function increase (red-yellow curves), the inverse process, a photoinduced work function decrease (blue curves), is modelled as well. The peak-like structure from 1PPE is visible in all traces, whereas the gap is only visible for a photoinduced work function increase and gets more pronounced for steeper $\Phi(I)$, i.e. larger $\gamma$. e) Shows calculated spectra, when assuming a linear dependence between light intensity and work function change again for a photoinduced increase (red, yellow) and decrease (blue). Both exhibit a peak at low energies as well as a gap-like structure. The measured spectral data from photoemission experiments on $D_2O/Cu(111)$ is described remarkably well by this simple phenomenological model.

# References

[Ahn03] C. H. Ahn, J.-M. Triscone, & J. Mannhart. *Electric field effect in correlated oxide systems.* Nature **424**, 6952, (2003) 1015. URL `http://dx.doi.org/10.1038/nature01878`.

[Aiu02] Y Aiura, I Hase, H Bando, T Yasue, T Saitoh, & D.S Dessau. *Photoemission study of the metallic state of lightly electron-doped SrTiO3.* Surface Science **515**, 1, (2002) 61 . URL `http://www.sciencedirect.com/science/article/pii/S0039602802017843`.

[Alf70] R. R. Alfano & S. L. Shapiro. *Emission in the Region 4000 to 7000 Å Via Four-Photon Coupling in Glass.* Phys. Rev. Lett. **24**, (1970) 584. URL `http://link.aps.org/doi/10.1103/PhysRevLett.24.584`.

[Alf06] R. R. Alfano. *The Supercontinuum Laser Source.* Springer, Berlin, 2006.

[All03] Dana M. Alloway, Michael Hofmann, Darrin L. Smith, Nadine E. Gruhn, Amy L. Graham, Ramon Colorado, Vicki H. Wysocki, T. Randall Lee, Paul A. Lee, & Neal R. Armstrong. *Interface Dipoles Arising from Self-Assembled Monolayers on Gold: UV-Photoemission Studies of Alkanethiols and Partially Fluorinated Alkanethiols.* The Journal of Physical Chemistry B **107**, 42, (2003) 11690. URL `http://pubs.acs.org/doi/abs/10.1021/jp034665%2B`.

[Ang84] C. A. Angell & V. Rodgers. *Near infrared spectra and the disrupted network model of normal and supercooled water.* The Journal of Chemical Physics **80**, 12, (1984) 6245. URL `http://scitation.aip.org/content/aip/journal/jcp/80/12/10.1063/1.446727`.

[Arc07] E. Arcangeletti, L. Baldassarre, D. Di Castro, S. Lupi, L. Malavasi, C. Marini, A. Perucchi, & P. Postorino. *Evidence of a Pressure-Induced Metallization Process in Monoclinic* $VO_2$. Phys. Rev. Lett. **98**, (2007) 196406. URL `http://link.aps.org/doi/10.1103/PhysRevLett.98.196406`.

[Ash76] Neil W. Ashcroft & N. David Mermin. *Solid State Phyiscs.* Brooks/Cole, Cengage Learning, 1976.

[Bab03] Daisuke Baba, Tohru Higuchi, Hirofumi Kakemoto, Yoshinori Tokura, Shik Shin, & Takeyo Tsukamoto. *Unoccupied Electronic State of Lightly La-Doped* $SrTiO_3$ *Observed by Inverse-Photoemission Spectroscopy.* Japanese Journal of Applied Physics **42**, 7B, (2003) L837. URL `http://stacks.iop.org/1347-4065/42/i=7B/a=L837`.

[Bar11] Robert N. Barnett, Rina Giniger, Ori Cheshnovsky, & Uzi Landman. *Dielectron Attachment and Hydrogen Evolution Reaction in Water Clusters.* The Journal of Physical Chemistry A **115**, 25, (2011) 7378. URL `http://dx.doi.org/10.1021/jp201560n`. PMID: 21595455.

[Bau07]    Peter Baum, Ding-Shyue Yang, & Ahmed H. Zewail. *4D Visualization of Transitional Structures in Phase Transformations by Electron Diffraction.* Science **318**, 5851, (2007) 788. URL http://www.sciencemag.org/content/318/5851/788.abstract.

[Ber69]    C. N. Berglund & H. J. Guggenheim. *Electronic Properties of VO2 near the Semiconductor-Metal Transition.* Phys. Rev. **185**, (1969) 1022. URL http://link.aps.org/doi/10.1103/PhysRev.185.1022.

[Ber09]    Mathieu Bertin, Michael Meyer, Julia Stahler, Cornelius Gahl, Martin Wolf, & Uwe Bovensiepen. *Reactivity of water-electron complexes on crystalline ice surfaces.* Faraday Discuss. **141**, (2009) 293. URL http://dx.doi.org/10.1039/B805198D.

[Bia81]    A. Bianconi, S. Stizza, & R. Bernardini. *Critical behavior of the plasmon resonance at the metal-insulator transition in $VO_2$.* Phys. Rev. B **24**, (1981) 4406. URL http://link.aps.org/doi/10.1103/PhysRevB.24.4406.

[Bie05]    S. Biermann, A. Poteryaev, A. I. Lichtenstein, & A. Georges. *Dynamical Singlets and Correlation-Assisted Peierls Transition in* $VO_2$. Phys. Rev. Lett. **94**, (2005) 026404. URL http://link.aps.org/doi/10.1103/PhysRevLett.94.026404.

[Blu00]    Hendrik Bluhm, Takahito Inoue, & Miquel Salmeron. *Formation of dipole-oriented water films on mica substrates at ambient conditions.* Surface Science **462**, (2000) L599 . URL http://www.sciencedirect.com/science/article/pii/S0039602800005951.

[Bon00]    Mischa Bonn, Daniel N. Denzler, Stephan Funk, Martin Wolf, S.-Svante Wellershoff, & Julius Hohlfeld. *Ultrafast electron dynamics at metal surfaces: Competition between electron-phonon coupling and hot-electron transport.* Phys. Rev. B **61**, (2000) 1101. URL http://link.aps.org/doi/10.1103/PhysRevB.61.1101.

[Bon06]    S. Bonora, I. Capraro, L. Poletto, M. Romanin, C. Trestino, & P. Villoresi. *Wave front active control by a digital-signal-processor-driven deformable membrane mirror.* Review of Scientific Instruments **77**, 9, (2006) . URL http://scitation.aip.org/content/aip/journal/rsi/77/9/10.1063/1.2337096.

[Bov03]    Uwe Bovensiepen, Cornelius Gahl, & Martin Wolf. *Solvation Dynamics and Evolution of the Spatial Extent of Photoinjected Electrons in D2O/Cu(111).* The Journal of Physical Chemistry B **107**, 33, (2003) 8706. URL http://pubs.acs.org/doi/abs/10.1021/jp034654g.

[Bov09]    U. Bovensiepen, C. Gahl, J. Stähler, M. Bockstedte, M. Meyer, F. Baletto, S. Scandolo, X.-Y. Zhu, A. Rubio, & M. Wolf. *A Dynamic Landscape from Femtoseconds to Minutes for Excess Electrons at Ice-Metal Interfaces.* The Journal of Physical Chemistry C **113**, 3, (2009) 979. URL http://pubs.acs.org/doi/abs/10.1021/jp806997d.

[Boy08]    Robert W. Boyd. *Nonlinear Optics*. Elsevier, 2008.

[Bra09]    M. Bradler, P. Baum, & E. Riedle. *Femtosecond continuum generation in bulk laser host materials with sub-$\hat{I}\frac{1}{4}J$ pump pulses.* Applied Physics B **97**, 3, (2009) 561. URL http://dx.doi.org/10.1007/s00340-009-3699-1.

[Bud14]    John D. Budai, Jiawang Hong, Michael E. Manley, Eliot D. Specht, Chen W. Li, Jonathan Z. Tischler, Douglas L. Abernathy, Ayman H. Said, Bogdan M. Leu, Lynn A. Boatner, Robert J. McQueeney, & Olivier Delaire. *Metallization of vanadium dioxide driven by large phonon entropy.* Nature **advance online publication**, (2014) . URL http://dx.doi.org/10.1038/nature13865.

[Cam99]    I. Campillo, J. M. Pitarke, A. Rubio, E. Zarate, & P. M. Echenique. *Inelastic Lifetimes of Hot Electrons in Real Metals.* Phys. Rev. Lett. **83**, (1999) 2230. URL http://link.aps.org/doi/10.1103/PhysRevLett.83.2230.

[Cav01]    A. Cavalleri, Cs. Tóth, C. W. Siders, J. A. Squier, F. Ráksi, P. Forget, & J. C. Kieffer. *Femtosecond Structural Dynamics in $VO_2$ during an Ultrafast Solid-Solid Phase Transition.* Phys. Rev. Lett. **87**, (2001) 237401. URL http://link.aps.org/doi/10.1103/PhysRevLett.87.237401.

[Cav04]    A. Cavalleri, Th. Dekorsy, H. H. W. Chong, J. C. Kieffer, & R. W. Schoenlein. *Evidence for a structurally-driven insulator-to-metal transition in $VO_2$: A view from the ultrafast timescale.* Phys. Rev. B **70**, (2004) 161102. URL http://link.aps.org/doi/10.1103/PhysRevB.70.161102.

[Cen08]    C. Cen, S. Thiel, G. Hammerl, C. W. Schneider, K. E. Andersen, C. S. Hellberg, J. Mannhart, & J. Levy. *Nanoscale control of an interfacial metal-insulator transition at room temperature.* Nat Mater **7**, 4, (2008) 298. URL http://dx.doi.org/10.1038/nmat2136.

[Cha99]    Jean-Noël Chazalviel. *Coulomb Screening by Mobile Charges.* Birkhäuser, 1999.

[Cha10]    Young Jun Chang, Aaron Bostwick, Yong Su Kim, Karsten Horn, & Eli Rotenberg. *Structure and correlation effects in semiconducting $SrTiO_3$.* Phys. Rev. B **81**, (2010) 235109. URL http://link.aps.org/doi/10.1103/PhysRevB.81.235109.

[Cil10]    Federico Cilento, Claudio Giannetti, Gabriele Ferrini, Stefano Dal Conte, Tommaso Sala, Giacomo Coslovich, Matteo Rini, Andrea Cavalleri, & Fulvio Parmigiani. *Ultrafast insulator-to-metal phase transition as a switch to measure the spectrogram of a supercontinuum light pulse.* Applied Physics Letters **96**, 2, (2010) . URL http://scitation.aip.org/content/aip/journal/apl/96/2/10.1063/1.3291105.

[Coc12]    T. L. Cocker, L. V. Titova, S. Fourmaux, G. Holloway, H.-C. Bandulet, D. Brassard, J.-C. Kieffer, M. A. El Khakani, & F. A. Hegmann. *Phase diagram of the ultrafast photoinduced insulator-metal transition in vanadium*

*dioxide.* Phys. Rev. B **85**, (2012) 155120. URL `http://link.aps.org/doi/10.1103/PhysRevB.85.155120`.

[Con99]   A. Continenza, S. Massidda, & M. Posternak. *Self-energy corrections in* $VO_2$ *within a model* GW *scheme.* Phys. Rev. B **60**, (1999) 15699. URL `http://link.aps.org/doi/10.1103/PhysRevB.60.15699`.

[Cou13]   John E. Coulter, Efstratios Manousakis, & Adam Gali. *Limitations of the hybrid functional approach to electronic structure of transition metal oxides.* Phys. Rev. B **88**, (2013) 041107. URL `http://link.aps.org/doi/10.1103/PhysRevB.88.041107`.

[Cri11]   N. Crivillers, A. Liscio, F. Di Stasio, C. Van Dyck, S. Osella, D. Cornil, S. Mian, G. M. Lazzerini, O. Fenwick, E. Orgiu, F. Reinders, S. Braun, M. Fahlman, M. Mayor, J. Cornil, V. Palermo, F. Cacialli, & P. Samori. *Photoinduced work function changes by isomerization of a densely packed azobenzene-based SAM on Au: a joint experimental and theoretical study.* Phys. Chem. Chem. Phys. **13**, (2011) 14302. URL `http://dx.doi.org/10.1039/C1CP20851A`.

[D'A12]   M. D'Angelo, R. Yukawa, K. Ozawa, S. Yamamoto, T. Hirahara, S. Hasegawa, M. G. Silly, F. Sirotti, & I. Matsuda. *Hydrogen-Induced Surface Metallization of* $SrTiO_3$(001). Phys. Rev. Lett. **108**, (2012) 116802. URL `http://link.aps.org/doi/10.1103/PhysRevLett.108.116802`.

[Dac11]   H Dachraoui, N Müller, G Obermeier, C Oberer, S Horn, & U Heinzmann. *Interplay between electronic correlations and coherent structural dynamics during the monoclinic insulator-to-rutile metal phase transition in VO2.* Journal of Physics: Condensed Matter **23**, 43, (2011) 435402. URL `http://stacks.iop.org/0953-8984/23/i=43/a=435402`.

[Dam04]   Andrea Damascelli. *Probing the Electronic Structure of Complex Systems by ARPES.* Physica Scripta **2004**, T109, (2004) 61. URL `http://stacks.iop.org/1402-4896/2004/i=T109/a=005`.

[Dav08]   Humphry Davy. *Electro-Chemical Researches, on the Decomposition of the Earths; With Observations on the Metals Obtained from the Alkaline Earths, and on the Amalgam Procured from Ammonia.* Philosophical Transactions of the Royal Society of London **98**, (1808) 333. URL `http://rstl.royalsocietypublishing.org/content/98/333.short`.

[DC12a]   S. Dal Conte, C. Giannetti, G. Coslovich, F. Cilento, D. Bossini, T. Abebaw, F. Banfi, G. Ferrini, H. Eisaki, M. Greven, A. Damascelli, D. van der Marel, & F. Parmigiani. *Disentangling the Electronic and Phononic Glue in a High-Tc Superconductor.* Science **335**, 6076, (2012) 1600. URL `http://www.sciencemag.org/content/335/6076/1600.abstract`.

[DC12b]   R. Di Capua, M. Radovic, G. M. De Luca, I. Maggio-Aprile, F. Miletto Granozio, N. C. Plumb, Z. Ristic, U. Scotti di Uccio, R. Vaglio, & M. Sal-

luzzo. *Observation of a two-dimensional electron gas at the surface of annealed SrTiO$_3$ single crystals by scanning tunneling spectroscopy.* Phys. Rev. B **86**, (2012) 155425. URL `http://link.aps.org/doi/10.1103/PhysRevB.86.155425`.

[Dei11] Jan-Christoph Deinert. *Zeit- und winkelaufgelöste Zweiphotonen-Photoemissionsspektroskopie: Aufbau und Charakterisierung des Experiments anhand der Cu(111)- und der D2O/Cu(111)-Oberfläche.* Diplomarbeit, Freie Universität Berlin (2011).

[Dek93] T. Dekorsky, W. KÃ¼tt, T. Pfeifer, & H. Kurz. *Coherent Control of LO-Phonon Dynamics in Opaque Semiconductors by Femtosecond Laser Pulses.* EPL (Europhysics Letters) **23**, 3, (1993) 223. URL `http://stacks.iop.org/0295-5075/23/i=3/a=011`.

[Dem02] J. Demsar, L. Forró, H. Berger, & D. Mihailovic. *Femtosecond snapshots of gap-forming charge-density-wave correlations in quasi-two-dimensional dichalcogenides* $1T - \mathrm{TaS}_2$ *and* $2H - \mathrm{TaSe}_2$. Phys. Rev. B **66**, (2002) 041101. URL `http://link.aps.org/doi/10.1103/PhysRevB.66.041101`.

[DF00] N. Del Fatti, C. Voisin, M. Achermann, S. Tzortzakis, D. Christofilos, & F. Vallée. *Nonequilibrium electron dynamics in noble metals.* Phys. Rev. B **61**, (2000) 16956. URL `http://link.aps.org/doi/10.1103/PhysRevB.61.16956`.

[Duh08] Steffen Duhm, Georg Heimel, Ingo Salzmann, Hendrik Glowatzki, Robert L. Johnson, Antje Vollmer, Jurgen P. Rabe, & Norbert Koch. *Orientation-dependent ionization energies and interface dipoles in ordered molecular assemblies.* Nat Mater **7**, 4, (2008) 326. URL `http://dx.doi.org/10.1038/nmat2119`.

[Eer13] P. D. Eerkes, W. G. van der Wiel, & H. Hilgenkamp. *Modulation of conductance and superconductivity by top-gating in LaAlO3/SrTiO3 2-dimensional electron systems.* Applied Physics Letters **103**, 20, (2013) . URL `http://scitation.aip.org/content/aip/journal/apl/103/20/10.1063/1.4829555`.

[Eic11] Christian Eickhoff, Martin Teichmann, & Martin Weinelt. *Two-State Double-Continuum Fano Resonance at the Si(100) Surface.* Phys. Rev. Lett. **107**, (2011) 176804. URL `http://link.aps.org/doi/10.1103/PhysRevLett.107.176804`.

[Ein05] A. Einstein. *Über einen die Erzeugung und Verwandlung des Lichtes betreffenden heuristischen Gesichtspunkt.* Annalen der Physik **322**, 6, (1905) 132. URL `http://dx.doi.org/10.1002/andp.19053220607`.

[EM11] Fedwa El-Mellouhi, Edward N. Brothers, Melissa J. Lucero, & Gustavo E. Scuseria. *Modeling of the cubic and antiferrodistortive phases of SrTiO$_3$ with screened hybrid density functional theory.* Phys. Rev. B **84**, (2011) 115122. URL `http://link.aps.org/doi/10.1103/PhysRevB.84.115122`.

[Ern04]    Ralph Ernstorfer. *Spectroscopic investigation of photoinduced heterogeneous electron transfer*. Dissertation, Free University Berlin (2004).

[Eye02]    V. Eyert. *The metal-insulator transitions of VO2: A band theoretical approach*. Annalen der Physik **11**, 9, (2002) 650. URL `http://dx.doi.org/10.1002/1521-3889(200210)11:9<650::AID-ANDP650>3.0.CO;2-K`.

[Eye11]    V. Eyert. *VO2: A Novel View from Band Theory*. Phys. Rev. Lett. **107**, (2011) 016401. URL `http://link.aps.org/doi/10.1103/PhysRevLett.107.016401`.

[Fan61]    U. Fano. *Effects of Configuration Interaction on Intensities and Phase Shifts*. Phys. Rev. **124**, (1961) 1866. URL `http://link.aps.org/doi/10.1103/PhysRev.124.1866`.

[Fan92]    W. S. Fann, R. Storz, H. W. K. Tom, & J. Bokor. *Direct measurement of nonequilibrium electron-energy distributions in subpicosecond laser-heated gold films*. Phys. Rev. Lett. **68**, (1992) 2834. URL `http://link.aps.org/doi/10.1103/PhysRevLett.68.2834`.

[Fan11]    W. Fan, J. Cao, J. Seidel, Y. Gu, J. W. Yim, C. Barrett, K. M. Yu, J. Ji, R. Ramesh, L. Q. Chen, & J. Wu. *Large kinetic asymmetry in the metal-insulator transition nucleated at localized and extended defects*. Phys. Rev. B **83**, (2011) 235102. URL `http://link.aps.org/doi/10.1103/PhysRevB.83.235102`.

[Fau94]    Thomas Fauster. *Two-photon photoemission*. Prog. Surf. Sci. **46**, (1994) 177 . URL `http://www.sciencedirect.com/science/article/pii/0079681694900779`.

[Fau12]    J. Faure, J. Mauchain, E. Papalazarou, W. Yan, J. Pinon, M. Marsi, & L. Perfetti. *Full characterization and optimization of a femtosecond ultraviolet laser source for time and angle-resolved photoemission on solid surfaces*. Review of Scientific Instruments **83**, 4, (2012) . URL `http://scitation.aip.org/content/aip/journal/rsi/83/4/10.1063/1.3700190`.

[Fog11]    Laura Foglia. *Transient reflectivity and coherent phonon excitation: An ultrafast probe of the metal-to-insulator transition in VO$_2$*. Diplomarbeit, Freie Universität Berlin (2011).

[Fuj92]    A. Fujimori, I. Hase, M. Nakamura, H. Namatame, Y. Fujishima, Y. Tokura, M. Abbate, F. M. F. de Groot, M. T. Czyzyk, J. C. Fuggle, O. Strebel, F. Lopez, M. Domke, & G. Kaindl. *Doping-induced changes in the electronic structure of $La_xSr_{1-x}TiO_3$: Limitation of the one-electron rigid-band model and the Hubbard model*. Phys. Rev. B **46**, (1992) 9841. URL `http://link.aps.org/doi/10.1103/PhysRevB.46.9841`.

[Gae00]    Alexander L. Gaeta. *Catastrophic Collapse of Ultrashort Pulses*. Phys. Rev. Lett. **84**, (2000) 3582. URL `http://link.aps.org/doi/10.1103/PhysRevLett.84.3582`.

[Gah02] C. Gahl, U. Bovensiepen, C. Frischkorn, & M. Wolf. *Ultrafast Dynamics of Electron Localization and Solvation in Ice Layers on Cu(111).* Phys. Rev. Lett. **89**, (2002) 107402. URL `http://link.aps.org/doi/10.1103/PhysRevLett.89.107402`.

[Gah04] Cornelius Gahl. *Elektronentransfer- und Solvatisierungsdynamik in Eis adsorbiert auf Metalloberflächen.* Dissertation, Free University Berlin (2004).

[Gar96] G. A. Garrett, T. F. Albrecht, J. F. Whitaker, & R. Merlin. *Coherent THz Phonons Driven by Light Pulses and the Sb Problem: What is the Mechanism?* Phys. Rev. Lett. **77**, (1996) 3661. URL `http://link.aps.org/doi/10.1103/PhysRevLett.77.3661`.

[Gat07a] Matteo Gatti. *Correlation effects in valence-electron spectroscopy of transition-metal oxides: many-body perturbation theory and alternative approaches.* Dissertation, LEcole Polytechnique (2007).

[Gat07b] Matteo Gatti, Fabien Bruneval, Valerio Olevano, & Lucia Reining. *Understanding Correlations in Vanadium Dioxide from First Principles.* Phys. Rev. Lett. **99**, (2007) 266402. URL `http://link.aps.org/doi/10.1103/PhysRevLett.99.266402`.

[Gav72] Anibal Gavini & Clarence C. Y. Kwan. *Optical Properties of Semiconducting $VO_2$ Films.* Phys. Rev. B **5**, (1972) 3138. URL `http://link.aps.org/doi/10.1103/PhysRevB.5.3138`.

[GC12] Ricardo Grau-Crespo, Hao Wang, & Udo Schwingenschlögl. *Why the Heyd-Scuseria-Ernzerhof hybrid functional description of $VO_2$ phases is not correct.* Phys. Rev. B **86**, (2012) 081101. URL `http://link.aps.org/doi/10.1103/PhysRevB.86.081101`.

[Geb97] Florian Gebhard. *The Mott Metal-Insulator Transition.* Springer, 1997.

[Ger70] R.L. Gerlach & T.N. Rhodin. *Binding and charge transfer associated with alkali metal adsorption on single crystal nickel surfaces.* Surface Science **19**, 2, (1970) 403 . URL `http://www.sciencedirect.com/science/article/pii/0039602870900506`.

[Giu82] Gabriele F. Giuliani & John J. Quinn. *Lifetime of a quasiparticle in a two-dimensional electron gas.* Phys. Rev. B **26**, (1982) 4421. URL `http://link.aps.org/doi/10.1103/PhysRevB.26.4421`.

[Goo71] John B. Goodenough. *The two components of the crystallographic transition in {VO2}.* Journal of Solid State Chemistry **3**, 4, (1971) 490 . URL `http://www.sciencedirect.com/science/article/pii/0022459671900910`.

[Grü94] G. Grüner. *Density Waves in Solids, Vol. 89 of Frontiers in Physics.* Addison-Wesley, 1994.

[Gra10]    J. Graf, S. Hellmann, C. Jozwiak, C. L. Smallwood, Z. Hussain, R. A. Kaindl,
           L. Kipp, K. Rossnagel, & A. Lanzara. *Vacuum space charge effect in laser-
           based solid-state photoemission spectroscopy.* Journal of Applied Physics **107**,
           1, (2010) . URL `http://scitation.aip.org/content/aip/journal/jap/`
           `107/1/10.1063/1.3273487.`

[Gue95]    Th. Guerlin, H. Sauer, W. Engel, & E. Zeitler. *The role of strontium in the
           formation of unoccupied electronic states in SrTiO3 investigated by electron
           energy loss spectroscopy.* physica status solidi (a) **150**, 1, (1995) 153. URL
           `http://dx.doi.org/10.1002/pssa.2211500113.`

[Had10]    Masaki Hada, Kunio Okimura, & Jiro Matsuo. *Characterization of struc-
           tural dynamics of $VO_2$ thin film on c-Al−$2O_3$ using in-air time-resolved x-ray
           diffraction.* Phys. Rev. B **82**, (2010) 153401. URL `http://link.aps.org/`
           `doi/10.1103/PhysRevB.82.153401.`

[Had11]    Masaki Hada, Kunio Okimura, & Jiro Matsuo.  *Photo-induced lattice
           softening of excited-state VO2.*  Applied Physics Letters **99**, 5, (2011)
           . URL `http://scitation.aip.org/content/aip/journal/apl/99/5/10.`
           `1063/1.3621900.`

[Hag09]    Sebastian Hagen. *Isomerization behavior of photochromic molecules in direct
           contact with noble metal surfaces.* Dissertation, Free University Berlin (2009).

[Har98]    M J Harris, M E Hagen, M T Dove, & I P Swainson. *Inelastic neutron scat-
           tering, phonon softening, and the phase transition in sodium nitrate.* Journal
           of Physics: Condensed Matter **10**, 30, (1998) 6851. URL `http://stacks.`
           `iop.org/0953-8984/10/i=30/a=022.`

[Has96]    M. Hase, K. Mizoguchi, H. Harima, S. Nakashima, M. Tani, K. Sakai, &
           M. Hangyo.  *Optical control of coherent optical phonons in bismuth films.*
           Applied Physics Letters **69**, 17, (1996) 2474. URL `http://scitation.aip.`
           `org/content/aip/journal/apl/69/17/10.1063/1.117502.`

[Has05]    Muneaki Hase, Kunie Ishioka, Jure Demsar, Kiminori Ushida, & Masahiro
           Kitajima. *Ultrafast dynamics of coherent optical phonons and nonequilibrium
           electrons in transition metals.* Phys. Rev. B **71**, (2005) 184301. URL `http://`
           `link.aps.org/doi/10.1103/PhysRevB.71.184301.`

[Hed65]    Lars Hedin. *New Method for Calculating the One-Particle Green's Function
           with Application to the Electron-Gas Problem.* Phys. Rev. **139**, (1965) A796.
           URL `http://link.aps.org/doi/10.1103/PhysRev.139.A796.`

[Hel95]    G. Held & D. Menzel.  *Isotope effects in structure and kinetics of water
           adsorbates on Ru(001).* Surface Science **327**, 3, (1995) 301 . URL `http://`
           `www.sciencedirect.com/science/article/pii/0039602894008361.`

[Hel09]    S. Hellmann, K. Rossnagel, M. Marczynski-Bühlow, & L. Kipp. *Vacuum
           space-charge effects in solid-state photoemission.* Phys. Rev. B **79**, (2009)
           035402. URL `http://link.aps.org/doi/10.1103/PhysRevB.79.035402.`

[Hel12]   S. Hellmann, T. Ott, L. Kipp, & K. Rossnagel. *Vacuum space-charge effects in nano-ARPES.* Phys. Rev. B **85**, (2012) 075109. URL `http://link.aps.org/doi/10.1103/PhysRevB.85.075109`.

[Hen78]   Victor E. Henrich, G. Dresselhaus, & H. J. Zeiger. *Surface defects and the electronic structure of SrTiO₃ surfaces.* Phys. Rev. B **17**, (1978) 4908. URL `http://link.aps.org/doi/10.1103/PhysRevB.17.4908`.

[Her87]   H. Hertz. *Ueber einen Einfluss des ultravioletten Lichtes auf die electrische Entladung.* Annalen der Physik **267**, 8, (1887) 983. URL `http://dx.doi.org/10.1002/andp.18872670827`.

[Her96]   T. Hertel, E. Knoesel, M. Wolf, & G. Ertl. *Ultrafast Electron Dynamics at Cu(111): Response of an Electron Gas to Optical Excitation.* Phys. Rev. Lett. **76**, (1996) 535. URL `http://link.aps.org/doi/10.1103/PhysRevLett.76.535`.

[Hüf10]   Stefan Hüfner. *Photoelectron Spectroscopy - Principles and Applications.* Springer, 2010.

[Hig02]   T. Higuchi, S. Nozawa, T. Tsukamoto, H. Ishii, R. Eguchi, Y. Tezuka, S. Yamaguchi, K. Kanai, & S. Shin. *Unoccupied electronic structure in the surface state of lightly doped* SrTiO₃ *by resonant inverse photoemission spectroscopy.* Phys. Rev. B **66**, (2002) 153105. URL `http://link.aps.org/doi/10.1103/PhysRevB.66.153105`.

[Hil07]   D. J. Hilton, R. P. Prasankumar, S. Fourmaux, A. Cavalleri, D. Brassard, M. A. El Khakani, J. C. Kieffer, A. J. Taylor, & R. D. Averitt. *Enhanced Photosusceptibility near $T_c$ for the Light-Induced Insulator-to-Metal Phase Transition in Vanadium Dioxide.* Phys. Rev. Lett. **99**, (2007) 226401. URL `http://link.aps.org/doi/10.1103/PhysRevLett.99.226401`.

[Iac98]   C. Iaconis & I.A. Walmsley. *Spectral phase interferometry for direct electric-field reconstruction of ultrashort optical pulses.* Opt. Lett. **23**, 10, (1998) 792. URL `http://ol.osa.org/abstract.cfm?URI=ol-23-10-792`.

[Ior12]   Federico Iori, Matteo Gatti, & Angel Rubio. *Role of nonlocal exchange in the electronic structure of correlated oxides.* Phys. Rev. B **85**, (2012) 115129. URL `http://link.aps.org/doi/10.1103/PhysRevB.85.115129`.

[Ish06]   Kunie Ishioka, Muneaki Hase, Masahiro Kitajima, & Hrvoje Petek. *Coherent optical phonons in diamond.* Applied Physics Letters **89**, 23, (2006). URL `http://scitation.aip.org/content/aip/journal/apl/89/23/10.1063/1.2402231`.

[Ish08]   Yukiaki Ishida, Ritsuko Eguchi, Masaharu Matsunami, Koji Horiba, Munetaka Taguchi, Ashish Chainani, Yasunori Senba, Haruhiko Ohashi, Hiromichi Ohta, & Shik Shin. *Coherent and Incoherent Excitations of Electron-Doped* SrTiO₃. Phys. Rev. Lett. **100**, (2008) 056401. URL `http://link.aps.org/doi/10.1103/PhysRevLett.100.056401`.

[Jac02]     John David Jackson. *Klassische Elektrodynamik.* De Gruyter, 2002.

[Jon10]     Andrew C. Jones, Samuel Berweger, Jiang Wei, David Cobden, & Markus B. Raschke. *Nano-optical Investigations of the Metal-Insulator Phase Behavior of Individual VO2 Microcrystals.* Nano Letters **10**, 5, (2010) 1574. URL `http://pubs.acs.org/doi/abs/10.1021/nl903765h`.

[Kan93]     D.J. Kane & R. Trebino. *Characterization of arbitrary femtosecond pulses using frequency-resolved optical gating.* Quantum Electronics, IEEE Journal of **29**, 2, (1993) 571.

[Kan97]     S. Kane & J. Squier. *Fourth-order-dispersion limitations of aberration-free chirped-pulse amplification systems.* J. Opt. Soc. Am. B **14**, 5, (1997) 1237. URL `http://josab.osa.org/abstract.cfm?URI=josab-14-5-1237`.

[Küb07]     C. Kübler, H. Ehrke, R. Huber, R. Lopez, A. Halabica, R. F. Haglund, & A. Leitenstorfer. *Coherent Structural Dynamics and Electronic Correlations during an Ultrafast Insulator-to-Metal Phase Transition in $VO_2$.* Phys. Rev. Lett. **99**, (2007) 116401. URL `http://link.aps.org/doi/10.1103/PhysRevLett.99.116401`.

[Kim06]     Hyun-Tak Kim, Yong Wook Lee, Bong-Jun Kim, Byung-Gyu Chae, Sun Jin Yun, Kwang-Yong Kang, Kang-Jeon Han, Ki-Ju Yee, & Yong-Sik Lim. *Monoclinic and Correlated Metal Phase in $VO_2$ as Evidence of the Mott Transition: Coherent Phonon Analysis.* Phys. Rev. Lett. **97**, (2006) 266401. URL `http://link.aps.org/doi/10.1103/PhysRevLett.97.266401`.

[Kir09]     Patrick S. Kirchmann. *Ultrafast Electron Dynamics in Low-Dimensional Materials.* Dissertation, Free University Berlin (2009).

[Kli02]     V.A. Klimov, I.O. Timofeeva, S.D. Khanin, E.B. Shadrin, A.V. Ilinskii, & F. Silva-Andrade. *Hysteresis loop construction for the metal-semiconductor phase transition in vanadium dioxide films.* Technical Physics **47**, 9, (2002) 1134. URL `http://dx.doi.org/10.1134/1.1508078`.

[Kno95]     E. Knoesel, T. Hertel, M. Wolf, & G. Ertl. *Femtosecond dynamics of electronic excitations of adsorbates studied by two-photon photoemission pulse correlation: CO/Cu(111).* Chemical Physics Letters **240**, (1995) 409 . URL `http://www.sciencedirect.com/science/article/pii/000926149500527B`.

[Kno96]     E. Knoesel, A. Hotzel, T. Hertel, M. Wolf, & G. Ertl. *Dynamics of photoexcited electrons in metals studied with time-resolved two-photon photoemission.* Surface Science **368**, 368, (1996) 76 . URL `http://www.sciencedirect.com/science/article/pii/S0039602896010321`. Vibrations at Surfaces.

[Ko11]      Changhyun Ko, Zheng Yang, & Shriram Ramanathan. *Work Function of Vanadium Dioxide Thin Films Across the Metal-Insulator Transition and the Role of Surface Nonstoichiometry.* ACS Applied Materials & Interfaces **3**, 9, (2011) 3396. URL `http://pubs.acs.org/doi/abs/10.1021/am2006299`.

[Koe06]  T. C. Koethe, Z. Hu, M. W. Haverkort, C. Schüßler-Langeheine, F. Venturini, N. B. Brookes, O. Tjernberg, W. Reichelt, H. H. Hsieh, H.-J. Lin, C. T. Chen, & L. H. Tjeng. *Transfer of Spectral Weight and Symmetry across the Metal-Insulator Transition in* $VO_2$. Phys. Rev. Lett. **97**, (2006) 116402. URL `http://link.aps.org/doi/10.1103/PhysRevLett.97.116402`.

[Koo34]  T Koopmans. *Über die Zuordnung von Wellenfunktionen und Eigenwerten zu den Einzelnen Elektronen Eines Atoms.* Physica **1**, (1934) 104 . URL `http://www.sciencedirect.com/science/article/pii/S0031891434900112`.

[Kop07]  Konrad Kopitzki & Peter Herzog. *Einführung in die Festkörperphysik.* Teubner, 2007.

[Kor02]  M. A. Korotin, N. A. Skorikov, & V. I. Anisimov. *Variation of orbital symmetry of the localized 3d(1) electron of the V4+ ion upon the metal-insulator transition in VO2.* Phys. Met. Metallogr. **94**, (2002) 17.

[Kor03]  M. A. Korotin, N. A. Skorikov, & V. I. Anisimov. *Variation of orbital symmetry of the localized* $3d^1$ *electron of the* $V^{4+}$ *ion upon the metal-insulator transition in* $VO_2$. arXiv:cond-mat/0301347v1 [cond-mat.str-el] .

[Kor06]  J. D. Koralek, J. F. Douglas, N. C. Plumb, Z. Sun, A. V. Fedorov, M. M. Murnane, H. C. Kapteyn, S. T. Cundiff, Y. Aiura, K. Oka, H. Eisaki, & D. S. Dessau. *Laser Based Angle-Resolved Photoemission, the Sudden Approximation, and Quasiparticle-Like Spectral Peaks in* $Bi_2Sr_2CaCu_2O_{8+\delta}$,. Phys. Rev. Lett. **96**, (2006) 017005. URL `http://link.aps.org/doi/10.1103/PhysRevLett.96.017005d`.

[Kor07]  J. D. Koralek, J. F. Douglas, N. C. Plumb, J. D. Griffith, S. T. Cundiff, H. C. Kapteyn, M. M. Murnane, & D. S. Dessau. *Experimental setup for low-energy laser-based angle resolved photoemission spectroscopy.* Review of Scientific Instruments **78**, 5, (2007) . URL `http://scitation.aip.org/content/aip/journal/rsi/78/5/10.1063/1.2722413`.

[Kov99]  S. A. Kovalenko, A. L. Dobryakov, J. Ruthmann, & N. P. Ernsting. *Femtosecond spectroscopy of condensed phases with chirped supercontinuum probing.* Phys. Rev. A **59**, (1999) 2369. URL `http://link.aps.org/doi/10.1103/PhysRevA.59.2369`.

[Kuc79]  D. Kucharczyk & T. Niklewski. *Accurate X-ray determination of the lattice parameters and the thermal expansion coefficients of VO2 near the transition temperature.* Journal of Applied Crystallography **12**, 4, (1979) 370. URL `http://dx.doi.org/10.1107/S0021889879012711`.

[Kut92]  W.A. Kutt, W. Albrecht, & H. Kurz. *Generation of coherent phonons in condensed media.* Quantum Electronics, IEEE Journal of **28**, 10, (1992) 2434.

[Lav14]  J. Laverock, S. Kittiwatanakul, A. A. Zakharov, Y. R. Niu, B. Chen, S. A. Wolf, J.W. Lu, & K. E. Smith. *Direct observation of decoupled structural and*

*electronic transitions and an ambient pressure monocliniclike metallic phase of VO₂*. Phys. Rev. Lett. **to be published**.

[Lea13]    G. Leahu, R. Li Voti, C. Sibilia, & M. Bertolotti. *Anomalous optical switching and thermal hysteresis during semiconductor-metal phase transition of VO2 films on Si substrate*. Applied Physics Letters **103**, 23, (2013) . URL `http://scitation.aip.org/content/aip/journal/apl/103/23/10.1063/1.4838395`.

[Leu03]    T. C. Leung, C. L. Kao, W. S. Su, Y. J. Feng, & C. T. Chan. *Relationship between surface dipole, work function and charge transfer: Some exceptions to an established rule*. Phys. Rev. B **68**, (2003) 195408. URL `http://link.aps.org/doi/10.1103/PhysRevB.68.195408`.

[Leu11]    Dominik Leuenberger, Hirofumi Yanagisawa, Silvan Roth, Jürg Osterwalder, & Matthias Hengsberger. *Disentanglement of electron dynamics and space-charge effects in time-resolved photoemission from h-BN/Ni(111)*. Phys. Rev. B **84**, (2011) 125107. URL `http://link.aps.org/doi/10.1103/PhysRevB.84.125107`.

[Li06]    Yongyao Li, Xiangqian Luo, & Helmut Krầ¶ger. *Bound states and critical behavior of the Yukawa potential*. Science in China Series G **49**, 1, (2006) 60. URL `http://dx.doi.org/10.1007/s11433-004-0020-5`.

[Lon70]    John M. Longo & Peder Kierkegaard. *A Refinement of the Structure of VO₂*. Acta Chem. Scand. **24**, (1970) 420.

[Lop02]    R. Lopez, T. E. Haynes, L. A. Boatner, L. C. Feldman, & R. F. Haglund. *Size effects in the structural phase transition of VO₂ nanoparticles*. Phys. Rev. B **65**, (2002) 224113. URL `http://link.aps.org/doi/10.1103/PhysRevB.65.224113`.

[Lou00]    R. Loudon. *The Quantum Theory of Light*. Oxford University Press, 2000.

[Lüt01]    Hans Lüth. *Solid Surfaces, Interfaces and Thin Films*. Springer-Verlag Berlin Heidelberg, 2001.

[Lys06]    S. Lysenko, A.J. Rua, V. Vikhnin, J. Jimenez, F. Fernandez, & H. Liu. *Light-induced ultrafast phase transitions in {VO2} thin film*. Applied Surface Science **252**, 15, (2006) 5512 . URL `http://www.sciencedirect.com/science/article/pii/S0169433205018027`. Proceedings of the Eight International Conference on Atomically Controlled Surfaces, Interfaces and Nanostructures and the Thirteenth International Congress on Thin Films ACSIN8/ICTF13.

[Mar87]    O.E. Martinez. *3000 times grating compressor with positive group velocity dispersion: Application to fiber compensation in 1.3-1.6 µm region*. Quantum Electronics, IEEE Journal of **23**, 1, (1987) 59.

[Mat72]    L. F. Mattheiss. *Effect of the 110° K Phase Transition on the SrTi*$O_3$ *Conduction Bands.* Phys. Rev. B **6**, (1972) 4740. URL `http://link.aps.org/doi/10.1103/PhysRevB.6.4740`.

[Müc88]    W. Mückenheim, P. Lokai, B. Burghardt, & D. Basting. *Attaining the wavelength range 189-197 nm by frequency mixing in BBO.* Applied Physics B **45**, 4, (1988) 259. URL `http://dx.doi.org/10.1007/BF00687154`.

[McW74]    D. B. McWhan, M. Marezio, J. P. Remeika, & P. D. Dernier. *X-ray diffraction study of metallic VO2.* Phys. Rev. B **10**, (1974) 490. URL `http://link.aps.org/doi/10.1103/PhysRevB.10.490`.

[Mee11]    W. Meevasana, P. D. C. King, R. H. He, S-K. Mo, M. Hashimoto, A. Tamai, P. Songsiriritthigul, F. Baumberger, & Z-X. Shen. *Creation and control of a two-dimensional electron liquid at the bare SrTiO3 surface.* Nat Mater **10**, 2, (2011) 114. URL `http://dx.doi.org/10.1038/nmat2943`.

[Mey08]    Michael Meyer, Julia Stähler, Daniela O. Kusmierek, Martin Wolf, & Uwe Bovensiepen. *Determination of the electron's solvation site on D2O/Cu(111) using Xe overlayers and femtosecond photoelectron spectroscopy.* Phys. Chem. Chem. Phys. **10**, (2008) 4932. URL `http://dx.doi.org/10.1039/B807314G`.

[Mey11]    Michael Meyer. *Ultrafast Electron Dynamics at Alkali/Ice Structures Adsorbed on a Metal Surface.* Dissertation, Free University Berlin (2011).

[Mon12]    Oliver L. A. Monti. *Understanding Interfacial Electronic Structure and Charge Transfer: An Electrostatic Perspective.* The Journal of Physical Chemistry Letters **3**, 17, (2012) 2342. URL `http://pubs.acs.org/doi/abs/10.1021/jz300850x`.

[Mor59]    F. J. Morin. *Oxides Which Show a Metal-to-Insulator Transition at the Neel Temperature.* Phys. Rev. Lett. **3**, (1959) 34. URL `http://link.aps.org/doi/10.1103/PhysRevLett.3.34`.

[Mor14]    Vance R. Morrison, Robert. P. Chatelain, Kunal L. Tiwari, Ali Hendaoui, Andrew Bruhács, Mohamed Chaker, & Bradley J. Siwick. *A photoinduced metal-like phase of monoclinic VO2 revealed by ultrafast electron diffraction.* Science **346**, 6208, (2014) 445. URL `http://www.sciencemag.org/content/346/6208/445.abstract`.

[Mot49]    N F Mott. *The Basis of the Electron Theory of Metals, with Special Reference to the Transition Metals.* Proceedings of the Physical Society. Section A **62**, 7, (1949) 416. URL `http://stacks.iop.org/0370-1298/62/i=7/a=303`.

[Mot74]    N. F. Mott & L. Friedman. *Metal-insulator transitions in VO2, Ti2O3 and Ti2-x V x O3.* Philosophical Magazine **30**, 2, (1974) 389. URL `yua`.

[Nag08]    Joyeeta Nag & R F Haglund Jr. *Synthesis of vanadium dioxide thin films and nanoparticles.* Journal of Physics: Condensed Matter **20**, 26, (2008) 264016. URL `http://stacks.iop.org/0953-8984/20/i=26/a=264016`.

[Nag11]   Joyeeta Nag, E. Andrew Payzant, Karren L. More, & Richard F. Haglund. *Enhanced performance of room-temperature-grown epitaxial thin films of vanadium dioxide*. Applied Physics Letters **98**, 25, (2011) . URL `http://scitation.aip.org/content/aip/journal/apl/98/25/10.1063/1.3600333`.

[Nik91]   D.N. Nikogosyan. *Beta barium borate (BBO)*. Applied Physics A **52**, 6, (1991) 359. URL `http://dx.doi.org/10.1007/BF00323647`.

[Oga96]   S. Ogawa & H. Petek. *Femtosecond dynamics of hot-electron relaxation in Cu(110) and Cu(100)*. Surface Science **357 - 358**, 0, (1996) 585 . URL `http://www.sciencedirect.com/science/article/pii/0039602896002282`.

[Oga01]   T. Ogasawara, T. Kimura, T. Ishikawa, M. Kuwata-Gonokami, & Y. Tokura. *Dynamics of photoinduced melting of charge/orbital order in a layered manganite* $La_{0.5}Sr_{1.5}MnO_4$. Phys. Rev. B **63**, (2001) 113105. URL `http://link.aps.org/doi/10.1103/PhysRevB.63.113105`.

[Oga02]   S. Ogawa, H. Nagano, & H. Petek. *Optical Intersubband Transitions and Femtosecond Dynamics in Ag /Fe(100) Quantum Wells*. Phys. Rev. Lett. **88**, (2002) 116801. URL `http://link.aps.org/doi/10.1103/PhysRevLett.88.116801`.

[Oht04]   A. Ohtomo & H. Y. Hwang. *A high-mobility electron gas at the LaAlO3/SrTiO3 heterointerface*. Nature **427**, 6973, (2004) 423. URL `http://dx.doi.org/10.1038/nature02308`.

[Par90]   J. C. Parker. *Raman scattering from* $VO_2$ *single crystals: A study of the effects of surface oxidation*. Phys. Rev. B **42**, (1990) 3164. URL `http://link.aps.org/doi/10.1103/PhysRevB.42.3164`.

[Pas11]   A. Pashkin, C. Kübler, H. Ehrke, R. Lopez, A. Halabica, R. F. Haglund, R. Huber, & A. Leitenstorfer. *Ultrafast insulator-metal phase transition in* $VO_2$ *studied by multiterahertz spectroscopy*. Phys. Rev. B **83**, (2011) 195120. URL `http://link.aps.org/doi/10.1103/PhysRevB.83.195120`.

[Per06]   L. Perfetti, P. A. Loukakos, M. Lisowski, U. Bovensiepen, H. Berger, S. Biermann, P. S. Cornaglia, A. Georges, & M. Wolf. *Time Evolution of the Electronic Structure of* $1T$-$TaS_2$ *through the Insulator-Metal Transition*. Phys. Rev. Lett. **97**, (2006) 067402. URL `http://link.aps.org/doi/10.1103/PhysRevLett.97.067402`.

[Pin66]   D. Pines & P. Nozieres. *The Theory of Quatum Liquids, Vol. I of Advanced Book Classic Series*. W. A. Benjamin, Inc., 1966.

[Pis04]   S Piskunov, E Heifets, R.I Eglitis, & G Borstel. *Bulk properties and electronic structure of SrTiO3, BaTiO3, PbTiO3 perovskites: an ab initio HF/DFT study*. Computational Materials Science **29**, 2, (2004) 165 . URL `http://www.sciencedirect.com/science/article/pii/S0927025603001812`.

[Plu14]   N. C. Plumb, M. Salluzzo, E. Razzoli, M. Månsson, M. Falub, J. Krempasky, C. E. Matt, J. Chang, M. Schulte, J. Braun, H. Ebert, J. Minár, B. Delley, K.-J. Zhou, T. Schmitt, M. Shi, J. Mesot, L. Patthey, & M. Radović. *Mixed Dimensionality of Confined Conducting Electrons in the Surface Region of* $SrTiO_3$. Phys. Rev. Lett. **113**, (2014) 086801. URL `http://link.aps.org/doi/10.1103/PhysRevLett.113.086801`.

[Pow09]   C.J. Powell & A. Jablonski. *Surface sensitivity of X-ray photoelectron spectroscopy.* Nuclear Instruments and Methods in Physics Research Section A: Accelerators, Spectrometers, Detectors and Associated Equipment **601**, (2009) 54 . URL `http://www.sciencedirect.com/science/article/pii/S0168900208020123`. Special issue in honour of Prof. Kai Siegbahn.

[Qaz07]   M. M. Qazilbash, M. Brehm, Byung-Gyu Chae, P.-C. Ho, G. O. Andreev, Bong-Jun Kim, Sun Jin Yun, A. V. Balatsky, M. B. Maple, F. Keilmann, Hyun-Tak Kim, & D. N. Basov. *Mott Transition in* $VO_2$ *Revealed by Infrared Spectroscopy and Nano-Imaging.* Science **318**, 5857, (2007) 1750. URL `http://www.sciencemag.org/content/318/5857/1750.abstract`.

[Qia05]   Zhixin Qian & Giovanni Vignale. *Lifetime of a quasiparticle in an electron liquid.* Phys. Rev. B **71**, (2005) 075112. URL `http://link.aps.org/doi/10.1103/PhysRevB.71.075112`.

[Rad95]   C Radzewicz, Y.B Band, G.W Pearson, & J.S Krasinski. *Short pulse nonlinear frequency conversion without group-velocity-mismatch broadening.* Optics Communications **117**, (1995) 295 . URL `http://www.sciencedirect.com/science/article/pii/003040189500103F`.

[Ret02]   B. Rethfeld, A. Kaiser, M. Vicanek, & G. Simon. *Ultrafast dynamics of nonequilibrium electrons in metals under femtosecond laser irradiation.* Phys. Rev. B **65**, (2002) 214303. URL `http://link.aps.org/doi/10.1103/PhysRevB.65.214303`.

[Ret12]   L Rettig, P S Kirchmann, & U Bovensiepen. *Ultrafast dynamics of occupied quantum well states in Pb/Si(111).* New Journal of Physics **14**, 2, (2012) 023047. URL `http://stacks.iop.org/1367-2630/14/i=2/a=023047`.

[Rey07]   N. Reyren, S. Thiel, A. D. Caviglia, L. Fitting Kourkoutis, G. Hammerl, C. Richter, C. W. Schneider, T. Kopp, A.-S. Rüetschi, D. Jaccard, M. Gabay, D. A. Muller, J.-M. Triscone, & J. Mannhart. *Superconducting Interfaces Between Insulating Oxides.* Science **317**, 5842, (2007) 1196. URL `http://www.sciencemag.org/content/317/5842/1196.abstract`.

[Ric03]   Davide Ricci, Giuseppe Bano, Gianfranco Pacchioni, & Francesc Illas. *Electronic structure of a neutral oxygen vacancy in* $SrTiO_3$. Phys. Rev. B **68**, (2003) 224105. URL `http://link.aps.org/doi/10.1103/PhysRevB.68.224105`.

[Rie07]   E Riedel & C Janiak. *Anorganische Chemie.* de Gruyter, 2007.

[Roa71]    W.R. Roach & I. Balberg. *Optical induction and detection of fast phase transition in {VO2}*. Solid State Communications **9**, 9, (1971) 551 . URL `http://www.sciencedirect.com/science/article/pii/003810987190144X`.

[Ros11]    K Rossnagels. *On the origin of charge-density waves in select layered transition-metal dichalcogenides*. Journal of Physics: Condensed Matter **23**, 21, (2011) 213001. URL `http://stacks.iop.org/0953-8984/23/i=21/a=213001`.

[Rul05]    Claude Rullière. *Femtosecond Laser Pulses*. Springer, 2005.

[Sae09]    K. Saeki, T. Wakita, Y. Muraoka, M. Hirai, T. Yokoya, R. Eguchi, & S. Shin. *Band dispersion near the Fermi level for $VO_2$ thin films grown on $TiO_2$ (001) substrates*. Phys. Rev. B **80**, (2009) 125406. URL `http://link.aps.org/doi/10.1103/PhysRevB.80.125406`.

[Sch96]    C.A. Schmuttenmaer, C. Cameron Miller, J.W. Herman, J. Cao, D.A. Mantell, Y. Gao, & R.J.D. Miller. *Femtosecond time-resolved photoemission study of hot electron relaxation at the GaAs(100) surface*. Chemical Physics **205**, (1996) 91 . URL `http://www.sciencedirect.com/science/article/pii/0301010495003282`. Surface Reaction Dynamics.

[Sch02]    Peter Schilbe. *Raman scattering in $VO_2$*. Physica B: Condensed Matter **316 - 317**, 0, (2002) 600 . Proceedings of the 10th International Conference on Phonon Scatte ring in Condensed Matter.

[Sch08]    F. Schmitt, P. S. Kirchmann, U. Bovensiepen, R. G. Moore, L. Rettig, M. Krenz, J.-H. Chu, N. Ru, L. Perfetti, D. H. Lu, M. Wolf, I. R. Fisher, & Z.-X. Shen. *Transient Electronic Structure and Melting of a Charge Density Wave in $TbTe_3$*. Science **321**, 5896, (2008) 1649. URL `http://www.sciencemag.org/content/321/5896/1649.abstract`.

[Sco74]    J. F. Scott. *Soft-mode spectroscopy: Experimental studies of structural phase transitions*. Rev. Mod. Phys. **46**, (1974) 83. URL `http://link.aps.org/doi/10.1103/RevModPhys.46.83`.

[Sea79]    M. P. Seah & W. A. Dench. *Quantitative electron spectroscopy of surfaces: A standard data base for electron inelastic mean free paths in solids*. Surface and Interface Analysis **1**, 1, (1979) 2. URL `http://dx.doi.org/10.1002/sia.740010103`.

[Sha98]    N. Shanthi & D. D. Sarma. *Electronic structure of electron doped $SrTiO_{3-\delta}$ and $Sr_{1-x}La_xTiO_3$*. Phys. Rev. B **57**, (1998) 2153. URL `http://link.aps.org/doi/10.1103/PhysRevB.57.2153`.

[Shi77]    Takashi Shibaguchi, Hideo Onuki, & Ryumyo Onaka. *Electronic Structures of Water and Ice*. Journal of the Physical Society of Japan **42**, 1, (1977) 152. URL `http://dx.doi.org/10.1143/JPSJ.42.152`.

[Shi90]   S. Shin, S. Suga, M. Taniguchi, M. Fujisawa, H. Kanzaki, A. Fujimori, H. Daimon, Y. Ueda, K. Kosuge, & S. Kachi. *Vacuum-ultraviolet reflectance and photoemission study of the metal-insulator phase transitions in* $VO_2$, $V_6O_{13}$, *and* $V_2O_3$. Phys. Rev. B **41**, (1990) 4993. URL `http://link.aps.org/doi/10.1103/PhysRevB.41.4993`.

[Shi12]   Ryota Shimizu, Katsuya Iwaya, Takeo Ohsawa, Susumu Shiraki, Tetsuya Hasegawa, Tomihiro Hashizume, & Taro Hitosugi. *Effect of oxygen deficiency on SrTiO3(001) surface reconstructions.* Applied Physics Letters **100**, 26, (2012) . URL `http://scitation.aip.org/content/aip/journal/apl/100/26/10.1063/1.4730409`.

[Sob12]   J. A. Sobota, S. Yang, J. G. Analytis, Y. L. Chen, I. R. Fisher, P. S. Kirchmann, & Z.-X. Shen. *Ultrafast Optical Excitation of a Persistent Surface-State Population in the Topological Insulator* $Bi_2Se_3$. Phys. Rev. Lett. **108**, (2012) 117403. URL `http://link.aps.org/doi/10.1103/PhysRevLett.108.117403`.

[SPEa]   SPECS. *PHOIBOS CCD Imaging Detector User Manual 2.0.*

[SPEb]   SPECS. *SpecsLab, Juggler and CCDAcquire Software for 2D and 3D Detectors.*

[Squ98]   Jeff Squier, Chris P. J. Barty, François Salin, Catherine Le Blanc, & Steve Kane. *Use of mismatched grating pairs in chirped-pulse amplification systems.* Appl. Opt. **37**, 9, (1998) 1638. URL `http://ao.osa.org/abstract.cfm?URI=ao-37-9-1638`.

[SS11]   A. F. Santander-Syro, O. Copie, T. Kondo, F. Fortuna, S. Pailhes, R. Weht, X. G. Qiu, F. Bertran, A. Nicolaou, A. Taleb-Ibrahimi, P. Le Fevre, G. Herranz, M. Bibes, N. Reyren, Y. Apertet, P. Lecoeur, A. Barthelemy, & M. J. Rozenberg. *Two-dimensional electron gas with universal subbands at the surface of SrTiO3.* Nature **469**, 7329, (2011) 189. URL `http://dx.doi.org/10.1038/nature09720`.

[SS14]   A. F. Santander-Syro, F. Fortuna, C. Bareille, T. C. Rödel, G. Landolt, N. C. Plumb, J. H. Dil, & M. Radovic. *Giant spin splitting of the two-dimensional electron gas at the surface of* $SrTiO_3$. Nat Mater **advance online publication**, (2014) . URL `http://dx.doi.org/10.1038/nmat4107`.

[Stä07a]   J. Stähler, M. Mehlhorn, U. Bovensiepen, M. Meyer, D. O. Kusmierek, K. Morgenstern, & M. Wolf. *Impact of Ice Structure on Ultrafast Electron Dynamics in* $D_2O$ *Clusters on Cu(111).* Phys. Rev. Lett. **98**, (2007) 206105. URL `http://link.aps.org/doi/10.1103/PhysRevLett.98.206105`.

[Stä07b]   Julia Stähler. *Freezing Hot Electrons - Electron Transfer and Solvation Dynameics at* $D_2O$ *and* $NH_3$*-Metal Interfaces.* Dissertation, Free University Berlin (2007).

[Stä11]    Julia Stähler, Michael Meyer, Uwe Bovensiepen, & Martin Wolf. *Solvation dynamics of surface-trapped electrons at $NH_3$ and $D_2O$ crystallites adsorbed on metals: from femtosecond to minute timescales.* Chem. Sci. **2**, (2011) 907. URL `http://dx.doi.org/10.1039/C0SC00644K`.

[Stä12]    Julia Stähler, Cornelius Gahl, & Martin Wolf. *Dynamics and Reactivity of Trapped Electrons on Supported Ice Crystallites.* Accounts of Chemical Research **45**, 1, (2012) 131. URL `http://pubs.acs.org/doi/abs/10.1021/ar200170s`.

[Stä14]    J. Stähler, J.-C. Deinert, D. Wegkamp, S. Hagen, & M. Wolf. *Real time measurement of the vertical binding energy during the birth of a solvated electron.* J. Am. Chem. Soc. **submitted**.

[Sug09]    S Suga, A Sekiyama, S Imada, T Miyamachi, H Fujiwara, A Yamasaki, K Yoshimura, K Okada, M Yabashi, K Tamasaku, A Higashiya, & T Ishikawa. *~8 keV photoemission of the metal-insulator transition system $VO_2$.* New Journal of Physics **11**, 10, (2009) 103015. URL `http://stacks.iop.org/1367-2630/11/i=10/a=103015`.

[Suh04]    J. Y. Suh, R. Lopez, L. C. Feldman, & R. F. Haglund. *Semiconductor to metal phase transition in the nucleation and growth of VO2 nanoparticles and thin films.* Journal of Applied Physics **96**, 2, (2004) 1209. URL `http://scitation.aip.org/content/aip/journal/jap/96/2/10.1063/1.1762995`.

[Tak09]    M. Takizawa, K. Maekawa, H. Wadati, T. Yoshida, A. Fujimori, H. Kumigashira, & M. Oshima. *Angle-resolved photoemission study of Nb-doped $SrTiO_3$.* Phys. Rev. B **79**, (2009) 113103. URL `http://link.aps.org/doi/10.1103/PhysRevB.79.113103`.

[Tak13]    Kotaro Takeyasu, Keisuke Fukada, Masuaki Matsumoto, & Katsuyuki Fukutani. *Control of the surface electronic structure of $SrTiO_3(001)$ by modulation of the density of oxygen vacancies.* Journal of Physics: Condensed Matter **25**, 16, (2013) 162202. URL `http://stacks.iop.org/0953-8984/25/i=16/a=162202`.

[Tam13]    A. Tamai, W. Meevasana, P. D. C. King, C. W. Nicholson, A. de la Torre, E. Rozbicki, & F. Baumberger. *Spin-orbit splitting of the Shockley surface state on Cu(111).* Phys. Rev. B **87**, (2013) 075113. URL `http://link.aps.org/doi/10.1103/PhysRevB.87.075113`.

[Tao12]    Zhensheng Tao, Tzong-Ru T. Han, Subhendra D. Mahanti, Phillip M. Duxbury, Fei Yuan, Chong-Yu Ruan, Kevin Wang, & Junqiao Wu. *Decoupling of Structural and Electronic Phase Transitions in $VO_2$.* Phys. Rev. Lett. **109**, (2012) 166406. URL `http://link.aps.org/doi/10.1103/PhysRevLett.109.166406`.

[Tob08]   R. I. Tobey, D. Prabhakaran, A. T. Boothroyd, & A. Cavalleri. *Ultrafast Electronic Phase Transition in* $La_{1/2}Sr_{3/2}MnO_4$ *by Coherent Vibrational Excitation: Evidence for Nonthermal Melting of Orbital Order.* Phys. Rev. Lett. **101**, (2008) 197404. URL `http://link.aps.org/doi/10.1103/PhysRevLett.101.197404`.

[Tre69]   E. Treacy. *Optical pulse compression with diffraction gratings.* Quantum Electronics, IEEE Journal of **5**, 9, (1969) 454.

[Tre00]   Rick Trebino. *Frequency-Resolved Optical Gating: The Measurement of Ultrashort Laser Pulses.* Kluwer Academic Publishers, 2000.

[vB01]    K. van Benthem, C. Elsässer, & R. H. French. *Bulk electronic structure of SrTiO3: Experiment and theory.* Journal of Applied Physics **90**, 12, (2001) 6156. URL `http://scitation.aip.org/content/aip/journal/jap/90/12/10.1063/1.1415766`.

[Ver68]   Hans W. Verleur, A. S. Barker, & C. N. Berglund. *Optical Properties of* $VO_2$ *between 0.25 and 5 eV.* Phys. Rev. **172**, (1968) 788. URL `http://link.aps.org/doi/10.1103/PhysRev.172.788`.

[Wal09]   Ian A. Walmsley & Christophe Dorrer. *Characterization of ultrashort electromagnetic pulses.* Adv. Opt. Photon. **1**, 2, (2009) 308. URL `http://aop.osa.org/abstract.cfm?URI=aop-1-2-308`.

[Wal11]   S. Wall, D. Brida, S. R. Clark, H. P. Ehrke, D. Jaksch, A. Ardavan, S. Bonora, H. Uemura, Y. Takahashi, T. Hasegawa, H. Okamoto, G. Cerullo, & A. Cavalleri. *Quantum interference between charge excitation paths in a solid-state Mott insulator.* Nat Phys **7**, 2, (2011) 114. URL `http://dx.doi.org/10.1038/nphys1831`.

[Wal12]   S. Wall, D. Wegkamp, L. Foglia, K. Appavoo, J. Nag, R.F. Haglund, J. Stähler, & M. Wolf. *Ultrafast changes in lattice symmetry probed by coherent phonons.* Nat Commun **3**, (2012) 721. URL `http://dx.doi.org/10.1038/ncomms1719`.

[Wal13]   S. Wall, L. Foglia, D. Wegkamp, K. Appavoo, J. Nag, R. F. Haglund, J. Stähler, & M. Wolf. *Tracking the evolution of electronic and structural properties of* $VO_2$ *during the ultrafast photoinduced insulator-metal transition.* Phys. Rev. B **87**, (2013) 115126. URL `http://link.aps.org/doi/10.1103/PhysRevB.87.115126`.

[Weg11]   D. Wegkamp, D. Brida, S. Bonora, G. Cerullo, J. Stähler, M. Wolf, & S. Wall. *Phase retrieval and compression of low-power white-light pulses.* Applied Physics Letters **99**, 10, (2011) . URL `http://scitation.aip.org/content/aip/journal/apl/99/10/10.1063/1.3635396`.

[Weg13]   Daniel Wegkamp, Michael Meyer, Clemens Richter, Martin Wolf, & Julia Stähler. *Photoinduced work function modifications and their effect*

*on photoelectron spectroscopy.* Applied Physics Letters **103**, 15, (2013) . URL http://scitation.aip.org/content/aip/journal/apl/103/15/ 10.1063/1.4823591.

[Weg14] Daniel Wegkamp, Marc Herzog, Lede Xian, Matteo Gatti, Pierluigi Cudazzo, Christina L. McGahan, Robert E. Marvel, Jr Richard F. Haglung, Angel Rubio, Martin Wolf, & Julia Stähler. *Instantaneous Band Gap Collapse in Photoexcited monoclinic* $VO_2$ *due to Photocarrier Doping.* Phys. Rev. Lett. **accepted**.

[Wen94] Renata M. Wentzcovitch, Werner W. Schulz, & Philip B. Allen. $VO_2$*: Peierls or Mott-Hubbard? A view from band theory.* Phys. Rev. Lett. **72**, (1994) 3389. URL http://link.aps.org/doi/10.1103/PhysRevLett.72.3389.

[Wes61] Sven Westman. *Note on a Phase Transition in* $VO_2$. Acta Chemica Scandinavica **15**, (1961) 217.

[Wu98] Z P Wu, S Yamamoto, A Miyashita, Z J Zhang, K Narumi, & H Naramoto. *Single-crystalline epitaxy and twinned structure of vanadium dioxide thin film on (0001) sapphire.* Journal of Physics: Condensed Matter **10**, 48, (1998) L765. URL http://stacks.iop.org/0953-8984/10/i=48/a=002.

[Yos14] Rikiya Yoshida, Takashi Yamamoto, Yukiaki Ishida, Hiroki Nagao, Tsubasa Otsuka, Kuninari Saeki, Yuji Muraoka, Ritsuko Eguchi, Kyoko Ishizaka, Takayuki Kiss, Shuntaro Watanabe, Teruto Kanai, Jiro Itatani, & Shik Shin. *Ultrafast photoinduced transition of an insulating* $VO_2$ *thin film into a non-rutile metallic state.* Phys. Rev. B **89**, (2014) 205114. URL http://link. aps.org/doi/10.1103/PhysRevB.89.205114.

[Yua12] Xun Yuan, Yubo Zhang, Tesfaye A. Abtew, Peihong Zhang, & Wenqing Zhang. $VO_2$*: Orbital competition, magnetism, and phase stability.* Phys. Rev. B **86**, (2012) 235103. URL http://link.aps.org/doi/10.1103/PhysRevB. 86.235103.

[Yua13] Xun Yuan, Wenqing Zhang, & Peihong Zhang. *Hole-lattice coupling and photoinduced insulator-metal transition in* $VO_2$. Phys. Rev. B **88**, (2013) 035119. URL http://link.aps.org/doi/10.1103/PhysRevB.88.035119.

[Zee99] Erik Zeek, Kira Maginnis, Sterling Backus, Ulrich Russek, Margaret Murnane, Gérard Mourou, Henry Kapteyn, & Gleb Vdovin. *Pulse compression by use of deformable mirrors.* Opt. Lett. **24**, 7, (1999) 493. URL http:// ol.osa.org/abstract.cfm?URI=ol-24-7-493.

[Zei92] H. J. Zeiger, J. Vidal, T. K. Cheng, E. P. Ippen, G. Dresselhaus, & M. S. Dresselhaus. *Theory for displacive excitation of coherent phonons.* Phys. Rev. B **45**, (1992) 768. URL http://link.aps.org/doi/10.1103/PhysRevB.45. 768.

[Zha06]   Jin Zhao, Bin Li, Ken Onda, Min Feng, & Hrvoje Petek. *Solvated Electrons on Metal Oxide Surfaces.* Chemical Reviews **106**, 10, (2006) 4402. URL `http://pubs.acs.org/doi/abs/10.1021/cr050173c`.

[Zyl75]   A. Zylbersztejn & N. F. Mott. *Metal-insulator transition in vanadium dioxide.* Phys. Rev. B **11**, (1975) 4383. URL `http://link.aps.org/doi/10.1103/PhysRevB.11.4383`.

# List of Publications

## Publications within this thesis

D. Wegkamp, D. Brida, S. Bonora, G. Cerullo, J. Stähler, M. Wolf and S. Wall, *Phase retrieval and compression of low-power white-light pulses*,
Applied Physics Letters **99**, (2011), 101101

S. Wall, D. Wegkamp, L. Foglia, K. Appavoo, J. Nag, RF. Haglund Jr, J. Stähler and M. Wolf, *Ultrafast changes in lattice symmetry probed by coherent phonons*,
Nature Communications **3**, (2012), 721

S. Wall, L. Foglia, D. Wegkamp, K. Appavoo, J. Nag, RF. Haglund Jr, J. Stähler and M. Wolf, *Tracking the evolution of electronic and structural properties of VO2 during the ultrafast photoinduced insulator-metal transition*,
Physical Review B **87**, (2013), 115126

D. Wegkamp, M. Meyer, C. Richter, M. Wolf and J. Stähler, *Photoinduced work function modifications and their effect on photoelectron spectroscopy*,
Applied Physics Letters **103**, (2013), 151603

D. Wegkamp, M. Herzog, L. Xian, M. Gatti, P. Cudazzo, C.L. McGahan, R.E. Marvel, R.F. Haglund Jr, A. Rubio, M. Wolf and J. Stähler, *Instantaneous band gap collapse in photoexcited monoclinic VO$_2$ due to photocarrier doping*,
Physical Review Letters **113**, (2014), 216401

## Publications concerning other topics

J.-C. Deinert, D. Wegkamp, M. Meyer, C. Richter, M. Wolf, and J. Stähler, *Ultrafast exciton formation at the ZnO(10$\bar{1}$0) surface*,
Physical Review Letters **113**, (2014), 057602

M. Meyer, M. Bertin, U. Bovensiepen, D. Wegkamp, M. Krenz and M. Wolf, *Ultrafast Dynamics at the Na/D$_2$O/Cu(111) Interface: Electron Solvation in Ice Layers and Na$^+$-Mediated Surface Solvation*,
The Journal of Physical Chemistry C **115**, (2010), 204

# In preparation

J. Stähler, J.-C. Deinert, D. Wegkamp, S. Hagen, M. Wolf, *Real time measurement of the vertical binding energy during the birth of a solvated electron*,
Submitted to Journal of the American Chemical Society

J. Stähler, D. Wegkamp and S. Wall,
*The photoinduced phase transition in VO$_2$*,
Invited for Progress in Surface Science

# Academic curriculum vitae

Daniel Wegkamp
12051 Berlin

---

| | |
|---|---|
| **15.10.1982** | Born in Coburg, Germany |
| **1989-1993** | Grundschule Ketschendorf, Coburg |
| **1993-2002** | Gymnasium Casimirianum, Coburg |
| **2002-2003** | Alternative civilian service (in lieu of military service) at the Klinikum Coburg, Coburg |
| **2003-2009** | Study of Physics, Freie Universität Berlin |
| **2009** | Diploma in the group of Prof. Dr. Martin Wolf at the Freie Universität Berlin with the topic: *Schnelle Elektronendynamiken an Grenzflächen untersucht mit einer NOPA-basierenden Femtosekunden-Lichtquelle* |
| **2009-2014** | PhD thesis regarding *Ultrafast electron dynamics and the role of screening* in the Department of Physical Chemistry (Prof. Dr. Martin Wolf) at the Fritz Haber Institute of the Max Planck Society in Berlin and the Free University Berlin |

# Acknowledgments

An erster Stelle möchte ich Martin Wolf dafür danken, dass er es mir ermöglicht hat über viele Jahre hinweg im Zuge meiner Doktorarbeit zu forschen. Die Ausstattung in Labor und Büro lies nichts zu wünschen übrig, was mir die Arbeit ungemein erleichtert hat. Viele angeregte Diskussionen, meist über Physik, manchmal auch über das kreative Chaos auf meinem Schreibtisch, haben mir sehr geholfen und viel Spass gemacht.

Martin Weinelt, meinem Zweitgutachter, danke ich ganz herzlich für sein stetes und stets gut gelauntes Interesse an meiner Arbeit. Auch im Zusammenhang mit der von ihm ins Leben gerufenen Doktorandenschule *Dynamics in New Light* (Leibniz Graduate School), die alle Teilnehmer sowohl in finanzieller Hinsicht als auch durch exzellente wissenschaftliche Betreuung in Form von Seminaren, Kursen und kleinen Tagungen unterstützt hat, habe ich viel von ihm gelernt.

Julia Stähler, in deren Arbeitsgruppe ich in den letzten Jahren schuften durfte, danke ich als erstes dafür, dass sie mich vor vielen vielen Jahren überredet hat in ihrer Gruppe anzufangen, auch wenn das Labor damals aus nichts als einem leeren Raum bestand. Immerhin Parkettfußboden. Mittlerweile hat sich das Labor mehr ins Gegenteil eines leeren Raumes gewandelt, als einem manchmal lieb ist, aber dankbar bin ich immernoch. Bei den meist freundlichen Meinungsverschiedenheiten zur Interpretation der Daten (Bis jetzt konnten wir uns ja immer einigen.) angefangen, über viel konstruktive Kritik und Unterstützung beim verfassen von Texten bis hin zum ein oder anderen Feierabend-Bier (zumindest bevor der Nachwuchs kam) fühlte ich mich immer bestens betreut. Wenn per Smartphone am Wochenende noch weiteranalysiert wurde, dann manchmal auch etwas zu gut.

A lot of thanks to Simon Wall, with whom I shared an office for a long time. Starting from exciting and funny lab-days, over countless discussions regarding related or totally unrelated problems in physics and life, and ending at beer and champions league, I have learned quite a lot from you. See you soon!

Es ist immer beruhigend, wenn man nicht der einzige ist, den die Arbeit in den Wahnsinn zu treiben droht. Liebe Melanie, danke, dass Du mich mit davor bewahrt hast. Deine Gesellschaft an langen Messtagen und danach bei Hanoi oder Pizza essen waren immer ein Vergnügen.

Micha, schon bei meiner Diplomarbeit hast Du mir gezeigt wie man 2PPE Experimente durchführt. Dann am FHI wie man Elektronen solvatisiert und mit in Stickstoff eingefrorenen Bananen Nägel ins Holz hämmert. Man hat immer viel Freude mit Dir und deiner lieben Familie.

Die meisten der bis jetzt erwähnten sind in den letzten Jahren auch über die Arbeit hinaus gute Freunde geworden. überhaupt ist es schön, dass das Verhältnis im Grunde zu allen anderen Kollegen in der Abteilung PC und darüber hinaus am Institut, sehr gut war. Lieben Dank an die Mitlaboranten und Kollegen Jan, Marc, Alex, Lutz, Clemens, Ralph, Laura, Lea, Selene, Claude und wie sie nicht alle heißen.

Technisch bestens unterstützt gefühlt habe ich mich vor allem von Marcel (Computer, Laser, Messzeug), Albrecht und Sven (UHV und basteln). Ihr wart immer eine große Hilfe und ich danke euch stellvertretend für die weiteren Techniker-Kollegen und das Office Management. So heißt das heutzutage, glaube ich. Oder, Manuel?

Natürlich könnte man diese Liste noch eine ganze Weile fortsetzen. Oder man sagt einfach, dass man sich in den letzten Jahren an seinem Arbeitsplatz wohl gefühlt hat und immer auf Hilfe und Unterstützung vieler zählen konnte. Entschuldigung an all die Vergessenen.

Über das Arbeitsumfeld hinaus habe ich mich in den letzten Jahren immer unterstützt und sicher gefühlt. Das habe ich meiner lieben Familie zu verdanken, von der man keine bessere haben könnte. Und größer geworden ist sie auch. Erst ein lieber Gruße nach Finnland, dann zum wichtigsten Menschen: Auch wenn dir unser Sohn Jonathan diesbezüglich Konkurrenz macht, liebste Anna, den allergrößten Dank, dass Du es mit mir, trotz meiner vielen langen Arbeitstage, ausgehalten hast. Ich kann es mir nicht ohne Dich vorstellen.

# Selbstständigkeitserklärung gemäß § 7 der Promotionsordnung

Sämtliche verwendeten Hilfsmittel, Hilfen und Quellen sind an der entsprechenden Stelle angegeben. Ich versichere, dass ich auf dieser Grundlage diese Arbeit selbstständig verfasst habe. Diese Arbeit wurde bisher weder in gleicher noch ähnlicher Form einer anderen Prüfungskomission vorgelegt oder veröffentlicht.

Berlin, den

Daniel Wegkamp